Optical and excitonic properties of 2D colloidal nanocrystals: type-II CdSe/CdTe core/crown hetero-structures and CsPbBr3 perovskite nanoplatelets

Violette Steinmetz

THÈSE DE DOCTORAT
DE SORBONNE UNIVERSITÉ

Spécialité : Physique

École doctorale n°564: Physique en Île-de-France

réalisée

à l'Institut des Nano-Sciences de Paris

sous la direction de Laurent Legrand

co-encadrée par Thierry Barisien

présentée par

Violette STEINMETZ

pour obtenir le grade de :

DOCTEUR DE SORBONNE UNIVERSITÉ

Sujet de la thèse :

Optical and excitonic properties of 2D colloidal nanocrystals: type-II CdSe/CdTe core/crown hetero-structures and $CsPbBr_3$ perovskite nanoplatelets

soutenue le 5 Octobre 2020

devant le jury composé de :

Mme	Emmanuelle DELEPORTE	Rapporteure
M.	Philippe TAMARAT	Rapporteur
Mme	Paulina PLOCHOCKA	Examinatrice
M.	Jérôme TIGNON	Examinateur
M.	Laurent LEGRAND	Directeur de thèse
M.	Thierry BARISIEN	Co-encadrant

Remerciements

J'aimerais tout d'abord remercier les membres du jury d'avoir pris le temps d'évaluer ces travaux de thèse, les rapporteurs : Philippe Tamarat et Emmanuelle Deleporte, ainsi que les examinateurs : Paulina Plochocka Maude et Jérôme Tignon.

Je souhaite ensuite remercier chaleureusement mes deux encadrants : Thierry et Laurent. Ce fut un plaisir de travailler avec vous, vous m'avez beaucoup appris et vous avez toujours été disponibles pour répondre à mes nombreuses interrogations et doutes. Je me suis beaucoup amusée au cours de ces trois années (et demi) grâce à vous et pour cela merci beaucoup !

J'ai pu bénéficier, tout au long de cette thèse, du soutien technique des trois ingénieurs de l'équipe PHOCOS : Florent Margaillan, Mathieu Bernard et Maxime Vabre et je tiens à les en remercier. Merci pour votre disponibilité, votre efficacité et votre bonne humeur ! Je souhaite aussi remercier Silbe Majrab et Francis Breton pour l'interfaçage des différentes expériences, cela m'a permis de gagner un temps précieux !

J'aimerais aussi remercier tous les membres de l'équipe PHOCOS : Maria, Fred, Christophe et Alex, qui ont, à travers leur aide théorique et de nombreuses discussions scientifiques, participé à ces travaux de thèse. J'aimerais aussi grandement remercier Julien, qui m'a beaucoup aidée en début de thèse que ça soit scientifiquement ou moralement.

Pas de spectroscopie possible sans objet à étudier ! C'est pourquoi je tiens à remercier vivement Emmanuel Lhuillier, Sandrine Ithurria et Marion Dufour, grâce à qui j'ai pu étudier ces beaux objets que sont les nano-plaquettes et qui nous ont apporté leurs expertises des cristaux colloïdaux. Merci à eux pour ces innombrables batchs !

Au cours de cette thèse j'ai pu collaborer avec de nombreuses personnes à travers le monde, ce qui a été très enrichissant d'un point de vue personnel et scientifique. J'aimerais tout d'abord remercier chaleureusement Raj: I hope you had as much fun working with me than I had working with you ! J'aimerais aussi remercier les différentes personnes avec qui j'ai travaillé lors des deux semaines passées au HFML à Nijmegen : Yuttapoom Puttisong, Richard Chen, Anatolie Mitioglu et Peter Christianen. Je tiens aussi à remercier Akshay Rao et son groupe au Cavendish Laboratory et particulièrement David Paleček pour m'avoir accueillie pendant une semaine à Cambridge et permis de découvrir et d'utiliser leur setup de transient absorption. De plus, cette thèse a été enrichie par de nombreux travaux théoriques et numériques, j'aimerais donc également remercier Juan Climente, Josep Planelles et le groupe de Kais Boudjaria pour leurs soutiens.

Ce fut un plaisir de travailler à l'INSP grâce aux différentes personnes qui y travaillent, j'aimerais donc remercier tous ceux avec qui j'ai pu interagir de près ou de loin au cours de ces trois dernières années et tout particulièrement Cécile Lefebvre, Aline Levaillant, Cindy Gobing, Isabelles Borges, Myriam Melois et Cécile Duflot, votre bonne humeur et votre gentillesse ont rendu les différentes tâches administratives beaucoup plus plaisantes, l'ensemble de l'équipe PMTeQ, avec qui j'ai partagé un couloir et différentes salles de manip, le service des basses

températures, mon parrain, Max Marangolo, et mon tuteur, Olivier Pluchery.

L'INSP ne serait pas ce qu'il est sans ses nombreux doctorants et stagiaires, j'aimerais donc les remercier. Ceux qui sont déjà docteurs et qui m'ont montré la voie : Camille (zout and cat power forever), Suzanne (j'ai hâte de redevenir ta collègue et co-bureau), Clément (on n'était peut-être pas les représentants des doctorants les plus sérieux mais avoir réussi à diffuser la coupe du monde de foot en 317 était quand même une belle réussite), Sunniva, Bertille, Richard, Dan, Juan, Piotr, Meriam, et les « soon-to-be » docteurs à qui je souhaite bon courage pour la suite : Ronei (why is Brazil so far away ?), Oliviero (you finally admitted that the CROUS was not that bad !), Ronan et Marine (best représentants des doctorants ever), Thomas, Charlie, Medhi, Sophie, Audrey, Mehdi, Sarah, Thibault D., Thibaut L., Arnaud et Samuel. Un grand merci à eux pour ces innombrables repas au CROUS, mots croisés, bières du mercredi soir et différentes soirées raclette/pizza/crêpes !

J'aimerais aussi remercier mes amis qui m'ont soutenue pendant ces trois dernières années en m'offrant de grands moments de rigolade et de détente : Mathis, Basile, Léon, Ali, Kévin, Alix, Nanna, Stelios, Élise, Juliette, Ralph, les Upplads, Marie (on se refait un petit confinement bientôt ?), Camille, Laure, Emma-Louise, Patou et Elsa.

Finalement, merci à ma famille, j'espère que vous avez compris ce qu'étaient les cristaux colloïdaux, et merci à Angus, pour la relecture de ce manuscrit, mais surtout pour tout le reste.

Contents

Introduction

Since the invention of the first transistors, much effort has been dedicated to the miniaturization of electronic components, bringing about the tremendous increase of computing power observed in the last fifty years. In parallel to these industrial innovations, miniaturization of semiconducting devices has also led to the creation of objects with dimensions smaller than the mean free path of electrons (given by the De Broglie wavelength), resulting in the confinement of the charge carriers in these structures. The motion of the electrons is strongly impacted in the confined directions, leading to new properties. The case of quantum dots, where the three dimensions are concerned, is arguably offering the most striking features with the complete discretization of the electronic energy levels. The energy of these levels being determined by the size and shape of the dots, the optical properties of these objects are easily tunable by modifying their geometries.

The first quantum wells, where carriers are confined in only one direction, were obtained in the 70's, through epitaxial growth. Then, in the beginning of the 80's, the group of Ekimov in Russia and the group of Brus in the USA observed the first nano-structures with confinement in all three directions [1,2], opening the path to the study of nano-objects. In the 90's, the control of the nucleation and growth of colloidal nanocrystals through chemical means revolutionized the field [3–5]. Colloidal nanocrystals are composed of a semiconducting core surrounded by a shell of organic ligands, which allows their stabilization in solution, prevents their aggregation, and provides a passivation of their surface. They offer a lot of advantages: being diluted in solution, they are easy to process; their sizes and shapes are easily tunable and their surfaces can be treated to induce interactions with specific molecules.

The fields of applications for colloidal structures are numerous. The one with the most striking results is the field of light display. Indeed, nanocrystals can already be found in some televisions, like the Samsung QLED. Efforts are also underway to use colloidal nanocrystals as biological labels [6, 7], lasing media [8], photo-detectors [9, 10], solar cells [11] or luminescent solar concentrators [12], among other things. More generally, the colloidal crystals family also represents a fantastic playground to probe the quantum theory of confined systems with possible applications in quantum technologies [13].

From the first spherical nanocrystals of the 90's, new syntheses have emerged allowing the formation of colloids with various shapes. In 2008, the LPEM group of the ESPCI have synthesized the first 2D shaped colloidal crystals: CdSe nanoplatelets (NPLs) [14]. These structures are sometimes considered as colloidal quantum wells, since they measure only a few atomic layers in thickness, while their lateral dimensions are much larger. Their thickness being controlled at the mono-layer scale, they offer a homogeneous confinement, leading to sharp emission and absorption lines. Furthermore, their large lateral area results in a large absorption cross section [15] and a shorter radiative lifetime compared to nanocrystals [16]. These properties are interesting for some of the applications mentioned above, such as lasing

[17]. Since the first core-only CdSe NPLs development, different structures were synthesized, such as core/shell [18] and core/crown [19–21] hetero-structures. The core/crown CdSe/CdTe NPLs, first synthesized in 2014, are greatly interesting from the fundamental point of view since they hold spatially indirect excitons: the electron, which is confined in the CdSe core of the NPL, being surrounded by the hole wave-function, which is confined in the CdTe crown [20]. This separation of the charge carriers induces different properties such as a red shift of the emission and a lengthening of the excitonic lifetime, two properties that may prove decisive for applications based on high gain media. Indirect excitons have been extensively studied in epitaxial quantum wells and superlattices [22–24], giving indications about the excitonic fine structure, and the role of symmetry and the interface in these core/crown NPLs. Despite several studies already carried out on these structures [25–28], many features of the excitations remain unclear such as the precise nature of the excitation (exciton or more complex charged species), the origin of the large linewidths or the excitonic fine structure. A large part of this work is thus dedicated to the study of the indirect exciton in these CdSe/CdTe core/crown NPLs.

This Thesis was also partly dedicated to the study of another type of semiconducting NPLs: cesium lead bromide ($CsPbBr_3$) NPLs. In the last five years, nanocrystals made of cesium lead halide perovskite have emerged as interesting alternative materials due to their high emission efficiency obtained without any protective shell [29]. The nature of the excitation and its fine structure have been quasi-exclusively studied in cubic $CsPbBr_3$ nanocrystals [30–33]. However, concerning their 2D counterparts, $CsPbBr_3$ NPLs, works have so far been limited to the investigation of the basic optical and structural properties [34–36]. There is thus still a large field opening that should aim at a deep understanding of the relationship between the dimensionality and the electronic structure in perovskite NPLs.

The thesis is organized as follows:

- In Chapter I, we present the basic concepts used in this work concerning excitons in II-VI semiconducting nano-structures. After a general summary of excitonic properties, the focus will be put on indirect excitons. The electronic fine structure of the indirect exciton in core/crown CdSe/CdTe NPLs is also addressed.

- Chapter II is dedicated to the presentation of the experimental set-ups used throughout this PhD to measure the absorption, photoluminescence and time-resolved photoluminescence of our samples.

- In Chapter III, the basic optical properties (absorption and photoluminescence) of relatively dense films of core/crown CdSe/CdTe NPLs is studied as a function of temperature. Then, the response of single CdSe/CdTe NPLs is presented and analyzed. These experiments, coupled to numerical simulations of the excitations' energy in these NPLs, highlight the importance of the LO phonon/exciton coupling in these NPLs, as well as the amplitude of spectral diffusion, these phenomena rationalizing the large emission linewidth observed on dense films of NPLs.

- In Chapter IV, we present the experiments carried out at the High Field Magnet Laboratory (HFML) in Nijmegen, where the degree of polarization of the luminescence of CdSe/CdTe NPLs as well as the time-resolved photoluminescence were recorded as a function of the mag-

netic field. We show that the experimental data can be analyzed with a model for the electronic fine structure comprising two linearly polarized bright states that seem to be weakly coupled to the dark states manifold.

- In Chapter V, a slightly different type of object is studied: core/alloyed crown $CdSe/CdSe_{1-x}Te_x$. For x between 0.6 and 0.8, these NPLs show a bicolor emission. To understand the emission structure, the photoluminescence of single NPLs is measured. Time-resolved photoluminescence measurements were also carried out in films for different crown compositions, *i.e.* different values of x.

- Finally, Chapter VI focuses on cesium lead bromide NPLs. After a short description of perovskite nanocrystals, we present a structural characterization of our samples through optical measurements and transmission electronic microscopy imaging. We show that a simple effective mass model allows us to reproduce the evolution of the excitonic transitions with the thickness of the NPLs. In order to unravel the electronic fine structure in these NPLs, a preliminary study of the exciton relaxation dynamics in these NPLs is also presented. The data are used to probe the models that have been so far developed to describe the response of 0D perovskite nanocrystals.

Chapter I

Indirect excitons in II-VI colloidal NPLs

This chapter will be focused on the properties of semiconductors belonging to the II-VI group (CdSe, CdTe), as most of the work presented in this thesis is centered around the properties of CdSe/CdTe nanoplatelets (NPLs). The properties of perovskite nano-structures will be addressed in Chapter VI, along with the rest of the work on these objects.

In the first section, a general description of excitons in colloidal NPLs is given. The specific properties of indirect excitons in hetero-structures is addressed in the second section. Finally, in the last section, the electronic fine structure of the indirect exciton in core/crown NPLs is presented.

I.1 Exciton in colloidal nanoplatelets

I.1.1 Bulk semiconductors

In solids, electronic carriers are subjected to a periodic potential created by the ions of the lattice. The Bloch theorem allows one to describe the electronic states in a periodic potential as a sum of Bloch waves, $\Psi_\lambda(\mathbf{r},\mathbf{k})$, expressed as follows [37]:

$$\Psi_\lambda(\mathbf{r},\mathbf{k}) = u_\lambda(\mathbf{r},\mathbf{k})e^{i\mathbf{k}\cdot\mathbf{r}}, \tag{I.1}$$

where the functions $u_\lambda(\mathbf{r},\mathbf{k})$ are Bloch functions, which have the periodicity of the lattice ($u_\lambda(\mathbf{r}+\mathbf{R},\mathbf{k}) = u_\lambda(\mathbf{r},\mathbf{k})$, where $\mathbf{R}$ is the real space lattice vector) and which vary quickly on the unit cell scale. They form a complete basis and are mutually orthogonal. The envelope function, which describes the variation on a scale larger than the unit cell, has the form of a plane wave $e^{i\mathbf{k}\cdot\mathbf{r}}$ for infinite crystals. The subscript λ allows us to distinguish between different local waves with the same k-vector. The energies of these wave-functions form bands, $E_\lambda(\mathbf{k})$, in k-space.

Semiconductors are materials where the Fermi level lies between two of these bands, where no electronic states are available. The electronic properties of these materials are then governed by the bands just below and above the Fermi level: the valence and conduction bands. In an undoped (intrinsic) semiconductor, the conduction band is empty of carriers while the valence band is full. II-VI semiconductors have a direct band-gap, meaning that the bottom (top) of the conduction (valence) band are found at the same wave-vector $\mathbf{k}$. This band-gap is found at the Γ point of the Brillouin zone at $\mathbf{k} = 0$, as can be seen, for example, from the band diagram of CdSe presented in figure I.1.a.

The optical properties and especially the emission properties of such a semiconductor are mainly governed by this band edge. It is thus usual to simplify the band diagram close to the band gap resorting to the effective mass approximation. This approximation helps to take into account the complex potential of the lattice felt by the carriers, while ignoring the atoms [37]. The carriers are described as free particles, however to do so their mass is replaced by an 'effective' mass, different from the mass of free electrons. In the effective mass approximation the vicinity of the maxima and minima of the conduction and valence bands are well approximated by parabolic functions with energies $E_c(\mathbf{k}) = \frac{\hbar^2 k^2}{2m_e^*} + E_g$ for the conduction band and $E_v(\mathbf{k}) = -\frac{\hbar^2 k^2}{2m_v^*}$ for the valence band, where the reference of energy is taken at the top of the valence band. E_g is the band-gap energy and $m_{c,v}^*$ are the effective masses of the carriers in the conduction and valence band and are given by the curvature of the bands at the Γ point. In II-VI semiconductors, the electron and hole effective masses are typically $\sim 0.1\ m_0$, where m_0 is the free electron mass.

In CdSe and CdTe, the conduction band is mainly formed from the 5s orbitals of the Cadmium metallic cation, while the valence band is mainly formed from the 4p orbitals of the Selenium or Tellurium anions. Due to its p nature, the valence band has a six-fold degeneracy (p_x, p_y, p_z + spin) while the conduction band is only two-fold degenerate (spin only). The spin orbit coupling will actually lift the degeneracy of the valence bands at the Γ point by an energy Δ_{SO}. This results into two sets of bands with different total angular momenta $J = L + S$: the so-called 'split-off' band with $J = 1/2$ and the heavy and light hole bands with $J = 3/2$. The heavy ($M_J = 3/2$) and light hole ($M_J = 1/2$) bands remain degenerate at k = 0, however they split for k $\neq$ 0, due to the difference in their effective mass. Figure I.1.b summarizes the band edge in a II-VI bulk semiconductor.

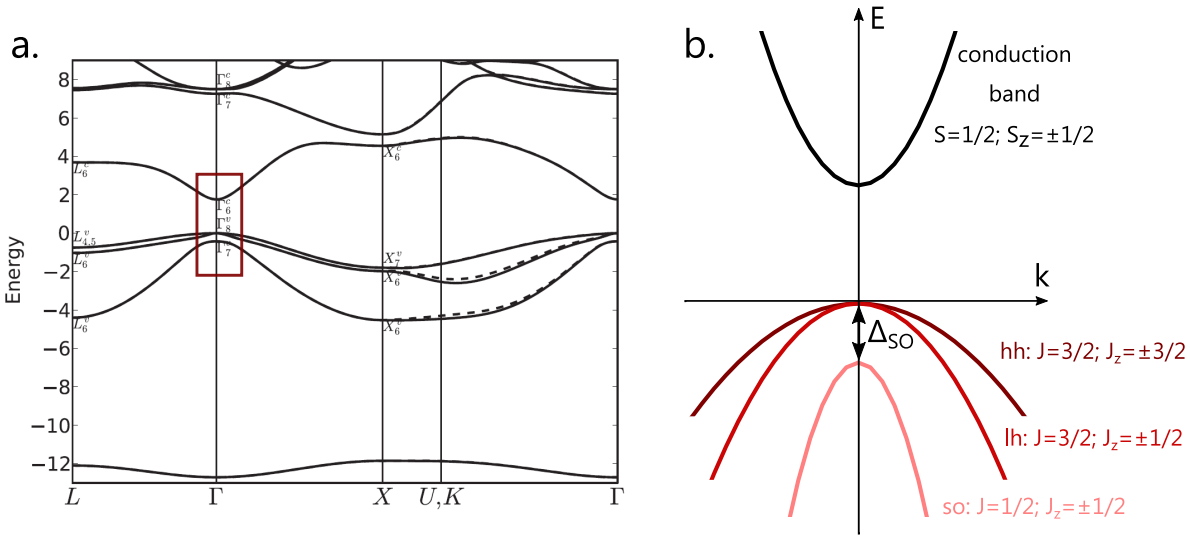

Fig. I.1 *(a) Band diagram of bulk CdSe (figure reproduced from ref. [38]). (b) Band edge in a II-VI semiconductor in the parabolic approximation. The heavy (light) hole band is labeled 'hh' ('lh'), while the split-off band is labeled 'so'.*

I.1.2 Electronic confinement

At a given temperature T, charge carriers are characterized by their de Broglie wavelength, λ_B. In a semiconducting structure, it is given by:

$$\lambda_B = \frac{h}{\sqrt{2\pi m^* k_B T}}. \tag{I.2}$$

At low temperature, the de Broglie wavelength of electrons, with an effective mass $m^* = 0.1\ m_0$, is typically ~ 100 nm. If the structure has one or several dimensions comparable to this wavelength, a spatial confinement of the carriers appears, which will greatly impact its electronic properties. When only one direction is confined, the structure is referred to as a 2D system (quantum well), when two directions are confined, the term 1D system is used (quantum wires or colloidal nanorods), finally systems confined in all three directions, are referred to as 0D systems (quantum dots or nanocrystals). Colloidal NPLs due to their thickness of only few atomic planes fall in the category of 2D systems, even if their lateral dimensions are finite.

a) Single particle electronic states

The Bloch theorem presented above is derived in the framework of an infinite material or in a material with periodic boundaries conditions. However, these conditions are not fulfilled anymore when one or several dimensions of a structure become smaller than the size of the electron and hole wave-functions. In the confined directions, the envelope function part of the carriers' wave-function cannot be described by plane waves anymore, since the wave functions have to vanish at the interface of the material. The plane waves have thus to be replaced by quantized standing wave functions, ζ_n, which are equal to 0 outside of the objects and where n denotes their energetic levels [37].

In the following, we are only interested in the band-edge excitation, close to $\mathbf{k} = 0$. In this case, it is common to approximate the Bloch function $u_\lambda(\mathbf{r}, \mathbf{k})$ to $u_\lambda(\mathbf{r}, \mathbf{k} \simeq 0)$ (their values at $\mathbf{k} = 0$), since the Bloch function do not vary much in the vicinity of the Γ point [37]. With this approximation, we can write the wave functions of single carrier in 2D (confined along the z-direction) and 0D structure as:

$$\begin{aligned} &\text{2D system}: \quad \Psi(\mathbf{r}, \mathbf{k}) = L_z^{-1} \zeta_n(z) e^{i(k_x x + k_y y)} u_\lambda(\mathbf{r}, \mathbf{k} \simeq 0), \\ &\text{0D system}: \quad \Psi(\mathbf{r}, \mathbf{k}) = \zeta_n(x)\zeta_m(y)\zeta_p(z) u_\lambda(\mathbf{r}, \mathbf{k} \simeq 0). \end{aligned} \tag{I.3}$$

As for any standing waves, the wave vectors, k_i, along the confined directions become quantized, with $k_i = \frac{n\pi}{L_i}$ (L_i being the size of the structure in the confined direction). In the case of an infinite quantum well with infinite potential barrier, the ζ_n functions are found to be sine and cosine functions according to the parity of n [37]:

$$\begin{aligned} \zeta_n^{even}(z) &= \sqrt{\frac{2}{L_z}} \cos\left(\frac{n\pi}{L_z}\right) \quad \text{for even values of } n, \\ \zeta_n^{odd}(z) &= \sqrt{\frac{2}{L_z}} \sin\left(\frac{n\pi}{L_z}\right) \quad \text{for odd values of } n. \end{aligned} \tag{I.4}$$

The quantization of the k-vector impacts the energy bands. In the case of an infinite 2D system, the energy states along the confined direction will become discrete. The energy of free carriers in the conduction band can thus be written:

$$E(n, k_x, k_y) = E_g + \frac{\hbar^2}{2m^c_{eff}}(k_x^2 + k_y^2 + \frac{\pi^2 n^2}{L_z^2}). \tag{I.5}$$

The energy of the band gap is increased by a value $E_n = \frac{\hbar^2\pi^2n^2}{2m_c^*L_z^2}$ due to the effect of the confinement. It is thus a powerful tool to tune the optical properties of a nano-structure since the energy of the lowest transition can be changed by reducing the dimensions of a structure. In the case of an ideal 2D system, electronic bands still exist in the (x, y) plane, while this is not the case in a 0D system where only discreet transitions exist close to the band edge.

b) Exciton

The particles (or more appropriately quasi-particles) at the center of this work are not single carriers but excitons. When an electron is promoted to the conduction band it leaves a hole in the valence one. These electron-hole pairs, interacting through the Coulombic forces, form hydrogenic like systems and are called excitons.

An exciton is characterized by its Bohr radius, a_0, which is the typical length scale between its two carriers and characterizes the extent of the relative motion between the carriers. The Bohr radius is equal to:

$$a_0 = \frac{4\pi\epsilon_0\epsilon\hbar^2}{e^2\mu}, \quad \text{with} \qquad \mu = \frac{m_e^* m_h^*}{m_e^* + m_h^*}, \tag{I.6}$$

where ϵ_0 is the vacuum permittivity, ϵ the relative dielectric constant of the material, e the elementary charge and μ the reduced mass of the exciton.

The influence of confinement can be also determined by comparing the exciton Bohr radius to the dimensions of the nano-structure. In CdSe and CdTe, the Bohr radii are respectively equal to 5.6 nm and 7.5 nm [39]. The thickness of the core/crown CdSe/CdTe NPLs studied in this work is smaller than 2 nm, the confinement in the z-direction will thus have a large impact on the properties of the exciton. Since their lateral dimensions range between 8 and 50 nm, the confinement of the excitons in the lateral plane is much weaker or even nonexistent. However, ref. [40] showed that in small NPLs (< 10 nm) lateral confinement was still important and could not be completely discarded. The author computed the energy and wave function of the exciton using the complete Schrödinger equation and compared it to the solution obtained when using the weak confinement approach, where lateral confinement is treated as a perturbation, and showed that large discrepancies existed between the two for small NPLs.

An exciton is also characterized by its binding energy. The Coulombic interaction between the hole and the electron being attractive, it lowers the energy of the excitonic system, by a value, E_b, called the binding energy. In a bulk semiconductor, the binding energy is expressed from the binding energy of the hydrogen atom, $E_{Ry} = 13.6$ eV, as:

$$E_b^{bulk} = \frac{\mu}{m_0\epsilon^2}E_{Ry}, \tag{I.7}$$

where m_0 is the mass of a free electron.

In confined systems, this binding energy increases above the one of the bulk materials due to the proximity of the electron and the hole. For example, in an infinitely thin quantum well, the binding energy of an exciton increases to its limit value given as 4 E_b^{bulk} [41].

To obtain a complete description of the motion and energies of an exciton in a semiconducting structure, its Schrödinger equation has to be solved. The excitonic Hamiltonian is composed of different terms:

$$H_{exc} = H_e + H_h + V_e + V_h + V_{e-h}, \tag{I.8}$$

where H_e and H_h account for the kinetic energy of the electron and hole, V_e and V_h are the confinement potentials, finally V_{e-h} describes the different electron/hole interactions. V_{e-h} is dominated by the Coulombic interaction between the electron and the hole but it also includes the exchange interaction (or indirect Coulomb term) which plays a major role in the determination of the fine structure of the exciton as we will see in the final section of this chapter.

The Schrödinger equation describing the exciton can only be analytically solved for specific geometries (spherical dot...) and under specific approximations such as the strong or weak confinement regimes. The strong confinement approach is a powerful tool to derive the exciton energy and wave functions in highly confined structures such as small nanocrystals [39]. Under this condition, the hole and electron wave functions can be decorrelated and the Coulombic interaction treated as a perturbation. Here this approach is relevant along the thickness of the NPL. However, for large enough NPLs, the strong confinement regime does not hold anymore in the lateral plane. The weak confinement approach, used in infinite quantum well structures, can thus be applied to treat the lateral motion of the exciton. Under weak confinement conditions, the exciton can be described by two components: the motion of its center of mass and the relative motion of its two carriers [22].

A complete study of strong and weak confinement approaches for colloidal NPLs was carried out in ref. [40]. The author shows that the excitonic ground state of square like NPLs with 'small' (< 10 nm) lateral dimensions could be well reproduced in the strong confinement approximation while for NPLs with 'large' (> 20 nm) lateral extension, the weak confinement approximation showed better results. However for intermediate cases, like rectangular NPLs with a 'small' width and a 'large' length, both approximations fail to accurately describe the exciton energy and wave functions. These tool models have to be abandoned in this case and no simple expression of the exciton energy would be really accurate. However, different numerical approaches lead to the calculations of these energies in homo and hetero-NPLs [38, 40, 42].

I.1.3 Dielectric confinement

On top of the electronic confinement, another kind of confinement also plays a major role in colloidal nano-structures: the dielectric confinement. This effect has its origin in the penetration of the electric field of the carriers outside of the nano-structure, where the dielectric constant is lower [43]. It is all the more important in colloidal objects, due to the large dielectric mismatch between the material and its environment, made of organic ligands (which have a dielectric constant much lower than the one of semiconducting materials) or even the vacuum if we consider that the layer of ligands surrounding the object is too thin to be actually felt by the electromagnetic field. The strength of an electric field being inversely proportional to the dielectric constant of the medium, its leakage in the environment surrounding the nano-structure will lead to an increase of all the Coulombic-related interactions.

The effect of the dielectric confinement on the energy of the exciton is usually explained using the method of image charges (commonly used in electrostatic problems). This method simplifies calculations since it allows one to replace the electric potential of a point charge close to a dielectric interface by the sum of the electric potential created by this point charge

in a homogeneous medium and the one created by its 'image charge' (the image charge being the mirror reflection of the point charge by the interface). In this framework, the two effects of the dielectric confinement can be easily understood. The first effect is referred to as the self interaction and leads to the 'self energy correction', it takes into account the interaction of each carrier with its own charge image [44]. Being a repulsive interaction, the 'self energy' terms will increase the exciton energy. The second effect of the dielectric confinement impacts the Coulomb interaction and hence the binding energy. The interaction of each carrier with the charge image of the other has to be added to the usual Coulombic interaction of the hole and electron [44]. This interaction being attractive, it increases the binding energy of the exciton and hence decreases the overall energy of the exciton. The expression of both terms is complex and strongly dependent on the geometry of the objects under study [45]. In most cases, analytical expressions are out of reach and a quantitative estimation requires appropriate calculations. In NPLs of CdSe, the self-energy term of each carrier has been calculated to be as large as several hundreds of meV [38].

The two effects of the dielectric confinement have opposite impacts on the exciton energy. They tend to cancel each other in spherical crystals [44]. However, in nanowires it has been shown that the self energy term prevails over the increase of the binding energy, leading to a blue-shift of the exciton emission with the decrease of the dielectric constant of the surrounding medium [46]. We will see in Chapter III that the same trend is found in NPLs. Moreover, in Chapter VI and more precisely in Appendix D, these dielectric effects in cesium lead bromide homo-NPLs will also be addressed.

I.1.4 Optical properties

Excitons can be created by the absorption of a photon and in the same manner they can recombine emitting one. Excitons can be thus studied through their optical properties which will be the main focus of the present work. Here, some of the properties measurable through optical experiments are presented.

Optical selection rules

The probability of transition between two states is central to describe the optical properties of a material, as it will define the strength of an optical transition and hence shape the absorption and emission spectra.

Let us consider the interaction between a semiconducting nano-structure and an electromagnetic field (laser beam in our experiments), characterized by its potential vector $\mathbf{A} = -\frac{iE_0}{2\omega}[e^{i(\mathbf{q}\cdot\mathbf{r}-\omega t)}\mathbf{e} + c.c.]$, where E_0 is the amplitude of the incident electric field, q its wave vector, ω its frequency and $\mathbf{e}$ the polarization vector of the incoming light. The probability per unit of time, $\tilde{P}_{if}$, of having a transition from an initial electronic state $|\Psi_i\rangle$ at an energy E_i to a final electronic state $|\Psi_f\rangle$ at an energy E_f, due to the absorption of a photon, is given by the Fermi Golden rule:

$$\tilde{P}_{if} = \frac{2\pi}{\hbar}|\langle\Psi_f|\, H_{eR}\, |\Psi_i\rangle|^2 \delta[E_f - E_i - \hbar\omega], \tag{I.9}$$

where H_{eR} is the Hamiltonian describing the interaction between the electrons and the electromagnetic field. It is given by [47]:

$$H_{eR} = \frac{e}{m_0}\mathbf{A}\cdot\mathbf{p}, \tag{I.10}$$

where $\mathbf{p}$ is the momentum operator. The quadratic term in $\mathbf{A}$ has been neglected here, since they only play a role at very high intensities. Moreover, since the wavelength of the light $\lambda = \frac{2\pi}{q}$ is much larger than the dimensions of the nano-structure it interacts with, the spatial dependence of $\mathbf{A}$ can be neglected as well. This approximation is called the linear dipole approximation and results in:

$$H_{eR} \approx -i\frac{eE_0\cos(\omega t)}{m_0\omega}\mathbf{e}\cdot\mathbf{p}. \tag{I.11}$$

The occupancy of the initial and final states $|\Psi_i\rangle$ and $|\Psi_f\rangle$ has to be taken into account: no-transition from a vacant state or to an occupied one can take place. For electrons, the occupancy of a state at an energy E_i and at a temperature T is given by the Fermi-Dirac distribution $f(E_i) = (\exp\left(\frac{E_i-\mu}{k_BT}\right)+1)^{-1}$, where μ is the electron chemical potential. The probability per unit of time for an electron to undertake a transition is then:

$$P_{if} = \tilde{P}_{if}f(E_i)[1-f(E_f)]. \tag{I.12}$$

The power absorbed by the nano-structure, which is equal to the power lost by the electromagnetic field, is thus given by summing over all the different initial and final states [47]:

$$P(\omega) = \frac{2\pi}{\hbar}\frac{e^2E_0^2}{m_0^2\omega^2}\hbar\omega\sum_{i,f}|\langle\Psi_f|\,\mathbf{e}\cdot\mathbf{p}\,|\Psi_i\rangle|^2[f(E_i)-f(E_f)]\delta[E_f-E_i-\hbar\omega]. \tag{I.13}$$

From this equation, we see that the selection rules of a transition are determined by the matrix elements $\langle\Psi_f|\,\mathbf{e}\cdot\mathbf{p}\,|\Psi_i\rangle$. In a semiconductor, we can decompose the initial and final states in their envelope, $\psi_{i/f}$, and Bloch, $u_{i/f}$, functions. The orthogonality of the Bloch functions leads to:

$$\langle\Psi_f|\,\mathbf{e}\cdot\mathbf{p}\,|\Psi_i\rangle = \langle\psi_f|\psi_i\rangle\,\langle u_f|\,\mathbf{e}\cdot\mathbf{p}\,|u_i\rangle\,. \tag{I.14}$$

In this work, we will meet the concept of oscillator strength. The oscillator strength, f_{osc}, is a dimensionless quantity commonly used to quantify the transition probability P_{if}. It is originally defined by comparing the rate of a specific transition to the one of a classical single electron oscillator [48]. The oscillator strength can thus be used to compare transitions in different materials. Experimentally the oscillator strength can be deduced from the total absorption cross section. For excitonic transitions in semiconductors, the appropriate relation is [49]:

$$Nf_{osc} = \frac{4m_0\epsilon_0cn}{e^2h}\int\alpha(E)dE, \tag{I.15}$$

where n is the refractive index of the material, α its absorption coefficient, E the photon energy and N the numbers of unit cells per volume in the semiconductor.

In bulk II-VI compounds the typical values for f_{osc} are of the order of 10^{-3}-10^{-4} and the transition probability per unit cell is thus quite low. However, because of large N the absorption coefficient reaches typically 10^4-10^5 cm^{-1} [49].

The small values of f_{osc} are attributed to the small probability of finding the electron and the hole in the same unit cell [50]. The transition probability is thus proportional to the ratio a/a_0^3 with a the unit cell volume and a_0 the exciton Bohr-radius (a_0^3 representing the exciton volume associated to the relative motion of the electron-hole pair). We thus note that excitons having smaller Bohr radii will be associated with stronger transitions.

In the single particle frame f_{osc} is proportional to the square of the factor highlighted in equation I.14. For an exciton it can be rewritten with the electron and hole wave-functions such that:

$$f_{osc} \propto |\langle\psi_h|\psi_e\rangle|^2 |\langle u_v| \mathbf{p} |u_c\rangle|^2. \tag{I.16}$$

The first term is the overlap of the envelope functions of the hole and electron and is non-zero only if the wave functions of the two carriers have similar symmetries. Only envelope functions with the same parity (s,p) will lead to a non-zero transition moment. The second term is an integral over the unit cell of the Bloch functions. It defines the polarization of the light emitted or absorbed during the transition. In the case of zinc blende NPLs, the heavy hole transition is only coupled to light polarized in the plane of the NPL since the dipoles associated to this transition lie in this plane [51, 52]. The different selection rules will be specifically presented at the end of this chapter in the case of CdSe/CdTe NPLs, when their electronic fine structure is addressed.

Let us finally note that, by definition (see equation I.14), f_{osc} is proportional to the probability of transition per unit of time (transition rate). f_{osc} is thus inversely proportional to the radiative lifetime of the transition.

Lifetime

Another important parameter characterizing the exciton emission is its lifetime, τ_r. The lifetime is the inverse of the total decay rate of the exciton, Γ_{tot}, which can be decomposed into two contributions: the radiative, Γ_r, and non-radiative, Γ_{nr}, rates.

The radiative rate Γ_r characterizes the rate of recombination of the exciton through the emission of a photon and is proportional to the oscillator strength. The non-radiative rate Γ_{nr} characterizes the recombination or 'loss' of excitons states from all other processes. When the exciton recombines non-radiatively, its energy is either dissipated through phonons in the lattice or is transferred to another carrier, one speaks in this case of Auger recombination [39].

In the simple case of a two level system (ground and excited states), the evolution of the number of excited state, N, is given by:

$$\frac{dN}{dt} = -\Gamma_{tot} N = -(\Gamma_r + \Gamma_{nr}) N. \tag{I.17}$$

Since the intensity of the luminescence, I, is proportional to number of excited states N, it will decay following a mono-exponential law with a characteristic time $\tau = 1/\Gamma_{tot}$, such that $I = I_0 \exp^{-t/\tau}$. As we will see, in II-VI semiconducting materials, the electronic fine structure of the exciton ground state is composed of two sets of levels (dark and bright ones). The dynamics of the luminescence decay stops being mono-exponential in this case and has to be treated with more complex models using population equations connecting the states of the exciton manifold [53]. This problem will be addressed in more detail in Chapters III and VI.

From the different decay rates, the quantum yield (QY) of an emitter can be defined as:

$$QY = \frac{\Gamma_r}{\Gamma_r + \Gamma_{nr}} = \frac{\tau_{nr}}{\tau_{nr} + \tau_r}. \tag{I.18}$$

The quantum yield is equal to the ratio of emitted photons and absorbed ones. Hence, it characterizes the efficiency of emission and is one of the most important parameters to consider for

application in the field of light display. More fundamentally, its understanding is particularly useful for it allows one to identify the radiative and non-radiative contributions in the exciton decay process once the 'effective' photoluminescence lifetime is measured ($\Gamma_r = \Gamma_{tot} QY$) [54].

Linewidth

Broadening of absorption and emission lines have several causes. First, when considering an ensemble of objects, the causes are mainly extrinsic in nature and related to the existence of a distribution in the energy of the transitions of the objects under focus (due to size inhomogeneities for example). This is referred to as inhomogeneous broadening and leads in general to emission lines with Gaussian shapes.

As far as emissions of single nano-objects is concerned, the emission is expected to have a Lorentzian shape, with linewidth intimately related to dephasing processes (loss of coherence) of the photo-created excitons. Different mechanisms or interactions govern the linewidth, including the temperature dependence [55]. The interactions between excitons, or more generally the carriers that compose it, and acoustic and longitudinal optical (LO) phonons provide one of the most efficient mechanisms determining the linewidth of the excitonic absorption and emission lines. Depending on the semiconductors and phonons considered in the problem, different interactions can be involved, deformation-potential and/or piezoelectric interaction with acoustic phonons, Fröhlich interactions with LO phonons, whose nature and magnitude determine the temperature behaviors [55]. Deviations from a Lorentzian profile can be observed and were first reported by Bescombes *et al.* in a single CdTe/ZnTe self-assembled quantum dot and described theoretically to account for the lateral side-bands in emission [56].

Another mechanism leading to the broadening of the lines, at the single object scale, comes from fluctuating electric fields in the environment of the exciton which shifts the lines through quantum (confined) Stark effect [57,58]. This so-called spectral diffusion phenomenon can be interpreted as due to charges created in the vicinity of the object or on its surfaces. This phenomenon will be addressed in more detail in Chapter III when studying CdSe/CdTe core/crown NPLs.

I.2 Indirect excitons

This work is centered on the properties of the indirect exciton (IX) of core/crown CdSe/CdTe and while the physics described above is relevant to IX, we would like to give more details on its specific properties.

I.2.1 Band alignment

The core/crown NPLs are hetero-structures, made of two different semiconducting materials: CdSe and CdTe (and an alloy of CdSeTe in Chapter V). The alignment of the conduction and valence band at the interface between the two materials will define the properties of the hetero-structure. Figure I.2 summarizes the different possibilities of band alignment.

Most of the hetero-structures studied have a so-called type-I band alignment. In this alignment both carriers (electron-hole pair) are confined in the same region of the structure, while the other material acts as a barrier. The excitonic properties of such systems are thus governed by the ones of the material where the carriers are confined. In the field of colloidal structures, this type of alignment can be found in core/shell NPLs or nanocrystals (CdSe/CdS

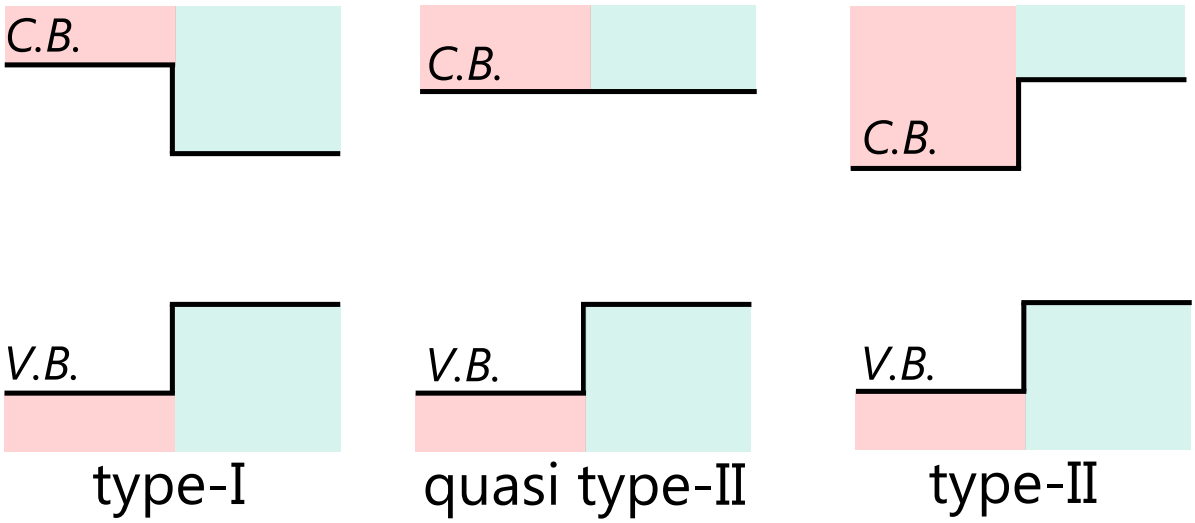

Fig. I.2 *Diagram of the different possible band alignments in hetero-structure.*

or CdSe/ZnS for example). It is often used to passivate the surface of the materials, hence reducing the number of traps and increasing the overall emission efficiency of the object [4].

Another possible band alignment is the quasi type-II one, which is an intermediate type between type-I and type-II. With this type of alignment, one of the carriers is confined in only one region of the hetero-structure while the other one is delocalized over the whole system. Such a regime is usually found in structures where the surrounding material (shell, crown...) is not large enough to confine a carrier. It is the case of CdTe/CdSe nanocrystals for example, when the shell is too thin, the electron is then delocalized over the whole structure [59].

The last type of band alignment is the type-II one, which is typical of the core/crown CdSe/CdTe NPLs studied here. With this band alignment the carriers are spatially separated and confined on each side of the interface between the two materials forming the hetero-structure. This type of band-alignment thus allows the formation of spatially indirect excitons. We would like to insist here on the difference between the case of indirect excitons separated in real space and the one of indirect excitons in k-space, related to semiconductors with indirect band-gap (when the top of the valence band and the bottom of the conduction one are not found at the same point of the Brillouin zone). CdSe and CdTe having both their band-gaps at the Γ point of the Brillouin zone, the indirect exciton in the CdSe/CdTe NPLs is only a spatially indirect exciton.

I.2.2 Properties of indirect excitons

The formalism described in the first section for a general exciton can be adapted to the case of the IX, by taking for each carrier the parameters (effective mass, band gap...) corresponding to the materials it is confined in. Nonetheless, its properties will be somehow modified by the separation of the two carriers. The main difference between direct and indirect excitons is their oscillator strengths. As mentioned, this quantity is proportional to the overlap of the electron and hole wave functions. The carriers being spatially separated, the oscillator strength is much lower for indirect excitons. This has several implications on the emission properties of an IX.

First, it leads to a large Stokes shift between the absorption edge and the photoluminescence

(PL) spectrum. For direct excitons, the value of the Stokes shift is related to the coupling with the phonons (the emission of a photon can be concomitant with the one of a phonon, shifting the emission by the energy of the emitted phonons) or the fine structure (the state absorbing the most might not be the lowest one in energy) [59]. Thus, in colloidal structures, the Stokes shift associated with the emission of direct exciton is only of a few meV. The oscillator strength of the indirect exciton being much weaker, it barely absorbs light and there is rarely an excitonic edge related to the IX absorption in the absorption spectrum. The first edge is the one associated with the direct exciton transition in one of the domains. This transition being clearly shifted compared to the energy of the IX emission, it leads to Stokes shifted PL in the hundred of meV range [59].

Another property related to the oscillator strength is the exciton radiative lifetime. Being inversely proportional to the electron and hole wave functions overlap, the radiative lifetime of an indirect exciton can be several orders of magnitude longer than the one of a direct exciton (up to the ms range at low temperature in GaAs/AlAs superlattices [60]). It is one of the most interesting properties of IXs, as it allows for example the study of the spin relaxation in these structures (as will be seen in Chapter IV). An enhanced lifetime also offers the possibility for type-II systems to act as 'photon storage' systems [61].

Finally, the spatial separation of the two carriers will lead to an enhancement of the polarisabilaty of the exciton and in the case of an asymmetric hetero-structure it will lead to the formation of a permanent dipole. An IX will thus show an enhanced Stark effect compared to a direct one [62] and an electric field can be used to tune its properties such as its lifetime [61]. Due to the symmetry of the core/crown NPLs, there is no permanent dipole moment linked to the IX in these structures, the electron being symmetrically surrounded by the hole wave function. Nonetheless, we will see in Chapter III that through its high polarisability, the IX is strongly coupled to its environment.

I.2.3 Previous works: a brief overview

Indirect excitons in epitaxially grown structures have been studied for more than 30 years. The first structures studied holding IX were GaAs/AlAs quantum wells and superlattices (sets of periodic layers forming an ensemble of quantum wells), where the nature of the exciton can be controlled by the thickness of the GaAs layer [24, 63]. More recently, GaAs/AlAs quantum wells were still used as platforms to study spin relaxation lifetimes, since the long excitonic lifetime found in these structures does not limit the spin relaxation processes [23].

Another noteworthy structure holding IX are GaAs coupled wells [61]. A type-II band alignment is artificially created by the application of a bias voltage perpendicularly to the well's plane, trapping each carrier in adjacent wells. Interesting fundamental studies have been achieved in these structures such as the observation of a Bose-Einstein condensate of excitons, an achievement made possible by the small overlap of the electrons and holes wave functions [64, 65]. Besides these fundamental discoveries, coupled wells are also considered for applications in the field of signal processing with excitonic signals considered as an alternative to electronic ones. One of the advantages of excitons for such a field is their direct coupling to light, leading for instance to the realization of optically controlled excitonic transistors [66].

In 2003 when the first colloidal type-II hetero-structure was synthesized [67], colloidal crystals were already promising materials for a large number of applications (light display, lasing, bio-imaging...). In this context, hetero-structures were seen as a new leverage to tune optical

properties and as a tool to engineer the electron and hole wave functions. Systems with type-II band alignment were specifically considered for applications in the fields of photovoltaics or photo-detectors, where the separation of charge carriers is critical. A considerable number of type-II hetero-structures were synthesized with a large variety of shapes (nanocrystals, tetrapods, dumbells...) and materials (CdSe/CdTe, ZnTe/CdSe, CdS/ZnSe...) [68–71]. Now, it appears that CdSe/CdTe nanocrystals and NPLs became the most studied ones.

Since the first syntheses, several aspects of the IX properties in CdSe/CdTe have been addressed. Its relaxation dynamics were studied and showed to be largely governed by trap states at the surface of the crystal [72]. The study of CdTe nanocrystals with increasing CdSe shell highlighted the transition from quasi type-II to type-II band alignment in these structures [59]. The exciton-phonon coupling has been shown to be larger for IX than for direct excitons [73] and, in CdTe/CdSe hetero-nanocrystals, the evolution of the IX lifetime with temperature and magnetic field has been rationalized taking into account the interplay between the exchange interaction and the electron-hole overlap [74].

Concerning more specifically the core/crown CdSe/CdTe NPLs, they were first synthesized in 2014 [20] and so far the different works found in the literature have mainly addressed the dynamics of the IX formation and its recombination (a detailed review on these works will be found in Chapter III). The NPL geometry offers several advantages: their thickness can be controlled with atomic precision, leading to uniform quantum confinement, while their large lateral extension results in good performance as lasing materials [75]. The NPL geometry also offers an interesting building block to create more complex structures as it has been demonstrated recently with ternary hetero-structure NPLs: a CdS barrier has been added between the CdSe and CdTe domains enabling two-photon fluorescence up-conversion [76].

I.3 Fine structure of the excitonic ground state

In this last section, we discuss the electronic fine structure (EFS) of the IX ground state in core/crown CdSe/CdTe NPLs. So far the exciton has been described without taking into account the degeneracies of the conduction and valence bands. To obtain the EFS of the IX, the spin, S_e, of the electron and the total angular momentum, J_h, of the hole forming the exciton have to be considered.

I.3.1 Electronic fine structure and exchange interaction

To the best of our knowledge, the EFS of the IX in CdSe/CdTe core/crown NPLs has never been investigated theoretically. However, the numerous theoretical works on the EFS of quantum wells [22, 77], epitaxially grown quantum dots [78] and nanocrystals [39] can be used to predict the EFS of these core/crown NPLs. The indirect nature of the exciton does not have an impact on the construction of the EFS, which can be constructed using the same theoretical framework as the one used for direct excitons [23, 24, 63].

The EFS is highly dependent on the symmetry of the object. Most quantum well and quantum dot structures are considered to have an in-plane rotational invariance. They thus belong to the D_{2d} symmetry group. It is not the case of the rectangular NPLs, which belong to the lower symmetry group D_2 (three C_2 axes along the x, y, and z direction). The symmetry group is determined by considering at the same time the parallelepiped shape of the NPL and its Zinc Blende lattice.

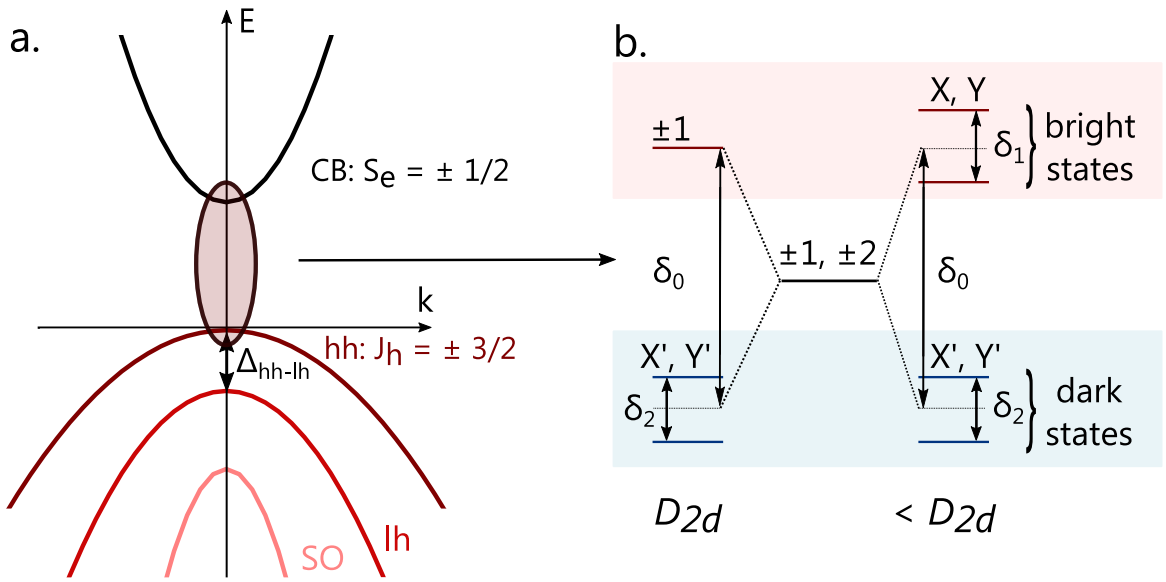

Fig. I.3 *(a) Conduction and valence bands diagram at the Γ point of the Brillouin zone in non-spherical structures. (b) Sketch of the EFS for systems with D_{2d} symmetry and lowered symmetries ($< D_{2d}$), in the case where the light hole bands have been neglected.*

In non-spherical nano-structures, the degeneracy of the heavy and light hole bands at the Γ point of the Brillouin zone is lifted (see figure I.3.a). The strength of the splitting increases with the anisotropy of the object [39]. Hence, it becomes really large in NPLs, with heavy/light hole splitting equal to hundreds of meV (for 4ML CdSe/CdTe NPLs: $\Delta_{hh-lh} = 130$ meV in the CdSe core and $\Delta_{hh-lh} = 250$ meV in the CdTe crown, see figure III.2 in Chapter III). This splitting being much larger than the energies at play in the EFS, we can safely neglect the light hole state's influence in the construction of the EFS in these core/crown structures [63, 78]. Hence, only the electron state forming the conduction band (spin $S_e = \pm 1/2$) and the hole states forming the heavy hole valence band (total angular momentum $J_h = \pm 3/2$) will be considered to form the excitonic states. This will reduce the exciton basis to four vectors, as will be seen below.

The IX ground state is composed of an electron in the conduction band of the CdSe core, with a spin $S_e = \pm 1/2$, and a hole in the heavy hole valence band of the CdTe crown, with a total angular momentum $J_h = \pm 3/2$. The four resulting excitonic states are then divided in two sets with either $|M| = 1$ or $|M| = 2$, where $M = J_h + S_e$ is the angular momentum of the exciton. The states $|\pm 1\rangle$ are called 'bright' states, since, with an angular momentum equal to $\pm$ 1, they are coupled to circularly polarized light. The states $|\pm 2\rangle$ are not coupled to light (photons having angular momentum of 0 or 1); they are optically inactive and are referred to as 'dark' states.

If no other interaction is taken into account, these four states would be degenerate. However, the exchange interaction which couples the spins of the electron and the hole can not be neglected in these systems. In the general case, the magnitude of the exchange interaction is

proportional to the following integral [78]:

$$E_{exchange} \propto \int\int d^3\mathbf{r_1} d^3\mathbf{r_2} \Psi^*_{exc}(\mathbf{r_e} = \mathbf{r_1}, \mathbf{r_h} = \mathbf{r_2}) \frac{1}{|\mathbf{r_1} - \mathbf{r_2}|} \Psi_{exc}(\mathbf{r_e} = \mathbf{r_2}, \mathbf{r_h} = \mathbf{r_1}). \quad \text{(I.19)}$$

The common approach is to separate this integral between a short range contribution, corresponding to the case where both electron and hole are in the same unit cell, and a long range contribution, where they are not. Equation I.19 can also be written in k-space and in this case the separation is made between an analytical (related to the short range part) and a non-analytical (related to the long range one) contribution [78]. We do not wish to enter here into the detail of the complex derivation of these quantities, which can be found in the literature (in ref. [77] for quantum wells or in [39] for nanocrystals). However, it is important to note that the exchange interaction is enhanced by the confinement of the exciton [79].

Following the work presented in ref. [22] for quantum wells, the Hamiltonian of the exchange interaction can be written, in the $\{|+1\rangle; |-1\rangle; |+2\rangle; |-2\rangle\}$ basis, as:

$$H_{exchange} = \frac{1}{2} \begin{pmatrix} \delta_0 & \delta_1 & 0 & 0 \\ \delta_1 & \delta_0 & 0 & 0 \\ 0 & 0 & -\delta_0 & \delta_2 \\ 0 & 0 & \delta_2 & -\delta_0 \end{pmatrix}, \quad \text{(I.20)}$$

where δ_0, δ_1 and δ_2 are energies depending on the strength of the exchange interaction and where generally $\delta_0 > \delta_1$, δ_2. The terms δ_0 and δ_1 are composed of two contributions: one for the short and one for the long range part of the exchange interaction, while δ_2 is solely composed of a term arising from the contribution of the short range part of the exchange interaction [22].

Symmetry considerations will lead to $\delta_1 = 0$ in structures belonging to the D_{2d} symmetry point group. However, for objects belonging to a lower symmetry, like the core/crown NPLs, $\delta_1 \neq 0$. We can thus derive the EFS from the Hamiltonian $H_{exchange}$. The bright ($|\pm1\rangle$) and dark ($|\pm2\rangle$) states are split by an energy δ_0, with the optically inactive states being placed at lower energies. In the case of D_{2d} symmetry, the bright states remain degenerate and coupled to circularly polarized light. However, for a lower symmetry, the bright states are mixed and split by an energy δ_1. The same happens to the dark states (for all symmetries) which will mix and split by an amount equal to δ_2. The new eigenstates of the system can thus be written:

$$\begin{cases} |X\rangle = \frac{|+1\rangle + |-1\rangle}{\sqrt{2}} \\ |Y\rangle = \frac{|+1\rangle - |-1\rangle}{\sqrt{2}} \\ |X'\rangle = \frac{|+2\rangle + |-2\rangle}{\sqrt{2}} \\ |Y'\rangle = \frac{|+2\rangle - |-2\rangle}{\sqrt{2}} \end{cases} \quad \text{(I.21)}$$

where the states $|X\rangle$ and $|Y\rangle$ are the new bright states, while $|X'\rangle$ and $|Y'\rangle$ are the new dark ones. Figure I.3.b summarizes the fine structure of the band edge exciton for both structures belonging to the D_{2d} and $< D_{2d}$ point groups.

On top of their splitting, the mixing of the two bright states change their polarization. They are now coupled to linearly polarized light and if the orientations of the associated dipoles are not known, they will be arbitrarily considered along the x (length) and y (width) directions of the NPL. We will see in Chapter IV that this theoretical prediction of an EFS composed of linearly polarized states was experimentally evidenced by a study of the luminescence under

high magnetic field.

I.3.2 Interaction with a magnetic field

Magnetic fields can split and mix the different levels of the EFS. They do so through the Zeeman interaction, which can be written in the general case of a magnetic field $B = (B_x, B_y, B_z)$ as [22, 78]:

$$H_{Zeeman} = -\mu_B \sum_i (g_{e,i} S_{e,i} - 2\kappa_i J_{h,i} - 2q_i J^3_{h,i}) B_i, \tag{I.22}$$

where μ_B is the Bohr magneton number, g_e is the Landé factor of the electron (which is a priori different along the different directions of the NPL), and κ_i and q_i are parameters related to the valence band. The Zeeman Hamiltonian has to be thus added to the exchange Hamiltonian to determine the EFS.

Here, we do not intend to go through the complete derivation of the new eigenstates and energies of the EFS under any magnetic field configuration. We will limit ourselves to qualitative remarks in two specific cases: (i) a magnetic field perpendicular to the NPL plane (along z, the so-called Faraday configuration) and (ii) a magnetic field in the plane of the NPL (in the (x, y) plane, the so-called Voigt configuration).

In the case of the Faraday configuration, the Zeeman Hamiltonian can be rewritten in the simple form [78]:

$$H_{Faraday} = -\mu_B (g_{e,z} S_{e,z} - \frac{g_{h,z}}{3} J_{h,z}) B_z, \tag{I.23}$$

where $g_{h,z}$ is the Landé factor of the hole and is a linear combination of the κ_z and q_z terms. This Hamiltonian being diagonal in the $\{|+1\rangle; |-1\rangle; |+2\rangle; |-2\rangle\}$ basis, it does not lead to a mixing of the states of the EFS. However, the Zeeman effect will further split these states. The magnetic field will also circularize the 'linear' $|X\rangle$ and $|Y\rangle$ states as we will see in Chapter IV where a complete derivation of the eigenstates and eigenenergies in this specific case is treated. The magnitude of the Zeeman splitting can be experimentally monitored by the degree of polarization of the luminescence: as the states split, the one lower in energy will become more populated leading to highly polarized emission [23, 80, 81].

The effect of a field in the Voigt configuration is more complex. In this case, H_{Zeeman} is not diagonal and the off-diagonal elements will mix the bright and dark states. A complete derivation of the new eigenstates (and associated energies) can be found in ref. [22]. Due to their mixing all the states become optically active, the higher the magnetic field the stronger the weight of the bright component. Experimentally, this can be evidenced by the 'apparition' of the dark state emission line in the luminescence spectrum [78, 82] and by the modification of the luminescence dynamics since a dark exciton will see its recombination rate increase [83].

Chapter II

Experimental techniques

II.1 Samples

In this work, three kinds of colloidal nanoplatelets (NPLs) are studied: core/crown CdSe/CdTe, core/crown CdSe/$CdSe_{1-x}Te_x$ and $CsPbBr_3$ perovskite NPLs. They all are chemically synthesized and dispersed in organic solvent, like hexane or toluene, after synthesis. The NPLs are stabilized by organic ligands with long aliphatic chains (oleic acid, oleylamine) which cover their surfaces. The thicknesses of these NPLs are controlled at the atomic mono-layer level, leading to a great homogeneity in their optical properties.

II.1.1 II-VI Nanoplatelets

The CdSe/CdTe and CdSe/$CdSe_{1-x}Te_x$ core/crown NPLs are synthesized by Marion Dufour and Sandrine Ithurria from the LPEM group at the ESPCI in Paris.

These NPLs are hetero-structures made of a core of CdSe and a crown of either pure CdTe

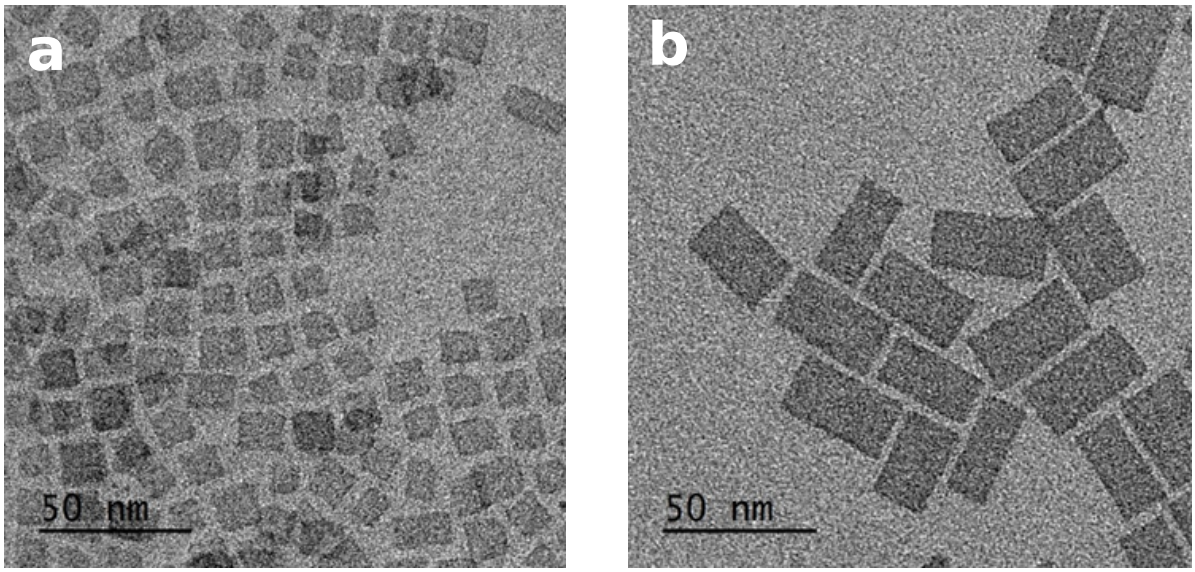

Fig. II.1 *(a) TEM pictures of the CdSe core only NPLs and (b) of the final CdSe/CdTe core/crown NPLs.*

or an alloy of $CdSe_{1-x}Te_x$. The synthesis of these NPLs is performed in two steps. First the CdSe core is synthesised by a method which was first described in Ithurria *et al.* [14]. The thickness of these original CdSe NPLs can be tuned by adjusting the time and the temperature of the reaction. As for the lateral size, it can also be controlled by adding additional precursors during the reaction. Then from these core-only NPLs, another reaction takes place where the CdSe NPLs are laterally extended with either a CdTe or $CdSe_{1-x}Te_x$ crown [20,84,85]. For the alloyed crown, the ratio of Se/Te is controlled by the stoichiometry of the Se and Te precursors. The thickness is kept constant during this reaction, since the crown only grows on the lateral side of the initial NPL. These NPLs crystallize in a zinc blende lattice and have their top and bottom faces perpendicular to the [001] direction [86].
The II-VI NPLs studied here have a thickness of four mono-layers (ML), meaning that they are composed of five planes of Cadmium and four planes of Selenium or Tellurium. For the CdSe/CdTe NPLs, the lateral dimensions of the CdSe core lie between $\sim$ 10 x 12 nm^2 and $\sim$ 10 x 35 nm^2, while for the overall CdSe/CdTe and $CdSe/CdSe_{1-x}Te_x$ NPLs they lie between $\sim$ 30 x 20 nm^2 and $\sim$ 20 x 100 nm^2. Figure II.1 shows typical TEM pictures of CdSe/CdTe NPLs.

II.1.2 Sample deposition

Most of the experiments presented below are carried out on thin solid films. To obtain such films, the solution of NPLs is drop-casted on a pre-cleaned glass slide. The original solution, obtained after synthesis, can be diluted up to 10000 times, in order to obtain the desired density, high dilution allowing to reach a spatial dispersion large enough to address a single NPL in far field optical measurements.

II.2 Absorption measurements

The absorption spectra are obtained using a CARY 5000 double-beam spectro-photometer (Agilent Company). It can be used to measure: (i) the absorption at room temperature of the NPLs in solution but also, (ii) the absorption of a film as a function of the temperature. To do so, a helium exchange gas cryostat is placed in the spectroscopic chamber so as to intercept the optical path. The NPLs deposited on a glass slide are glued on a holed cryogenic finger which is immersed in Helium gas. With the help of a heater on the cryogenic finger, the temperature of the sample can be controlled from 11 K to room temperature. The spectrometer is operated in a dual-channel mode in which the absorption of the substrate is measured simultaneously and serves as a background correction to reach the intrinsic response of the NPL material.

II.3 Photoluminescence measurements

The measurement of the photoluminescence (PL) is the main tool used during this work to study the electronic properties of NPLs film. All the PL measurements carried out in the course of this work share the same experimental set-up consisting of: the cryostat, the excitation sources and the optical set-up (including the optics allowing the signal analysis). The collected PL can be sent towards different instruments: a spectrometer for integrated PL measurements and a streak camera or an avalanche photo-diode for time-resolved PL measurements. In both cases, polarization optics can be added on the path of the collected

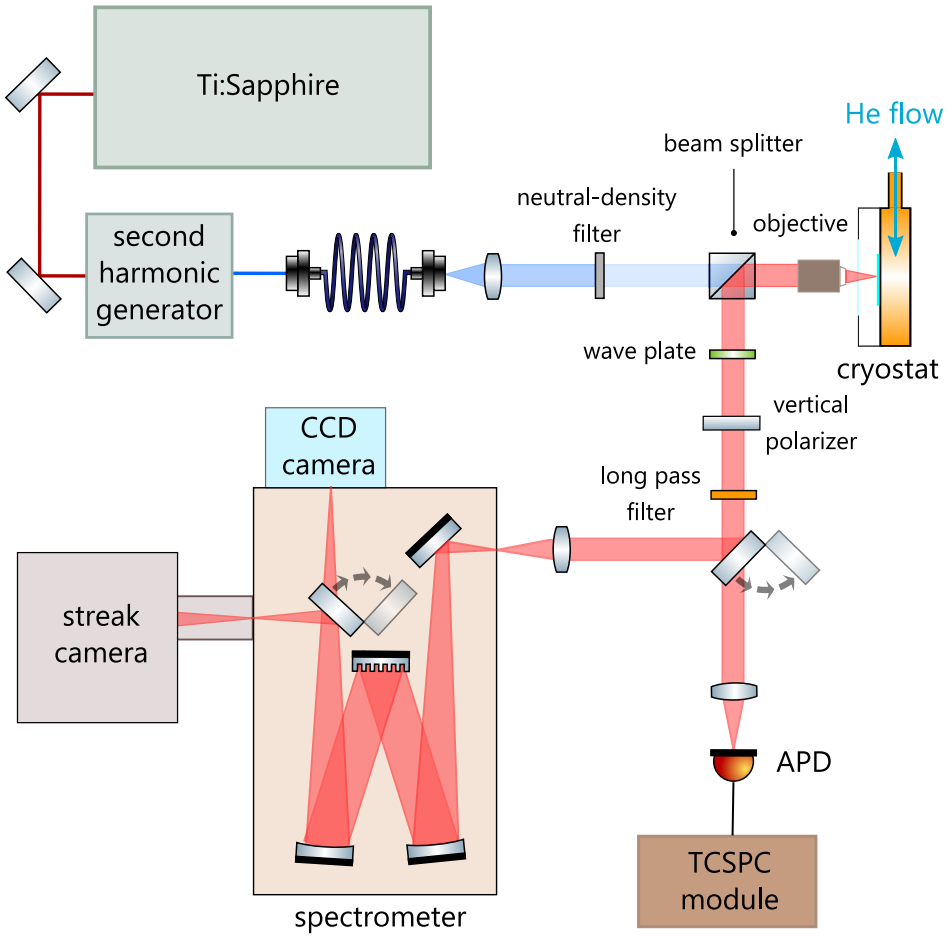

Fig. II.2 *Schematic of the photoluminescence experiment. The configuration used looks like a confocal geometry with two conjugated planes: the surface of the sample on one side and the spectrometer slit on the other one.*

PL to analyse its polarization properties. All measurements were performed in a reflection geometry (see below).

II.3.1 Cryostat

For the PL experiments, we use a cryostat from Oxford Instruments consisting of a cold finger made of copper which is cooled down with a flow of Helium, being pumped inside the cryostat from a dewar. The NPLs drop-casted on thin glasses, as described above, are glued with silver varnish on the cold plate of the cryostat. The control of the flow of Helium and a heating resistor placed on the cold finger of the cryostat allow the tuning of the sample temperature from 7 K up to room temperature.

II.3.2 Laser sources

The NPLs are excited with laser sources. It is necessary to adapt the excitation to the samples (wavelength of the source) but also to the type of measurements that are carried out (repetition rate, incident power). That is why three different types of lasers are used in this work.

First to perform integrated PL experiments, a continuous-wave diode-pumped solid state laser (Thorlabs DJ532) emitting at 532 nm is used. It is mounted in its temperature controlled laser mount (Thorlabs TCLDM9), which prevents any drift in power or in wavelength. This laser is specifically used to measure the PL response of single NPLs. Indeed, single particles are not stable under high power illumination. With a continuous source, unlike a pulsed laser, the power is spread out in time avoiding a large peak power which could lead to the destruction of the NPLs.

We use two kinds of pulsed lasers to carry out time-resolved photoluminescence (TRPL). First, for the measurements performed with the streak camera, a Titanium-Sapphire laser (Spectra Physics, Tsunami) operating at 82 MHz and delivering pulses of $\simeq$ 1.5 ps is used. The short pulses are obtained by a mode-locking technique using an acousto-optic modulator. Its emission can be tuned from 700 nm to 1000 nm, thanks to a birefringent filter. This laser can be sent to a second harmonic generator (BBO crystal) to obtain a light source between 350 nm and 500 nm. It can also be sent to an optical parametric oscillator (OPO) which will convert the incoming photons of energy $\hbar\omega_p$ into two beams of photons of lower energies called the 'signal' and the 'idler', composed of photons of energies $\hbar\omega_s$ and $\hbar\omega_i$ with $\hbar\omega_s + \hbar\omega_i = \hbar\omega_p$. At the exit of the OPO the second harmonic generation can also be implemented to extend the wavelength range; this typically allows us to reach the 600 - 660 nm band useful for the excitation of indirect excitons at their fundamental energy ('resonant excitation'). In addition to TRPL measurements, this laser can also be used to measure the integrated PL of different samples due to its large spectral tunability.

Finally, we also resorted to a picosecond laser photo-diode (Alphalas PICOPOWER-LD-405-50), delivering pulses of $\simeq$ 40 ps at 405 nm. The repetition rate of this laser can be tuned from a few Hz up to 40 MHz. Thanks to this large tunability in frequency, this laser allows us to carry out TRPL measurements on longer time-scales, up to the ms range.

II.3.3 Optical set-up

For the two main laser sources used (the continuous solid-state laser at 532 nm and the Ti:Sapphire), the beams are spatially filtered. To do so, in the case of the continuous solid-state laser, it is focused with a microscope objective on a 10 µm pin-hole. In the case of the Ti:Sapphire, the laser is collimated in a mono-mode fiber with a core of 3 µm. In both cases, the pin-hole or the end of the fiber is placed at the focal point of a lens which collimates the light into a large cylindrical beam. With these set-ups, we obtain large enough beams to illuminate the whole entrance pupil of the focusing objective, limiting diffraction effects. The pin-hole and the fiber tip are also used as positioning references: they are coupled to one point of the sample through the afocal entrance configuration and even if the mirrors of the laser cavity have to be moved for optimization, by aligning the beam back on the pin-hole or in the fiber, the exact same point of the sample is illuminated.

After the expansion, or otherwise, of their light beams, the different laser sources follow the same optical path. First, the light goes through a succession of neutral density filters which allow us to finely control the power sent to the sample. Then it goes through a beam splitter before being focused on the sample by a lens, which can be chosen with different focal length, according to the type of experiment one wants to perform. If one wishes to average the responses over a spot of roughly 5 µm of diameter, a lens (achromatic) with a focal length of 40 mm is used.

To perform micro-photoluminescence experiments, a microscope objective of effective focal

length f ≈ 6 mm and a numerical aperture of 0.6 is used. With this setup, the response of a spot with a diameter of ∼1 µm (size limited by diffraction effects only) can be obtained. This objective is mounted on piezoelectric transducers, which allows its motion to be finely controlled in the three dimensions (Δx, Δy, $\Delta z \sim 0.5$ µm). During the experiment, the objective is moved in a plane parallel to the sample plane until a region of interest is found. Note that this scan mode is reserved to microscopic motions to preserve the whole optical alignment. For large motions (mm range) the cryostat itself is moved.

The light emitted by the sample is then collected by the same lens, goes through the beam splitter and is sent towards the spectrometer. On the way, spectral filters are placed to select the spectral region of interest and suppress the reflection or scattered light from the laser. The light is then focused on the slit of a spectrometer (ACTON SP2760i Roper Scientific-Princeton Instruments) coupled to a nitrogen-cooled CCD camera (SPEC10-2KB-LN). In this manner, the plane of the spectrometer slit and the plane of the sample surface are perfectly conjugated. In this configuration the spectrometer slit itself also acts as a spatial filter and a good rejection of the scattered light is obtained. There is no other pin-hole inserted along the optical path and playing this role.

II.3.4 Time resolved photoluminescence

Streak camera

To resolve the relaxation dynamics happening between tens and hundreds of ps, a streak camera (C5680, Hamamatsu) is used. This streak camera is placed on the exit side of the spectrometer. This instrument provides 3D images where the intensity is plotted as a function of wavelength and time. The information on the wavelength comes directly from the spectrometer. Indeed, the light sent to the streak camera is the one which has been dispersed by the grating.

Once collected by the front optics of the streak camera, the photons are first converted into electrons by a photo-cathode. These electrons are then accelerated by an electric potential, which is quickly modulated with a sinusoidal wave (provided by an internal oscillator) with the same frequency as the repetition rate of the Ti: Sapphire laser (synchro-scan configuration). This potential will detect the electrons according to their time of arrival, since each of them will see a different potential. Then the electrons are sent to a phosphorescent screen, where they are converted back to photons, to be detected by a CCD camera. The information on the time of arrival is transformed into spatial information on the CCD camera. The camera used here has a time range going up to 2 ns, and can resolve ultimately decay as fast as 15 ps. The temporal resolution is determined by two parameters: the stability of the laser pulse train and the quality of the synchronization signal on one side and the quality of the image formed on the camera entrance slit (that will provide the 'electron stripe' that will be deflected inside the tube).

Time-correlated single photon counting

The streak camera is the perfect tool to measure fast relaxations, however the available model was unable to measure decays on the ns time scale. To record such decays, a time-correlated single photon counting (TCSPC) module (PicoQuant TimeHarp 260) is used. This module is connected on one side to the pulsed laser diode synchronization output and on the other to an avalanche photo-diode (APD) (MPD Photonics PD-50-CTE-FC).

In one configuration, this APD can directly collect the PL signal, as shown in figure (II.2). It can also be put on the side exit of the spectrometer instead of the streak camera, to collect

only the photons at the energy of interest. This APD is sensitive to single photons and sends an electric pulse to the TCSPC module every time a photon is detected.

The TCSPC module reconstructs the PL decay by recording an histogram of the delay between the time a laser pulse is sent and the time the APD collects a photon. With this set-up, we can measure decays from the hundreds of ps scale to the ms scale. We were careful to avoid the so-called pile-up effect, which happens when the count rate on the APD starts to be 5% or higher than the repetition rate of the laser. If the count rate on the APD is too high, the photons emitted early in the decay have a higher probability to be detected, since once a photon is detected, the APD cannot detect any events for a certain period of time (dead time of the APD). This effect results in deformed TRPL signals.

Time-gated photon counting

At the time when the TCSPC module was not in our possession, another TRPL technique was used to measure the relaxation of excitations on a 'long' time-scale: time-gated photon counting.

Here, the collected PL signal is sent on to an APD (Excelitas Technologies' SPCM-AQRH-13-FC) connected to a photon counter (Stanford Research Systems SR 400). The counter gives an histogram of the photon arrival time on the photo-diode. Indeed it only counts the photons arriving in a certain interval of time after a chosen t=0 origin. The interval is then swept across the whole time range of interest in order to reconstruct the histogram of the relaxation. For example, if the time interval is set to 100 ns, first all the photons arriving between 0 and 100 ns after the sending of a laser pulse are counted, then the interval is shifted in time by its own width (the counter will now count all the photons arriving between 100 and 200 ns), until the whole time range of interest is studied. The counts obtained by the time-gated counter are converted into a voltage and sent to an oscilloscope where the histogram is plotted and the data can be retrieved.

With this set-up, lifetimes up to the ms can be measured with a resolution of 5 ns. It was mainly used to measure the relaxation of $CdSe/CdSe_{1-x}Te_x$ core-crown NPLs dynamics that are presented in the Chapter V.

II.3.5 Polarization resolved photoluminescence

The polarization of the emitted PL provides a lot of information on the nature of the emitting state. It is therefore important to be able to finely characterize the polarization properties, like the degree of circular or linear polarization. We will discuss later what these notions entail; here we just give the experimental details of how we distinguish right from left circularly polarized light or how we detect orthogonal components of linearly polarized light.

To analyze circularly polarized light, a quarter wave plate and a polarizer are placed just after the beam splitter. The polarizer is placed with its transmission axis at the vertical, aligned with the grating grooves of the spectrometer to obtain the largest response on the CCD camera. The quarter wave-plate is set with its neutral axis at 45° of the vertical between the beam splitter and the polarizer. With such a combination, one of the two circular polarization state (right or left) will be modified into a linear polarization state along the vertical and transmitted through the polarizer towards the spectrometer. As for the other circular polarization state, it will be transformed into an horizontal linear polarization state and be blocked by the polarizer. By rotating the quarter wave-plate of 90° the other circular polarization state will be analyzed and sent to the spectrometer.

It can also be interesting to obtain a polarization diagram to check if the emitted PL is preferably polarized along one direction. In such a diagram, the intensity of the PL is plotted as a function of the angle of the analyzed polarization direction. To obtain it, a vertical polarizer aligned with the grating of the spectrometer and a motorized half wave-plate are used. The half wave-plate rotates the polarization of the emitted light by 2θ, where θ is the angle between the incoming polarization and the neutral axis of the wave-plate. A spectrum is acquired for each position of the half wave-plate. By rotating the half wave-plate over 45°, all the direction of polarization will be analyzed. Indeed, when one of the neutral axes of the half wave-plate is aligned with the polarizer, the vertical emission will be analyzed while when the neutral axes are at 45°, it is the horizontal emission which is analyzed.

The different polarization optics were carefully placed just after the beam splitter along the optical path, before any mirrors. Indeed, the polarization of the PL can be modified by the reflection process. Besides, we carefully chose our beam splitter to reduce its effect on the PL polarization. In particular, the beam splitter response in polarization was carefully studied so as to be able to retrieve the intrinsic properties of the PL emission. A (70:30) = (reflection: transmission) cube from Thorlabs was found to offer a good compromise between transmittance and polarization preservation performances.

II.4 Experiments carried out at high magnetic field

Magnetic field is, along with temperature, another parameter which is found to be extremely powerful to study the electronic levels of semiconductors nano-structures. Through the Zeeman interaction, it can indeed split the different levels of the exciton fine structure but also mix these levels as discussed later on. The magnitude of the Zeeman interaction is given by $g\mu_B B$. It depends on the Landé g-factor ($\simeq 1$) and the Bohr magneton number ($\simeq 60$ µeV) and gives the energy range accessible by varying B. High magnetic fields (Tesla and tens of Teslas) leads to levels splitting that start to compare to the thermal energy at low temperature. The splittings are accompanied by changes in the states symmetry and both lead to observable modifications that can be connected to the electronic structure.

The measurements, presented in Chapter IV, were performed at the High Field Magnet Laboratory (HFML) of the Radboud University which is located in Nijmegen in the Netherlands. This facility consists of a 50 mm bore resistive magnet, cooled down by a flow of water, which can create a continuous magnetic field of up to 31 T. The optical setup used is similar to the one described above and a complete description can be found in the supplementary information section of Pandya *et al.* [80]. The samples are mounted in an optical probe which is placed inside a liquid Helium bath cryostat, this cryostat being itself placed in the middle of the electromagnet. The measurements are carried out under pumped Helium at 1.6 K and two resistors attached to the sample holder allow the control of the temperature up to 40 K. Pulsed and continuous laser diodes are used as excitation sources; a spectrometer and a combination of an APD and a TCSPC module are used to measure the integrated and time-resolved PL. Finally a set of polarizers and wave-plates are added to the optical path to analyze the polarization of the emitted PL. The configuration is largely the same as the one described in the previous paragraph. Experiments were carried out over a 15 day period in May 2019.

Chapter III

Optical properties of CdSe/CdTe nanoplatelets

The interest in core/crown CdSe/CdTe nanoplatelets (NPLs) lies in their type-II band alignment resulting in the formation of indirect excitons (IXs). So far, the studies carried out in these NPLs were centered either on their optical properties at room temperature [20] or on the dynamics of the formation and relaxation of the ground state excitation [25, 27, 87]. However, some fundamental properties of the IX, such as its neutral or charged nature, its electronic fine structure or its coupling properties to the environment have never been addressed. In this context, we undertook a study of the single NPL photoluminescence (PL) response, to complete the understanding of such core/crown systems. The work presented here has been published in ref. [88].

In the first section, we quickly present the structural properties of the two types of NPLs studied in this work. Then in the second section, we present the basic optical properties of ensembles of CdSe/CdTe NPLs and their evolution with temperature. The emission dynamics and the formation of the IX is also addressed through a review of the existing literature. Finally, the last section is dedicated to the study of NPLs as individual objects dispersed on a glass substrate. We show that the emission spectrum of single NPLs is dominated by the recombination of the neutral IX and its vibronic replicas. With the help of numerical simulations performed by our collaborators Juan Climente and Josep Plannelles from the department "Quimi a Fìsica i Analìtica" of the University Jaume I in Castellò (Spain), we confirm the indirect nature of the exciton present in these NPLs and discuss the origin of its emission broadness.

III.1 Structural characterization

As we will see in the last section of this chapter, the lateral sizes of the core play a major role on the excitonic properties in these core/crown NPLs. For this reason, NPLs with distinctly different core lateral dimensions are studied. The two kinds of NPLs will be referred to as 'small' core (SC) NPLs and 'large' core (LC) NPLs. They are both 4 ML NPLs, meaning that they are made of 4 planes of Selenium/Tellurium and 5 planes of Cadmium. Figure III.1 shows the TEM picture of the CdSe core NPLs before the growth of the CdTe crown (III.1.a for SC and III.1.b for LC NPLs) and the overall core/crown NPLs at the end of the synthesis of the CdTe crown (III.1.c for SC and III.1.d for LC NPLs). The overall dimensions of the core and the crown are determined from such TEM pictures. The core is measured

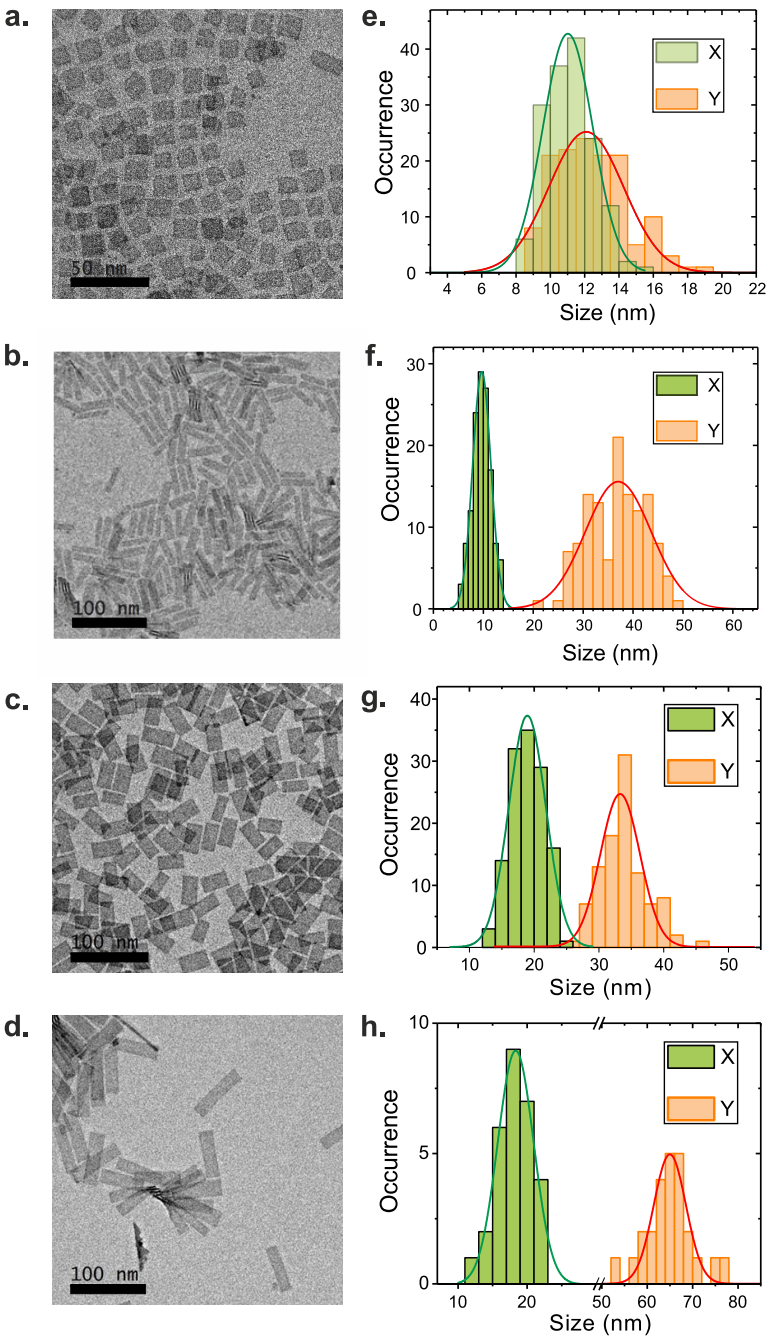

Fig. III.1 *TEM characterization of the NPLs under study. (a) and (b) TEM picture of the CdSe core and (c) and (d) the overall core/crown structure of SC ('small' core) and LC ('large' core) NPLs respectively. (e) and (f) Size distribution of the CdSe core for SC and LC NPLs respectively and (g) and (h) size distribution of the overall core/crown NPLs of SC and LC NPLs respectively. From these histograms an average core lateral dimension of ∼ 11 x 12 nm^2 and ∼ 10 x 37 nm^2 is determined for the SC and LC NPLs respectively and an overall dimension of ∼ 19 x 33 nm^2 and 18 x 65 nm^2 is determined for the SC and LC NPLs respectively.*

to be $\sim$ 11 x 12 nm^2 for the SC and $\sim$ 10 x 37 nm^2 for the LC NPLs. The core/crown surface ratio is kept roughly the same for the two kinds of NPLs with a crown dimension of $\sim$ 19 x 33 nm^2 for SC and $\sim$ 18 x 65 nm^2 for LC NPLs. From the histograms of the core dimensions presented in figure III.1.e and f, it is clear that our samples should be described by a fairly large distribution of sizes, however SC and LC NPLs can be unambiguously defined. However, these large distributions of lateral sizes can be responsible for differences in the energy of the IX transition from NPL to NPL.

In the different experiments presented below, the studied NPLs are dropcast on clean glass slides. The NPL's density in the obtained films is controlled by the dilution of the initial solution. It is different for each type of measurement: the films are relatively dense in order to carry out reliable absorption measurements, while for micro-PL experiments the density has to be low enough to reach the single NPL response.

III.2 Optical properties of nanoplatelets ensembles

Before exploring the emission properties of single NPLs, it is first important to review the optical properties of dense films. The absorption and PL steady-state properties presented below were investigated by ourselves as a function of temperature, while the discussion about the dynamical properties of the elementary excitations will be based on published literature.

III.2.1 Steady-state properties

The interest in CdSe/CdTe core/crown NPLs lies mainly in its type-II band alignment [89] which can support an IX, with the electron confined in the CdSe core and the hole confined in the CdTe crown. The existence of the IX is already clearly noticeable in basic spectroscopic measurements such as absorption and PL emission spectra. The main signature is a large Stokes shift ($\approx$ 300 meV) between the lower excitonic edge (labeled X_1) of the absorption

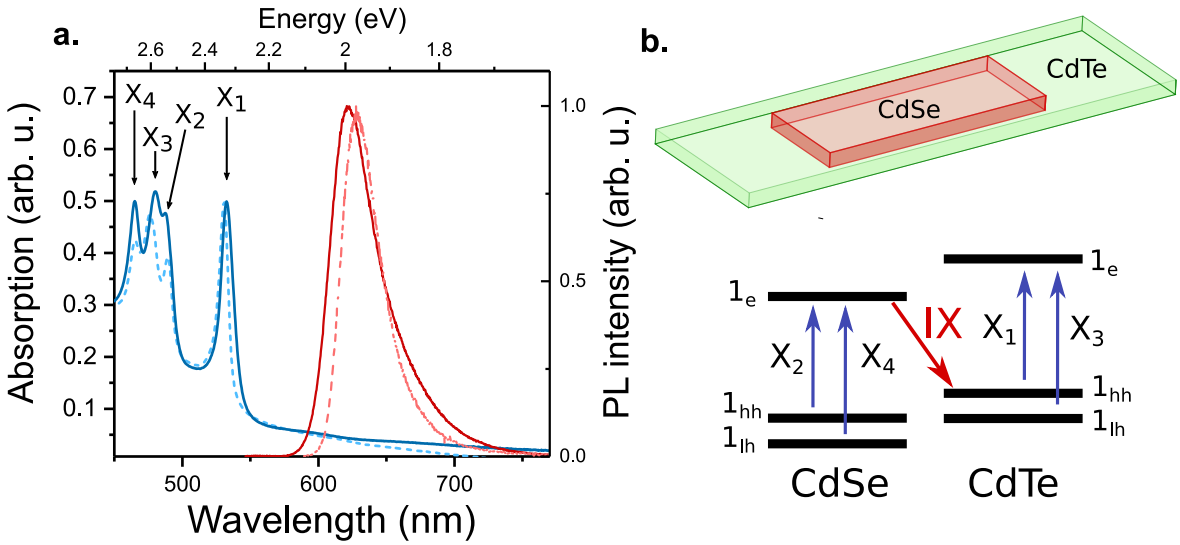

Fig. III.2 *(a) Absorption and PL spectra of a dense film of LC (solid lines) and SC (dotted lines) NPLs at $T \approx 10$ K. (b) Sketch of the CdSe/CdTe NPL geometry and diagram of the single carriers energy levels for both the core and crown domains.*

spectrum and the PL emission spectrum, see figure III.2.a. This large shift can be easily understood from a diagram of the single carrier levels in this structure, such as the one in figure III.2.b. The different absorption peaks (labeled X_i) correspond to the direct excitonic transitions of the CdSe and CdTe domains [20, 27], while the PL emission arises from the IX recombination (red arrow) which is, due to the type-II band alignment, at a lower energy compared to the X_i transitions.

The X_1 and X_3 transitions correspond respectively to the heavy and light-hole transitions of the CdTe crown (energy of 2.33 eV and 2.58 eV at T = 10 K). The X_2 and X_4 transitions correspond respectively to the heavy and light-hole transitions of the CdSe core (energy of 2.54 eV and 2.67 eV at T = 10 K). We notice that the energies of the different X_i transitions are similar for the LC and SC NPLs (they differ by only a few meV). This is explained by the fact that these energies are mainly driven by the thickness of the NPLs and to a lesser extent by the lateral size of the different domains. It is also interesting to remark that the weight of the absorption of the CdSe core compared to the one of the CdTe crown is less important in SC NPLs. This observation reflects the fact that the core/crown surface ratio is slightly smaller in SC NPLs than in LC ones (~ 1.3 for SC NPLs and ~ 1.5 for LC NPLs). Since the oscillator strength of a transition in these NPLs structures increases with their lateral areas [15], it is consistent with the fact that the CdSe absorption is weaker in the SC NPLs.

An absorption tail also extends from 1.7 eV to 2.2 eV, at energies lower than any of the domains transitions. This tail was attributed to the direct absorption of the IX transitions [25, 27]. This attribution is corroborated by the fact that exciting the NPLs in this broad tail region leads to the emission of the IX, as we will see in Chapter IV. In ref. [25], the oscillator strength of the IX could be estimated as ~ 1.5 % of that of the CdTe exciton.

Let us now turn to the PL emission spectrum at low temperature. It is composed of a single broad asymmetric peak, centered at 1.99 eV (1.97 eV) for the LC (SC) NPLs, arising from the recombination of the IX. The red-shift of ~ 20 meV between the LC and SC NPLs is much larger than the shifts observed between the absorption peaks of the two types of samples and has a physical origin. The recombination energy of the IX actually depends on the overlap of the electron and hole wave functions, which differs for different lateral sizes of the core, as we will see in the next section. This explains the shift observed in the PL spectra while the energies of the X_i transitions present in the absorption are mainly dependent on the band-gap of each domain. The formation of the IX takes place on a really short time-scale (< 1 ps) as we will discuss in the following and has an efficiency close to unity [27]. This is why the observation of the emission of the direct exciton of CdSe or CdTe can only be observed transiently [25] and that the IX emission dominates the PL. The emission at low temperature is unusually broad (FWHM of ~ 130 meV) for a structure where almost no inhomogeneities in the confinement direction can be evidenced. As seen later, the IX-phonons coupling as well as the residual inhomogeneities in the lateral sizes of the NPLs can help us rationalize this large emission width.

We now study how the PL and absorption properties evolve from low to room temperature.

a) Temperature dependent absorption

Figure III.3.a presents the evolution of the absorption spectrum of the SC CdSe/CdTe NPLs from 293 K down to 10 K. The different heavy and light-hole transitions of both domains are labelled in the same manner as previously described. We observe that, with the decrease of the temperature, the peaks get narrower and that they blue-shift by roughly 100 meV. The evolution with the temperature of the band-gaps of both domains (represented by the energy

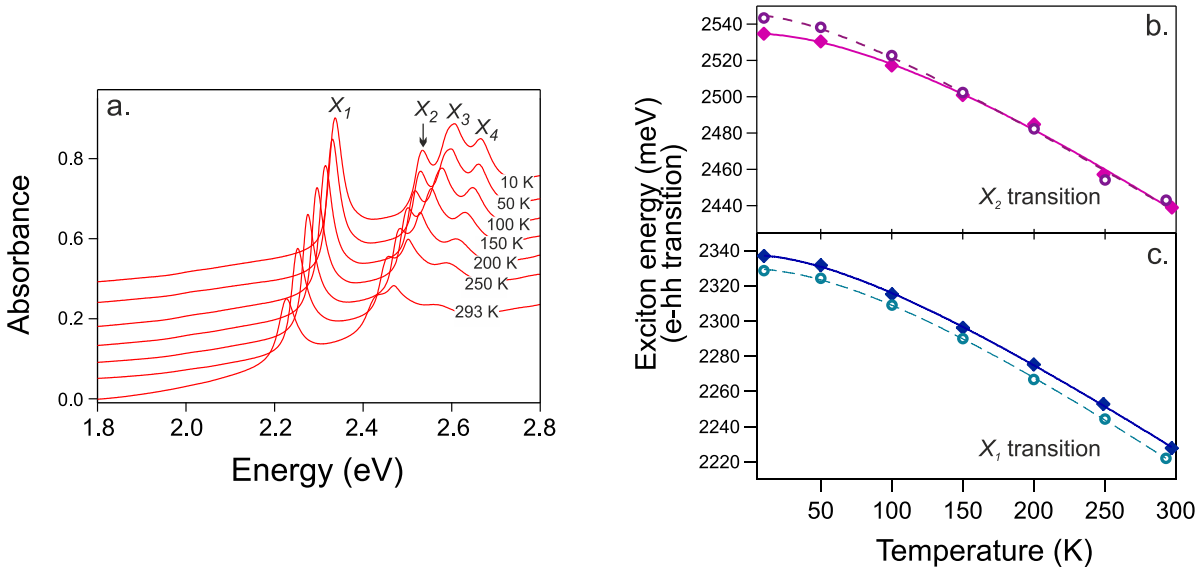

Fig. III.3 *(a) Evolution of the absorption of SC NPLs with the temperature. (b) Energies of the X_1 and X_2 transitions as a function of temperature for SC (solid diamonds) and LC (open circles) NPLs. The adjustments are obtained using the Varshni law (equation III.1).*

of the peak X_1 (X_2) for CdTe (CdSe)) can be adjusted by the commonly used semi-empirical Varshni law [90] given by:

$$E_g(T) = E_g(0) - \frac{\alpha T^2}{T + \beta}. \tag{III.1}$$

This equation accounts for the two origins of the evolution of the band-gap with the temperature. The first one is the dilatation of the lattice, which is shown to lead to a linear dependence of the bad-gap with the temperature. The other process is the evolution of the electron-lattice interaction, which lead to two distinct evolutions of the band-gap: below the Debye temperature $\Delta E_g \propto T^2$ while above the Debye temperature $\Delta E_g \propto T$.

We thus use equation III.1 to adjust the evolution of the X_1 and X_2 transitions (figure III.3.b and c) for SC (solid diamonds) and LC (open circles) NPLs. The values found from the fit are:

- for SC NPLs:
$E_{g,CdTe}(0) \approx 2.337 \pm 0.004$ eV, $\alpha_{CdTe} \approx 0.57 \pm 0.13$ meV/K and $\beta_{CdTe} \approx 166 \pm 107$ K.
$E_{g,CdSe}(0) \approx 2.535 \pm 0.003$ eV, $\alpha_{CdSe} \approx 0.62 \pm 0.22$ meV/K and $\beta_{CdSe} \approx 265 \pm 202$ K.

- for LC NPLs:
$E_{g,CdTe}(0) \approx 2.333 \pm 0.003$ eV, $\alpha_{CdTe} \approx 0.62 \pm 0.17$ meV/K and $\beta_{CdTe} \approx 199 \pm 133$ K.
$E_{g,CdSe}(0) \approx 2.545 \pm 0.004$ eV, $\alpha_{CdSe} \approx 0.50 \pm 0.10$ meV/K and $\beta_{CdSe} \approx 114 \pm 78$ K.

These values are similar to the ones reported in the literature [91], except for the value of β_{CdSe} in the LC NPLs where the present value is smaller than the one reported. This is explained by the fact that the adjustment depends weakly on β, as can be seen by the high values of uncertainty obtained for this parameter. A better estimation of β and α in these structures would require an improvement of the measurements as well as a larger sampling

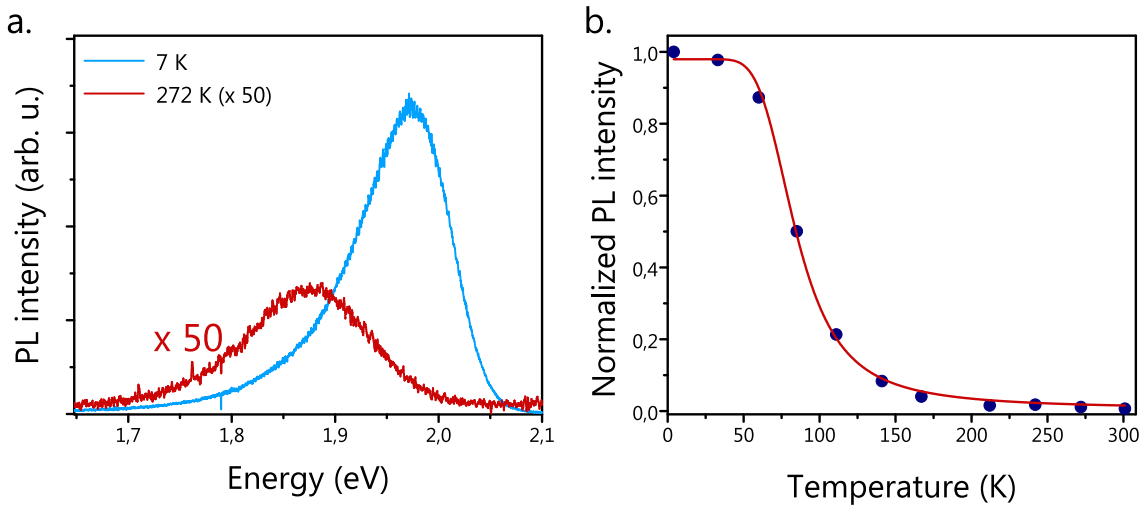

Fig. III.4 *(a) PL of SC NPLs at 7 K (blue) and at 270 K (red) with λ_{exc} = 532 nm. The PL spectrum at 270 K has been multiplied by 50 to allow the comparison of both spectra. (b) Evolution of the PL intensity (obtained from the integration of the PL spectra and normalized to the value at T = 7 K) with the temperature for SC NPLs. The red curve is an adjustment of the data made with equation III.2 modeling a thermally activated quenching mechanism.*

with respect to temperature. We finally notice that the smooth evolution of the $X_i(T)$ curves indicates that no phase transition occurs as the temperature is varied.

b) Temperature dependent photoluminescence

Figure III.4.a shows the emission of SC NPLs at low and high temperature (the spectrum obtained at 270 K is multiplied by 50 to allow the comparison of the two spectra). From 270 K to 4 K, the emission spectrum blue-shifts ($\sim$ 150 meV) and follows the shift observed in absorption for the CdSe core (X_2) and the CdTe crown (X_1). The shift in PL is actually not equal to the one in absorption, since the shift in emission results from the alignment of the conduction and valence bands of the core and the crown respectively which do not only depend on the absolute evolution of both of the domains' band-gaps. As the temperature decreases, the linewidth of the emission does not significantly change (FWHM $\sim$ 150 meV at T = 270 K and FWHM $\sim$ 130 meV at T = 7 K), as opposed to what is usually observed in pure CdSe NPLs where it decreases from 44 to 12 meV [81]. Our analysis will show that the broadening is not caused by coupling to acoustic phonons but likely results from the combination of exciton-longitudinal optical (LO) phonon coupling and strong spectral diffusion. This process being independent of temperature, the low temperature emission is almost as broad as the room temperature one.

Finally the most striking feature between the two temperatures is the large increase in the PL intensity as the temperature decreases. This trend is consistent with previous observations of an increase of the quantum yield with the lowering of the temperature [25, 28]. The intensity of the emission (obtained from the integral of the PL spectra) is measured at different temperatures and its evolution is shown in figure III.4.b. The temperature dependence of the intensity (normalized by the value obtained at T = 7 K) can be well adjusted by a thermally

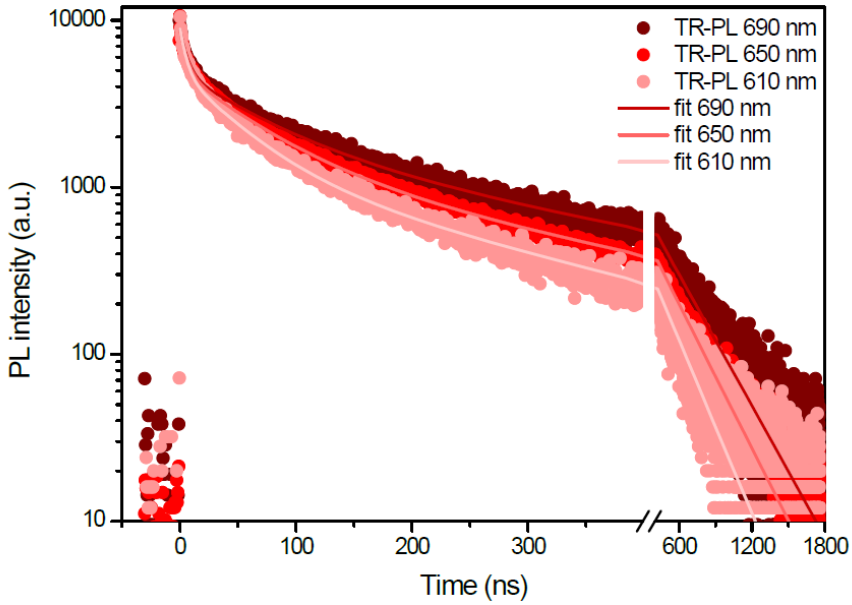

Fig. III.5 *Figure reproduced from ref. [26]. Wavelength dependent TRPL of the IX emission in core/crown CdSe/CdTe NPLs at room temperature.*

activated quenching process as done in ref. [28] according to:

$$I = \frac{1}{1 + a \exp\left(-\frac{E_a}{k_B T}\right)}, \tag{III.2}$$

where E_a is the activation energy of the quenching process. The adjustment shown in figure III.4.b is obtained with a value of $E_a = 42$ meV. The quenching process can be related to the opening of a new non-radiative decay path at high temperature. The value found for E_a can also give a lower bound for the binding energy of the IX. The lower bound of 42 meV found is in good agreement with the theoretical value of 50 meV (estimated from the numerical approach).

III.2.2 Relaxation dynamics

The relaxation of the energy was not studied as a function of time in the present work. However, it is at the center of numerous studies, specifically addressing the type-II band alignment and the indirect nature of the exciton. We provide a short review of the observations that were made in the field and that are relevant for us here.

a) Time-resolved photoluminescence

As we will see in Chapter IV, we measured the time-resolved PL (TRPL) of the CdSe/CdTe NPLs at high magnetic fields. However, these measurements were done under resonant excitation of the system and only at low temperature. We give here a review of the dynamics of the IX emission as it has been reported in the literature [20, 25–28] and compare the evidenced features to what has been observed in homo-NPLs of CdSe [92, 93].

Figure III.5 is extracted from the work of Cassette *et al.* and shows the decay of the IX emission at room temperature at different emission wavelengths [26]. These decays, as with

all the TRPL dynamics reported in literature, highlight that the IX is a long-lived one, with a half-life in the range of tens of ns (42 ns reported in ref. [27]), while it is only in the ns range in the CdSe NPLs [16]. The lengthening of the PL emission is common for an indirect exciton and is related to the weak overlap between the wave functions of the electron and the hole leading therefore to a weaker recombination probability.

In the case of figure III.5, the decays are well adjusted with multi-exponential decay functions, at 650 nm (maximum of the emission at room temperature). They are composed of three components of characteristic time (respective relative amplitude) of $\sim$ 6 ns (0.43), $\sim$ 63 ns (0.40) and $\sim$ 302 ns (0.17). Even if the exact values of the characteristic times differ from study to study, the IX dynamics always shows a multi-exponential decay with, most of the time, at least one characteristic time in the ns range, one in the tens of ns range and one in the hundreds of ns range [25–27]. When the experimental set-up allows one to measure the decay on a longer time-scale a fourth or fifth constant in the µs range is also needed to appropriately fit the tail of the decay [20, 27].

This type of multi-exponential decay cannot be considered as characteristic of the indirect nature of the excitation. It was actually already observed in homo-NPLs of CdSe [92]. Rabouw *et al.* studied the PL of CdSe NPLs up to 10 µs after the initial excitation and they observe that, after an initial exponential decay in the ns range, the decay of the emission exhibits non-exponential dynamics. These dynamics are attributed to the temporary charge separation of the two carriers. According to these authors, after the excitation of the structures, in some NPLs one of the two carriers can be trapped, blocking the possible recombination of the exciton. This trapping process being reversible, the recombination can happen much later on after the excitation (up to 10 of µs), leading to a so-called delayed PL. This claim is supported by the fact that the emission does not evolve spectrally in time. Using an analytical model based on this process they conclude that less than half of the emission arises from direct recombination of the exciton (leading to the initial exponential decay) but that up to 56 % arises from the recombination of excitons where one of the charge carriers is previously trapped. To the best of our knowledge, a similar study on a long time-scale has not been performed in type-II core/crown CdSe/CdTe NPLs. However, it is likely that similar processes are at play which would explain the long multi-exponential tail of the IX emission dynamics.

If we now turn towards the evolution of the PL dynamics with the temperature, there is, to the best of our knowledge, only one work reporting on this subject [28]. Surprisingly in ref. [28], the authors observe a bi-exponential decay for the IX dynamics, as opposed to the multi-exponential behavior described above. This observation may be explained by the fact that the explored time-range is shorter than the one considered in other works. The evolution of the two characteristic times of the IX dynamics with the temperature is reported and it is shown that the dynamics barely evolves with a first component ($\sim$ 12 ns) staying constant throughout the temperature change and another component increasing slightly from $\sim$ 60 ns at low temperature up to $\sim$ 80 ns at room temperature.

This evolution with the temperature is quite different from what has been observed so far in II-VI colloidal nano-structures and especially with what has been reported in core-only CdSe NPL [93]. As already described in Chapter I, the exciton fine structure in II-VI semiconductors is made of upper bright states and lower dark states. Both bright and dark excitons can recombine radiatively, with a much lower rate for the dark excitons. The overall PL emission, resulting from the recombination of the two types of states (bright and dark), will have bi-exponential dynamics, with two characteristic effective times which can be calculated

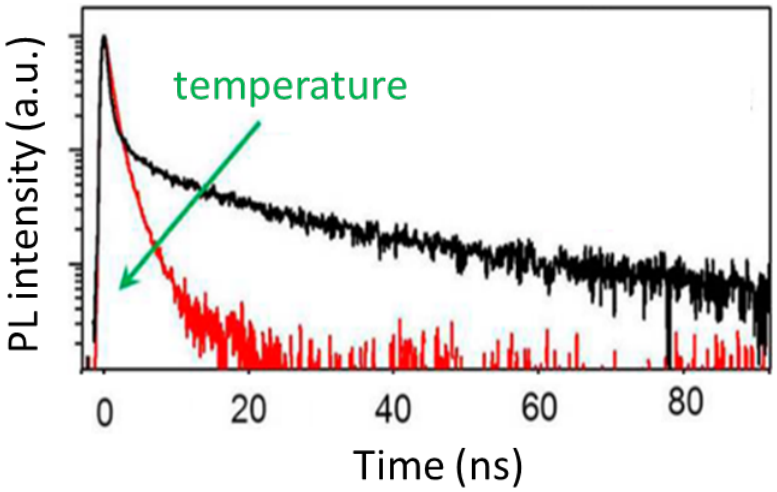

Fig. III.6 *Figure reproduced from ref. [93]. Evolution of the PL decays with the increase of the temperature, in the case of CdSe NPLs.*

from the differential equations modeling this three levels system. These characteristic times will depend on both the bright and dark exciton recombination rates but also the transfer rate from one state to the other [53]. Due to the temperature dependence of the back-transfer from the lower dark exciton to the upper bright one, the two characteristic times are expected to evolve with the temperature. Figure III.6 is reproduced from ref. [93] and shows how the PL decay of CdSe NPLs typically evolves with temperature. The main expected features are the following: (i) both characteristic times shorten with the temperature increase and (ii) the amplitude of the longer time component gains in weight over the shorter time one. We will see in more detail in Chapter VI how this model can be used to estimate the bright state-dark state energy splitting. It is striking that no such evolution of the decays is observed in the type II CdSe/CdTe NPLs studied here. No explanation is given in ref. [28] to rationalize the quasi-absence of evolution of the TRPL with the temperature. We will discuss this point in further detail in Chapter IV.

b) Formation of the IX

The different experiments presented in this work (addressing the IX relaxation in core/crown NPLs) are performed on time-scales over which the formation of the IX does not need to be considered as it will have already taken place. It is always the ground state of this IX that is studied. Nevertheless, it is interesting to look into the dynamics of its formation. Different studies based on differential absorption measurements investigated these dynamics [25–27,94].

From this literature, two processes, with distinct time-scales can be distinguished. The first one is quasi-instantaneous. It is at play when the IX transition is pumped resonantly: the formation of the IX is shown to happen in less than 10 fs [27]. A similar ultra-fast process ($\sim$ 70 fs) is also observed when the crown domain is excited (pump at 520 nm, between the heavy hole transitions of CdSe and CdTe) and is attributed to the formation of a 'hot'

IX [25]. According to ref [25], this 'hot' exciton relaxes in the ground state of the IX levels by the interplay of an interfacial phonon. The second channel supposes that a crown exciton is first generated and then the transfer of its electron to the core leads to the IX formation. This second process takes place on a longer timescale and requires the diffusion of the exciton through the CdTe domain until it meets the core/crown interface. This process was highlighted by the work of Li *et al.*, where it is observed that the formation of the IX takes a longer time in NPLs with larger crown extension [94]. The authors were able to model their results resorting to diffusion equations and found that the crown-core transport time was happening with a duration between 3 ps and 6 ps according to the size of the CdTe crown. A similar value of 5 ps was also reported in ref. [25]. At that point, it is clear that the exciton transport is always interpreted as a diffusive process and the authors, themselves, emphasize that there is no evidence of coherent ultra-fast transport through the crown.

It is important to note that the work by Cassette *et al.*, based on transient photo-induced absorption measurements, questions the generally accepted view in core/crown NPLs [26]. According to this work, a quasi type-II band alignment would characterize the structure, with the conduction bands of CdTe and CdSe being aligned. This kind of alignment results in the delocalisation of electrons over the whole NPL. The large Stokes shift between the absorption and the PL is then explained by the fact that the holes are trapped in mid band-gap states. We note that, to the best of our knowledge, there is no direct experimental evidence that would allow one to confirm or disprove the assumption made by Cassette *et al.*. In particular, a quasi type-II band alignment would be quite far from the numerical predictions in bulk CdSe/CdTe, where a conduction band offset of 0.58 eV is reported [89].

It is clear that there still exists some interrogations about the formation of this IX. However, in our analysis we will keep the commonly accepted hypothesis of a type-II band alignment in these materials, leading to the fast formation of an actual indirect exciton.

III.3 Study at the single object scale

Despite the different works carried out on CdSe/CdTe NPLs dense films, the issue of the excitonic fine structure has never been addressed. We believed that through the study of single NPLs emission, we would gain access to this fine structure, since this approach was successful for a number of nano-objects [32, 53, 82]. The single object study usually reveals fine emission lines since the broadening due to size inhomogeneities is suppressed. However, we discovered that in the case of core/crown CdSe/CdTe NPLs, the emission of the single object remains broad, hindering the observation of the fine structure. Instead, these experiments led us to focus on the role of the exciton-phonon coupling in core/crown structures. The experimental study reveals the large coupling between the IX and a LO phonon leading to several replicas in the PL spectrum at the single NPL level and resulting in the overall broadening of the emission. The numerical facet of the study allows us to confirm the indirect nature of the IX and rationalizes the role of the spectral diffusion phenomenon taking into account the trapping and detrapping of charges at the surface of the NPLs or at the hetero-interface. Despite the impact of electrostatic effects on the energy of the excitonic transition, it seems that the Stark effect at play in the structure and resulting from charge fluctuation is not strong enough to modify the strength of the exciton-phonon coupling, leading us to conclude that the relatively strong coupling with phonons is intrinsic to this type-II structure.

The experimental results will be described first. In a second section we will present the output of numerical simulations. Finally, we will discuss the conclusions that can be drawn

from these two complementary approaches.

III.3.1 Experimental results

Highly diluted films of core/crown NPLs are obtained by diluting the source solution up to 2000 times before dropcasting it on clean glass slides. The experiments are performed using the micro-PL set-up described in Chapter II, and systematically carried out at 7 K, the emission of the NPLs being the most intense at low temperature (see figure III.4). The NPLs are excited with a continuous-wave laser at $\lambda_{exc} = 532$ nm. The main difficulty we met is the poor photostability of the structures under illumination. To avoid as much as possible deterioration under illumination, the excitation fluence is kept as low as possible, around few $\mu W/\mu m^2$. As observed later on, the emission of the single NPLs remains spectrally broad. So, contrary to what is currently observed in CdSe or CdTe homostructures, the amplitude of the PL signal is relatively low. We thus need an integration time of at least 1 s to obtain an acceptable signal to noise ratio. Hence, the mechanisms taking place on a shorter time-scale are not reachable or can only be studied through their average effects in time.

a) PL of single CdSe/CdTe NPLs

Figure III.7.a shows the characteristic PL emission spectrum of a single SC NPL, the response of LC NPLs being similar in almost every aspect. All the recorded spectra are composed of evenly spaced peaks, with an energy difference of $\sim$ 22 meV, the intensity of each peak decreasing with their energy in most of the spectra recorded. The emission extends $\sim$ 100 meV, with up to 4 peaks clearly observable in the spectrum (figure III.7.a), while, for others, a non-structured tail at low energy is present (figure III.7.e). A multi-Gaussian fit leads to a good adjustment of the response, with peaks having a FWHM between 15 and 20 meV. This is two orders of magnitude larger that the width usually measured for other II-VI nanocrystals and NPLs [16, 85], where 'homogeneous' line width (limited by the dephasing time of the exciton), characterized by a lorentzian emission profile, are reported. Here, the Gaussian shape indicates that an inhomogeneous type of broadening is still at play at the level of a single object. The broadness of the emission explains the relatively low intensity of the core/crown NPLs' emission and thus the relatively poor signal to noise ratio: the PL intensity can be considered as spectrally spread out. As a comparison, the area below the emission spectra of single CdSe/CdTe NPLs is actually similar to the one measured in single CdSe homo-NPLs, excited in the same conditions, where all the intensity is 'concentrated' in a $\sim$ 400 µeV linewidth [16]. This observation is consistent with the high value ($\sim$ 86 %) of the quantum yield reported for core/crown structures at low temperature [25].

Figure III.7.c shows the evolution of the emission of a single NPL (different from the one presented in III.7.a) over several minutes. We observe fluctuations in the intensity as well as spectral rigid shifts of the PL, meaning that the overall shape of the spectrum is not modified. These shifts are highlighted in figure III.7.e, which shows some of the spectra forming the trace of figure III.7.c. They are characteristic of the spectral diffusion phenomena and find their origin in the modification of the electrostatic environment of the NPLs over time [58]. We can see from figure III.7.d that the amplitude of these shifts is $\sim$ 7 meV The spectral diffusion caused by trapped charges will be studied in more detail in the following section with the help of numerical simulations.

Let us now turn to the origin of this 'multi-peaked' emission. Three assumptions are

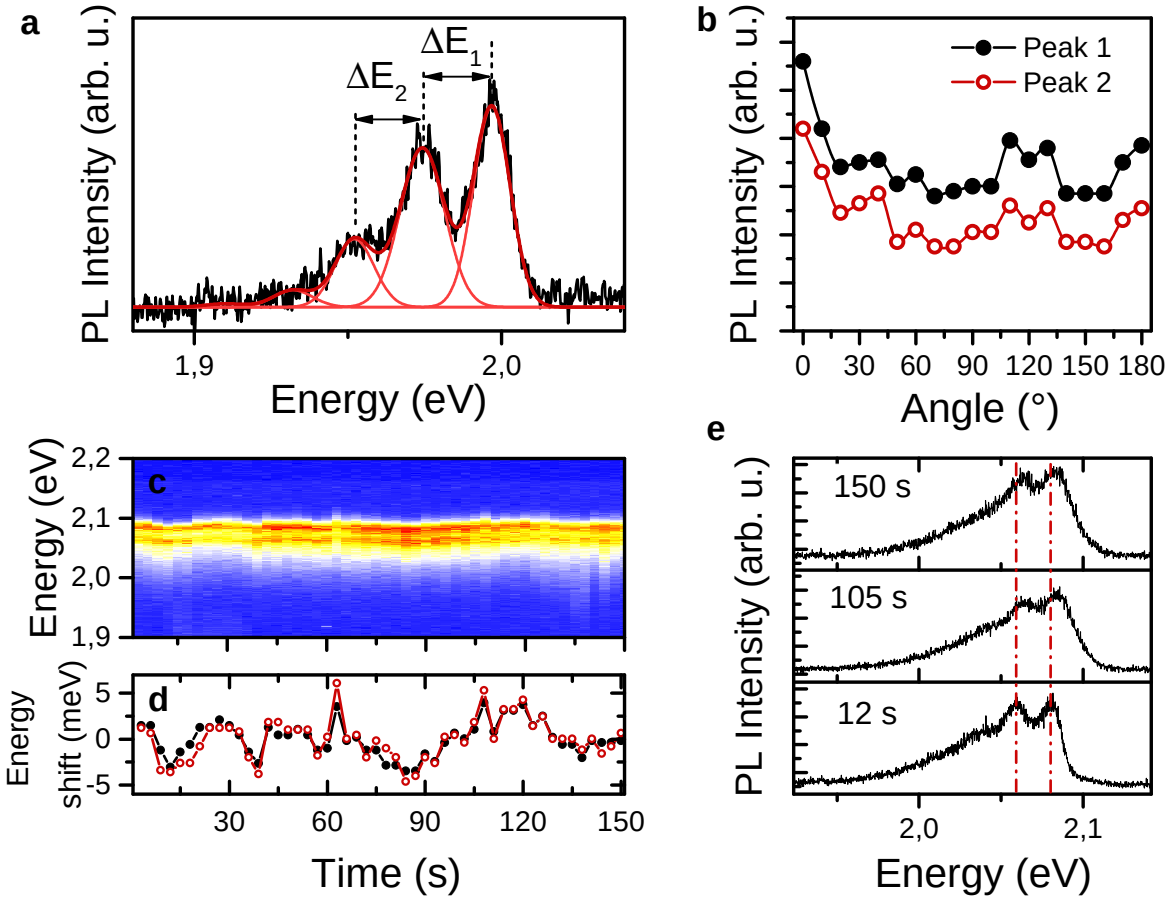

Fig. III.7 *(a) Typical emission of a single CdSe/CdTe NPLs and its multi-gaussian adjustment. (b) Polarization analysis of the highest peak in energy (peak 1) and its first replica (peak 2) of the single NPL spectrum (the lines are a guide for the eyes). (c) Evolution of the PL emission of another single NPL with time (integration time of 3 s) and (d) the associated spectral shift of peak 1 (black dots) and peak 2 (red dots). (e) PL spectra taken at given times of the trace in (c). The red dotted lines correspond to the position of peak 1 and 2 at 12 s.*

considered below: emission from the bright states of the electronic fine structure, shake-up processes and vibronic coupling.

It is common that the single object PL spectrum is representative of the fine structure of the object, with each peak corresponding to the emission of a different excitonic state [32, 82]. As we mentioned in Chapter I, the fine structure of the core/crown NPLs should be composed of two linearly polarized orthogonal non-degenerate states. The results obtained in the course of Chapter IV will indeed confirm that two states associated with linear dipoles are required to explain the polarization properties under high magnetic fields. We would thus expect to observe these two states in the form of two spectrally resolved peaks in the single NPL spectrum. However, as demonstrated in Chapter IV the energy splitting between these two states is of the order of tens of µeV, *i.e.* several order of magnitude lower than the tens of meV observed between the different peaks and than the width of these peaks themselves. The fine structure can hence be discarded as the origin of the multi-peaked emission.

The polarization properties of the emission were the subject of a complementary analysis. The anisotropic shape of the NPLs coupled to the large dielectric contrast between the NPLs and their environment leads to local field effects inside the NPLs causing a *pronounced* reduction of the internal electric field along the smallest dimensions (thickness and width) of the NPLs [44]. An estimation of these effects in the geometry characteristic of NPLs can be found in Appendix A. From these calculations, we expect that the emission intensities associated with each of the dipole composing the fine structure differ. The $|X\rangle$ state associated to the dipole aligned with the largest dimension should give rise to a more intense PL and the $|Y\rangle$ state associated to the smallest dimension should be less coupled to light. A ratio of ~ 1.5 is expected between I_X and I_Y in LC NPLs and ~ 1.2 in SC NPLs. In single NPLs a selection of each peak (I_X or I_Y) should be possible using the appropriate polarization analysis and we can expect to detect experimentally these differences. Figure III.7.b shows the polarization analysis of the two main peaks of the PL response (LC NPL). The analysis is hindered by the strong fluctuation in intensity of the NPL response and the effect of the NPL shape anisotropy can not be observed. However it is clearly noticeable that the two highest energy peaks show the same fluctuations, indicating that the two peaks share the same polarization properties, as expected for a zero phonon line and its vibronic replicas (see below).

Another process, called electron shake-up, has been shown to be responsible for the multi-peaked emission in core/shell CdSe/CdS NPLs [95]. In this process, the main excitation is a negative trion (two electrons and one hole). It can recombine through an Auger-assisted process: an electron-hole pair recombines and emits a photon while the remaining electron is promoted to higher electronic states of the NPLs. The energy of the emitted photon will then be the one of the trion transition reduced by the energy necessary to promote the remaining electron to the higher excited states. With such a process the overall single object spectrum does not have a constant pattern: the emission keeps evolving in time as the remaining electron is promoted to one state or another. The peaks arising from the shake-up process are not evenly spaced in energy. The energy difference between each peak is equal to the energy difference between the excited electronic levels that are themselves not evenly spaced in a parallelepipedal structure. For these reasons, the multi-peaked spectra observed in the CdSe/CdTe NPLs cannot be the result of Auger recombination. The regular separation in energy also rules out the possibility that the emission arises from a stack of NPLs, a possibility raised by a recent theoretical study [96]. The most likely and straightforward explanation is to attribute the different peaks to vibronic replicas of the excitonic transition.

To obtain a more representative picture of the properties of these core/crown NPLs, spectra from over ~ 25 objects are recorded for each core geometry, allowing us to perform a basic statistical analysis. The distributions of the most relevant parameters are presented in figure III.8 for LC and SC NPLs. The energy separation between the zero phonon line (ZPL, the line at higher energy) and its first replica is labeled ΔE_1, while the energy separation between the first and second phonon replica is labeled ΔE_2 (see figure III.7.a). Their respective distributions are presented in figure III.8.a and c. The energy separation between the peaks are clearly similar for LC and SC NPLs. The adjustments of the different distributions with a normal law allows us to determine their mean values and standard deviations to be $\Delta E_1 = 21.6 \pm 0.7$ meV and $\Delta E_2 = 20.2 \pm 1.2$ meV for LC NPLs and $\Delta E_1 = 21.8 \pm 0.5$ meV and $\Delta E_2 = 21.8 \pm 0.9$ meV for SC ones. The Raman spectrum (obtained in dense film) shows that there exists a LO phonon mode in these NPLs at 166 ± 2 cm^{-1}, *i.e.* an energy of 20.6 ± 0.3 meV, consistent with the value deduced from the single NPL's spectra (see figure III.9). A small difference is found in the FWHM of the ZPL for the two kinds of NPLs (figure

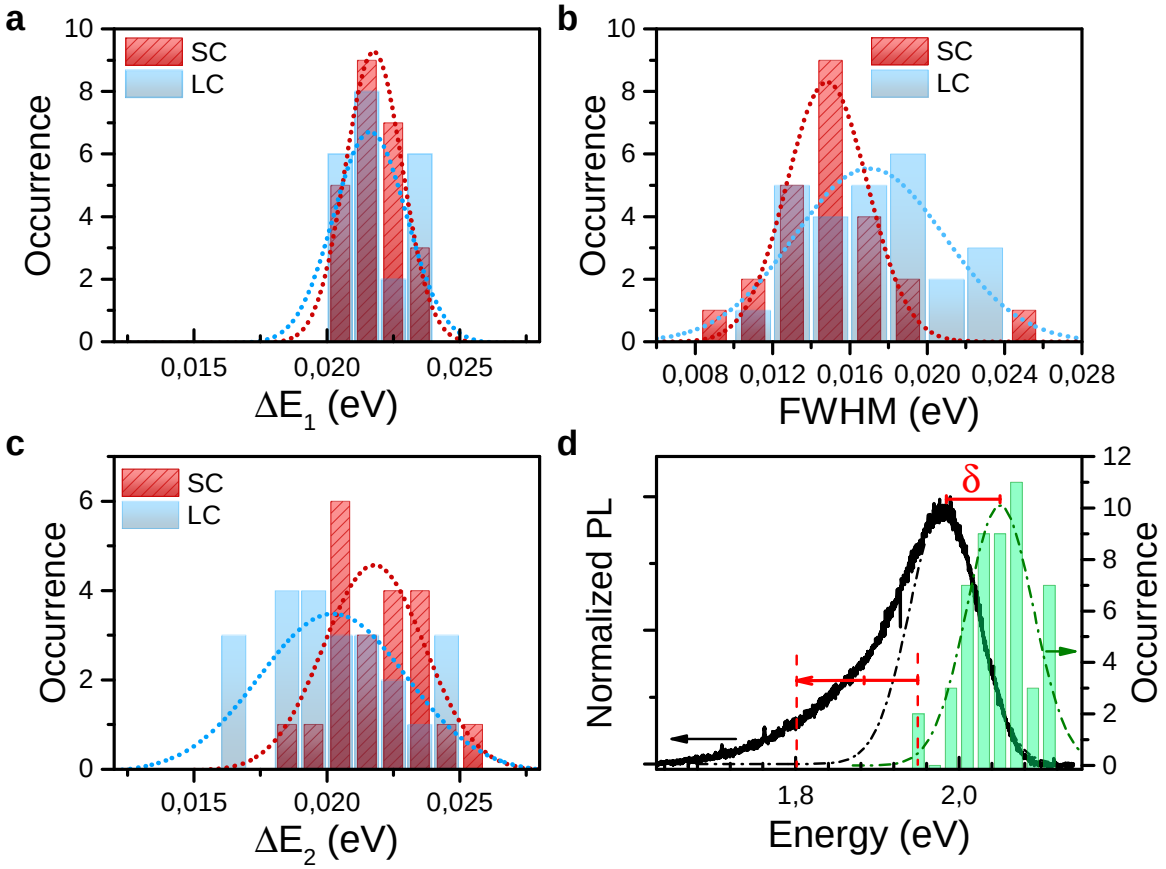

Fig. III.8 *Histograms of the energy differences between: (a) the zero phonon line (ZPL) and its first replica ΔE_1 and (c) the first and second replicas ΔE_2. (b) Histogram of the FWHM of the ZPL. (d) Comparison between the ZPL energy distribution (green) and the inhomogeneous PL of an ensemble of NPLs (black). The two are shifted by an energy δ. The red arrow corresponds to an energy of (4 ΔE_1 + δ) representative of the extension of the PL tail arising from the vibronic replica and taking into account the shift due to dielectric confinement. The dotted lines are the adjustment by a normal distribution of the different histograms.*

III.8.b), it increases from 14.8 ± 0.8 meV to 17.0 ± 1.5 meV as the core grows in size.

Finally, the last observation we would like to discuss is the ZPL energy position. Figure III.8.d shows the distribution of the ZPL energy distributions for both LC and SC NPLs. The ZPL is found in a relatively large band (FWHM of 80 meV), with a shape resembling the one of the high-energy parts of the ensemble spectrum. A shift δ of 79 ± 10 meV is found between this distribution and the ensemble emission. We will see further on that this shift is related to the change in the dielectric constant of the NPL environment. The large distribution in energy of the ZPL could be either attributed to fluctuations in the dielectric environment from one NPL to another or to inhomogeneities in the lateral sizes of the core/crown NPLs. Large variations of the dielectric medium felt by a single NPL deposited at the surface of a cover-glass are hardly conceivable, we are thus prone to attribute the large distribution to size inhomogeneities. This interpretation is also consistent with the existence of a broad distribution associated with the core and crown lateral sizes as can be seen in figure III.1. Adding an energy equivalent to

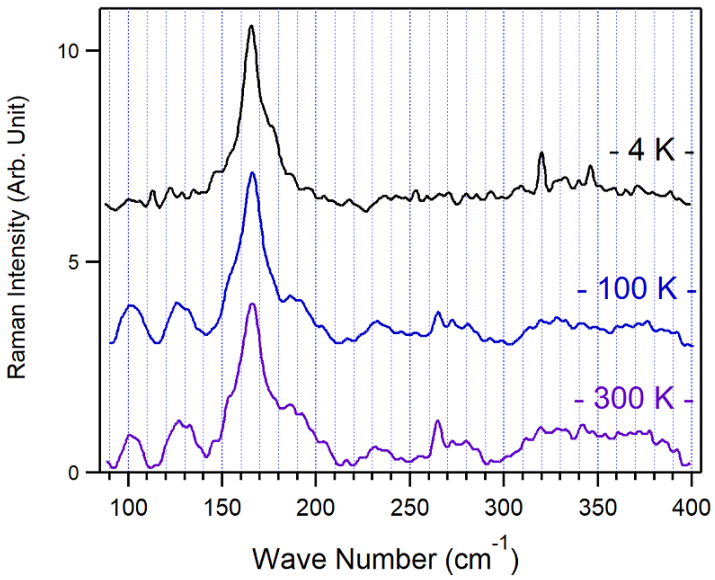

Fig. III.9 *Raman spectra of a film of LC CdSe/CdTe NPLs at 4 K, 100 K and 300 K. A single peak at 166 ± 2 cm^{-1} (= 20.6 ± 0.3 meV) dominates the spectra at all temperatures. These measurements were performed by our collaborators in Cambridge.*

$4\Delta E_1$ to the shift δ to account for the different phonon replicas (red arrow in figure III.8.d) allows one to reproduce quite well the low energy tail extension of the ensemble spectrum. This shows that the inhomogeneities in lateral sizes inherent to these core/crown structures and the large phonon side-band can indeed be held responsible for the observed broadness in the ensemble measurements.

b) Huang-Rhys factor

Now that we have established the importance of the phonon replicas in the emission of the core/crown NPLs, we would like to estimate the strength of the exciton-phonon coupling. This coupling is commonly quantified by the value of the Huang-Rhys factor, S, which can be determined from the evolution of the intensities of the different phonon replicas, as it was done by Groeneveld *et al.* for CdSe nanocrystals and CdTe/CdSe hetero-nanocrystals [73].

The Huang-Rhys factor is defined under an adiabatic approximation, where the mixing between the different electronic states due to phonon coupling is considered negligible. In this case, according to ref. [97], the complex motion of the lattice can be reduced to a one-dimensional configurational model, similar to the one used in the Franck-Condon principle in molecular systems with displaced harmonic-oscillators. According to this model at T = 0, the band-shape of an emission, related to the transition of an excited state (b) to a ground state (a), is given by [97]:

$$I_{ab}(E) = I_0 \sum_n F_n(0)\delta(E_{0,0} - n\hbar\omega - E), \tag{III.3}$$

where $E_{0,0} = E_{a,0} - E_{b,0}$ is the energy of the transition between the zero vibrational levels of the electronic states (b) and (a), $\hbar\omega$ the energy of the phonon, and n the number of phonons

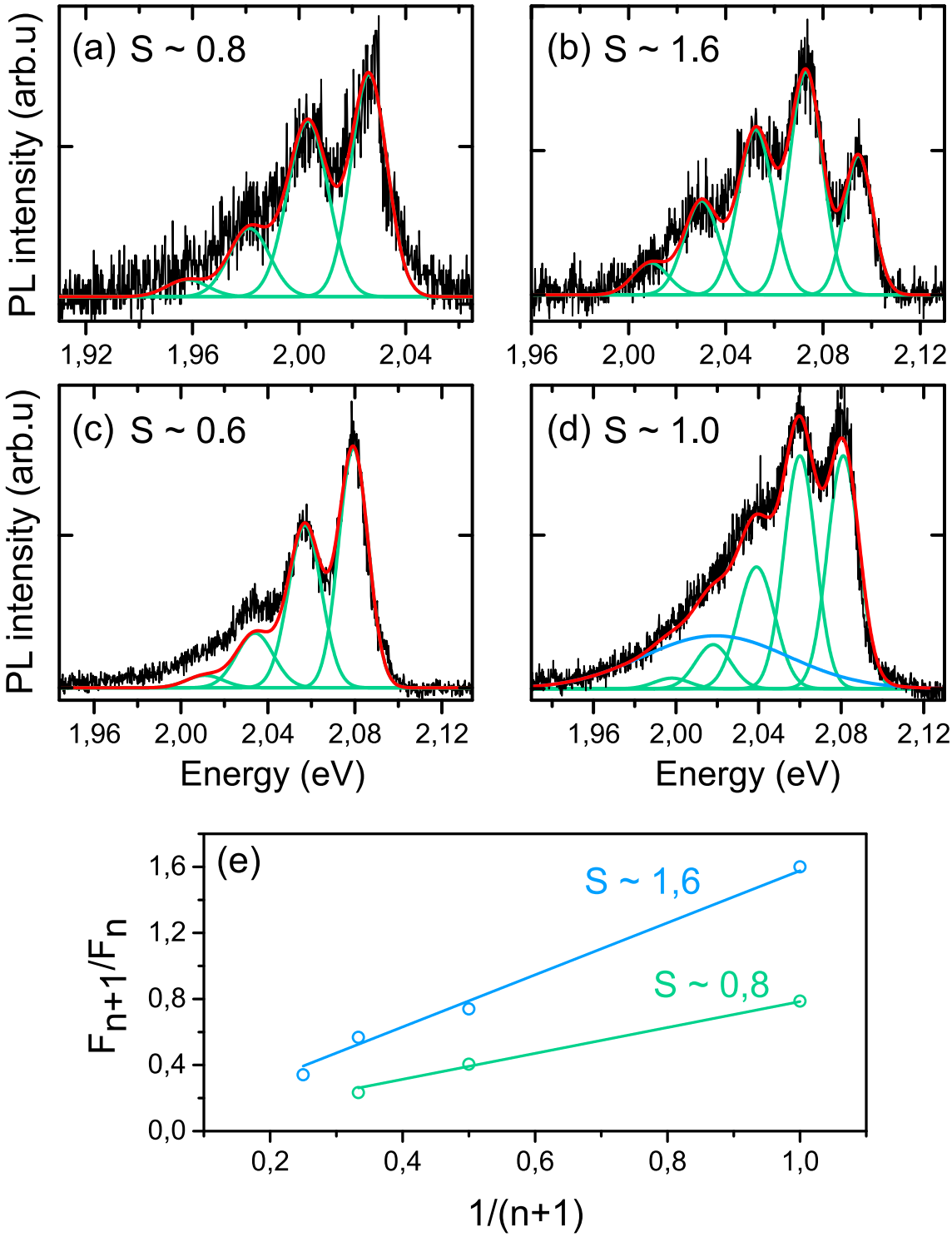

Fig. III.10 *(a-b) Single NPLs spectra and their multi-Gaussian fits, where the evolution given by equation III.5 is obtained. (c-d) Single NPLs spectra where a large emission at low energy has to be added to obtain the evolution given by equation III.5. (e) Evolution of the ratio of the intensities of the n+1 and n peaks of the spectrum as a function of 1/(n+1) for the spectra in (a) and (b). The linear adjustment of this evolution allows us to retrieve the Huang-Rhys factor S.*

generated in the transition. I_0 is the intensity of the full spectrum given by the b $\longrightarrow$ a transition probability. Finally, $F_n(0)$ is the Franck-Condon factor given by [97]:

$$F_n(0) = \frac{\exp(-S)S^n}{n!}. \tag{III.4}$$

The intensity of the ZPL line is thus equal to $I_0F_0 = I_0\exp(-S)$, while the n^{th}-replica has an intensity equal to I_0F_n. For $S = 0$, only the ZPL is present in the spectrum. As the Huang-Rhys factor increases, the phonon side-bands will gain in amplitude and when S becomes higher than 1, the first phonon replica will become more intense than the ZPL. Moreover we notice the ratio of the intensity of the $n+1$ and n peaks is equal to:

$$\frac{F_{n+1}(0)}{F_n(0)} = \frac{S}{n+1}. \tag{III.5}$$

This means that S can be determined from the evolution of the ratio of the intensity of adjacent peaks.

The evolution given by equation III.5 is found in some of the emission spectra, such as the ones presented in figures III.10.a and b or the one in figure III.7.a. From these, S can be unequivocally determined and values ranging between 0.6 and 1.6 are found, showing the large disparity in exciton-phonon coupling from NPL to NPL. Such disparity was also reported for CdSe nanocrystals [98]. For a vast number of spectra, another contribution in the low energy tail has to be added to recover the evolution given by the model (figures III.10.c and d), which hinders the estimation of S. This could highlight the presence of another emission band on top of the excitonic one. Further analysis of a larger number of spectra would be needed to settle this question. Finally, the Huang-Rhys factors measured here are consistent with the ones reported in CdTe/CdSe hetero-nanocrystals where slightly higher values ($S \sim 2.9$) are measured [73]. However, any further quantitative comparison between these two systems is hindered by their structural differences.

III.3.2 Numerical simulations

The experimental study of the single NPL's emission shows that the PL response is dominated by phonon side-bands. Nevertheless, numerical simulations can also provide useful information about the under-lying electronic structure in these NPLs. As we will see now, calculations provide insights into the role of the Coulombic interactions in these type-II structures (role of the dielectric confinement and influence of charged defects upon the exciton transition energy). They furthermore give indications about line broadening processes in core/crown NPLs. They were performed by our collaborators, Josep Plannelles and Juan Climente, from the University of Jaume I in Castellò, Spain.

The energies and the envelope of the wave functions of both electrons and holes are calculated in the $\mathbf{k}\cdot\mathbf{p}$ theory framework and use effective mass Hamiltonians. Details about the method used can be found in ref. [42] and [99]. The simulations are performed for a NPL with a crown of lateral sizes 18 x 40 nm^2 and a core equal to 10 x L_y nm^2, where the length of the core L_y (see figure III.11.a) is varied between 10 and 30 nm, allowing us to follow the evolution of the electronic structure from the SC to the LC NPLs.

a) Energies and wave functions of the IX

A first set of simulation leads to the wave functions and energies of the electrons and the holes, in the simple case of non-interacting electron/hole pairs. Figure III.11.c presents the

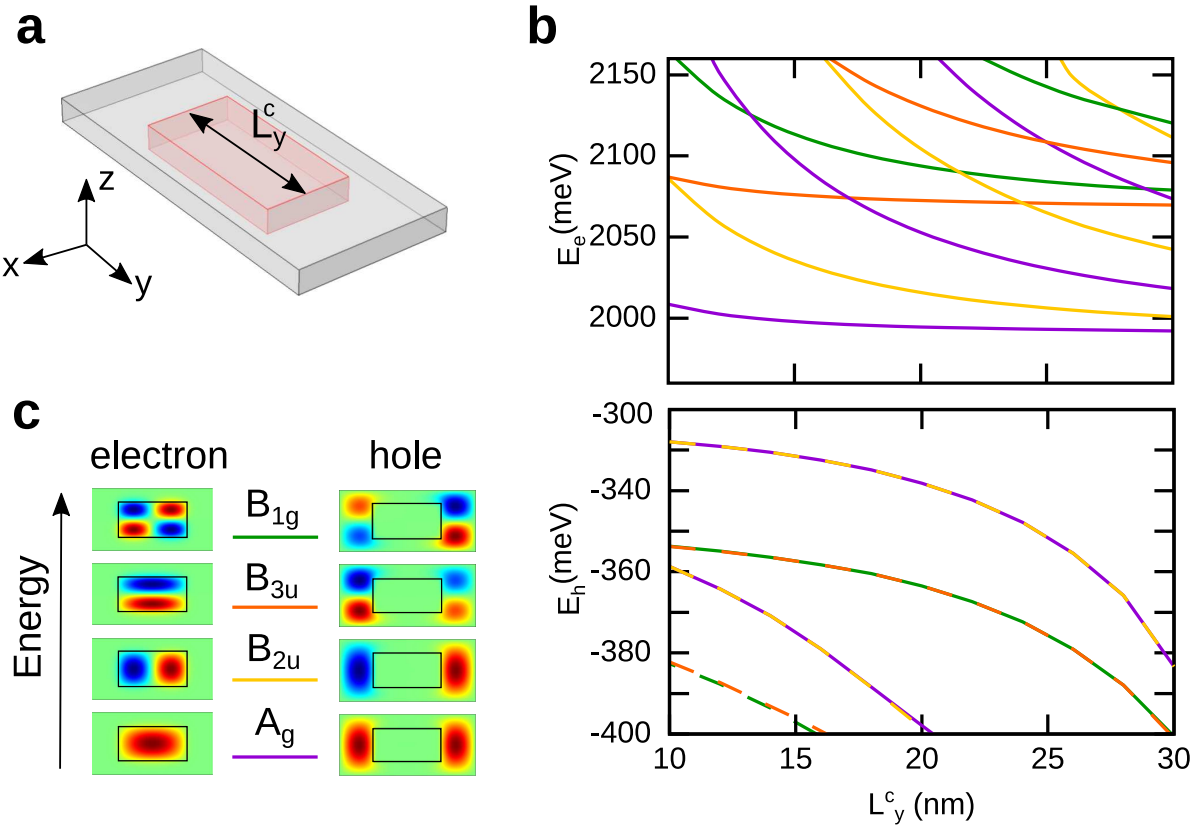

Fig. III.11 *(a) Geometry of the NPL used in the numerical simulations. (b) Evolution of the energies of the first excited states of the electrons (top) and the holes (bottom) with the length of the core L_y. (c) Envelops of the wave functions of the first excited states of the electrons and the holes and their symmetries (irreducible representations). The color ascribed to each symmetry is used in (b) for the energies.*

envelopes of the wave functions of the first four excited states of both charge carriers, while in figure III.11.b the evolution of the energy of these states is plotted as function of L_y (the colors of the plots for each symmetry of the states are given in figure III.11.c). Due to the core/crown geometry, the electrons and the holes do not exhibit the same behavior with the lengthening of the core. The electrons, confined in the CdSe core, behave like particles in a 2D box. As the length of the core increases, the energies of the states with the same number of nodes along y tend to converge, similar to what is observed in a 1D wire. The holes, confined in the CdTe crown, have their wave functions split in two on both sides of the core, with a vanishing density in the middle of the NPL along the x-direction (width of the NPL). Due to the small width of the NPL and the repulsive potential created by the core, the holes wave functions are two-fold degenerate solutions (A_g/B_{2u} and B_{3u}/B_{1g} doublets), similar to those found in a double quantum well. When the core gets longer, the quantum confinement of the holes increases, leading to the increase of their energies, as opposed to what is observed for the electrons energies.

Figure III.12.a presents the hole and electron density cross-sections for different levels of approximation. First, the simple case of a non-interacting electron/hole pair is shown in light green, while the density in dark green is the one obtained when the Coulombic interaction

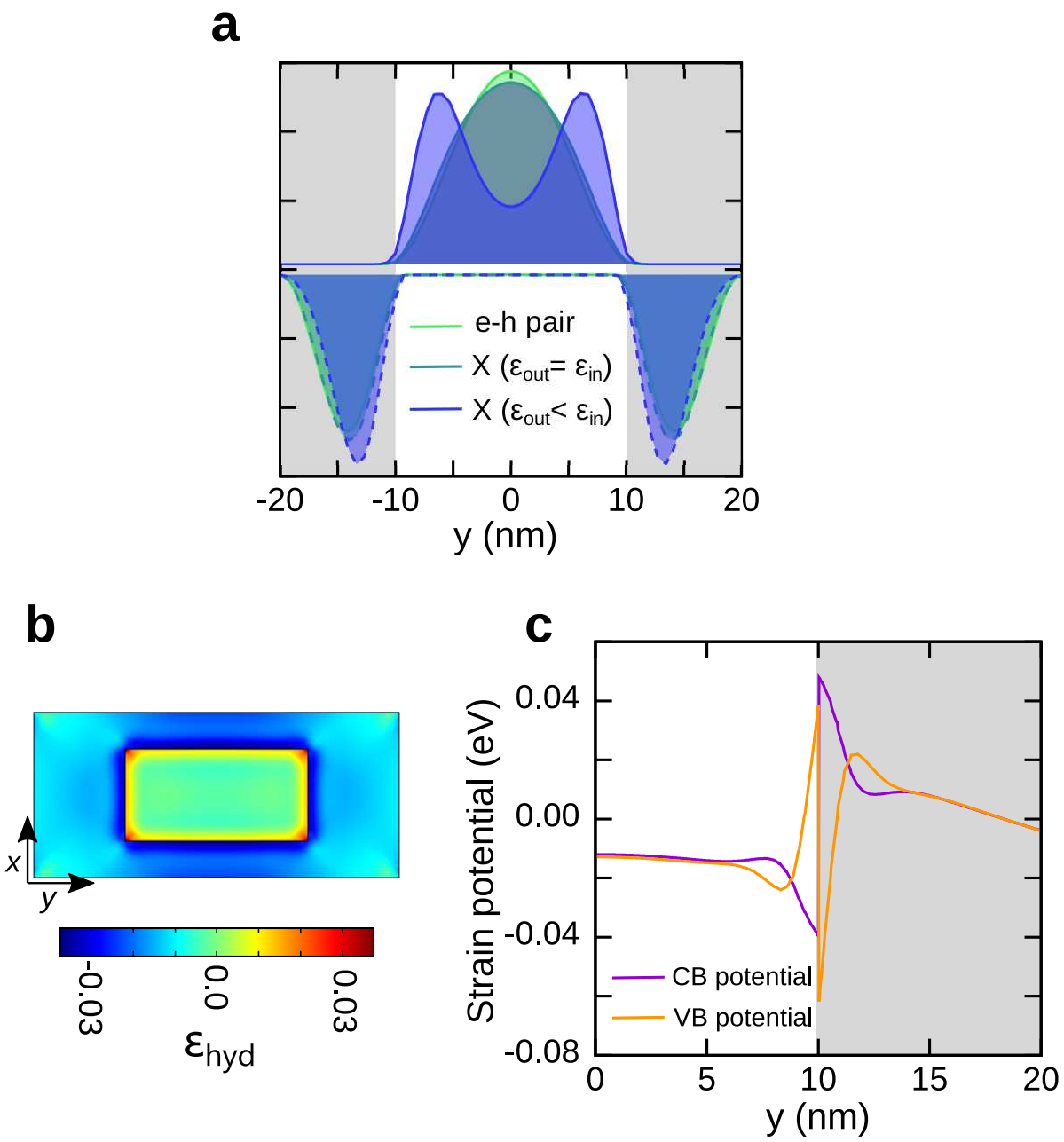

Fig. III.12 *(a) Exciton ground state charge density cross-sections for a NPL with L_y = 20 nm for: (i) a non-interacting electron-hole pair, in light green, (ii) an interacting electron/hole pair and no mismatch between the dielectric constants of the NPL and its environment ($\epsilon_{in} = \epsilon_{out} = 10$), in dark green, and (iii) an interacting electron-hole pair, $\epsilon_{in} = 10$ and $\epsilon_{out} = 2$, in violet. (b) Hydrostatic strain in the xy plane for a L_y = 20 nm NPL. (c) Resulting deformation potential at the core/crown interface for the conduction and valence bands. Grey regions correspond to the crown.*

between the electron and hole is switched on but without effect of the dielectric mismatch between the NPL and its environment. We see that the Coulomb interaction, itself, has a relatively small effect on the carriers' wave functions: the electron wave function slightly

spreads out and the hole is brought closer to the interface. However, it is clear that the density in violet obtained when the Coulombic interaction and the dielectric confinement are taken into account ($\epsilon_{in} = 10$ and $\epsilon_{out} = 2$), is completely different. The electron wave function splits in two, forming two lobes close to the interface, while the hole wave function is brought even closer to the hetero-interface. This modification is the result of the large enhancement of the binding energy of the IX due to the dielectric mismatch (see Chapter I). The dielectric confinement typically increases this binding energy from 10 meV to 50 meV, which is a considerably large value for an IX. This explains in particular that the IX PL can still be observed at room temperature.

We would like to stress that, in all the cases considered here, the IX retains its indirect nature: the two carriers are always clearly spatially separated. This results from the fact that the domains excitons binding energies (the binding energy of the excitons in CdSe or CdTe) are close to 200 meV [38], smaller than the band offsets, equal to 0.53 eV for the conduction bands and 0.69 eV for the valence ones [89]. Some processes could however lead to the localization of the exciton at the CdSe/CdTe interface. Trapping of the carriers in the potential well induced by strain is a well known process in hetero-structures and may have an important impact on the excitation structure itself. This is the point that was explored first. The strain field in these NPLs has thus been calculated by our collaborators (figure III.12.b) using a method detailed in ref. [99]. It is found to be tensile on the core side of the interface and compressive on the crown one. It hence creates potential wells for the electron and the hole at the interface, as can be seen in figure III.12.c where these potentials are plotted. However, the amplitudes of these wells (some tens of meV) are deemed too weak to lead to the localization of the exciton at the interface. Other phenomena were envisaged which could lead to the localisation of the exciton: the alloying of this interface resulting from inter diffusion processes during the NPL growth and the presence of charged defects trapped at the interface. It was found that (not shown here), like strain, they were not strong enough to localize the exciton.

b) Simulated emission spectra

To easily compare the experimental results to the theoretical ones, simulated emission spectra can be reconstructed from the energies of the different excitations in these NPLs. The intensity given to each line of the spectra is representative of the decay rates of each excitation, which is calculated from the overlap of the electron and hole wave functions (see ref. [42]). Figure III.13.a shows such spectra with the transition of the two most likely excitations, namely the neutral exciton (red) and the negative trion (blue), for different core lengths. The numerical simulations can not give the 'exact' absolute energy of the different emission lines. However, they can be trusted to reproduce the relative evolution of the different transitions with the core length. The increase of the core length does not noticeably have the same impact on the two types of excitations. The energy of the exciton blue-shifts (tens of meV) as the core length increases, while the energy of the trion emission red-shifts. Both evolutions are related to the change in the Coulombic interactions with the extension of the core. As the core gets longer, the electron/hole attractive interaction decreases, explaining the blue-shift of the exciton emission. The decrease of the electron/hole interaction also takes place in the case of the negative trion when the core gains in size. However, it is balanced out by the simultaneous decrease of the electron/electron repulsion inside the core. This last process prevailing over the first one, the trion emission red-shifts.

From these simulations, we can deduce that the emission in these NPLs arises mainly from

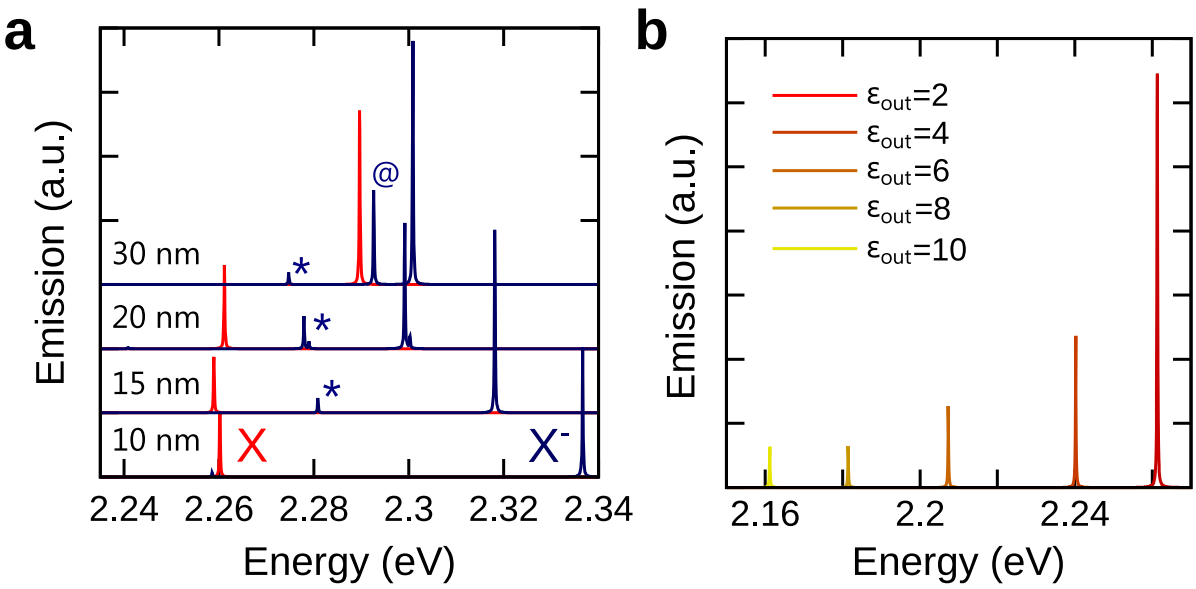

Fig. III.13 *(a) Simulated emission spectra, at $T = 7\ K$ and $\epsilon_{out} = 2$, of the neutral exciton (X) and negative trion (X^-) for L_y ranging between 10 nm to 30 nm. The lines labeled with an asterisk correspond to the so-called shake-up replicas and the one labeled with a @ corresponds to the recombination of a triplet trion. (b) Simulated emission spectra at $T = 7\ K$ of the neutral exciton with values of ϵ_{out} ranging between 2 (dielectric constant of the organic ligands) and 10 (dielectric constant of CdSe and CdTe).*

the recombination of a neutral exciton, since the emission of the LC NPLs is blue-shifted compared to the one of the SC NPLs (see figure III.2.a). Moreover, since we do not observe any change in the peak separation between the SC and LC NPLs, we can rule out the presence of charged excitations in the observed single NPLs spectra, as opposed to what has been observed in CdSe NPLs [100]. Finally, the lines with an asterisk in figure III.13.a represent the emission arising from the so-called shake-up process, mentioned in section I.3.1, where the trion recombination goes along with the promotion of the remaining electron to a higher state. The emission line labeled with a @ arises from the recombination of a triplet trion, where one of the two electrons is in a higher electronic state, this triplet trion being populated at low temperature. As already discussed, the shake-up process or the existence of a triplet trion do not lead to equidistant emission peaks in the PL. The fact that such emission peaks are not observed in the single NPL PL spectrum strengthens the claim that the emission has its origin in the neutral exciton recombination.

Simulations can help us to quantify the impact of the dielectric confinement on the emission of the NPLs. We already discussed in Chapter I the impacts of the mismatch between the dielectric constant of the NPLs and their surrounding environment. In a general manner, the dielectric confinement leads to the enhancement of the different Coulombic interactions. The dilution of the NPLs will lead to the increase of this dielectric confinement since the surrounding media of the NPLs will change from being composed of other NPLs, with $\epsilon_{CdSe} \approx \epsilon_{CdTe} \approx 10$, to organic ligands, with $\epsilon_{ligands} \approx 2$. Figure III.13.b shows the evolution of the neutral exciton transition line with the dielectric constant of the environment, ϵ_{out}. The exciton emission both

blue-shifts and increases in intensity with the lowering of ϵ_{out}. As the dielectric confinement increases, two processes compete with each other and explains the evolution in the energy of the exciton transition. First, as we already stated, the dielectric confinement enhances the electron/hole interaction leading to a lowering of the exciton transition energy. However here this process is outweighed by the increase of the self-energy potential which is repulsive [38], leading to the overall blue-shift of the emission. This latter process has already been shown to be of large importance in type-II systems [42]. As for the increase in the intensity, it can be directly related to the diminution of the exciton Bohr radius with the increase of the dielectric confinement, leading to faster recombination of the exciton [101].

Given the previous predictions, we can thus compare the energy shift observed between the PL of the ensemble measurements to the one of the single objects. The shift is found to be around 70 meV. This value is consistent with the numerical calculations. It puts ϵ_{out} between 6 and 8, close to the value expected in a dense film of NPLs where the dielectric environment is not well defined.

c) Role of trapped charges

Simulations can also help us to gain insights into the origin of the spectral diffusion and hence on the broadening of the spectral emission. One of the mechanisms usually mentioned to explain the occurrence of random spectral shifts is the Stark effect: as the electrostatic environment changes the exciton transition will see its energy modified. The formation of trapped charges can be one of the causes leading to the modification of the electrostatic environment [98]. The calculations of the energy of the neutral exciton and its envelope wave function were thus carried out in the case where a point charge Q, modeling a charge in a trap state, is either placed on the top of the NPL or at the core/crown interface. Figure III.14.a shows how the energy of the first excitonic transition evolves with the value of the charge. For a charge Q_{top}, it leads to an asymmetric shift with the sign of the trap charge. In the case of Q_{int} the response is almost symmetric and weaker. These effects can be understood with the help of figure III.14.b which shows the impact of a positive charge $Q = 0.5\ e$ on the envelope wave function. When the additional charge is placed at the interface, it attracts and repels the electron and the hole in a similar way, leading to some type of compensation of the two effects. While in the case of a Q_{top}, there is a strong impact on the electron while the hole remains relatively unperturbed. The lack of compensation would lead to a somewhat stronger effect on the overall shifts. The grey-shaded area in figure III.14.a corresponds to the spectral range explored by the exciton in our experiments ($\sim \pm$ 7 meV) and it is noticeable that only a small charge ($|Q| < 0.2$) already explains the observed shift.

As soon as the wave function of the exciton is known it becomes possible to understand how both the NPL geometry and the trapped charges may influence the strength of the exciton-phonon coupling through the calculation of the Huang-Rhys factor. Indeed, according to ref. [102], the Huang-Rhys factor is proportional to the $v_{\mu\mu}$ matrix element:

$$v_{\mu\mu}(\mathbf{k}) = \int d^3r_e\, d^3r_h\, \Psi_\mu^* \Psi_\mu \left[exp(i\mathbf{k}\cdot\mathbf{r_e}) - exp(i\mathbf{k}\cdot\mathbf{r_h})\right], \tag{III.6}$$

where Ψ_μ is the exciton wave-function, $\mathbf{k}$ the phonon wave vector and $\mathbf{r}_j$ (j = e, h) the position of the electron and hole. As a simplification, this formula considers bulk phonons, the calculations for confined objects requiring another level of complexity. The results given below should thus be considered as an indication of the evolution taking place in these NPLs only, as the core length increases. When trapped charges are not considered, a Taylor expansion of the plane

waves of equation III.6 shows that the lowest terms of the expansion are the quadrupolar ones. Indeed the dipolar terms (terms in $\mathbf{k} \cdot \mathbf{r}_j$) vanish due to the odd parity of r_j and the even parity of Ψ_μ. The quadrupolar terms can thus be written in the quadratic form as:

$$v_{\mu\mu}(\mathbf{k}) \approx -\frac{1}{2} \int d^3r_e \, d^3r_h \, \Psi_\mu^* \Psi_\mu \left[\mathbf{k}^T \mathcal{R}_e \mathbf{k} - \mathbf{k}^T \mathcal{R}_h \mathbf{k} \right], \tag{III.7}$$

where $\mathcal{R}_j$ are the polarization tensors. The integral will be dominated by the terms in y^2 since the length of the NPL lies in the y-direction. The exciton-phonon coupling terms are finally dominated by the following contribution:

$$v_{\mu\mu}(\mathbf{k}) \approx \frac{1}{2} k_y^2 \int d^3r_e \, d^3r_h \, \Psi_\mu^* \Psi_\mu \left[y_h^2 - y_e^2 \right]. \tag{III.8}$$

The Huang-Rhys factor amplitude is then deduced from easily accessible observables, *i.e.* from the difference between the y^2 expectation values of the hole and the electron. Figure III.14.c shows their evolution as a function of the core length. The evolution of $\langle y_h^2 \rangle$ with L_y is linear: as the core length increases, the hole is pushed further and further away from the center of the NPL. The value of $\langle y_e^2 \rangle$ also increases, since the electron wave function is driven to the core/crown interface when the core increases due to the Coulombic interactions (highlighted in figure III.12.a). The overall difference increases only slowly when going from SC to LC NPLs, explaining that similar Huang-Rhys factors can be observed for the two types of NPLs.

Trapped charges can lower the symmetry of the exciton wave function which should be associated with the apparition of dipolar terms in the exciton-phonon coupling factor of equation III.6. Following a similar development we find that the dipolar terms are dominated by the difference $\langle y_h - y_e \rangle$. Figure III.14.d shows this difference in the case of Q_{int} and Q_{top} and only the presence of Q_{int} leads to the appearance of dipolar terms. These numerical results should be handled with care. A direct comparison between the absolute values of dipolar and quadrupolar contributions is not possible, as the prefactors were not taken into account in the calculation and quantitative estimations would need the precise knowledge of the confined phonons modes at play in these NPLs. We can only give trends: the important point being that the formation of charge defects could lead to an increase in the phonon coupling strength. However, we believe that dipolar contributions never exceed the quadrupolar ones for two reasons. First, there is no visible change in the Huang-Rhys factor from SC to LC NPLs, while a significant modification of $\langle y_h - y_e \rangle$ would be expected. Then, all the observed shifts of the PL with time are 'rigid' shifts which implies that the presence of defect charges does not change the nature of the exciton-phonon coupling. If an increase of the coupling occurs, through the appearance of a dipolar contribution, it is not strong enough to modify the vibronic pattern in the PL emission as observed in ref. [57].

III.3.3 Complementary remarks

Before concluding, we would like to highlight several points. First, the coupling between the exciton and the LO phonons, characterized by the Huang-Rhys factor, is large in these core/crown structures. This coupling relies on the Frölich interaction: the relative displacement of the positive and negative ions of the lattice induces a lattice polarization field which can couple to the electric field of the charge carriers [103]. The large exciton-LO phonon coupling explains the large numbers of phonon replicas of the ZPL and hence the extension of the single NPLs emission spectra ($\sim$ 100 meV).

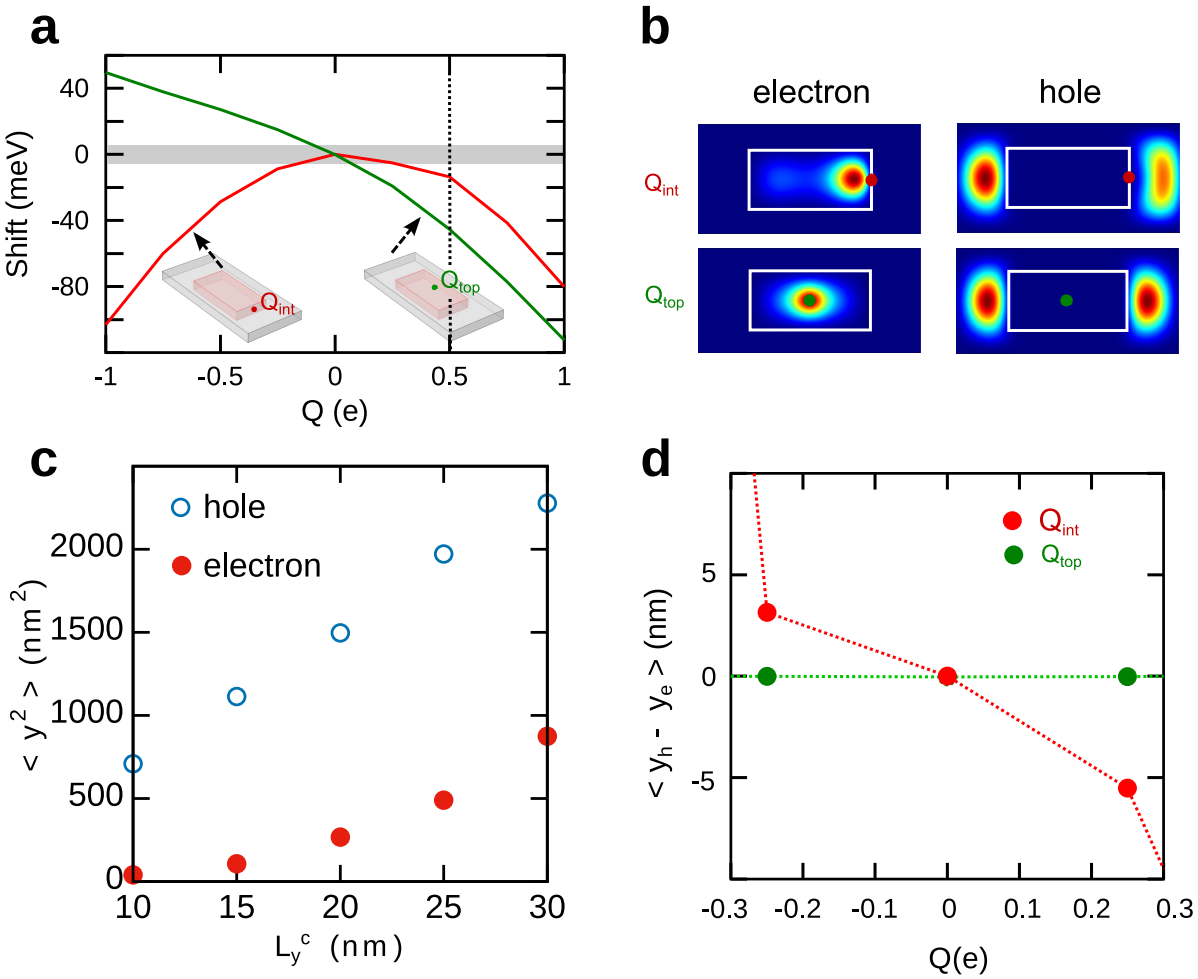

Fig. III.14 *(a) Exciton spectral shift induced by a point charge: in red, a charge Q_{int} positioned in the middle of the core/crown interface along y and, in green, a charge Q_{top} positioned in the middle of the NPL, 1.7 nm above the surface. The charge strength is varied between -e (unscreened electron) and +e (unscreened hole). (b) Charge densities of the electron and the hole when a charge $Q = 0.5$ e is added at the interface or on top of the NPL. (c) Evolution of the mean value of the y coordinate squared with the core length L_y for the electron (red filled circles) and the hole (open blue circles). (d) Evolution of the mean value of the electron/hole spacing along the y-direction with the strength of an added charge either at the interface (red circles) or on top (green circles) of the NPL.*

However, the exciton-LO phonon coupling cannot explain the broadness of the ZPL and its replicas with a FWHM of $\sim$ 15 meV. The coupling with acoustic phonons usually leads to homogeneous linewidths of the order of hundreds of µeV only [16, 85]. The fact that the ZPL line has a Gaussian and not Lorentzian shape additionally highlights that another process is at play, and we conjecture it is also of electrostatic nature: the trapping and detrapping of charges, as simulated here, or the rearrangement of the capping ligands on the surface of the NPLs are the two main processes mentioned in the literature to explain the fluctuations of the electrostatic environment [58, 104, 105].

Different studies in the literature showed that two time-scales are at play in the process of spectral diffusion [105, 106]. The 'long time scale' ($\sim$ s and fraction of s) is usually studied through single object spectroscopy [104] (the involved charge fluctuations then typically explain the rigid spectral shift observed in the trace of figure III.7.c). To be able to monitor the effects of the fastest events, experiments with a much better time resolution than the one offered by PL spectroscopy are required, such as photon-correlation Fourrier spectroscopy [105,107]. The work of Coolen *et al.* shows that this process saturates on a millisecond time-scale [107]. Even if the two types of spectral diffusion have different origin, they both occur through discrete jumps as opposed to a continuous drift of the emission lines [105, 106]. From the single NPL data collected here, different time scales are hardly discriminable. A study of the ZPL and replicas width as a function of the integration time could already help to do so. However such a study would require us to improve our ability to collect a large number of photons to be able to have our integration time progressively reduced.

The fluctuations in the electrostatic environment of the NPLs can also have an impact on the exciton-LO phonon coupling, as previously reported in the literature [57]. The work of Sagar *et al.* shed light on the issue of measuring the Huang-Rhys factor through Raman or spectral PL measurements. These techniques lead to the build-up of charges, resulting in more polar objects which have a stronger coupling to phonons through the Frölich interaction [108]. The Huang-Rhys factors found using these techniques would be several orders of magnitude higher than those found through temporal measurements that are able to probe the exciton-phonon coupling before any charges have time to appear (temporal measurements give a Huang-Rhys factor $\sim$ 0.03 in CdSe nanocrystals [108]).

The remark formulated previously is also useful here: we notice that the PL pattern (*i.e.* the ratio in intensity of the ZPL and its phonon replicas) does not change in most of the PL traces as a function of time. The addition of a charge in the exciton environment has thus no visible impact on the coupling with the optical phonons, opposite to what should be observed if the phonon coupling was driven by extra charges as shown in ref. [108]. We are led to conclude that the observed coupling properties are intrinsic to the core/crown structure and the indirect nature of the exciton. This conclusion is in line with the analysis of Groeneveld *et al.*, where the authors conclude that the high Huang-Rhys factors they measure in CdTe/CdSe hetero-nanocrystals (S $\sim$ 2.9) are characteristic of the intrinsic coupling (*i.e.* unaffected by resident charges) between an IX, having large polarisability, and LO phonons. In core/crown NPLs, the symmetry imposes that quadrupolar terms are mainly responsible for this coupling, which is an original feature.

Conclusion

In this chapter we studied the absorption and PL properties of CdSe/CdTe core/crown NPLs. In the first section, we presented measurements made on dense films of NPLs and showed that

the emission of the IX was particularly broad, even at low temperature despite the absence of dispersity in the NPLs thickness. PL measurements as a function of the temperature allowed us to give an estimation of the IX binding energy that is placed in the tens of meV range.

In the second section, the PL properties of NPLs studied as individual objects were investigated. This study was supported by numerical simulations, which shed light on the mechanisms impacting the IX properties. The PL emission is shown to be dominated by the recombination of the neutral IX and its phonon replicas. The experimental observations coupled to the numerical predictions allows us to discard the possibility of an emission dominated by trion recombination and Auger relaxation mechanisms ('shake-up' process). The large spectral diffusion ($\sim$ 7 meV) can be rationalized by the existence of trapped charges on the surface of the NPL or at its hetero-interface, which will modify the energy of the IX transition through Stark-related mechanisms. Moreover, we believe that the large linewidth of the ZPL and its phonon replicas detected at the single NPL level has a similar electrostatic origin. Finally, we do not observe any increase of the exciton-LO phonon coupling with the modification of the electrostatic environment, leading us to conclude that the relatively strong coupling measured in these core/crown NPLs is intrinsic to the IX, as opposed to extrinsic causes such as the building-up of charges in the NPLs.

Chapter IV

Magneto-optical study of CdSe/CdTe nanoplatelets

In the previous chapter, it was shown that the observation of the photoluminescence (PL) from single CdSe/CdTe nanoplatelets (NPLs) did not allow the observation of the indirect exciton (IX) fine structure (EFS), due to the large emission broadening. Another approach can be used to reveal this EFS: the study of the properties of the PL at high magnetic field [31, 109, 110]. The B-field, through the Zeeman effect, will split and mix the different levels of the EFS. Thus some of its parameters can be deduced from a careful modeling of the observations made at high magnetic field. Moreover, a magnetic field is required to study the spin lifetime. A long spin relaxation lifetime, coupled to the long lifetime of the exciton in these core-crown NPLs, could make them interesting objects for spintronics applications, where both qualities are required.

The magnitude in magnetic field needed to obtain a large enough effect on the PL properties of the NPLs is not trivial to obtain. That is why the investigations were carried out at the High Field Magnet Laboratory (HFML) from the Radboud University in the Netherlands, where we could use a resistive magnet creating a field of up to 31 T. These measurements were done in collaboration with the group of Akshay Rao from the Cavendish Laboratory in Cambridge (UK), and more precisely Raj Pandya, as well as Yuttapoom Puttisong from the Linköping University in Sweden. The results of these experiments are published in Pandya *et al.* [80].

In the first section of this chapter, we will present the results obtained from the high magnetic field measurements and explain how a model of the EFS composed of two linear bright states can rationalize the experimental observations. In the second section, experiments that corroborate our interpretation will be described and analysed. Finally in the last section, we will discuss to what extent our model is justified and address its limitations.

IV.1 High magnetic field experiments

In this first section, we present an overview of the different experiments done at the HFML and their results. We will see that an EFS made of two linear bright states, as predicted by theoretical considerations (see Chapter I), seems to match the experimental results. We will describe such a model under a magnetic field, and discuss the results obtained from its adjustment with the experimental data.

IV.1.1 Experimental results

The experimental set-up used in the HFML is described in Chapter II.4. The NPLs studied here have a thickness of 4 ML and lateral dimensions of $\sim$ 12 x 35 nm^2 for the CdSe core and of $\sim$ 20 x 50 nm^2 for the CdTe crown. The NPLs are this time diluted in a solution of polystyrene ($\sim$ 20 % weight per volume), which is then spin or blade coated on glass slides. With this technique, a thin polystyrene layer where the NPLs are randomly orientated is obtained on the glass slide. The lifetimes of the NPLs in the polystyrene film and in solution are similar, which indicates that the NPLs do not aggregate when they are spin-coated in the polystyrene solution.

a) Non-resonant and quasi-resonant excitation

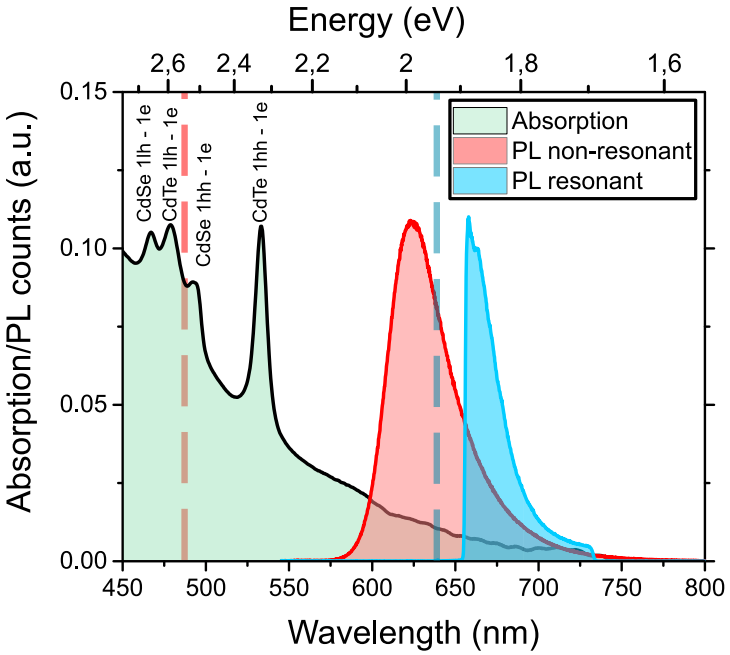

Fig. IV.1 *Absorption of CdSe/CdTe NPLs at 4 K and their normalized luminescence at 1.6 K. The red PL spectrum corresponds to the luminescence collected under non-resonant excitation at 485 nm (red dotted line), while the blue PL spectrum corresponds to the luminescence collected under quasi-resonant excitation at 640 nm (blue dotted line). In this case a sharp edge band-pass filter allows us to remove the contribution from the laser, causing this sharp edge in the PL.*

In the experiments shown below, two different lasers are used as excitation sources. They are both picosecond laser diodes, one of them emitting at 485 nm and the other at 640 nm. They are either used in a continuous wave mode for the measurements of the steady-state PL or pulsed at 250 kHz for the measurements of the time-resolved photoluminescence (TRPL). The polarization of the excitation is controlled with wave plates, in order to have a well defined circular or linear polarized excitation.

Figure IV.1 shows the absorption of the NPLs at 4 K as well as the PL at 1.6 K for different excitation energies. First, the red spectrum represents the PL collected when the NPLs are

excited non-resonantly at 485 nm, corresponding to an energy of 2.56 eV, an energy higher than the heavy hole transitions of both the core and the crown.

The other laser emitting at 640 nm is used to excite quasi-resonantly the samples. The blue spectrum of figure IV.1 indicates the PL collected in this case; a sharp edge band-pass filter (660-730 nm) is used to suppress the light coming from the laser, explaining the sharp edge of the spectrum. This quasi-resonant excitation is possible because the indirect exciton has a non-zero absorption cross-section, in spite of its indirect nature (see Chapter III and [25]). The quasi-resonant excitation is useful because it allows the creation of well defined spin configurations. Indeed, by choosing carefully the polarization of the incoming light, only the states that have the corresponding angular momentum will be excited (see Chapter I). Moreover, the resonant excitation suppresses the processes of charge transfer from core to crown or *vice versa* that would normally occur otherwise during the formation of the IX, as well as the momentum relaxations from higher levels, both processes leading to the loss of the initial spin configurations.

b) Degree of circular polarization

We showed in Chapter I that when a magnetic field is applied to a semiconductor, it splits the levels of the EFS due to the Zeeman effect. Since the levels are populated following a Boltzmann distribution, as the amplitude of the splitting increases and starts to be in the order of k_BT, the lowest level in energy will be more and more populated, leaving the upper levels empty. This would lead to a highly polarized emission, since the emission arises from a single level with a well determined polarization. The degree of polarization of the emission thus gives information on the amplitude of the Zeeman effect and on the original EFS.

In this first part, we will focus on the degree of circular polarization (DCP). Indeed, at high magnetic field the levels of EFS tend to be circularly polarized, regardless of their polarization at 0 T [111]. The DCP is defined by:

$$DCP = \frac{I_{\sigma+} - I_{\sigma-}}{I_{\sigma+} + I_{\sigma-}}, \tag{IV.1}$$

where $I_{\sigma+}$ ($I_{\sigma-}$) is the intensity of the PL which is emitted in σ^+ (σ^-) polarization. In the general case found in bulk semiconductors, where the two emitting levels are circularly polarized and degenerate at 0 T, the absolute value of the DCP increases when a magnetic field is applied on a material. Indeed, at a given temperature, when applying the B-field, the two levels split and the lowest level, which emits a light either σ^+ or σ^- polarized, will be more and more populated while the upper level with the opposite polarization will be depleted.

Figure IV.2 shows the evolution of the DCP with the magnetic field for different experimental conditions. In figure IV.2.a, we see that at 30 T the emission is predominantly σ^- polarized, leading to a negative DCP. The absolute value of the DCP at 30 T goes from ~ 40 % at 660 nm to ~ 10 % in the low energy tail. Here we limit our study to the range 660-670 nm, where the DCP has a flat response and which is the closest to the excitation.

Let us first consider figure IV.2.c where the DCP under non-resonant excitation is presented. Its evolution is similar to what has been observed in other colloidal crystals [81, 112]. It steadily increases until 10 T, then it has a plateau at $\sim$ - 40 %. This saturating value is quite low compared to the theoretical value of 75 % which should be reached in the case of randomly

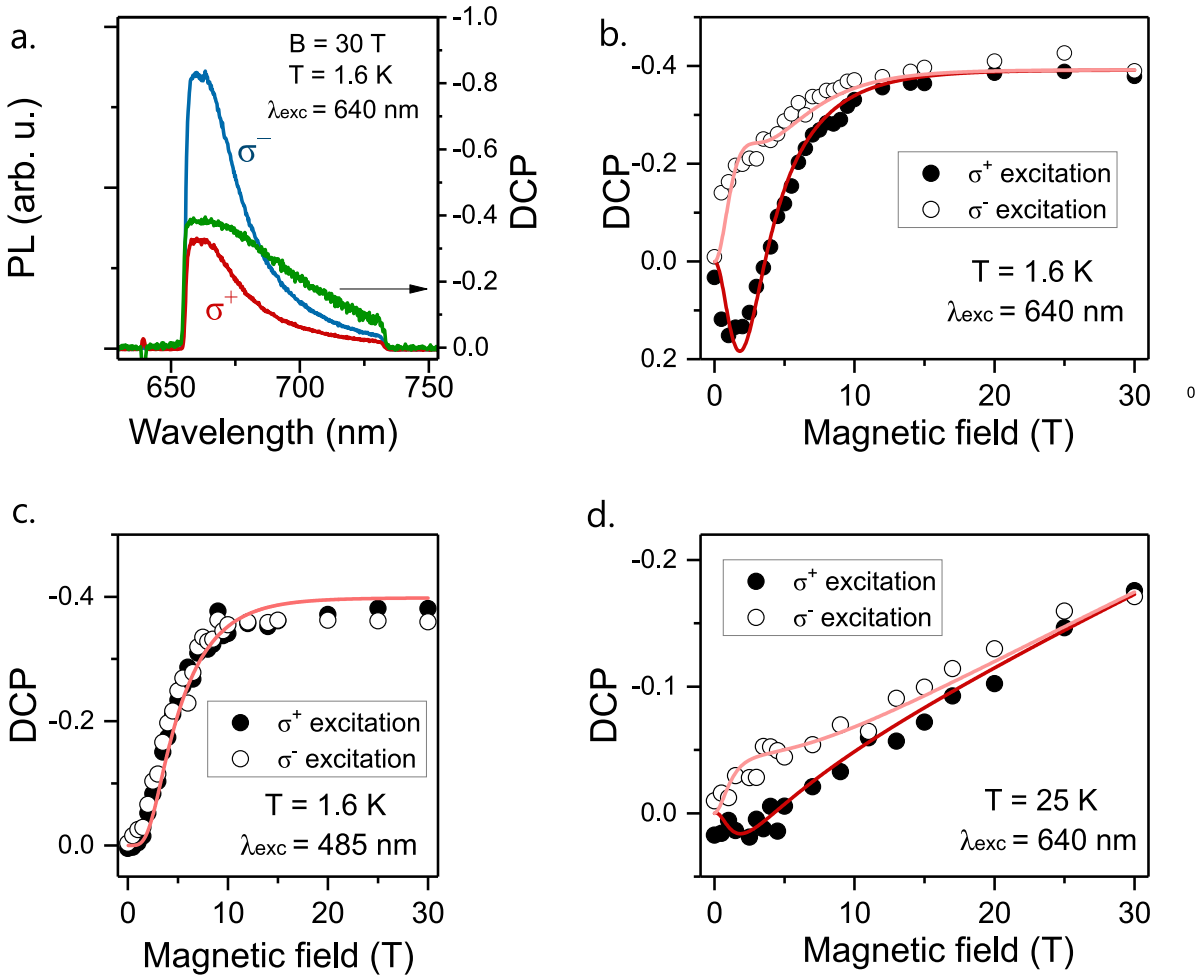

Fig. IV.2 *Degree of circular polarization. (a) PL of the film of NPLs at 30 T and 1.6 K under resonant excitation for σ^+ (red) and σ^- (blue) circularly polarized light and the resulting DCP (green). Evolution of the DCP with the magnetic field at 1.6 K for (b) quasi-resonant excitation and (c) non-resonant excitation. (d) Evolution of the DCP with the magnetic field at 25 K for quasi-resonant excitation. The red curves corresponding to the fits from equations IV.18 and IV.20*

orientated spherical nanocrystals [113]. We will see in the next part that this low saturating value can be explained by the different possible orientations of the NPLs with respect to the magnetic field.

Figure IV.2.b and d shows the DCP obtained under quasi-resonant excitation. We observe a striking non-monotonic behavior of the DCP under σ^+ excitation. In the case T = 1.6 K, the DCP first increases to 15 % at low field before decreasing to a plateau at $\sim$ - 40 %, joining the value of the DCP obtained under σ^- excitation. The fact that the DCP is different for the two circular excitation polarizations shows that with the quasi-resonant excitation, the selection of the levels by polarized light is partly efficient. Moreover, it also indicates that at least two electronic states contribute to the emission.

It is also important to highlight that the DCP at 0 T under quasi-resonant excitation is equal to zero. In the case of states which are initially circularly polarized, we would expect a non-zero value for the DCP at 0 T. Indeed, in the conditions of quasi-resonant excitation, the state with the angular momentum corresponding to the polarization of the light will be preferentially addressed leading to a polarized emission. Since it is not the case here, it indicates that the simple model of degenerate circular states at zero field is not applicable. This experimental result shows that the hypothesis, postulated in Chapter I.3, of an EFS made of two linearly non-degenerate emissive states has to be favored. In the next part, we will see how states of the EFS will acquire a circular symmetry as the B-field increases, leading to the observed DCP values.

At T = 25 K, the same non-monotonic behavior is observed. However, the DCP does not reach its saturating value even at high field and the magnitude of the positive dip at low field is less significant. This observation can be easily rationalized: for a given B-field, the DCP will always be lower for the higher temperature, due to the thermal occupation of the upper states oppositely polarized.

We will see in the second part of this chapter how these results can be modeled and more precisely how the interplay between the spin relaxation lifetime τ_s between the two bright levels at play here and the exciton recombination lifetime τ_r explains the non-monotonic evolution of the DCP. Before going to these considerations, we will first present how both parameters can be reached and how they evolve with the magnetic field.

c) The exciton relaxation lifetime τ_r

The TRPL is recorded at every field for both σ^+ and σ^- polarized excitation and the detection is also polarization dependent. So, for each field, a total of four different decays are recorded corresponding to the four different configurations of excitation/detection (σ^+/σ^+, σ^+/σ^-, σ^-/σ^+, σ^-/σ^-).

The measurements of the relaxation lifetime of the exciton has to be done independently of the polarization of the emission. Indeed, we want to measure the relaxation dynamics of the IX on average, without considering the EFS level from which it is emitted. To do so, for both types of excitation, we consider the total dynamics $I_{tot}(t)$ defined by:

$$I_{tot}(t) = I_{\sigma+}(t) + I_{\sigma-}(t), \tag{IV.2}$$

where $I_{\sigma+/\sigma-}(t)$ is the dynamics obtained for a σ^+/σ^- emission polarized. In this way, we artificially recreate the decay we would have obtained if the emission were not resolved in polarization.

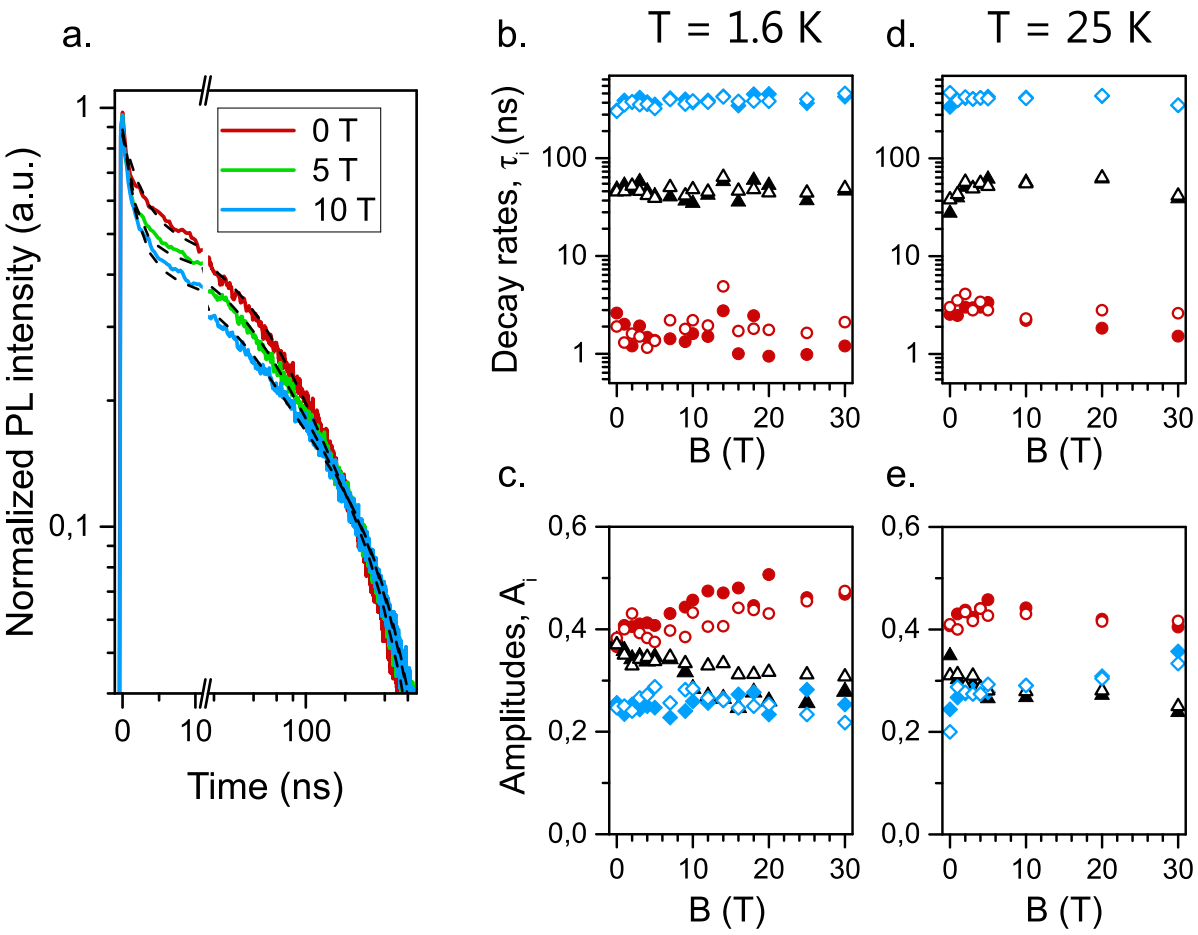

Fig. IV.3 *(a) Relaxation dynamics of the IX for different values of the B-field and in black their fits with exponential decays with three different components. Evolution of the characteristic times (b) and their relative amplitudes (c) of the decays for σ^+ (filled symbols) and σ^- (open symbols) excitation at T = 1.6 K. (d) and (e) are the same as (b) and (c) at T = 25 K.*

Figure IV.3.a shows the decays obtained with formula IV.2 for different magnetic fields at T = 1.6 K. The curves are well adjusted by a multi-exponential decay function with three components. The decay times and their relative amplitudes can be found in figures IV.3.b and c, for both σ^+ (filled symbols) and σ^- (open symbols) excitations at T = 1.6 K, and in figures IV.3.d and IV.3.e at T = 25 K. As already discussed in Chapter III, these types of multi-exponential decays are characteristic of complex relaxation mechanisms. However what we would like to stress here are the little changes in the decays with the magnetic field compared to what is observed in other colloidal crystals [110,114]. The decays usually shorten with the increase of the magnetic field, due to the mixing of the bright and dark states of the EFS and the more efficient recombination from these dark states. This is partly the case here, the magnitude of the fastest component (red dots) gaining amplitude with the B-field, but this effect is really marginal. Moreover, if we compare the data obtained at the different temperatures, we also notice the absence of change between the two, while a back-transfer from the dark states to the bright ones should accelerate the decays at higher temperature [93].

The lack of evolution of the exciton lifetime with the B-field and the temperature indicates

a weak influence of the dark states in these NPLs emission. This will be further discussed in the last section of the chapter.

d) The spin relaxation lifetime τ_s

The other physical quantity which can be deduced from the TRPL measurements is the spin relaxation lifetime of the exciton τ_s. In the case of two circular states, this is the characteristic time it takes for the exciton to flip its spin from $M_s = +1$ to $M_s = -1$. It can also be seen as the thermal relaxation lifetime, since it is the characteristic time required for an exciton to relax from the higher level to the lower level.

The spin relaxation lifetime is deduced from the evolution of the DCP in time, the DCP(t) being easily computed from the TRPL data as:

$$DCP(t) = \frac{I_{\sigma+}(t) - I_{\sigma-}(t)}{I_{\sigma+}(t) + I_{\sigma-}(t)}. \tag{IV.3}$$

Figure IV.4 shows the DCP(t) for different values of the field when the excitation is σ^+ polarized at T = 1.6 K. Despite the non-exponential nature of the TRPL, the DCP(t) traces are strikingly well adjusted by a mono-exponential decay. The spin relaxation lifetime τ_s is then equal to the characteristic time of the decay as is shown in Appendix B. The mono-exponential decay of the DCP is the sign that a single process dominates the spin relaxation mechanism as we shall see in the third part of this chapter. We believe that the dominant process here is the simultaneous flip of both the spins of the electron and the hole, leading to the 'direct' flip of the exciton.

On the right side of figure IV.4, the evolution of τ_s is reported for T = 1.6 K (open symbols) and T = 25 K (filled symbols). At T = 1.6 K, $\tau_s(B)$ is proportional to $B^{-3.2}$ (red curve). As for T = 25 K, we see that τ_s has first a plateau at low field before showing the same evolution as at T = 1.6 K at higher field. This evolution can be well adjusted by the formula $1/\tau_s = \Gamma_S = \Gamma_{S,0} + aB^{-\alpha}$ (blue curve) with $\alpha = -3$ and $1/\Gamma_{S,0} \approx 17$ ns. The time-range of our set-up did not allow us to measure τ_s for $B \leq 3$ T at T = 1.6 K. By analogy with the curve found for $\tau_s(B)$ at 25 K, we can expect a plateau of τ_s at lower field, setting the value of $\tau_s(3T) \sim 600$ ns as a lower limit for the spin relaxation lifetime at low magnetic field. Since the beginning of this plateau is not yet visible, we can even expect a value of τ_s in the µs range at 1.6 K. Such a value is comparable to the spin relaxation rate measured in type-II epitaxially grown QWs, where the exciton is indirect spatially as well as in the k-space [23] and is much higher than the one measured in type-I core/shell CdSe/CdS NPLs, where it is found in the ns range [81].

To the best of our knowledge, the spin relaxation mechanism has not been studied in type-II colloidal systems. Nevertheless, a similar B^{-3} dependence was found throughout calculations in the paper of Tsitsishvili *et al.* [115]. In this paper the spin relaxation dynamics of direct exciton in asymmetrical epitaxially grown quantum dots is considered. In their model, the electron and the hole spin flip goes along the emission of an acoustic phonon. This transition is allowed through the valence band mixing of the heavy and light holes, this mixing itself arising from the interplay of the short range exchange interaction and phonon-induced deformation of the lattice. We note that such calculations can not be readily applied in our case, since the authors consider bulk phonons exclusively, modeled by plane waves that are suited to the description of self-assembled embedded quantum dots. The approach should be revisited in self-standing hetero-structures with nanometric sizes, in particular by taking into account the confined nature of the phonons. This is a demanding task which moreover requires taking

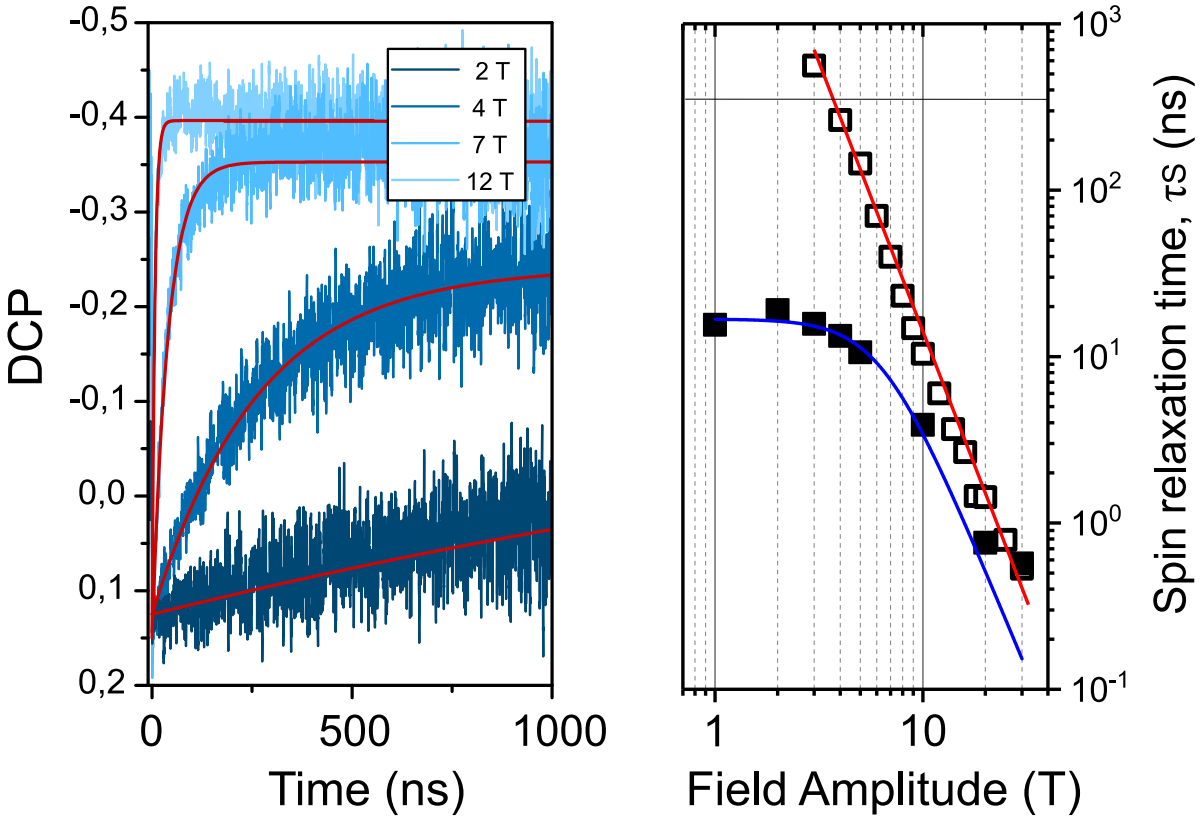

Fig. IV.4 *On the left side: DCP(t) for different value of the B-field and their mono-exponential fit (red). On the right side: evolution of τ_s the spin relaxation lifetime for $T = 1.6$ K (open squares) and $T = 25$ K (filled squares). The red and blue lines are the adjustment of these curves with $aB^{-3.2}$ and $1/(\Gamma_{S,0} + kB^{-3})$ with $1/\Gamma_{S,0}$ =17 ns, respectively. The grey horizontal line corresponds to the relaxation lifetime, $\tau_r = 350$ ns, at 1.6 K, obtained from the average of the different multi-exponential components (see IV.1.2.b).*

into account the composite nature of the NPLs, in the framework of a type-II band alignment. These theoretical investigations are beyond the scope of this work but we provide here experimental material which should make possible the tackling of the issue of the evolution of τ_s with the magnetic field in a prototypical hetero-structure.

The plateau of $\tau_s(B)$ observed for T = 25 K indicates that at least one other process is also at play at low magnetic field. The absence of dependence on the magnetic field could be the signature of multi-phonon processes. Indeed, with such a process the phonon energies do not need to match the Zeeman splitting and the field dependence relies purely on the spin-phonon coupling mechanisms itself, not on the phonon density. A similar saturation of τ_s at low field has already been reported [116]. However, the results found in ref. [116] can not be readily transposed since the authors only consider the spin-flip of the holes while here we believe that the exciton spin-flip is the leading mechanism.

Let us see now how the experimental results can be explained and how an adjustment of the DCP curves can lead to the determination of some of the EFS parameters, despite the large inhomogeneous broadening that characterizes the PL emission.

IV.1.2 Modelling of the magneto-optical response

We saw in Chapter I.3 that, as a result of the exchange interaction in objects with a symmetry lower than D_{2d}, the two bright states of the EFS will hybridize leading to the formation of two linearly polarized states $|X\rangle$ and $|Y\rangle$. At B = 0 T, the absence of DCP at zero-magnetic field under quasi-resonant excitation seems to support this hypothesis. Here, the evolution with the magnetic field of the original EFS will be given. Then, we will see how the DCP can be computed from the model. Finally, the adjustments of the different DCP curves will be discussed as well as the parameters found from them.

a) Theory

In the following calculations, we will consider an EFS composed of two orthogonal and linearly polarized states lying in the plane of the NPL and split by an energy δ_1 (EFS at zero field). The associated dipoles are assumed to be aligned with the X and Y dimensions of the NPL (see figure IV.5).

In this picture the two dark states (linear combination of the $|+2\rangle$ and $|-2\rangle$ states) will also experience the effects of the magnetic field. They will further split and under certain conditions of orientation of the NPL with the B-field, they will mix with the bright states. In the following calculations, the approximation of not considering the dark states is made. In the last section of this chapter, we will discuss this approximation and will provide evidence that the coupling between the bright and dark states is negligible.

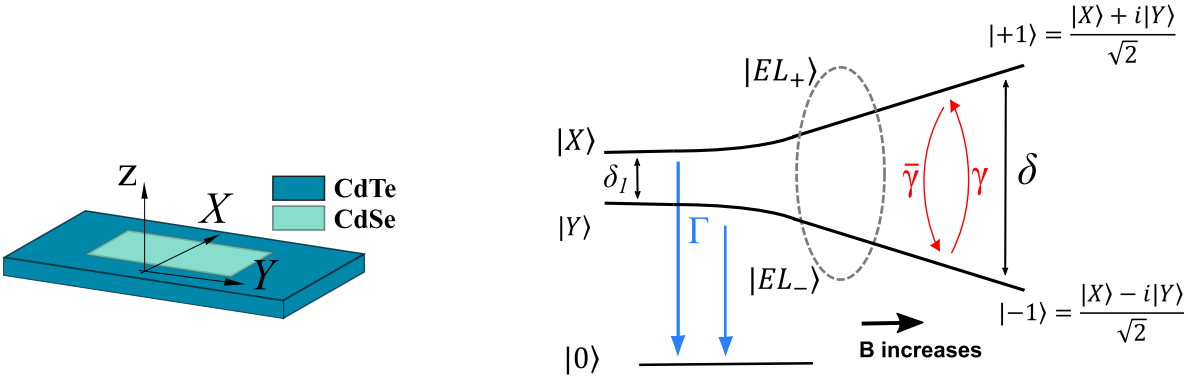

Fig. IV.5 *Sketch of the EFS and how it evolves with the B-field in the case of 'flat' lying NPLs.*

The NPLs studied here were dispersed in polystyrene, hence we expect them to be randomly oriented compared to the B-field direction. It is extremely important to consider this orientation when calculating the effect of the B-field on the EFS as we will see. However, it is not trivial to take into account the infinite possibilities of orientations. Thus, in order to render calculations feasible, we consider an effective medium made of only two populations. First, the population of the NPLs lying 'flat' is denoted by n_{hor}, this population corresponding to NPLs which have their plane perpendicular to the B-field. Then, the population of NPLs lying on

their 'edge', which experiences an in-plane B-field, is denoted by n_{ver}, with $n_{ver} = 1 - n_{hor}$. Let us see now how we can model the emission of both populations, in order to compute an expression for the DCP.

'Flat' lying NPLs population

The case of 'flat' lying NPLs experiencing a magnetic field perpendicular to their planes corresponds to the so-called Faraday configuration. In this configuration, there is no mixing between the bright and dark states [78]. Thus, here, the approximation of not considering the dark states consists of neglecting the relaxation from the bright exciton levels towards the dark ones. The Hamiltonian describing the system is then the following [111]:

$$H = \left(\hbar\omega_0 - \frac{\delta_1}{2}\right)|X\rangle\langle X| + \left(\hbar\omega_0 + \frac{\delta_1}{2}\right)|Y\rangle\langle Y| + \left(\frac{g_{ex}\mu_B B}{2}\right)(|+1\rangle\langle+1| - |-1\rangle\langle-1|), \quad \text{(IV.4)}$$

where $\hbar\omega_0$ is the energy of the IX transition, δ_1 the splitting between the $|X\rangle$ and $|Y\rangle$ states, g_{ex} is the exciton g-factor along the z-axis and $|\pm1\rangle = (|X\rangle \pm i\,|Y\rangle)/\sqrt{2}$ are the Zinc Blende exciton states of momentum $M_S = \pm1$.

The two eigen-states of this Hamiltonian denoted $|EL+\rangle$ and $|EL-\rangle$ can be expressed as:

$$\begin{cases} |EL+\rangle = \sin\alpha\,|X\rangle + i\cos\alpha\,|Y\rangle \\ |EL-\rangle = \cos\alpha\,|X\rangle - i\sin\alpha\,|Y\rangle \end{cases} \quad \text{(IV.5)}$$

with:

$$\alpha = \frac{1}{2}arctan(\frac{g_{ex}\mu_B B}{\delta_1}), \quad \text{(IV.6)}$$

and their respective eigen-energies as:

$$E_\pm = \hbar\omega_0 \pm \frac{1}{2}\sqrt{\delta_1^2 + (g_{ex}\mu_B B)^2}. \quad \text{(IV.7)}$$

The two states $|EL+\rangle$ and $|EL-\rangle$ acquire an elliptical structure as B increases, before becoming purely circular states at high field when $g_{ex}\mu_B B \gg \delta_1$. Concerning the energies of these states, the magnetic field will lead to a further splitting leading to a total energy separation $\delta = \sqrt{\delta_1^2 + (g_{ex}\mu_B B)^2}$ (see figure IV.5).

If we address now the different relaxation pathways in this EFS, we can model them using three parameters. First there is the exciton recombination rate, $\Gamma = 1/\tau_r$, which is assumed to be the same for both states. To a good approximation, it does not depend on the B-field as shown experimentally by figure IV.3. Then there are the spin relaxation rates γ and $\bar{\gamma}$ that connect the $EL+$ and EL- branches (see figure IV.5). The thermalization of the reservoir (NPL crystal) imposes that $\bar{\gamma} = \gamma\exp\left(-\frac{\delta}{k_b T}\right)$. It is shown in Appendix B that the spin relaxation lifetime is equal to $\tau_s = \frac{2}{\gamma+\bar{\gamma}}$. Let us notice that in this model, the spin relaxation ensures the thermalisation within the EFS.

The intensity of the σ^+ (σ^-) circularly polarized emitted light $I_\sigma+$ ($I_\sigma-$), needed to find an expression of the DCP, can be readily expressed as:

$$I_{\sigma\pm} \propto |\langle\pm1|EL+\rangle|^2 N_+ + |\langle\pm1|EL-\rangle|^2 N_-, \quad \text{(IV.8)}$$

where N_+ (N_-) is the population of the state $|EL+\rangle$ ($|EL-\rangle$).

The measurements of the DCP as a function of the field were done under continuous wave (c.w.) excitation. The equations providing the time evolution of N_+ and N_- populations are:

$$\begin{cases} \frac{dN_+}{dt} = -(\Gamma + \frac{\gamma}{2})N_+ + \frac{\bar{\gamma}}{2}N_- + G_+ \\ \frac{dN_-}{dt} = -(\Gamma + \frac{\bar{\gamma}}{2})N_- + \frac{\gamma}{2}N_+ + G_- \end{cases} \tag{IV.9}$$

where G_+ and G_- are the injection rates in the two states.

In the case of a σ^+ excitation one can express them as:

$$G_\pm = |\langle +1|EL\pm\rangle|^2 G_0, , \tag{IV.10}$$

and for a σ^- circularly polarized field one has:

$$G_\pm = |\langle -1|EL\pm\rangle|^2 G_0, , \tag{IV.11}$$

where G_0 is a constant for a c.w. excitation.
In the stationary regime, one obtains:

$$\begin{cases} N_+ = \frac{(\Gamma + \frac{\bar{\gamma}}{2})G_+ + \frac{\bar{\gamma}}{2}G_-}{\Gamma(\Gamma + \frac{\gamma+\bar{\gamma}}{2})} \\ N_- = \frac{(\Gamma + \frac{\gamma}{2})G_- + \frac{\gamma}{2}G_+}{\Gamma(\Gamma + \frac{\gamma+\bar{\gamma}}{2})} \end{cases} \tag{IV.12}$$

From equations IV.8 and IV.12 the DCP can be easily computed for the 'flat' lying population.

'Edge' lying NPLs population

The issue of knowing how 'Edge' lying NPLs contribute is more complicated to grasp. Indeed, the orientation of the magnetic field perpendicular to the NPL high confinement direction, *i.e.* in the (X, Y) plane, changes the matrix representation of the Zeeman interaction [78]. In contrast to the Faraday configuration, the matrix, expressed in the ($|+1\rangle$; $|-1\rangle$; $|+2\rangle$; $|-2\rangle$) exciton states basis, now has off-diagonal elements. The breaking of the in-plane rotational symmetry due to the magnetic field leads to the mixing of the bright ($|\pm 1\rangle$) and dark ($|\pm 2\rangle$) excitons. Following ref. [78], it is easy to show that in the same manner a mixing occurs between the bright 'hybridized' $|X\rangle$, $|Y\rangle$ states and their dark analogous $|X'\rangle$, $|Y'\rangle$ states, expressed as the following:

$$\begin{cases} |X\rangle = (|+1\rangle + |-1\rangle)/\sqrt{2} \\ |Y\rangle = (|+1\rangle - |-1\rangle)/\sqrt{2} \\ |X'\rangle = (|+2\rangle + |-2\rangle)/\sqrt{2} \\ |Y'\rangle = (|+2\rangle - |-2\rangle)/\sqrt{2} \end{cases} \tag{IV.13}$$

This mixing of bright and dark states due to the Voigt configuration is completely neglected here. Thus, in our approximation without the dark states, the $|X\rangle$ and $|Y\rangle$ states are completely decoupled from the field. They remain unchanged in their structures and do not further split with the magnetic field. Hence, we consider the spin relaxation rates constant and equal to the values extrapolated at zero field, γ_0 and $\bar{\gamma_0}$.

The populations of the states $|X\rangle$ and $|Y\rangle$ are then written following equations IV.9 to IV.12:

$$\begin{cases} N_Y = \frac{(\Gamma+\frac{\bar{\gamma_0}}{2})G_Y+\frac{\bar{\gamma_0}}{2}G_X}{\Gamma(\Gamma+\frac{\gamma_0+\bar{\gamma_0}}{2})} \\ \\ N_X = \frac{(\Gamma+\frac{\gamma_0}{2})G_X+\frac{\gamma_0}{2}G_Y}{\Gamma(\Gamma+\frac{\gamma_0+\bar{\gamma_0}}{2})} \end{cases} \tag{IV.14}$$

where γ_0 and $\bar{\gamma_0}$ are the values of γ and $\bar{\gamma}$ at zero-field and G_X (G_Y) the injection rate in the $|X\rangle$ state ($|Y\rangle$ state).

For 'edge' lying NPLs, the contribution of circularly polarized light has to be computed with care. Indeed the state whose dipole is parallel to the magnetic field is also parallel to the incoming light and cannot be excited. Moreover, the propagation direction of its emitted light is perpendicular to the detection direction, so the light emitted from this state does not contribute.

When the magnetic field is along the Y direction, only the light from the $|X\rangle$ state is detected, so one has:

$$I^X_{\sigma\pm} = |\langle\pm1|X\rangle|^2 N_X \text{ and } G_Y = 0,\ G_X = \frac{1}{2}G_0. \tag{IV.15}$$

In the same way, when the field is applied parallel to the X direction, one obtains light from the $|Y\rangle$ state:

$$I^Y_{\sigma\pm} = |\langle\pm1|Y\rangle|^2 N_Y \text{ and } G_Y = \frac{1}{2}G_0,\ G_X = 0. \tag{IV.16}$$

In this model, these 'edge' lying NPLs emit a linear polarized light along their axes perpendicular to the B-field, regardless of the value of this B-field. Their PL will act as a parasitic non-circularly polarized emission, lowering the overall value of the DCP, explaining why the latter quantity saturates around - 40 %.

'Total' DCP

The DCP that will be representative of the whole medium can now be expressed as:

$$DCP(B) = \frac{n_{hor}(I^{hor}_{\sigma+} - I^{hor}_{\sigma-})}{n_{hor}(I^{hor}_{\sigma+} + I^{hor}_{\sigma-}) + \frac{n_{ver}}{2}(I^X_{\sigma+} + I^X_{\sigma-} + I^Y_{\sigma+} + I^Y_{\sigma-})}, \tag{IV.17}$$

since $I^{X/Y}_{\sigma+} = I^{X/Y}_{\sigma-}$ and where the assumption of equal fraction for 'edge' lying NPLs lying on X and Y edges was made (n_X=n_Y=$\frac{n_{ver}}{2}$).

Replacing the different intensities, one ends up with the following formula for the DCP as a function of the magnetic field for resonant σ^+/σ^- excitation:

$$DCP(B)_{\sigma\pm} = \sin(2\alpha)\left[\frac{\tanh\left(\frac{\delta}{2k_BT}\right)}{(\frac{2\Gamma}{\gamma+\bar{\gamma}}+1)(1+\frac{n_{ver}}{4n_{hor}}\frac{2+\frac{\gamma_0+\bar{\gamma_0}}{2\Gamma}}{1+\frac{\gamma_0+\bar{\gamma_0}}{2\Gamma}})} \mp \frac{\sin(2\alpha)}{(1+\frac{\gamma+\bar{\gamma}}{2\Gamma})(1+\frac{n_{ver}}{4n_{hor}}\frac{2+\frac{\gamma_0+\bar{\gamma_0}}{2\Gamma}}{1+\frac{\gamma_0+\bar{\gamma_0}}{2\Gamma}})}\right], \tag{IV.18}$$

where

$$\sin(2\alpha) = \frac{g_{ex}\mu_B B}{\sqrt{(g_{ex}\mu_B B)^2 + \delta_1^2}}. \tag{IV.19}$$

In the case of a non-resonant excitation, the only parameters which will differ are the injection rates G_+ and G_-. In this case, we can consider that the two states are equally populated by cascade relaxation from higher states so $G_+ = G_- = \frac{G_0}{2}$. Then the DCP no more depends on the polarization of the excitation and is equal to:

$$DCP(B) = \frac{\sin(2\alpha)\tanh\left(\frac{\delta}{2k_BT}\right)}{(\frac{2\Gamma}{\gamma+\bar{\gamma}}+1)(\frac{n_{ver}}{2n_{hor}}+1)}. \tag{IV.20}$$

Equations IV.18 and IV.20 can be thus used to adjust the data presented in figure IV.2. From these fits, the different parameters of the model can be deduced.

b) Fit of the experimental results

The first adjustment performed is the one of the DCP at T = 1.6 K under quasi-resonant excitation (figure IV.2.b). Equation IV.18 is used to fit simultaneously the data obtained under σ^+ and σ^- excitation. Four parameters are left free during the fit: the fraction of 'flat' lying NPLs n_{hor}, the splitting between the two levels of the EFS, δ_1, the exciton g-factor g_{ex} and the exciton relaxation rate Γ. The value $\frac{2}{\gamma+\bar{\gamma}}$ is set to the expression found in the adjustment of $\tau_s(B)$ in part IV.1.1.

We see in figure IV.2 that the fitting of the experimental data with this model is satisfactory. It is obtained with the value $n_{hor} = 0.24$, $\delta_1 = 60$ µeV, $g_{ex} = 0.7$ and $1/\Gamma = 620$ ns. This set of parameters is then injected into equation IV.20 to obtain the adjustment of the non-resonant DCP (figure IV.2.c). We see that the experimental data is once again well reproduced by the model.

To adjust the DCP curves at T = 25 K, we used the values found for δ_1 and g_{ex} by the fit performed at T = 1.6 K, since these parameters are not dependent on temperature. However, Γ is left free since the exciton relaxation rate can change with temperature. n_{hor} is also left free, the measurements of the DCP at 1.6 K and 25 K were done at different locations in the sample. The adjustment shown in figure IV.2.d is thus obtained with $1/\Gamma = 250$ ns and $n_{hor} = 0.31$.

The values found for n_{hor} show that the majority of the NPLs are lying on their edges. These values are coherent with TEM images of the NPLs in the polystyrene film, collected by our collaborators in Cambridge. With a technique of ultramicrotomy, it was possible to obtain thin slices ($\sim$ 150 nm) of the polystyrene film, which was studied with an electronic microscope. Some of the pictures obtained are shown in figure IV.6. They corroborate the idea that the majority of NPLs are lying on their edges.

The Landé g-factor for the IX along the z-direction g_{ex} is comparable to what has already been measured in other II-VI NPLs [81]. Unfortunately, here we are not able to distinguish between the contribution of the electron and the hole, in this g-factor. However, if we compare to what has been measured in CdSe/CdS core/shell NPLs, we can assume that the electron has a positive g-factor while the hole has a negative one. For this reason, g_{ex}, being equal to the sum of the two, has a relatively small amplitude, explaining why high magnetic field are required to study such materials.

Concerning the value obtained from the fit, $1/\Gamma$ can be compared to the measured average relaxation time $\overline{\tau_r}$. The average value of the exciton recombination time is obtained by

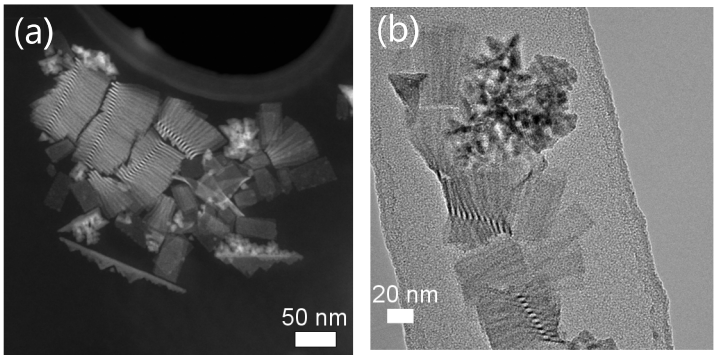

Fig. IV.6 *Characteristic TEM pictures of thin slices of the polystyrene film obtained by ultramicrotomy. Most of the NPLs are lying on their edge, which is consistent with the value of n_{hor} found when adjusting the DCP.*

$\overline{\tau_r} = \sum \frac{N_i \tau_i}{N_i}$ where $N_i = A_i \tau_i$ is the number of emitted photons through the channel i and τ_i and A_i are the respective relaxation lifetimes and amplitudes of the channel i. With such a formula, we found a value of $\overline{\tau_r} \approx 350$ ns at T = 1.6 K. This value is comparable to the 650 ns found from the fit. However, the fit provides $\overline{\tau_r} = 1/\Gamma = 250$ ns at T = 25 K which seems to indicate an acceleration of the recombination of the exciton. This is not verified experimentally (see figure IV.3).

Finally, we would like to discuss the value obtained for the splitting of the two bright states δ_1. This parameter is expected to be lower in the indirect exciton compared to the direct one due to the reduced exchange interaction in this structure, explained by the spatial separation of the wave functions of the two carriers. However, the value of 60 µeV is relatively high for an indirect exciton. It is of the same order of magnitude to what is found in Ga(In)As type-I quantum dots ($\sim$ 100 µeV). Nevertheless, it is an order of magnitude lower than what is found in II-VI CdSe colloidal nanocrystals where the bright states splitting is in the meV range [117]. In our opinion, the strong dielectric confinement present in these NPLs can be held responsible for the relatively high value of δ_1. As already discussed (Chapters I and III), the dielectric mismatch will enhance all the Coulombic interaction terms including the exchange interaction responsible for the splitting.

c) Interplay between the exciton recombination lifetime τ_r and the spin relaxation lifetime τ_s

Beyond the different values found from the fit, it is interesting to understand which parameters drive the shape of the DCP under quasi-resonant excitation. By looking carefully at equation IV.18, we notice that the ratio $\frac{2\Gamma}{\gamma+\bar{\gamma}} = \frac{\tau_s}{\tau_r}$ plays an essential role, as illustrated in figure IV.7 where the DCP curves obtained from equation IV.18 are shown for different values of Γ while all the other parameters are set to the values found by the fit. As the ratio increases (*i.e.* Γ increases), the positive dip the DCP under σ^+ excitation gains in amplitude.

This interplay between τ_s and τ_r can be rationalized as follows. First let us recall that for B $\neq$ 0, a σ^+ excitation will preferably lead to the formation of an exciton in the $|EL+\rangle$ state, this selection being more and more efficient as the field grows.

In the case of a low magnetic field, we have $\tau_s > \tau_r$. Hence, the exciton in the $|EL+\rangle$ state will be more likely to recombine, emitting a photon, than to relax to the lower level $|EL-\rangle$. The photon emitted from the $|EL+\rangle$ state will have an elliptical polarization with a higher σ^+

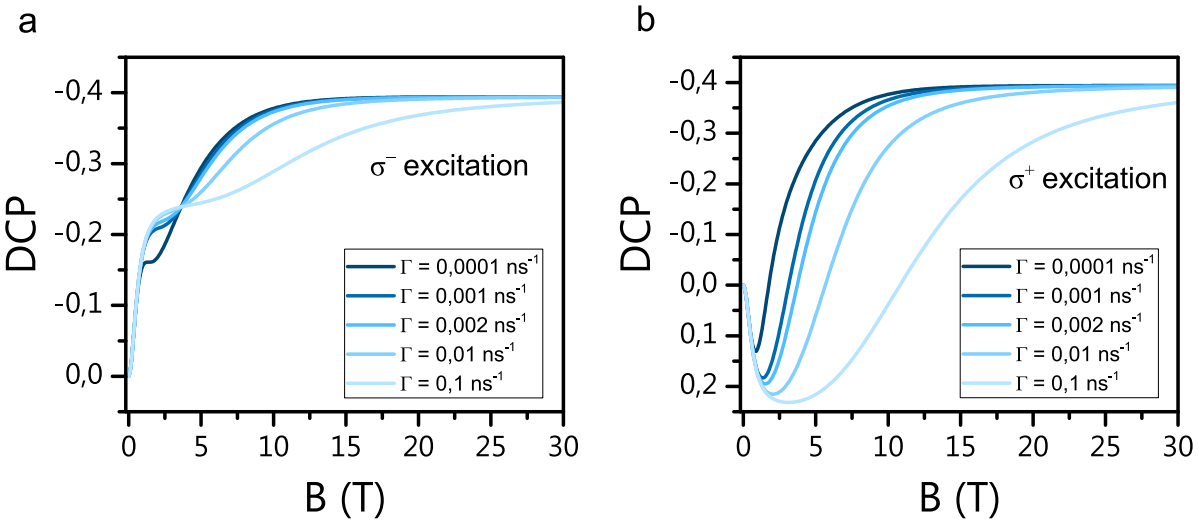

Fig. IV.7 *DCP traces obtained from equation IV.18 for different values of Γ and all the other parameters set to those find from the fit of the DCP at 1.6 K under resonant excitation. DCP obtained under σ^-/σ^+ excitation (a)/(b).*

component than a σ^-, leading to an overall positive DCP. In the other limiting case of a high magnetic field, we have $\tau_s \ll \tau_r$. The exciton created in the $|EL+\rangle$ state will quickly relax to the lower $|EL-\rangle$, before recombining emitting a σ^- polarized photon. The DCP is this time negative as we observed experimentally. It is also similar to the one observed with a σ^- excitation, since in both cases the emission comes from the lower $|EL-\rangle$ state. Another point reinforcing this interpretation is that the inversion of the DCP curve under σ^+ excitation and the crossing of $\tau_s(B)$ and τ_r at B $\approx$ 3 T are concomitant (see horizontal grey line in figure IV.4, right panel). The fact that the PL is never purely σ^- polarized is explained by the 'edge' lying population of NPLs, which will emit a linearly polarized light, contributing equally to both circular polarizations.

The DCP measured at T = 25 K can be understood following the same considerations. However, in this case we have to take into account the ratio between $\delta(B)$, the total splitting between the two states, and the energy k_BT. The occupation of both states depends on this ratio, the condition $\delta(B) \gg k_BT$ then needs to be fulfilled so that the majority of excitons relax on the lower state $|EL-\rangle$ and a strong negative DCP is obtained. At T = 25 K, $k_BT \approx 2$ meV while even at $B = 30$ T, $\delta = 1.2$ meV. This explains why the saturation of the DCP is not reached at this temperature. When the thermal occupation of the states compete with the splitting $\delta(B)$, it is also expected to have a smaller difference between the DCP curves associated with σ^+/σ^- excitation whatever the value of the B-field and this is indeed observed.

IV.2 Complementary experiments

The theoretically predicted EFS composed of two linear bright states $|X\rangle$ and $|Y\rangle$ matches the results obtained from the high magnetic field experiments. This model can also be tested through other experiments. The most obvious one is the measurement of the degree of linear polarization (DLP). Indeed, the states being linearly polarized it is possible to selectively excite one or the other with a linearly polarized resonant excitation. This will result in an overall

linearly polarized emission which can be characterized by its DLP. The results obtained from the DLP measurements will be presented in the first section, as well as their modelling using the same approach as the one used for the DCP.

Another more challenging experiment has also been performed: the generation of quantum beats between the $|X\rangle$ and $|Y\rangle$ states of the EFS. The frequency of the beatings being equal to the splitting between the two states, this measurement provides another access to δ_1 (found from the modelling of the DCP). This experiment was performed by our collaborators in Cambridge, where the ultrafast lasers facilities were available. We will present these results in a second section as well as the calculations necessary to interpret them.

IV.2.1 Degree of linear polarization

The DLP, like the DCP, is an observable which allows one to probe the polarization of the EFS. It is especially interesting in our case where the EFS is composed of two linearly polarized states. The DLP is expressed as followed:

$$DLP = \frac{I_{\parallel} - I_{\perp}}{I_{\parallel} + I_{\perp}}, \tag{IV.21}$$

where $I_{\parallel}$ ($I_{\perp}$) is the intensity of the PL light polarized parallel (perpendicular) to the polarization of the excitation source.

The DLP was measured under two different experimental conditions. First, at the INSP we measured it without any magnetic field and for different incoming polarization of the quasi-resonant and non-resonant excitation. The evolution of the DLP with the B-field has also been recorded at the HFML under experimental conditions similar to the ones previously described for the DCP.

a) DLP at B = 0T

The measurements of the DLP at 0 T are done under quasi-resonant excitation ($\lambda_{exc} = 640$ nm) or under non-resonant excitation ($\lambda_{exc} = 485$ nm) and at a temperature of 7 K. The set-up composed of the motorized half-wave plate described in Chapter II.3.e, is used to obtain the polarization diagram shown in figure IV.8.a. In light blue, the diagrams obtained under quasi-resonant excitation are plotted for different incoming linear polarization directions forming an angle β with the horizontal. The resulting PL is always highly polarized in the direction of the excitation (characterized by the 'peanut' shaped diagrams whose main axis is aligned with the incoming polarization). This result is consistent with the picture of the EFS deduced from previous measurements and analysis. Indeed, the incoming light will selectively excite the state ($|X\rangle$ or $|Y\rangle$) aligned with the incoming polarization. Due to a long spin relaxation lifetime at B = 0 T, the exciton recombination will likely take place from this initial populated state, leading to a photon polarized in the same direction as the excitation. From these diagrams the DLP can be easily computed and values between 40 % and 70 % are found. These values are consistent with the ones predicted by the model developed below. Moreover, figure IV.8.a shows also in black a polarization diagram obtained with a non-resonant excitation. Such an excitation results in a non-polarized emission, showing once again that the initial spin configuration is lost during the relaxation of the high-lying excitonic states and populations cascade towards the lower levels. With the non-resonant excitation, the $|X\rangle$ and $|Y\rangle$ states become equally populated, regardless of the incoming polarization, leading to a non-polarized emission.

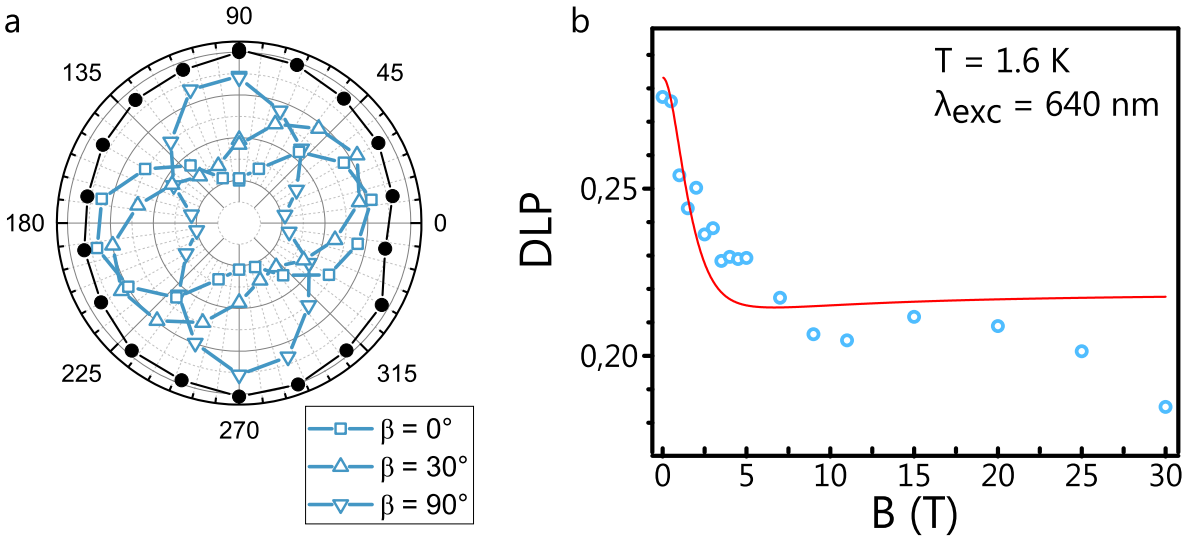

Fig. IV.8 *Degree of linear polarization. (a) Polarization diagrams of the PL under quasi-resonant excitation, λ_{exc} = 640 nm (open symbols), and non-resonant excitation, λ_{exc} = 485 nm (filled circles), at T = 7 K. The incoming light is linearly polarized along the direction forming an angle β with the horizontal. (b) Evolution of the DLP with the magnetic field under quasi-resonant excitation and at T = 1.6 K. The red curve is given by the adjustment of equation IV.30.*

b) DLP(B)

At the HFML, the DLP was also recorded as a function of B. The measurements of the DLP(B) have to be done with more caution than those of the DCP. Indeed, under the high magnetic field applied here, the microscope objective used to focus and collect the light will see a change in its birefringence due to the Faraday effect. This change in the optical indices of the objective will lead to a rotation of the polarization of the incoming excitation as well as the one of the PL. This effect can not be neglected at 30 T where the rotation of the polarization angle is around $\sim 10°$. Therefore, it is necessary to compensate for it with the half-wave plate to measure the correct $I_{\parallel}$ and $I_{\perp}$.

Figure IV.8.b shows the results obtained for DLP(B). As expected the DLP decreased with the application of the B-field, as the states become circularly polarized. However, it only reaches a value of 30 % at 0 T, lower than the 50 % expected. It also does not reach a zero value as would be expected for 'flat' lying NPLs with random orientation around their z-axis. Once again the contribution of the 'edge' lying NPLs explains the finite value of the DLP at high magnetic field as seen below.

c) Modelling of the degree of linear polarization

An analytical expression of the DLP is found using the same approach as the one presented in section IV.1.2. Two types of NPLs are considered ('flat-lying' or 'edge-lying' ones) and the approximation consisting of neglecting the dark states is made once again. When estimating the DLP, the NPL orientation plays a major role since the rotational invariance related to the σ^+/σ^- excitation is lost. In the following we derive expressions that incorporate orientational

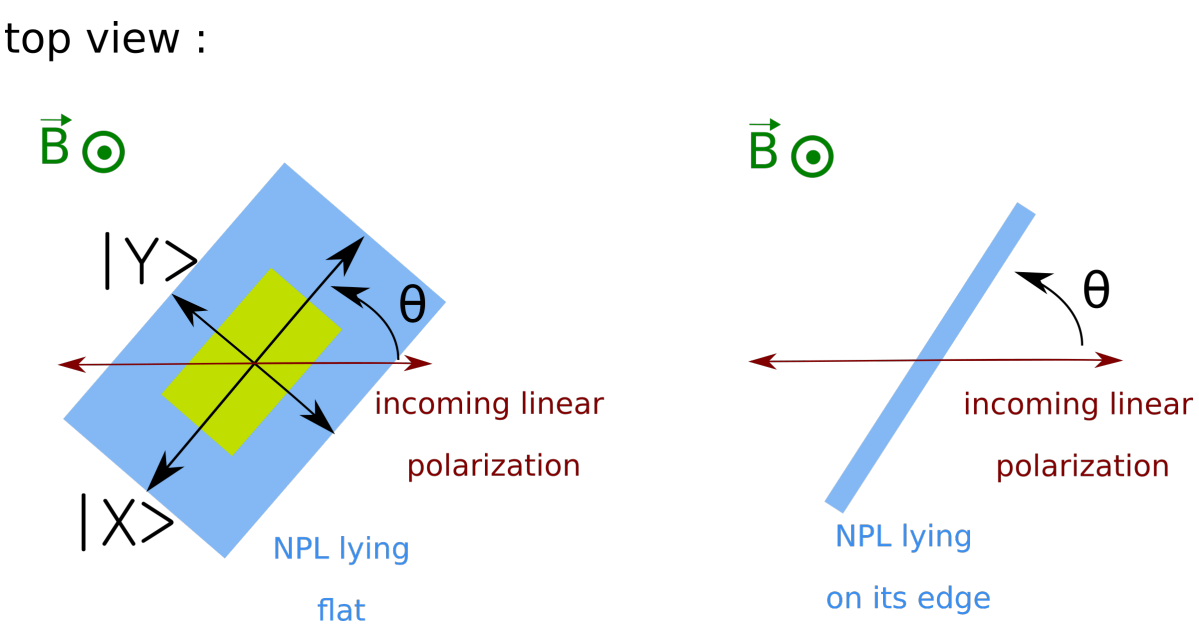

Fig. IV.9 *Sketch of the orientation of the NPLs compared to the incoming polarization.*

effects. In particular the DLPs are calculated for randomly organised NPLs but also for phases that possess a partial degree of order. To that end we define, θ, the angle between the incoming polarization and the NPL X axis (see Figure IV.9).

For the class of NPLs arranged flatwise, the intensities of the light emitted in the $\parallel$ and $\perp$ direction are equal to:

$$\begin{aligned} I_{\parallel}^{hor} =& \cos^2(\theta)(|\langle X|EL+\rangle|^2 N_+ + |\langle X|EL-\rangle|^2 N_-) \\ &+ \sin^2(\theta)(|\langle Y|EL+\rangle|^2 N_+ + |\langle Y|EL-\rangle|^2 N_-), \\ I_{\perp}^{hor} =& \sin^2(\theta)(|\langle X|EL+\rangle|^2 N_+ + |\langle X|EL-\rangle|^2 N_-) \\ &+ \cos^2(\theta)(|\langle Y|EL+\rangle|^2 N_+ + |\langle Y|EL-\rangle|^2 N_-). \end{aligned} \tag{IV.22}$$

And in this case the injection rates are given by:

$$\begin{aligned} G_+ =& (\cos^2(\theta)|\langle X|EL+\rangle|^2 + \sin^2(\theta)|\langle Y|EL+\rangle|^2) G_0, \\ G_- =& (\cos^2(\theta)|\langle X|EL-\rangle|^2 + \sin^2(\theta)|\langle Y|EL-\rangle|^2) G_0. \end{aligned} \tag{IV.23}$$

Now let us consider the fraction of NPLs lying on their edge. If the field, and consequently the direction of the propagation of the excitation, is collinear to Y, only the $|X\rangle$ state can be excited and only the light emitted by this state can be detected. Neglecting once again the bright and dark states mixing, we obtain:

$$I_{\parallel}^{X} = \cos^2(\theta) N_X \quad I_{\perp}^{X} = \sin^2(\theta) N_X \quad \text{and} \quad G_Y = 0 \quad G_X = \cos^2(\theta) G_0. \tag{IV.24}$$

In the same manner, if the magnetic field is collinear to X, only the $|Y\rangle$ state should be considered and we obtain:

$$I_{\parallel}^{Y} = \cos^2(\theta) N_Y \quad I_{\perp}^{Y} = \sin^2(\theta) N_Y \quad \text{and} \quad G_Y = \cos^2(\theta) G_0 \quad G_X = 0. \tag{IV.25}$$

The DLP as a function of the field then reads:

$$DLP(B) = \frac{\int_0^\pi f_{or}(\theta)(n_{hor}(I_\parallel^{hor} - I_\perp^{hor}) + \frac{n_{ver}}{2}(I_\parallel^X - I_\perp^X + I_\parallel^Y - I_\perp^Y))d\theta}{\int_0^\pi f_{or}(\theta)(n_{hor}(I_\parallel^{hor} + I_\perp^{hor}) + \frac{n_{ver}}{2}(I_\parallel^X + I_\perp^X + I_\parallel^Y + I_\perp^Y))d\theta}, \tag{IV.26}$$

where $f_{or}(\theta)$ is a function accounting for the spatial orientation of the NPLs.

In the case of a purely randomized organization, f_{or} is constant over [0,2π], $f_{or} = \frac{1}{2\pi}$, and the DLP reads:

$$DLP(B) = \frac{1}{2}\frac{\frac{\Gamma\cos^2(2\alpha)}{\Gamma + \frac{\gamma+\overline{\gamma}}{2}} + \frac{n_{ver}}{4n_{hor}}\frac{2\Gamma + \frac{\gamma_0+\overline{\gamma_0}}{2}}{\Gamma + \frac{\gamma_0+\overline{\gamma_0}}{2}}}{1 + \frac{n_{ver}}{4n_{hor}}\frac{2\Gamma + \frac{\gamma_0+\overline{\gamma_0}}{2}}{\Gamma + \frac{\gamma_0+\overline{\gamma_0}}{2}}}, \tag{IV.27}$$

where

$$\cos^2(2\alpha) = \frac{1}{1 + (g\mu_B B/\delta_1)^2}. \tag{IV.28}$$

In the limit $\Gamma \gg \frac{\gamma+\overline{\gamma}}{2}$(equivalent to $\tau_r \ll \tau_s$), verified at low-field and low temperature, the DLP is according to this formula equal to 50 % at B = 0 T. This prediction is consistent with the measurements of figure IV.8 where the DLP is found between 40 % and 70 %.

However, with the formula IV.27 the DLP(B) can not be well adjusted, since it is close to 30% at 0 T instead of 50%. Nevertheless, within the model and through the f_{or} function it is possible to check if a local order at some points inside the sample can help rationalize the DLP results. To do so, we consider a f_{or} peaked function that, in its simplest form, can be chosen as a normalized square function defined as:

$$\begin{cases} f_{or} = \frac{1}{2\kappa} & \text{for} \quad \beta_0 - \kappa < \theta < \beta_0 + \kappa, \\ f_{or} = 0 & \text{otherwise.} \end{cases} \tag{IV.29}$$

where β_0 is the direction along which the NPLs are partially aligned and κ the width of the distribution.

With this formula for f_{or}, the DLP can be expressed as:

$$\begin{aligned} DLP(B) =& \frac{n_{hor}}{\Gamma + \frac{\gamma+\overline{\gamma}}{2}} \frac{(\Gamma\cos^2(2\alpha)(\kappa + \frac{1}{4}\sin(4\kappa)\cos(4\beta_0)) + \frac{\gamma-\overline{\gamma}}{2}\cos(2\alpha)\sin(2\kappa)\cos(2\beta_0))}{2n_{hor}\kappa + \frac{n_{ver}}{4}\frac{(2\Gamma + \frac{\gamma_0+\overline{\gamma_0}}{2})}{\Gamma + \frac{\gamma_0+\overline{\gamma_0}}{2}}(2\kappa + \sin(2\kappa)\cos(2\beta_0))} \\ &+ \frac{n_{ver}}{4(\Gamma + \frac{\gamma_0+\overline{\gamma_0}}{2})} \frac{(2\Gamma + \frac{\gamma_0+\overline{\gamma_0}}{2})(\kappa + \frac{1}{4}\sin(4\kappa)\cos(4\beta_0) + \sin(2\kappa)\cos(2\beta_0))}{2n_{hor}\kappa + \frac{n_{ver}}{4}\frac{(2\Gamma + \frac{\gamma_0+\overline{\gamma_0}}{2})}{\Gamma + \frac{\gamma_0+\overline{\gamma_0}}{2}}(2\kappa + \sin(2\kappa)\cos(2\beta_0))}. \end{aligned} \tag{IV.30}$$

This equation was used to fit the data of figure IV.8.b with the parameters $g_{ex} = 0.72$, $\delta_1 = 61$ µeV, $1/\Gamma = 620$ ns fixed to the values given by the fit of the DCP data, and with the fitting parameters $n_{hor} = 0.07$, $\beta_0 = 90°$ and $\kappa = 74°$. The fit is not perfect but the overall evolution is well reproduced. The point here is not to extract any parameters of the EFS from this adjustment but to check the global consistency of the data and interpretation. We see that

the orientation of the NPLs has a great impact on the DLP observable even for a quite broad distribution. Our simple model of only two populations of NPLs starts to be limited when trying to simulate the DLP dependence. However, we notice with equation IV.30 how quickly the formulas become intractable when a higher degree of complexity is added concerning the orientation and a more realistic description of the NPLs organisation.

IV.2.2 Beating experiments at zero-field

There exists a more direct way to probe the splitting δ_1 than through the fit of the DCP data: the observation of the temporal quantum beats between the $|X\rangle$ and $|Y\rangle$ states which would have a characteristic frequency equal to $\delta_1/\hbar$. Indeed, a resonant excitation can create a coherent superposition of the two states and the evolution of this superposition in time is supposed to show some quantum interference effects. These effects can be measured in the form of quantum beats in the TRPL signal [24, 118] or in the differential transmission of a probe pulse [119, 120]. This latter option is used here to obtain another estimation of δ_1.

a) Theory

Before presenting the experimental results obtained, it is necessary to perform a theoretical analysis in order to know which experimental conditions should be fulfilled, and especially under which pump and probe polarization the quantum beats can be observed.

The theoretical development allowing us to obtain a formula of the differential transmittance $\frac{\Delta T}{T}$ are adapted from a previous work done in the team [119] and are described in detail in Appendix C. In this case, the pump and the probe are taken to be linearly polarized and collinear to each other. The calculation describes how the probe signal is affected by the crossing of the sample where a coherent excitation is created by the pump at a time Δt (delay) before the arrival of the probe. The formula found for a 'flat' lying NPL is:

$$\frac{\Delta T}{T} \quad \alpha \quad (3+\cos^2(2\theta))e^{-\Delta t/\tau_r} + |\sin(2\theta)|\sin(2\theta)e^{-\Delta t/T_2}\cos(\omega_1 \Delta t), \tag{IV.31}$$

where θ is the angle between the incoming polarization and the X axis of the NPL ($-\pi/2 \leq \theta \leq +\pi/2$).

The response is made of two terms: the first one is an exponential decay with the characteristic time τ_r the lifetime of the IX. The second component is the oscillatory one, with a frequency ω_1 related to the splitting δ_1 by $\hbar\omega_1 = \delta_1$. The oscillations decay with a characteristic time T_2, the decoherence time between the $|X\rangle$ and $|Y\rangle$ states.

We see in this formula the importance of the parameter θ. The optimal contrast is obtained for $\theta = \pi/4$. No beats can be observed for a random assembly of 'flat' lying NPLs, as averaging over θ would lead to an overall zero term in front of the oscillatory one ($\sin(2\theta)$ being odd). The quantum beats can thus be observed in an optimum way in zones of the sample where the NPLs show a preferential orientation at 45° of the incoming pump and probe polarization. These conditions make the observation of these oscillations quite challenging.

The NPLs lying on their 'edge' are not taken into account here. Due to their orientation, the formation of a coherent superposition of the $|X\rangle$ and $|Y\rangle$ is impossible. Such NPLs will then only contribute to the non-oscillatory term of the differential transmittance, with the characteristic time τ_r, adding a signal to the overall background.

b) Experimental results

As already mentioned the quantum beats could be observed using transient optical spectroscopy techniques in Cambridge by our collaborators of the opto-electronic group of the Cavendish Laboratory. Let us note that an equation similar to equation IV.31 could be obtained in the case of TRPL and we tried to observe the quantum beats in the decay of the PL at the laboratory (INSP) without success.

To observe the beating presented in figure IV.10.b, the NPLs are diluted in a toluene/polystyrene solution and then deposited on a clean glass slide. The dilution allows us to obtain a relatively low density of NPLs in the film, with around $\sim$ 50 - 100 NPLs under the excitation spot contributing to the signal. The sample is then mounted in a cryostat and cooled down to a temperature of 6 K. The pump beam is tuned resonantly with the IX transition at 618 nm. Its spectral width is 6 meV $\gg \delta_1$ allowing the simultaneous excitation of the $|X\rangle$ and $|Y\rangle$ states, necessary to generate a coherence between the two states. A white-light continuum is used as the probe. The pump and the probe have the same linear polarization, which is the condition to obtain quantum beats. A more detailed description of the pump-probe set-up can be found in ref. [80].

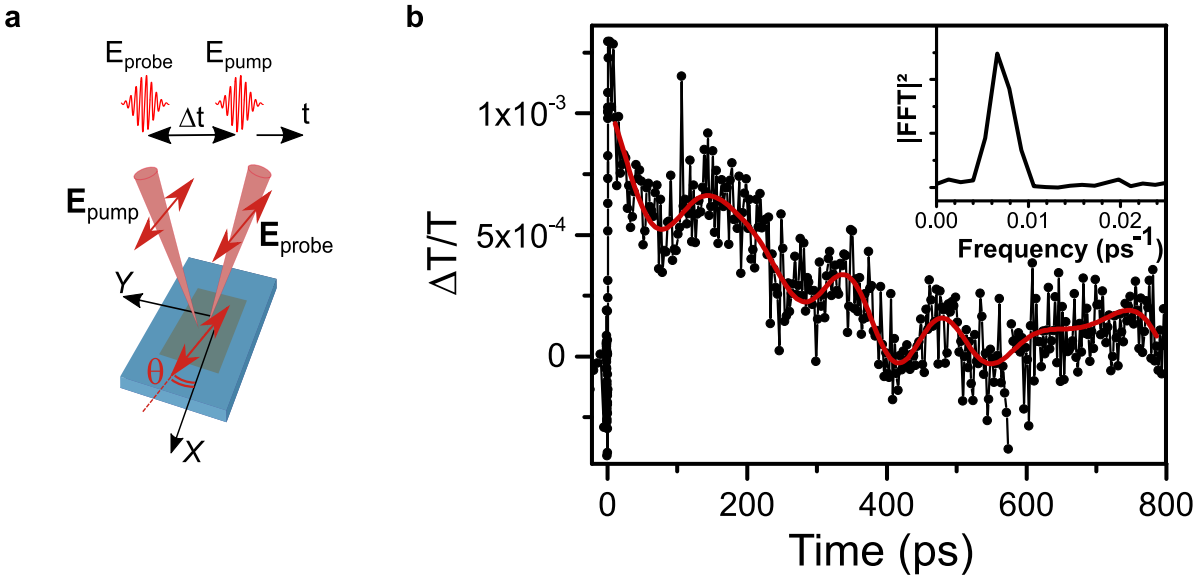

Fig. IV.10 *(a) Sketch of the excitation configuration: the probe and the pump have the same linear polarization forming an angle θ with the X axis of the NPL. (b) Differential transmittance signal at $\lambda_{probe} = 622$ nm. The red curve is a guide to the eye. The Fourier transform of the oscillating part of the signal is shown in the inset. The peak found at $\sim$ 140 ps corresponds to a δ_1 value of $\sim$ 30 µeV.*

The signal shown in figure IV.10.b is consistent with the theoretical derivation. The oscillations are superimposed on a decay and the amplitude of these oscillations also decay as expected. Such oscillations could not be found for every spot in the sample but only at specific positions. Once again, this is consistent with the theoretical predictions: only areas where the NPLs have a sufficient degree of local order can provide a signal.

We see from the Fourier transform of the signal presented in figure IV.10.b the oscillating part of the signal has a period of $\sim$ 140 ps which corresponds to $\delta_1 \approx 30$ µeV. This value is comparable with the 60 µeV found previously, placing the bright state-bright state splitting in

the tens of µeV range. Values of $\tau_r \approx 290$ ps and $T_2 \approx 300$ ps are also found from the adjustment of the differential transmittance. The value of τ_r found here is an order of magnitude smaller than the fastest component found from the TRPL decay. This fast decay can be the signature of multi-excitonic effects (exciton-exciton annihilation) having their origins in the higher fluence used here to be able to observe the differential absorption compared to the ones used in PL experiments.

The value of T_2 would be in the case of a single NPL the decoherence lifetime of the superposition. However, here the measurements are made on an ensemble of different NPLs and we believe that T_2 is, in this case, more representative of an inhomogeneous dephasing, due to the distribution in the δ_1 values among the different NPLs [24]. The oscillations of different frequencies will add up, leading to dephasing and destructive interferences within a time interval $\sim T_2$. The value found here for T_2 is in the upper range of what is found in the literature where values from 20 ps to hundreds of ps are reported [111, 121]. This could be an interesting feature for possible quantum devices applications which are based on coherent manipulations.

The complementary experiments presented in this section strengthen, therefore, the model of an EFS composed of two linear states split at 0 T by a value of tens of µeV. However, an important part of the EFS has not been considered so far: the dark states manifold. Let us discuss now the implications of this approximation.

IV.3 Justification and limits of the model

The experimental results which demonstrate the existence of an EFS made of two linearly polarized states were presented in the previous sections. The model used gives a good adjustment of our data, in spite of the fact that it is based on a strong assumption: the absence of coupling between the bright and dark states of the EFS. Other experimental observations such as the weak dependency of the value of the exciton lifetime, τ_r, on the magnetic field or on the temperature also point towards an absence of coupling.

We would like to discuss here several aspects which were not directly included in the starting assumptions. We first consider the possible role of charged species (trions) in the NPLs emission properties. Then we discuss the approximation that consisted in neglecting the coupling between bright states and dark states. Finally, we raise the possibility that the emission studied here directly results from the radiative recombination of the dark states.

IV.3.1 Trions

The possibilities of an emission dominated by trion recombination has to be considered once again since they could partially explain some of the experimental results.

A trion is an excitation composed of three charge carriers: two electrons and one hole for a negative trion or two holes and one electron for a positive one. They are created by the photo-charging of the material studied: one of the photo-generated carriers can be trapped by defects of the structure, presumably at the surface in the case of NPLs, leaving the other charge free in the material. After a new excitation another electron-hole pair can be created, the NPL ending up with carrying a three-charge-carrier complex.

Trions have been observed in other types of colloidal crystal [31] and even in CdSe/CdS core/shell NPLs [81]. Contrary to the exciton, the EFS of a trion is only composed of two

bright states. To show this, let us take the example of negatively charged trions, composed of two electrons and one hole. The two electrons must have opposite spin following the Pauli exclusion principle. Thus, regardless of the spin of the hole, the recombination of an electron-hole pair is always allowed. Due to the presence of both possible values of spin for the electron ($\pm$ 1/2), there will always be a combination of electron-hole with a total angular momentum equal to $\pm$ 1.

Due to the presence of only two optically active states in the trion fine structure, the application of a magnetic field or the modification of the temperature only marginally modifies the TRPL arising from trion recombination. No mixing can occur with lower lying optically inactive states when a magnetic field is applied and no modification of the exciton population dynamics, due to back transfer processes, can occur when the temperature is raised. The absence of modification in the TRPL with the application of a magnetic field is actually used as an evidence of a PL signal dominated by trion recombination [31, 81]. For these reasons, such an emission seems here an interesting hypothesis to explain our observations. However, this attribution has to be ruled out by the linear nature of the emission at 0 T. The presence of linear states is incompatible with trions. Indeed the exchange interaction is reduced to zero in such complexes, since, keeping the example of negative trions, the contribution of each electron with the hole will cancel out due to their opposite spin value. Moreover, as shown in Chapter III, the study of single NPLs emission also led us to rule out trion relaxation as the main origin of the PL signal.

IV.3.2 Role of the dark states

In this last section, we would like to briefly present some of the arguments that led us to neglect the dark states and their interactions in the relaxation processes.

a) Strong coupling and small bright states-dark states splitting

A first possibility is that the bright states-dark states coupling is not as weak as we assumed up to now and that the bright states-dark states splitting Δ is lower than the values of k_BT whatever the temperature. This was observed in type-II core/shell CdTe/CdSe nanocrystals and explained by a really weak exchange interaction in these structures [74].

In that specific case, the rising of the temperature would not lead to a back-transfer from the dark states to the bright ones, as both bright and dark states would already be equally populated at low temperature. In ref. [74], a complex model is developed which also rationalizes the absence of evolution of τ_s with the magnetic field.

However, in our case this hypothesis leads to a vanishing value for Δ. Indeed one would need that $\Delta \ll k_BT$ at 1.6 K, *ie* 140 µeV. This is contradictory with the value found for the bright states splitting δ_1 of $\sim$ 30 - 60 µeV. This relatively large δ_1 value for a type-II system shows that the exchange interaction in these NPLs is relatively strong and is not consistent with a small value of Δ. Therefore, in our view, the possibility of a small bright states-dark states splitting has to be discarded.

b) Weak coupling to the dark states

Another hypothesis which could explain our experimental data would be the one of a weak coupling between the bright and dark states, justifying the absence of relaxation to the dark states in our model for the case of 'flat' lying NPLs. We favor this hypothesis since it is supported by several experimental observations and basic numerical modelling where the dark

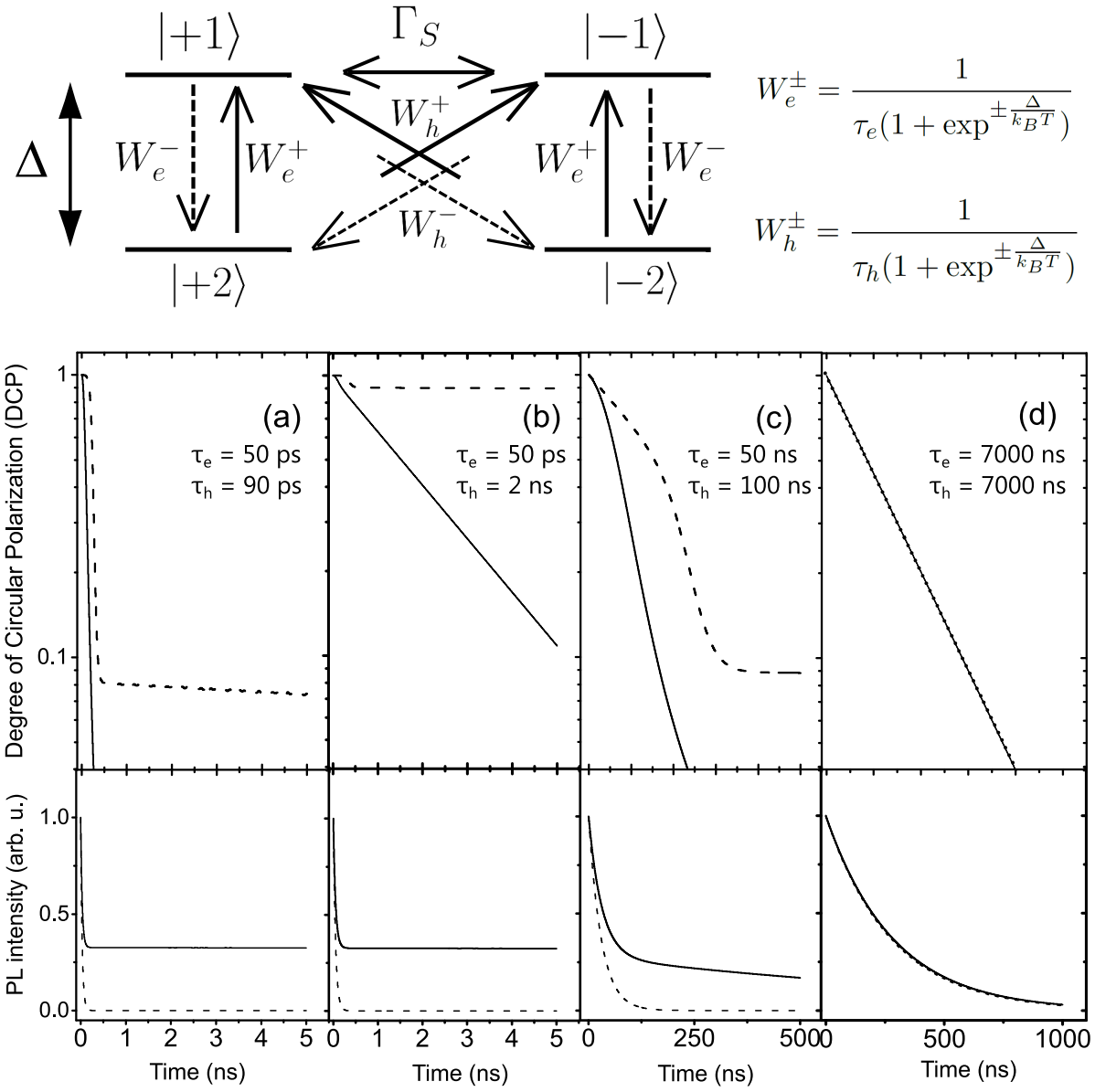

Fig. IV.11 *Top part: sketch of the four-levels systems with the different relaxation rates between each levels [77]. Bottom part: Results of the numerical simulations for the DCP(t) ($\propto (N_{+1} - N_{-1})/(N_{+1} + N_{-1})$) and the TRPL ($\alpha$ $N_{+1} + N_{-1}$) at $T = 1.6$ K. The simulations are carried out with $\tau_r = 300$ ns, $\tau_s = 500$ ns and (a) $\tau_e = 50$ ps, $\tau_h = 90$ ps, (b) $\tau_e = 50$ ps, $\tau_h = 2$ ns, (c) $\tau_e = 50$ ns, $\tau_h = 100$ ns, (d) $\tau_e = 7000$ ns, $\tau_h = 7000$ ns and for $\Delta = 0.1$ meV (solid line) and $\Delta = 1$ meV (dotted line).*

states were considered, as we will see now.

Let us consider a four-level system composed of two $|\pm 1\rangle$ bright states and two $|\pm 2\rangle$ dark states, as the one developed in Maialle *et al.* for an 'ideal' quantum well [77]. Circularly polarized states are considered here as they are easy to comprehend, nevertheless the same

type of reasoning can be used with the linear or elliptical states that characterize the NPLs EFS.

The upper part of figure IV.11 summarizes the different relaxation processes between the states. Two different spin flip processes are at play here to obtain a transition between the two $|\pm1\rangle$ bright states. First, there is the exciton spin flip or 'direct' spin flip where both carriers flip their spin at the same time, characterized by a rate $\Gamma_s = 1/\tau_s$. There is also the 'indirect' spin flip which involves the sequential spin flips of each carrier and where the $|\pm2\rangle$ states play the role of intermediate states. The flip of single carriers is characterized by the rates $W_e^{\pm}$ for the electrons and $W_h^{\pm}$ for the holes. In the case of thermal equilibrium with the phonon bath, these rates can be expressed as:

$$W_e^{\pm} = \frac{1}{\tau_e(1+\exp^{\pm\frac{\Delta}{k_B T}})}, W_h^{\pm} = \frac{1}{\tau_h(1+\exp^{\pm\frac{\Delta}{k_B T}})}, \tag{IV.32}$$

where τ_e and τ_h are the respective spin relaxation times of electrons and holes. To complete the model, the recombination rate $\Gamma_r = 1/\tau_r$ of the bright $|\pm1\rangle$ exciton has to be considered.

We can numerically model the evolution of the population N_{+1}, N_{-1}, N_{+2}, N_{-2} of each state with time and from these populations the DCP(t) and the total PL(t) can be computed. Indeed, the DCP is proportional to $(N_{+1}-N_{-1})/(N_{+1}+N_{-1})$ while the total PL is proportional to the sum $N_{+1} + N_{-1}$.

We fix in our simulations $\tau_r = 300$ ns and $\tau_s = 500$ ns, the values found experimentally (the same simulations were performed with $\tau_s = 50$ ns and gave similar results). The lower part of figure IV.11 shows the results obtained using Matlab software routines to solve the differential equations governing the $|\pm1\rangle$ and $|\pm2\rangle$ states' populations. The plots are for different values of τ_e and τ_h and for $\Delta = 0.1$ meV (solid line) and $\Delta = 1$ meV (dotted line).

In the case of figures IV.11.a and b, the conditions τ_e, $\tau_h \ll \tau_r$ lead to quick loss of the DCP and the apparition of a fast component in the TRPL, due to the quick relaxation onto the dark states. In the case of figure IV.11.c, where τ_e, $\tau_h \approx \tau_r$, the DCP exhibits a bi-exponential behavior. These two possibilities do not correspond to what is observed experimentally. Indeed, the DCP(t) is clearly mono-exponential (figure IV.4) and even if a fast component in the TRPL could have been missed by the measurements presented previously due to their relatively low resolution (figure IV.3), the decays obtained with the streak camera and presented in figure IV.12 ruled out the existence of such a fast component.

Finally the only combination that explains at the same time a mono-exponential decay of the DCP and the absence of a fast component in the TRPL is the case presented in IV.11.d where both τ_e, $\tau_h \gg \tau_r$. For these reasons, the hypothesis of a weak coupling between the bright and dark states seems justified in our view.

It is interesting to wonder why this coupling is so weak in these core/crown NPLs. In fact, such weak coupling is also found in quantum dots and can have several origins: (i) suppression of the single spin-flip processes relying on the motion of the exciton (D'Yakonov-Perel mechanism [122]), this motion being frozen in quantum dots compared to quantum wells [77,115], (ii) inefficiency of relativistic processes related to spin-orbit coupling in quantum dots structures [123] or (iii) presence of an acoustic phonon bottleneck for certain system like core/shell CdSe nanocrystals [124], where the absence of low-energy acoustic phonons prevents the spin relaxation through the emission of such phonons. It is interesting to note that core/crown NPLs share the properties of quantum dots and do not behave as homo-NPLs.

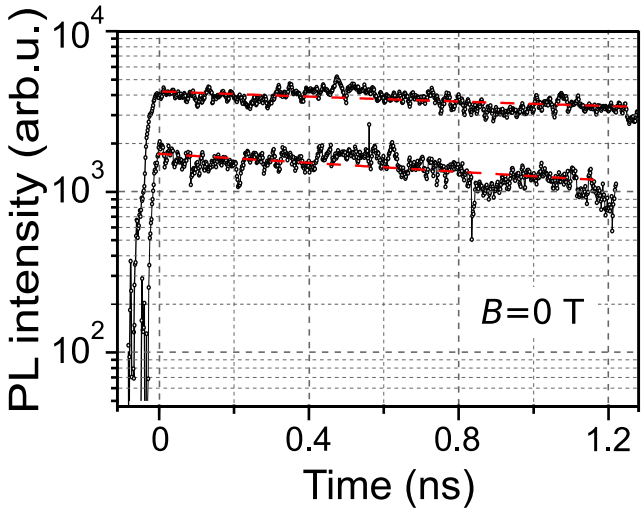

Fig. IV.12 *TRPL decays obtained under resonant excitation ($\lambda_{exc} \approx 610$ nm) of the IX transition at $T = 5$ K and $B = 0$ T. These curves are obtained with the streak camera. The red dotted curves correspond to an adjustment of the data by a mono-exponential decay of $\tau = 2.7$ ns, consistent with the values found from the other TRPL measurements shown in figure IV.3.*

In pure CdSe NPLs, the single carrier flip process is found to be efficient with associated relaxation time smaller than 100 ps for the single carriers [125]. Homo-NPLs thus share more properties with quantum wells and likely support excitons with larger in plane spatial coherence and possible motion.

As discussed in Chapter III, two factors can be held responsible for the difference between homo and hetero-NPLs: (i) the type-II band alignment with a strong confinement of the electron and (ii) the strong dielectric confinement which accentuate the localisation of the carriers wave functions at the hetero-interface (figure III.12). The localisation of the carriers wave-functions at the interface can be responsible for a lower motion of the exciton in this system as found in quantum dots, explaining in part the lower coupling with the dark states. It is also interesting to note that long spin relaxation lifetime is also observed in epitaxially grown coupled quantum wells [126, 127]. In these systems, the application of an electric field perpendicular to the wells plane leads to the formation of indirect excitons, with each carrier in adjacent wells. To the best of our knowledge, the lengthening of the spin relaxation lifetime in these systems compared to the basic quantum well has not been explained theoretically either whereas dark states should also play an important role. This general problem clearly deserves exhaustive investigations.

In the CdSe/CdTe core/crown NPLs the dominant process is thus more likely the 'direct' exciton spin flip governed by the exchange interaction, that is enhanced by the dielectric confinement. The coupling to the dark states resulting from the flip of a single carrier seems inefficient. This may justify in our view the approximation made to model the 'flat' lying NPLs response. However, the case of 'edge' lying NPLs where a mixing of the dark and bright states should occur with the application of a B-field remains problematic. Even with a weak coupling, the mixing of the states is unavoidable in the Voigt configuration. This mixing being governed by the ratio $g_{ex}\mu_B B/\Delta$, it would be tempting to assign the absence of signature in

the experimental data to large Δ values, *ie* $\Delta > 1$ meV ($\approx g_{ex}\mu_B B$ at 30 T). This is not a sustainable option either. Further studies and modelling are still required to access the impact of bright states-dark states mixing.

c) 'Grey' states

The last hypothesis we would like to mention is the possibility that the emission studied here is the one arising from the dark states directly. The dark states would be 'grey' states, emitting light efficiently and being responsible for the majority of the PL observed.

Theoretically, the radiative recombination rate of the dark states Γ_D is equal to zero, since they are not coupled to light. Nevertheless, in real systems the recombination rate of the dark states Γ_D is finite due to some relaxation of the selection rules by different processes and it is usual to have $\Gamma_B \gg \Gamma_D$, where Γ_B is the recombination rate of the bright states. Thus, in the systems where the bright states-dark states splitting Δ is relatively small compared to the values of k_BT at play, the emission from the bright states will predominate as the excitation in the dark states will be transferred back in the bright states with the help of thermal processes. This is the case of bulk II-VI semiconductors, epitaxially grown quantum wells and quantum dots or even certain types of colloidal nanocrystals where Δ is relatively small and $\Gamma_B \gg \Gamma_D$ [78, 82].

However, in highly confined colloidal nanocrystals where Δ can reach a dozen of meV, it is believed that the totality of the PL emission arises from the dark states at low temperature as the back transfer to the bright states is inefficient [83]; this model was used to analyze the experimental observations of different studies in CdSe nanocrystals and NPLs [110, 114]. In such a model, the coupling between the dark and bright states would be strong as all the excitation ends up on these lower levels.

Ref. [83] exposed the different mechanisms leading to the activation of the radiative recombination of dark states. The different processes all involve a mixing of the lower dark states with the bright ones, since only these ones are coupled to light. The most studied one is the application of an external magnetic field leading to a mixing through the Zeeman effect as we already saw. Then, at zero magnetic field, two mechanisms are possible: admixture through absorption or emission of phonons and a process involving the spin of the dangling bonds at the crystal surface.

Let us first consider the recombination through dangling bonds. The dangling bonds defects at the surface of the NPLs (atoms of Cd not well coordinated by ligands) possess a spin. It is then possible to have a recombination of a dark exciton through the simultaneous flip of the spin of the electron of the dark exciton and of the spin of a dangling bonds [128]. Such a process is allowed according to the selection rules if the spin of the dangling bonds is opposite to the one of the electron in the exciton. This process couples the lower dark states with the bright states energetically directly above, $|\pm 1\rangle$ (or $|X/Y\rangle$ in the case of linear states). The polarization of the emission of the dark states is then the one of the bright state it is coupled to.

The other process allowing the recombination of dark excitons relies on acoustic or optical phonon emission (as well as absorption at higher temperature). It is in this case the spin of the hole which can flip through the emission or absorption of a phonon. The energy of the emitted photon is then shifted from the dark state transition by an energy equal to the phonon one [83]. In the case of CdSe nanocrystals, the mixing of the dark states can occur with the higher energy lying, like the close $|\pm 1\rangle$ bright states leading to a circular polarization, but it can also happen with a higher energy linear bright state of zero angular momentum, leading

to linear polarization. The overall polarization will then be a mix of the two.

To the best of our knowledge, these two mixing processes were not described in the case of linear hybridized states. It is thus difficult to develop a model based on these processes and we did not try to tackle this issue. In a first approximation where we would consider these mixing processes independent of the magnetic field and the polarization of the dark states to be that of the upper bright ones, it is likely that the model developed in the section IV.1.2 could be applied almost as it is. Indeed, due to these mixing processes the new eigenstates of the system are linear combinations of the former bright and dark states (combination of $|X\rangle$ and $|X'\rangle$ on the one hand and $|Y\rangle$ and $|Y'\rangle$ on the other). Since light is only coupled to the bright component of these states, the formula of the DCP, obtained through projection of the states on the polarization vectors of the light, would be similar. Thus in this case the observed linear polarization of these 'grey' states would reflect the linear polarization of the above bright states and the splitting of δ_1 found would be the splitting of these two 'grey' states.

However, it is important to keep in mind that such a reasoning requires many approximations, for example the process of mixing with the help of dangling bonds is likely to be magnetic field dependent due to the alignment of the spin of these bonds with the B-field. The formula obtained for the DCP would then be much more complex.

We would like to conclude saying that the hypothesis of a PL dominated by the emission of 'grey' states is worth considering but that further theoretical developments are needed to fully develop a model clarifying the different mixing processes of the 'grey' states with the bright ones. Moreover, it is also important to note that the dangling bond polarization mechanism is not necessary to explain our experimental data contrary to the case of pure CdSe NPLs [114].

Finally, we would like to stress that even if this hypothesis could explain the weak signature of the dark states for 'flat' lying NPLs, it cannot be transposed to the 'edge' lying ones. Indeed, the mixing of dark and bright states due to the Voigt configuration in 'edge' lying NPLs should still take place in this hypothesis and a significant change in $\tau_r(B)$ as a function of B should then be observed [114].

Conclusion

In this chapter, we studied the EFS of CdSe/CdTe NPLs with the help of high magnetic fields.

In the first section, we presented the results of PL measurements resolved in polarization and in time under high magnetic field performed in the HFML laboratory. A model was developed for the EFS, consisting of two non-degenerate and optically active linear states at zero-field which acquire elliptical and then circular symmetry as the magnetic field increases. The model is shown to well adjust the experimental data. From these adjustments the bright states splitting can be determined ($\sim$ 60 µeV) as well as the exciton g-factor ($g_{ex} \approx 0.7$). The evolution of the spin relaxation time, τ_s, was also studied as a function of the B-field and a relatively high value of $\sim$ 500 ns was measured at low field; an estimation of the spin lifetime at zero field is obtained through qualitative extrapolation of the data ($\tau_s \sim$ µs). Furthermore, we evidenced a characteristic behavior of the spin relaxation time ($\tau_s \ \alpha \ B^{-3}$), whose origin still has to be explained.

In the second section, complementary experiments which strengthen the relevance of the model were presented. The DLP measured at 0 T shows without ambiguity the presence of linear states and the evolution of the DLP with the magnetic field can be rationalized with the

model. The observation of quantum beats in the differential absorption signal at a frequency corresponding to an energy separation of ~ 30 µeV confirms the picture deduced from the high magnetic field study.

Finally, in the last section, we discussed the role of the dark states in the relaxation processes. The experimental data being well adjusted by a model where the dark states are not taken into account, some questions are raised regarding the position of the dark states and their coupling with the bright ones. We believed that a weak coupling between the dark and bright states is at play in these NPLs. An alternative model, that remains to be explored, would consider an emission arising only from 'grey' states, *i.e.* the lower dark states with a non-zero radiative recombination rate, due to phonon coupling or recombination with the help of the spin of dangling bonds at the surface of the NPLs. Further theoretical development would be needed to describe how these mixing mechanisms evolve with the magnetic field and to be able to know if they are readily applicable to the case of linear states.

The exact splitting between the dark and bright states in these core/crown NPLs could not be deduced from our experiments, even if we believe it to be large enough to prevent any efficient role of acoustic phonon in their coupling. The issue of describing the excited states and elucidating the position and precise role of dark states would benefit from an experimental approach that would allow the fine control of the NPLs organization. Self-organization of NPLs in either flat or edge configurations was demonstrated for CdSe NPLs through advanced deposition procedure [129]. With such assembly, the orientation of the NPLs with the magnetic field would be perfectly known and with it its main effect on the NPLs: the splitting of the different states for the 'flat' NPLs or the mixing of these states for the NPLs on their edges. The experimental data obtained in such conditions would be easier to analyze, as averaging on the different position would no longer be necessary. We believe that performing again experiments in such self-organized samples would allow important progress in the physics of dark states and bright states-dark states interactions in the core/crown configuration.

Chapter V
CdSe/$CdSe_{1-x}Te_x$ nanoplatelets

In this chapter, we will present the study carried out to understand the emission properties of a new type of core/crown nanoplatelets (NPLs), obtained by forming an alloy of the crown. Structures of the type: CdSe/$CdSe_{1-x}CdTe_x$ NPLs are considered here, where x is the Tellurium content and can be tuned from 0 to 1. The process of alloying opens a new pathway to tune the optical properties of the core/crown NPLs, while keeping this core/crown structure intact.

This work was done in close collaboration with the group that elaborated the structures in LPEM (ESPCI). It is published in Dufour *et al.* [85] and is also described in Marion Dufour's PhD thesis [130].

The LPEM group performed the synthesis and optical characterizations at room temperature, which will be presented in the first section of this chapter. Then, in the second and third section, we will focus on the results of the experiments performed at the INSP: the study of single NPLs' emission at 5 K and the characterization of the time-resolved photoluminescence (TRPL) of NPLs ensembles at room temperature. Finally, an interpretation of the bicolor emission will be given in the last section.

V.1 Optical properties of CdSe/$CdSe_{1-x}Te_x$ nanoplatelets as a function of x

V.1.1 State of the art

With alloying, the band gap energy of NPLs can be tuned, while keeping the same structural properties and hence the same degree of confinement (as opposed to the growth of a shell for example). $CdSe_{1-x}Te_x$ alloyed NPLs were first synthesized in 2016 [131]. In this work, the authors studied the evolution of the optical properties with x the 'degree' of alloying. Concerning the absorption properties, the band edge energy of $CdSe_{1-x}Te_x$ NPLs shows a non-monotonic evolution with the Te amount, x. The band-edge first red-shifts of ~ 50 nm when x increases from 0 to 0.5 then for larger values of x it blue-shifts towards the value of the band edge in pure CdTe NPLs. This effect is well known in II-VI ternary alloyed semiconductors and is referred to as the bowing effect [132]. The latter is also finely characterized in core/crown structures in the following paragraph. The most striking result of this study is however the evolution of the photoluminescence (PL) emission. Despite the non-monotonic evolution of the absorption band edge, a constant red-shift of the emission is observed from pure CdTe NPLs to $CdSe_{1-x}Te_x$ with a large amount of Se ($x < 0.1$). It leads to an abrupt blue-shift of

the emission between the NPLs with low concentration in Te and pure CdSe NPLs. To better understand this transition, the authors synthesized NPLs with very low Te content. From single NPLs spectroscopy, they were able to show that the presence of CdTe clusters (more than one Te atom on neighbouring sites), in the overall CdSe lattice, led to the formation of mid-gap hole states, resulting in a red-shifted PL. As the content in Te is increased, these trap states disappear and the emission becomes characteristic of an excitonic transition of the $CdSe_{1-x}Te_x$ alloy.

A year later, a group from Bilkent University in Turkey synthesized the first CdSe/$CdSe_{1-x}Te_x$ hetero-structures, composed of a core of CdSe and an alloyed $CdSe_{1-x}Te_x$ crown [133]. By adjusting x, they were able to continuously tune the luminescence of the NPLs from 570 nm to 660 nm. The authors could explain the evolution of the PL energy by the continuous transformation from a quasi type-II hetero-structure, at low value of x (the hole is localized around the CdTe clusters, in line with the work of Tenne *et al.* [131], while the electron is still delocalized across the NPL) to a pure type-II structure for high x values, where the electron is confined in the core. Their measurements of TRPL corroborate this idea, since they measure a slow down of the PL with the increase of x, which is characteristic of the formation of an indirect exciton. However, the authors only observe a single broad luminescence peak, for all x values, in opposition to what we are going to report below, where two distinctive PL signatures are observed.

V.1.2 Absorption and photoluminescence at room temperature

Figure V.1 presents both the absorption and the PL of CdSe/$CdSe_{1-x}CdTe_x$ NPLs for a value of x ranging from 0 to 1. Concerning the absorption, two optical features are visible in these spectra. First, the signature of the pure CdSe core is present through the peaks at 510 nm and 478 nm (green line), corresponding, respectively, to the heavy-hole and light-hole transitions. As x increases, the signature of the excitonic transition of the crown gains in amplitude. For non-zero values of x, the heavy-hole transition of the crown can be observed ranging from 540 nm to 590 nm (grey curve). The evolution in energy of this transition is clearly not monotonic, with a minimum obtained at $x = 0.6$. It is characteristic of a bowing effect, name given to the non-monotonic evolution (parabolic evolution) of the band-gap observed in ternary II-VI alloy, like $CdSe_{1-x}CdTe_x$, with the composition of the alloy represented by the value of x [132].

This effect was already described for 3ML core-only $CdSe_{1-x}CdTe_x$ NPLs [131]. The same model can be applied here using the following equation to describe the evolution of the band gap of the $CdSe_{1-x}CdTe_x$ crown:

$$E_{CdSe_{1-x}CdTe_x} = xE_{CdTe} + (1-x)E_{Cdse} - bx(1-x), \tag{V.1}$$

where E_{CdTe} and E_{CdSe} are the band gap energies of 4 ML CdTe and CdSe NPLs and b is the bowing parameter. Here, the band gap of the crown is well adjusted with $b = 0.78$. This value is in good agreement with values already reported in the literature [131–133], showing that the composition of the alloy is well monitored.

Concerning the PL, it evolves dramatically with the Te content. For $x \leq 0.2$, a broad emission is observed, similar to what Tenne *et al.* reported in core-only $CdSe_{1-x}CdTe_x$ NPLs [131]. The authors suggested that this emission was resulting from the recombination of the exciton around Te clusters or atoms, where the hole is localized. The broadness was attributed to the inhomogeneous alloying of the crown and the formation of deep traps around clusters

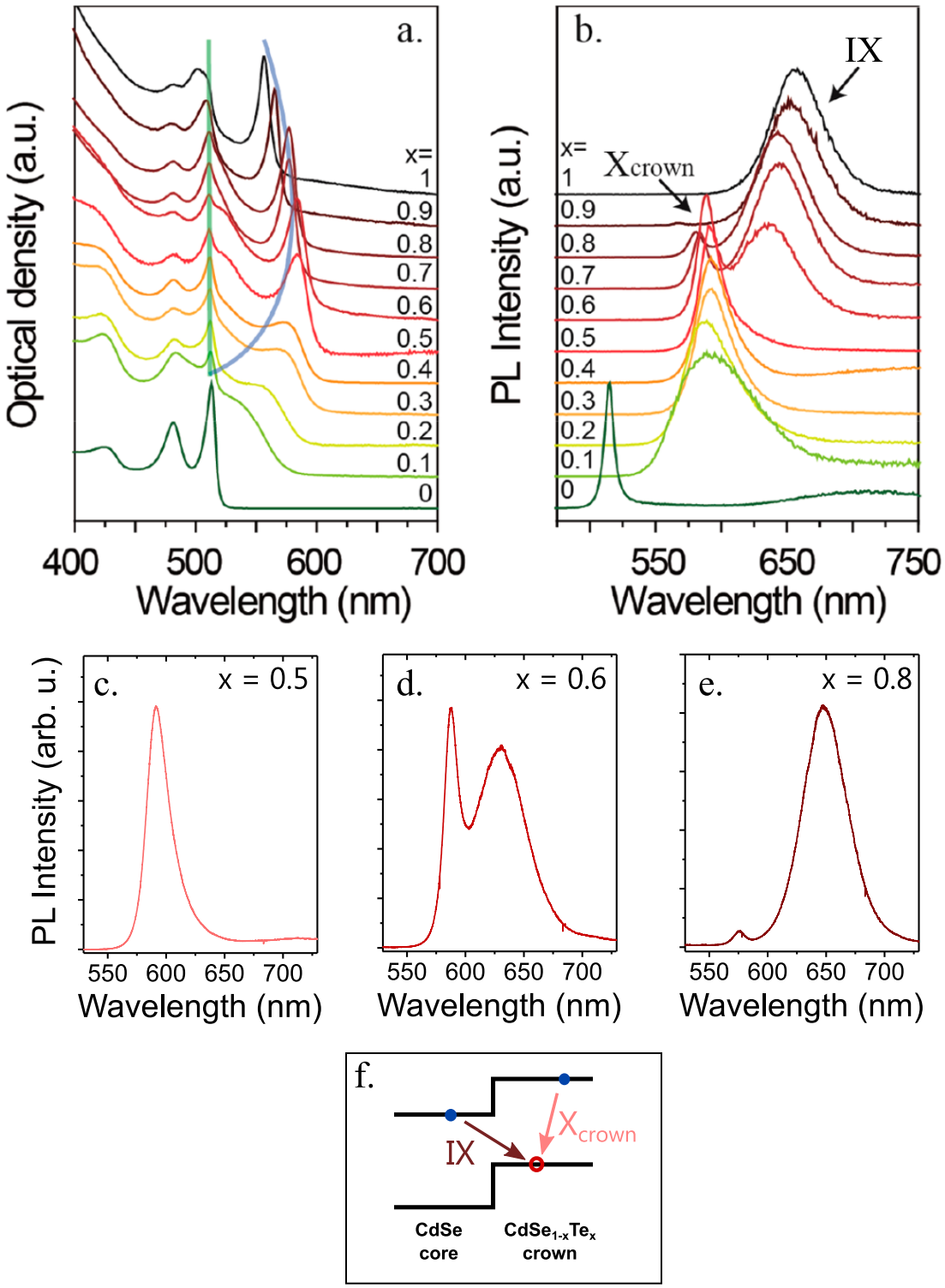

Fig. V.1 *(a) Absorption of a solution of $CdSe/CdSe_{1-x}Te_x$ NPLs at room temperature for x ranging from 0 to 1. The green line follows the signature of the heavy-hole transition in the CdSe core, while the grey bowed line follows the heavy-hole transition of the crown. (b) Its corresponding PL emission. For clarity the PL spectra of $x = 0.5$ (c), $x = 0.6$ (d) and $x = 0.8$ (e) are reproduced below. (f) diagram of the band alignment in $CdSe/CdSe_{1-x}Te_x$ and the different recombination channels.*

of Te atoms. We believe that the PL emission of core/crown NPLs for $x \leq 0.2$ has the same origin and is dominated by the alloyed crown emission.

For $0.3 \leq x \leq 0.5$, the emission becomes narrower. Its Stokes shift with the absorption peak of the crown is then below 25 meV. Moreover, it shows a similar bowing effect to the one experienced by the crown. This PL is thus attributed to the direct recombination of the exciton in the crown, X_{crown} (see figure V.1.f).

For $0.6 \leq x \leq 0.8$, the spectra present a striking bicolor emission as can be seen in figures V.1.d and e. On the high energy side, a narrow (FWHM $\sim$ 60 meV) peak, with a small Stokes shift compared to the absorption, is attributed to the direct emission of the exciton in the alloyed crown, X_{crown}. On the low energy side, the second peak has a much larger linewidth ($\geq$ 130 meV) and is clearly red-shifted compared to the absorption. This emission is similar to the emission arising from the recombination of indirect excitons in non-alloyed CdSe/CdTe NPLs (studied in Chapters III and IV). It is thus attributed to the recombination of the indirect exciton (IX), composed of an electron in the CdSe core and a hole in the $CdSe_{1-x}CdTe_x$ crown. For $x > 0.8$, the emission of the crown can not be detected anymore and the IX recombination emission is the only one observed.

To the best of our knowledge, it is the first time that such a bicolor emission is observed in core/crown NPLs hetero-structures. Even in the work of Kelestemur *et al.* in which the same type of structures are synthesized, a single luminescence peak is reported [133]. We attribute the difference in our observations to the difference in the lateral dimensions of the crown. In Kelestemur *et al.*, the crowns were only 23 x 30 nm^2 for a core of 12 x 16 nm^2, while larger crown NPLs were synthesized here ($\sim$ 20 x 100 nm^2 for a core dimension of 9 x 22 nm^2). Our collaborators at the LPEM showed that the crown has to be large enough to allow the recombination of the direct exciton X_{crown} by following the optical properties of the NPLs obtained for different quantities of crown precursors [85]. When too few crown precursors are added, leading to a small lateral size of the crown, the X_{crown} PL is never observed. This observation is furthermore supported by an experimental study, indicating that the oscillator strength of transitions in NPLs increases with their lateral sizes [15].

This bicolor emission opens the path for interesting light display device applications. Indeed, one usually needs three different emitters to create a white LED, with multicolor emission as the one presented here, the number of emitters needed would be reduced. It also raises an interesting fundamental question: usually the 'hot' excitation always relaxes towards the lower excitonic levels of the system before recombining radiatively, leading to a single emission. Why is it not the case here? To tackle this issue, the dynamics of both emissions are studied, as well as the band alignment between the core and the crown. However, the first step in the investigation consists in showing that the bicolor emission is intrinsic to an alloyed NPL and does not arise from 'sub-populations' of NPLs emitting at different wavelengths.

V.2 Photoluminescence of single nanoplatelets

To show that the bicolor emission had to be associated to the response of a single NPL, we studied the emission of single $CdSe/CdSe_{0.4}CdTe_{0.6}$ NPLs (value of x for which X_{crown} and IX emission have similar intensities). To do so, the solution of NPLs are diluted up to 6000 times and deposited on glass slides. The samples are then studied at 7 K, where the broadening effects due to the temperature are reduced to their minimum. Exceptionally, a continuous wave Argon laser emitting at 515 nm was used as the excitation source.

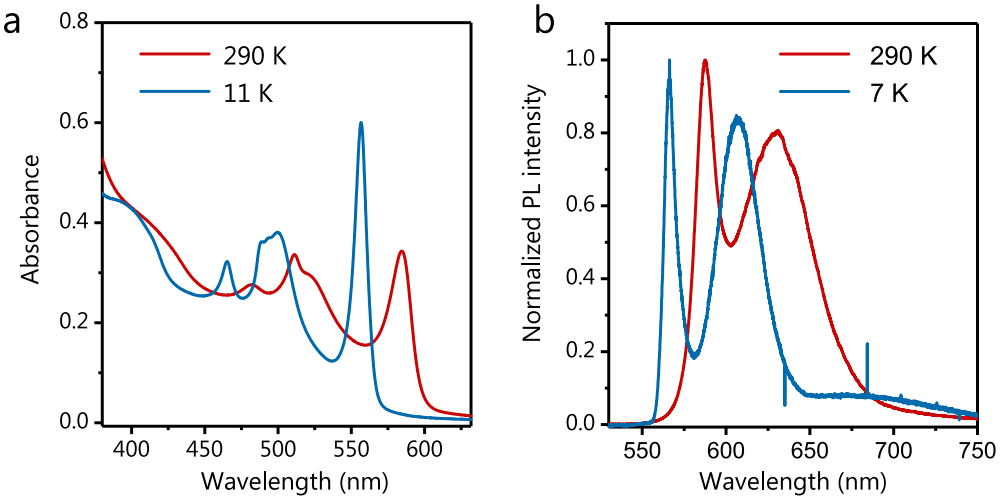

Fig. V.2 *(a) Absorption spectra of a film of CdSe/CdSe$_{0.4}$Te$_{0.6}$ at room temperature (red) and 11 K (blue), (b) PL spectra of a similar film at room temperature (red) and 7 K (blue).*

Figure V.2 shows the absorption and PL of a thin film of CdSe/CdSe$_{0.4}$Te$_{0.6}$ NPLs at both room temperature and $\sim$ 10 K. The deposition on a glass slide does not change fundamentally the optical properties of the objects compared to the solution: the bicolor emission remains present in the film. Both the absorption and the PL are blue-shifted by $\sim$ 80 meV as the temperature is lowered. This well-known phenomenon in semiconductors is explained by a relative shift in the position of the conduction and valence bands due to the temperature dependence of the lattice dilatation and the electron-lattice interactions [90] (see Chapter III.2.1). The spectra are also much narrower, consistent with the diminution, at low temperature, of the exciton-phonon coupling.

We see in figure V.3.a how the dilution impacts the PL spectra. Above a dilution factor of x 4000, the inhomogeneous X$_{\text{crown}}$ line splits into several sharp peaks. Then, by increasing the dilution ($\sim$ x 6000), several objects can be repeatedly observed as the surface of the sample is scanned. One of this characteristic spectrum is shown in figure V.3.b and is attributed to the response of a single NPL. The two emissions are still present, showing that the bicolor emission is indeed intrinsic to a single NPL. For the X$_{\text{crown}}$ emission the response has a Lorenztian shape (see figure V.3.e) with a width found within the 380-450 µeV range ($\sim$ 20 single objects could be observed throughout the study). However, the IX emission peak remains large with a FWHM of $\sim$ 100 meV. It is very likely that the mechanisms described in Chapter III, such as spectral diffusion and coupling through LO phonons, are at play here explaining once again the broadness of the IX emission. This remaining broadness is responsible for the low amplitude of the IX emission compared to the X$_{\text{crown}}$ one. Indeed, the ratio of the integrated intensity of X$_{\text{crown}}$ and IX at the scale of the single object is comparable to the one measured in the dense film of NPLs, showing that the dilution do not lead to the opening of non-radiative channel of the IX emission. In addition, we note that the vibronic structure inside the IX PL is not resolved in alloyed crown hetero-structures. This point was not examined further.

The width of the X$_{\text{crown}}$ emission is extremely narrow and comparable to the one measured

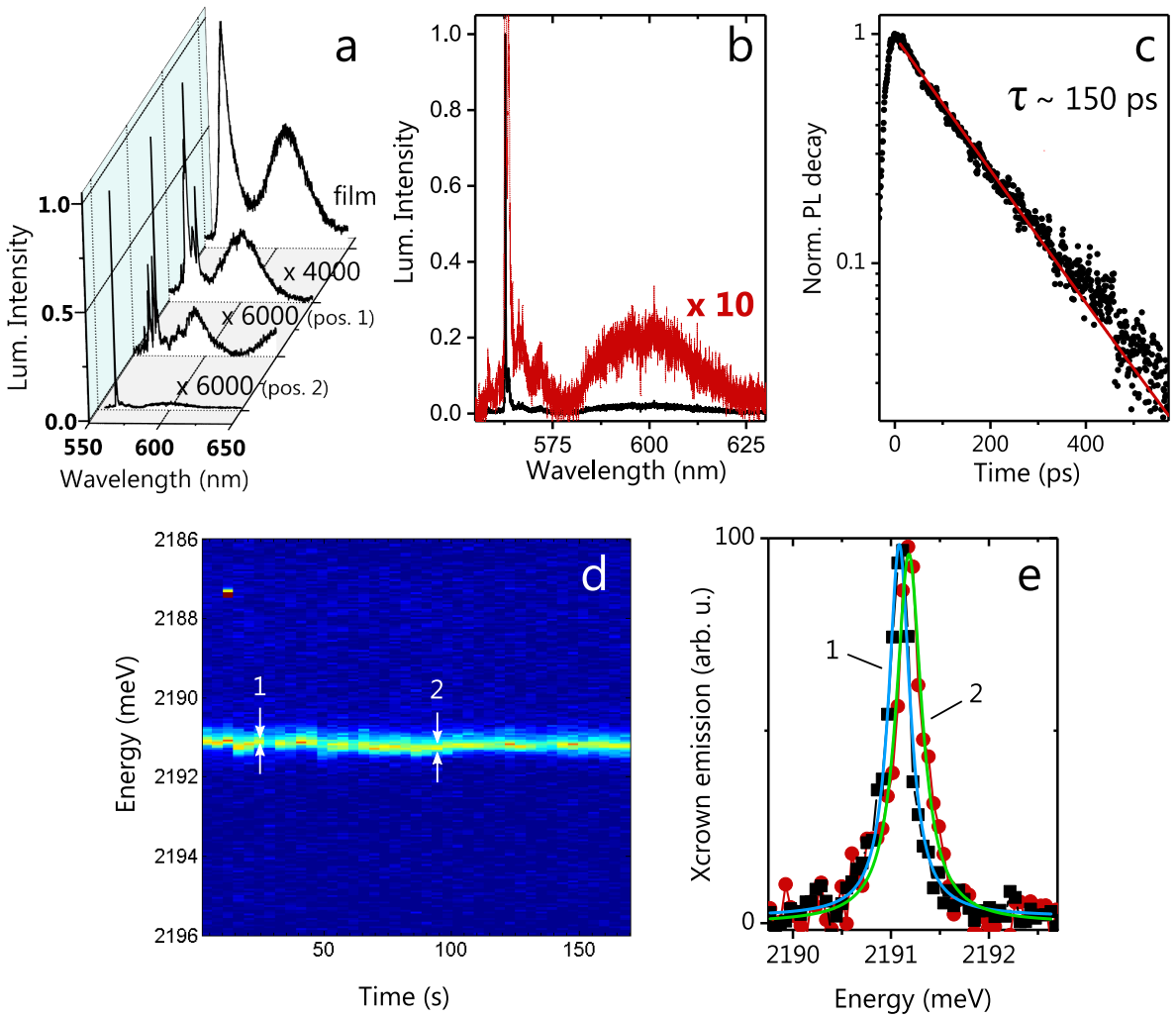

Fig. V.3 *(a) PL spectra recorded for different dilutions of the initial CdSe/*$CdSe_{0.4}CdTe_{0.6}$ *NPLs solution (b) PL spectrum of a single CdSe/*$CdSe_{0.4}CdTe_{0.6}$ *NPL (black). The red trace represents the same spectrum multiplied by ten, to highlight the indirect exciton emission. (c) PL decay of the direct exciton* X_{crown} *from a single NPL and its mono-exponential fit with a time constant of 150 ps. (d) Trace of the* X_{crown} *emission over 170 s. (e) Spectra at the times marked 1 and 2 on the trace. A spectral shift of the emission is observed between the two times, while the shape is the same, characteristic of the spectral diffusion phenomena.*

in single CdSe NPL [16]. By following the PL of X_{crown} over a long period of time (see figures V.3.d and e), we notice that the emission goes through some rigid shifts in its emission energy, characteristic of spectral diffusion. Moreover, the fluctuations in intensity over a long period of time are representative of blinking. These effects are not studied further but both behaviors are characteristic of microscopic phenomena operating at the scale of the single object, as described in Chapter III.

The decay of the X_{crown} luminescence is also measured with the streak camera for different single NPLs, one of these being presented in figure V.3.c. The decay is mono-exponential with a characteristic time between 70 and 190 ps, depending on the NPL, and no long lived contribution could be observed. These lifetimes are similar to the ∼200 ps ones measured in single CdSe NPLs [16]. This observation supports the claim that the X_{crown} emission originates from the direct recombination of the exciton in the crown. The TRPL signal associated with the IX emission could not be observed using the streak camera; this is the first indication of the long-lived nature of the IX state. Let us study more in detail the dynamics of the two emissions in solution and at room temperature, to gain insight into the origin of the bicolor emission.

V.3 Time-resolved photoluminescence measurements

To gain insight into the generation mechanism of the X_{crown} and IX emissions, we measured the TRPL at room temperature of NPLs diluted in hexane. We decide to measure these decays at room temperature, since it is important to understand the different underlying processes at play in the conditions of their possible future applications as emitters in light display. The NPLs are sufficiently diluted to ensure that no stacking occurs while keeping a good signal to noise ratio. To record the decay on the short time scale with the streak camera, the solutions are excited with the Ti:Sapphire laser, tuned at 405 nm. To address longer time-scales (µs range), the picosecond laser diode emitting at 405 nm and set to a frequency of 200 kHz is used. The excitation energy being relatively high compared to the band edge absorption of our NPLs, both the core and the crown are excited in these experiments. In the case of the time-gated TRPL, we were careful to use the appropriate band-pass filters in front of our APD to collect only one of the two emissions.

V.3.1 Dynamics on the short time-scale (10 ps - 2 ns)

Figures V.4.a and b present the results obtained with the streak camera. We first notice that the IX emission is not visible at short delays after the excitation (V.4.a). This was already noticed in the response of the deposited NPLs at low temperature and confirms the long-lived nature of the IX. Indeed, only a relatively low amount of photons are emitted per time unit through the IX channel. The streak camera does not have the required sensibility to detect them, thus the IX peak does not appear inside the 'time resolved' spectra despite its presence in the time-integrated signal.

Concerning the X_{crown}, the decays are recorded for three different values of x: $x = 0.5$ when there is no emission from IX, $x = 0.6$ when the two emissions are similar in intensity, and $x = 0.8$ when it is mainly the IX which is present (see figures V.1.c, d and e). In this time window, for $x = 0.5$ and 0.6, the decays can be fitted with a bi-exponential function with characteristic lifetimes of 40 ps and 325 ps, and 35 ps and 270 ps respectively. We see that the weight of the short lived component increases with x. For the highest amount of Te $x = 0.8$,

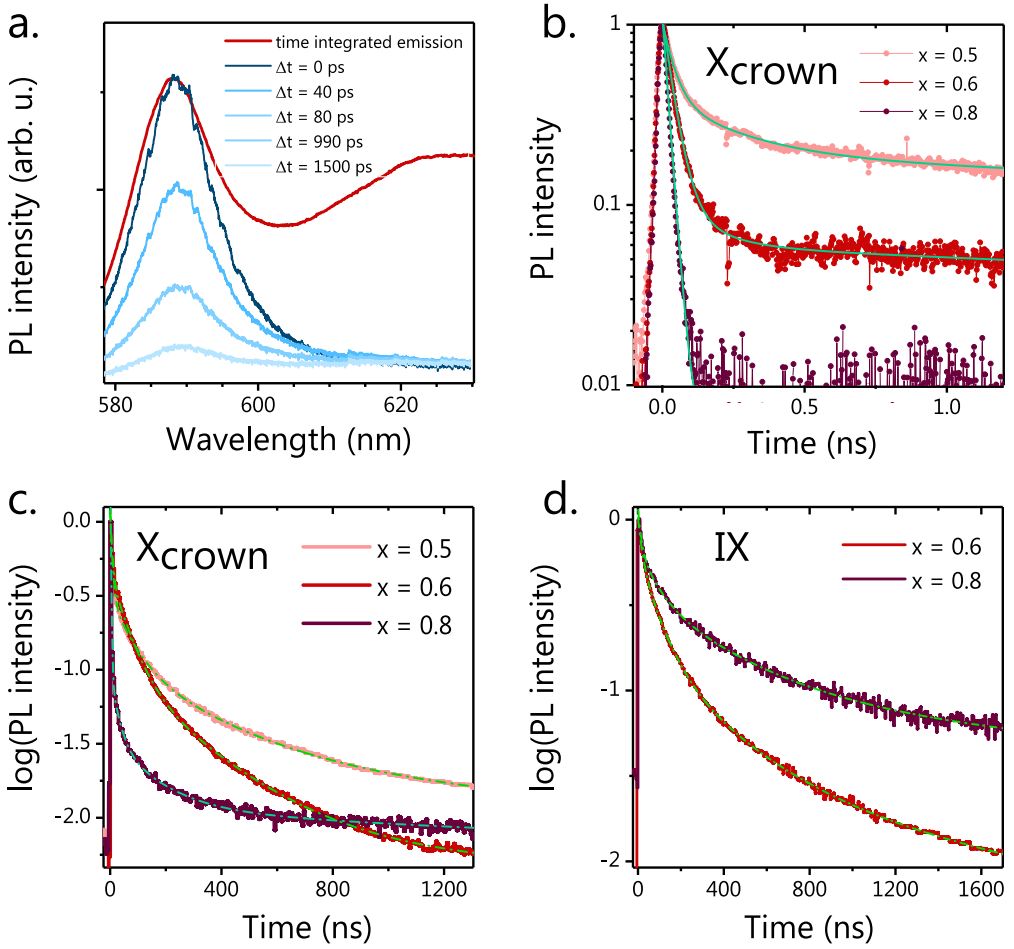

Fig. V.4 *Room temperature TRPL of CdSe/*$CdSe_{1-x}CdTe_x$ *NPLs (hexane solution). (a) In blue, PL spectra at early times after the excitation, obtained with the streak camera, for a solution of CdSe/*$CdSe_{0.4}CdTe_{0.6}$ *NPLs. In red, integrated spectrum obtained with the spectrometer (steady-state luminescence). The absence of the IX emission in the signal recorded with the streak camera, shows that it is a long lived emission. (b) Decays of the* X_{crown} *emission, obtained with the streak camera, for different values of* x *and their fits in green. Decays obtained with the time-gated photon counter of the* X_{crown} *emission (c) and the IX emission (d) for different values of* x *and their multi-exponential fits in green.*

the decay is much faster with a single constant found below the time resolution of the streak camera ($\sim$ 15 ps), showing the ultra-fast relaxation of the crown species.

V.3.2 Dynamics on the long time-scale (5 ns - 1 µs)

In figure V.4.c and d, the decays collected with a time-gated photon counter are shown. We see that in the range 100 ns - 1 µs, the relaxation dynamics of X_{crown} and IX are fairly similar. These decays confirm that the X_{crown} emission becomes faster with the increase of the Te content. However, the increase in Te actually slows down the dynamics of the IX recombination.

Both emissions present multi-exponential decays, which are here fitted with four different components, ranging from $\sim$ 10 ns to $\sim$ 1 µs. For example at $x = 0.6$, a satisfactory fit is obtained with characteristic times (and respective weighting factors) of 6 ns (0.627), 60 ns (0.290), 250 ns (0.079), and 2.0 µs (0.004) for the crown peaks, while the values of 18 ns (0.38), 80 ns (0.44), 350 ns (0.15), and 1.7 µs (0.03) are obtained from the IX decays. These values are similar to the one observed in ref. [133]. Interpreting each one of these constants would be specious, and the same discussion made in Chapter III.2.2 is readily applicable here. These non-exponential decays are the signature of complex processes, such as delayed luminescence [92]. We would like to stress that the alloying of the crown (and possible formation of trop states) is far from being the only mechanism explaining these observations, since the same type of decays were already observed in non-alloyed CdSe/CdTe NPLs (see Chapter III and IV). The study of these different processes were however not the subject of this work.

Despite the lack of a global model to fully comprehend the relaxation processes at play in these NPLs, some useful information can be extracted from these measurements. From $x = 0.6$ to $x = 0.8$, a clear acceleration of the dynamics of X_{crown} is observed. This acceleration is concomitant with a decrease in the intensity of the X_{crown} emission compared to the IX one. These two observations qualitatively lead us to suppose that a non-radiative channel opens when the Te content increases. A likely hypothesis would be that this non-radiative channel corresponds to the transfer of the electron from the crown to the core, leading to the formation of IX. To experimentally prove such an hypothesis would require a thorough dynamical study, as was done for the pure CdSe/CdTe system [25, 27, 94].

V.4 Origin of the bicolor emission

In this last section, we would like to expose a model explaining the evolution of the PL emission with the Te content x. Why is it that for $x \leq 0.5$ or $x \geq 0.9$, only the direct X_{crown} or the indirect IX emission occurs while for x between 0.6 and 0.8 both emissions are present? To answer this question, we follow a purely static 'thermodynamic-like' approach without taking into account any dynamical considerations. To that end, we compare the X_{crown} binding energy to the energy gained during the formation of the IX (the binding energy of the IX, being in the tens of meV range, is neglected in this comparison). The latter can be deduced from the offsets in the alignment of the conduction and valence bands of the CdSe core and the $CdSe_{1-x}CdTe_x$ crown. As one can see in figure V.5, ΔV_c (ΔV_v), the offsets in energy between the conduction (valence) band of the core and the crown, can be calculated from the energies of the absorption peaks of the crown E_{crown} and the core E_{core} and the energy of the

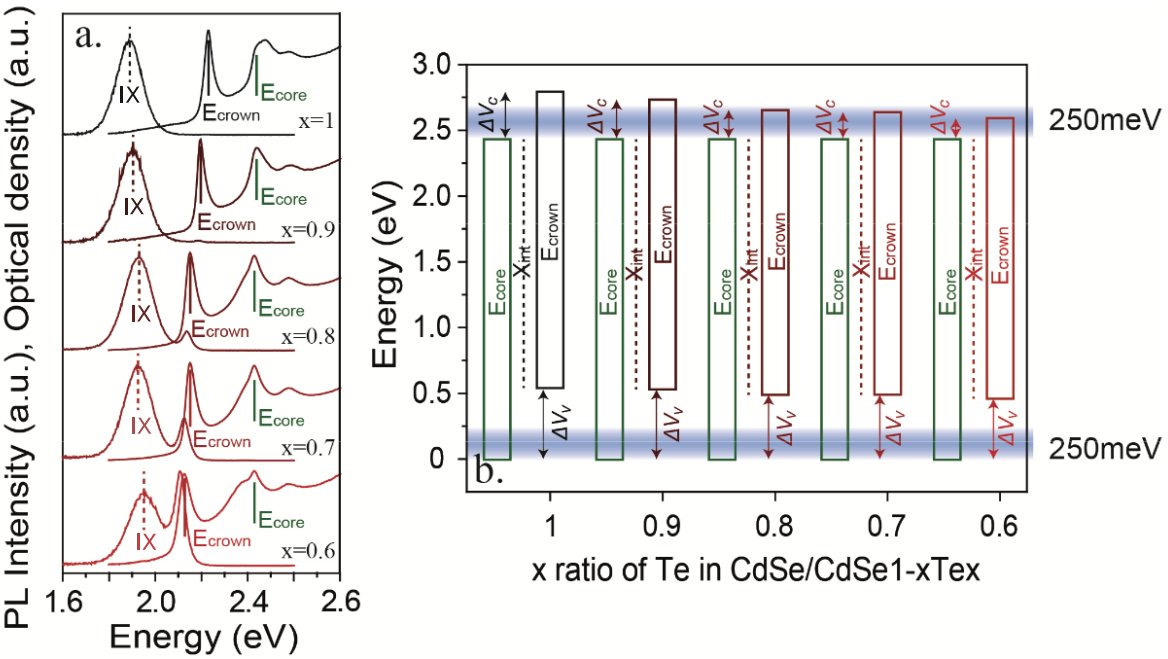

Fig. V.5 *Determination of the band alignment of the CdSe core and the* $CdSe_{1-x}CdTe_x$ *crown from the position of the absorption peaks of the core and the crown and the emission of IX. The 250 meV grey bands on the right diagram represent the binding energy of the direct* X_{crown} *exciton.*

luminescence of the IX emission E_{IX}:

$$\Delta V_c = E_{crown} - E_{IX}, \tag{V.2}$$

$$\Delta V_v = E_{core} - E_{IX}. \tag{V.3}$$

We notice that ΔV_v does not change significantly with x and stays around 0.5 eV. However, ΔV_c sees its value increase from 0.15 eV at $x = 0.6$ to 0.35 eV at $x = 1$. These offsets will drive the transfer of the carriers to either the core or the crown.

Another force will go against this transfer process: the Coulombic interaction between the two carriers represented by the value of the binding energy $E_{binding}$ of the direct excitons X_{crown} or X_{core}. According to different studies, $E_{binding}$ is close to 0.25 eV in NPLs [38, 134], much greater than in nanocrystals due to the dielectric confinement which enhances the Coulombic interactions.

For a direct exciton in the core, we see that $E_{binding} < \Delta V_v$ regardless of the value of x. The hole will be quickly transferred to the crown, hence we never observe the emission related to the recombination of the direct exciton of the core.

For the direct exciton of the crown, the picture is more complex. For values of $x > 0.8$, $E_{binding} < \Delta V_c$ and the formation of the IX is once again energetically favorable, leading to a single emission of the IX. However for $0.6 \leq x \leq 0.8$, $E_{binding}$ is higher than or equal to ΔV_c. In this case, the two processes will compete and the transfer of the electron to the core will be slowed down, leading to the apparition of the X_{crown} emission. This is consistent with the observation made in the previous section: the short decay associated to non-radiative processes leading to the quenching of the X_{crown} PL decreases in amplitude with the lowering of x. We

see here that it is really the interplay between the magnitudes of $E_{binding}$ and ΔV_c that drives the ratio between the two channels of emission.

Conclusion

In this chapter, the optical properties of $CdSe/CdSe_{1-x}CdTe_x$ NPLs were studied. We have shown that the shape of the PL spectra is highly dependent on the value of x. For the first time a bicolor emission in NPLs hetero-structures was observed, when x is between 0.6 and 0.8. This bicolor emission arises from two different relaxation channels: the recombination of the direct exciton of the crown X_{crown} and the recombination of the IX. Then, we showed, through micro-PL experiments, that this bicolor emission corresponds to the intrinsic response of the NPL.

In the third part, we studied the relaxation dynamics of these two emissions. These relaxations are complex, showing multi-exponential behaviors. However two conclusions can be drawn from these measurements. First, IX is a long-lived state, as expected due to its indirect nature. Secondly, increasing x induces a shortening of the dynamics of X_{crown}, which seems to indicate the opening of an additional relaxation channel when x increases. It is likely that this process corresponds to the transfer of the X_{crown} electron to the core. However further studies are needed to confirm this point.

In the last part, we showed that the bicolor emission arises from a competition between two driving forces which are, on the one hand: the band offsets between the core and the crown, on the other: the binding energy of the crown direct exciton. When the amplitudes of these two parameters are similar, the formation of the indirect exciton is not so energetically favorable, leading to the appearance of the X_{crown} emission.

This work more generally shows the potential of the hetero-structure engineering in the colloidal field.

Chapter VI
$CsPbBr_3$ Perovskite Nanoplatelets

In this chapter, we present a preliminary study performed on a different kind of semiconducting 2D shaped nano-structure: cesium lead bromide perovskite nanoplatelets (NPLs). While the work presented here is not as accomplished as the one presented in the previous chapters, it opens the way to the characterization of the electronic fine structure properties of highly confined perovskite systems.

Cesium lead halide crystals have already been studied for about 40 years [135]. However, the interest in these structures has been renewed recently as its hybrid organic-inorganic counterpart showed a stunning evolution of its efficiency as a solar cell, reaching today an efficiency of 25 % [136]. Protesescu *et al.* synthesized, in 2015, the first nanocrystals of $CsPbX_3$ (with X = Cl, Br, I) [29]. These nano-structutres were readily studied by a large number of research groups. They show interesting properties such as a emission quantum yield close to unity [29] (due to their 'defect tolerant' electronic structure [137]), single photon emission at room temperature with high repetition rate working capabilities [13] and non-blinking emission properties [138]. Moreover, their emission properties can be finely tuned over the whole visible range through the control of the halide content. These nanocrystals were also at the center of a large number of fundamental studies, interested in the nature of the exciton and its fine structure [30–33]. From the first synthesis of perovskite nanocrystals, efforts have been made to obtain other shapes than cubes and especially 2D structures [34, 35, 139, 140]. Here, we focus on these 2D objects in order to understand how the strong confinement at play in these structures is reflected in the exciton fundamental properties.

In the first section we will present the general properties of cesium lead halide structures. Then in the second section, we show that transmission electron microscopy (TEM) coupled to absorption and photoluminescence (PL) spectroscopy allow us to structurally characterize these NPLs. Finally, in the last section, we try to tackle the question of the fine structure (dark state position in particular). In this work, single NPLs spectroscopy could not be achieved; this will remain an objective for future investigations. We thus turn to the analysis of the exciton relaxation dynamics in NPLs ensembles prepared as thin solid films.

VI.1 General properties

The general theory exposed in Chapter I used to describe exciton remains relevant for perovskite nano-structures. However, there exists a certain number of differences between II-VI and perovskite materials with respect to their electronic properties (band structure, role of symmetry, *etc*...). In this section, the main differences and their impacts on the exciton are

addressed.

VI.1.1 Structural properties

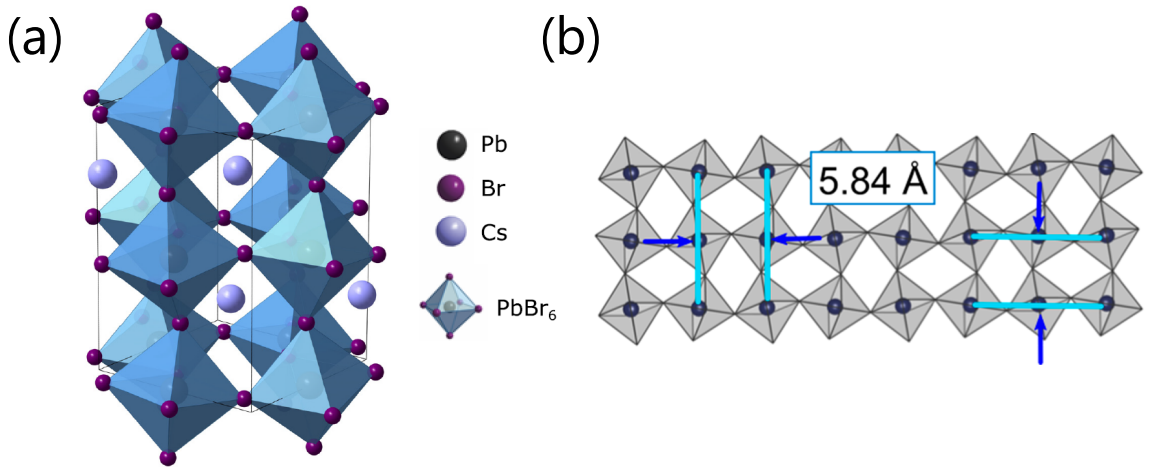

Fig. VI.1 *(a) Sketch of the orthorhombic perovskite unit cell (adapted from ref. [33]). (b) Diagram of the facets of $CsPbBr_3$ NPLs, highlighting the inter-planar distance, a = 0.58 nm (adapted from ref. [36]).*

In the perovskite cubic structure, the unit cell of a $CsPbBr_3$ crystal is composed of a cesium atom in the center of a square lattice, while the lead atoms sit on the corners of this lattice and are surrounded by bromine atoms in an octahedral coordination. A $CsPbBr_3$ bulk crystal undergoes several phase transitions with temperature: above T = 130 °C it has a cubic structure, then between T = 130 °C and 88 °C, it has a tetragonal structure and finally below T = 88 °C, it settles in an orthorhombic structure belonging to the *Pnma* group [141]. Two studies based on X-ray total scattering techniques and high resolution transmission electronic spectroscopy (HRTEM) showed that, in $CsPbBr_3$ nanocrystals [142] and NPLs [36], the crystallographic structure is also orthorhombic at room temperature. It is characterized by a tilting of the $PbBr_6$ octahedra, as can be seen in figure VI.1.a, where the orthorhombic unit cell is presented.

Bertolotti *et al.* showed that the $CsPbBr_3$ NPLs present the {1,0,1} and {0,1,0} orthorhombic planes on their facets which means that they retain a pseudo-cubic faceting, as can be seen in figure VI.1.b [36]. It is thus relevant to define a mono-layer (ML) thickness, a, which corresponds to the thickness of a single octahedral layer (equivalent to the inter-planar distance between two octahedral planes). Hence, it is possible to characterize the NPLs by their numbers, n, of MLs, their thickness, L_z, being equal to na. Using HRTEM, several studies showed that in $CsPbBr_3$ NPLs the inter-planar distance, a, is equal to 0.58 nm [34, 36, 140, 143].

Studied of the $CsPbBr_3$ single nanocrystal emission revealed that two distinct crystalline structures still existed at low temperature: the expected orthorhombic phase described above and the 'more symmetric' tetragonal phase [30, 32]. To the best of our knowledge, no study of the emission of single $CsPbBr_3$ NPLs have been performed yet. Hence, it is unclear if NPLs with a tetragonal phase exist at room temperature and below.

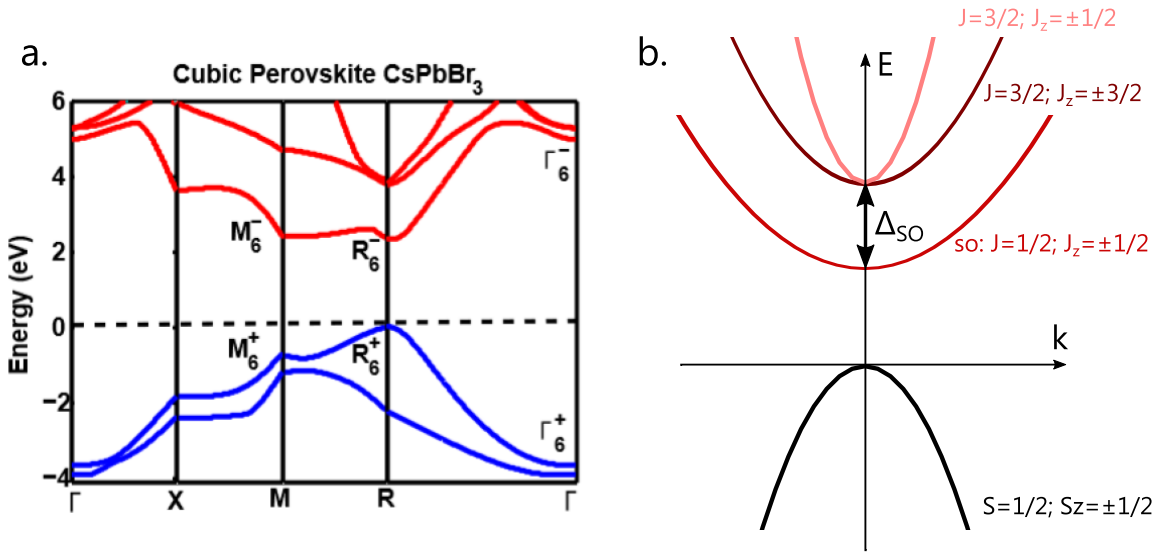

Fig. VI.2 *(a) Energy band structure of bulk cubic $CsPbBr_3$, obtained from a 40-band $\mathbf{k}\cdot\mathbf{p}$ model [143]. (b) Sketch of the band edge in $CsPbBr_3$.*

VI.1.2 Band structure and fine structure

On top of these structural differences, the band structure of lead halide perovskite semiconductor also largely differs from the one of II-VI semiconductors. In the cubic phase, the band gap is found at the R point of the Brillouin zone [144]. Figure VI.2.a shows the band structure in bulk cubic $CsPbBr_3$ calculated by our collaborators from Carthage University, with a 40-band $\mathbf{k}\cdot\mathbf{p}$ model [143]. However, going from a cubic to an orthorhombic lattice leads to a folding of the bands and the band gap ends up at the Γ point of the Brillouin zone in the orthorhombic crystal, similar to what is found in II-VI semiconductors [144, 145].

The major difference between perovskite and conventional II-VI structure is the 'inversion' of the band structure. The valence band is composed of a mixture of the 6s orbitals of the lead and the 4p orbitals of the bromide, but retains a s-symmetry and is thus only doubly degenerate with a total angular momentum $J = 1/2$ [144]. As for the conduction band, it is made of the 6p orbitals of the lead atoms and hence has a six-fold degeneracy. A strong spin-orbit coupling exists in these structures, which leads to a large splitting of the conduction bands (~ 1 eV see figure VI.2.a and ref. [32]). At the bottom, the split-off band is found with a total angular momentum $J = 1/2$, while the two heavy and light electrons bands are found at higher energies with a total angular momentum $J = 3/2$ [144].

The band edge exciton in these perovskite structures is thus composed of a hole with $J_h = 1/2$ and an electron with $J_e = 1/2$. The resulting excitons can be decomposed into two subgroups: a singlet dark state with $J_{exc} = J_h - J_e = 0$ and a triplet of bright states with $J_{exc} = J_h + J_e = 1$. Different interactions will split the bright and dark states. If only exchange interaction and crystal field effects are taken into account the dark state is expected to lie below the bright ones [146]. However, according to some studies, a Rashba effect might possibly be at play and could reverse this ordering and leave the bright states as the ground state of the electronic fine structure (EFS) [33, 147]. Rashba effect occurs in structures with large spin-orbit coupling and an inversion asymmetry [148], while strong spin-orbit coupling has been demonstrated and quantified in purely inorganic nanocrystals, the origin of the inversion asymmetry is still unclear. Moreover, in $FAPbBr_3$ (FA = formamidinium), which

has a similar structure than $CsPbBr_3$, but where the metallic cesium atom is replaced by the organic formamidinium molecule, a recent study demonstrated that the EFS ground state was the singlet dark excitonic state [82]. The question about the ordering of bright and dark states in the cesium counterpart remains debated in the literature [146, 147].

If we now focus on the structure of the bright states, in the case of a cubic lattice the three levels remain degenerate. However, for tetragonal and orthorhombic lattices, the crystal field and spin orbit interaction lift the degeneracy of the $J = 1$ states [32, 146]. In the case of a tetragonal lattice, it results into one linearly polarized state (along the uniaxial axis) positioned below two degenerate circularly polarized states [30, 149]. For an orthorhombic lattice, the degeneracy is completely lifted and the EFS is composed of three states, usually referred to as $|X\rangle$, $|Y\rangle$, $|Z\rangle$ coupled to linearly polarized light [30]. The bright levels of the EFS have been experimentally observed in nanocrystals of $CsPbBr_3$ and splitting in the order of ~ 1 meV are found between these states [30,32,40,82]. However, it has not been yet revealed in NPLs and the following study has originally been undertaken with this aim. In particular, we expect the different splittings in the EFS to become larger, due to the enhancement of the exchange interaction in systems characterized by a strong transverse confinement.

VI.2 Structural Characterization

Before any investigation about the fundamental properties of the exciton in $CsPbBr_3$ NPLs can be carried out, a precise structural characterization of the objects under study is required. Here, we show that similar syntheses, differing only by the add of HBr, lead to different objects: nanosticks (NSTs), characterized by an elongated length and reduced width and thickness, and large square-shape NPLs. A study of the absorption spectra of these objects coupled to TEM imaging allows us to precisely characterize them.

VI.2.1 Nanosticks

a) Synthesis

Both NSTs and NPLs were synthesized by our colleague Emmanuel Lhuillier at the laboratory (INSP). The synthesis follows the protocol described in Akkerman *et al.* [34], the only difference being the multiplication by 8 of the different precursors and solvents to increase the yield of the reaction and the monodispersity of the synthesized objects. At room temperature, a solution, where the lead and halide precursor ($PbBr_2$) is diluted, is added to a mixture composed of the Cs precursor (Cs oleate) and the aliphatic chains (oleic acid and oleylamine) as the future ligands stabilizing the NPLs. After 10 s of stirring, acetone is added to the mixture leading to the nucleation of the NPLs.

Figure VI.3.a and VI.3.b show TEM pictures of the objects obtained after synthesis, each picture corresponding to two different batches. The right panel of figure VI.3.a shows a HRTEM image of NSTs and allows us to measure the thickness associated to an octahedral layer, $a = 0.58$ nm, consistent with the previously reported values in the literature [34,36,140]. In figure VI.3.b, the thickness and width of the NSTs can be measured independently, as two arrangements with respect to the substrate are observed. In the lower part of the picture, the NSTs are arranged parallel to the surface and appear in a lower shade of grey, while in the upper part of the image, the NSTs appear darker since they are standing perpendicular to the substrate.

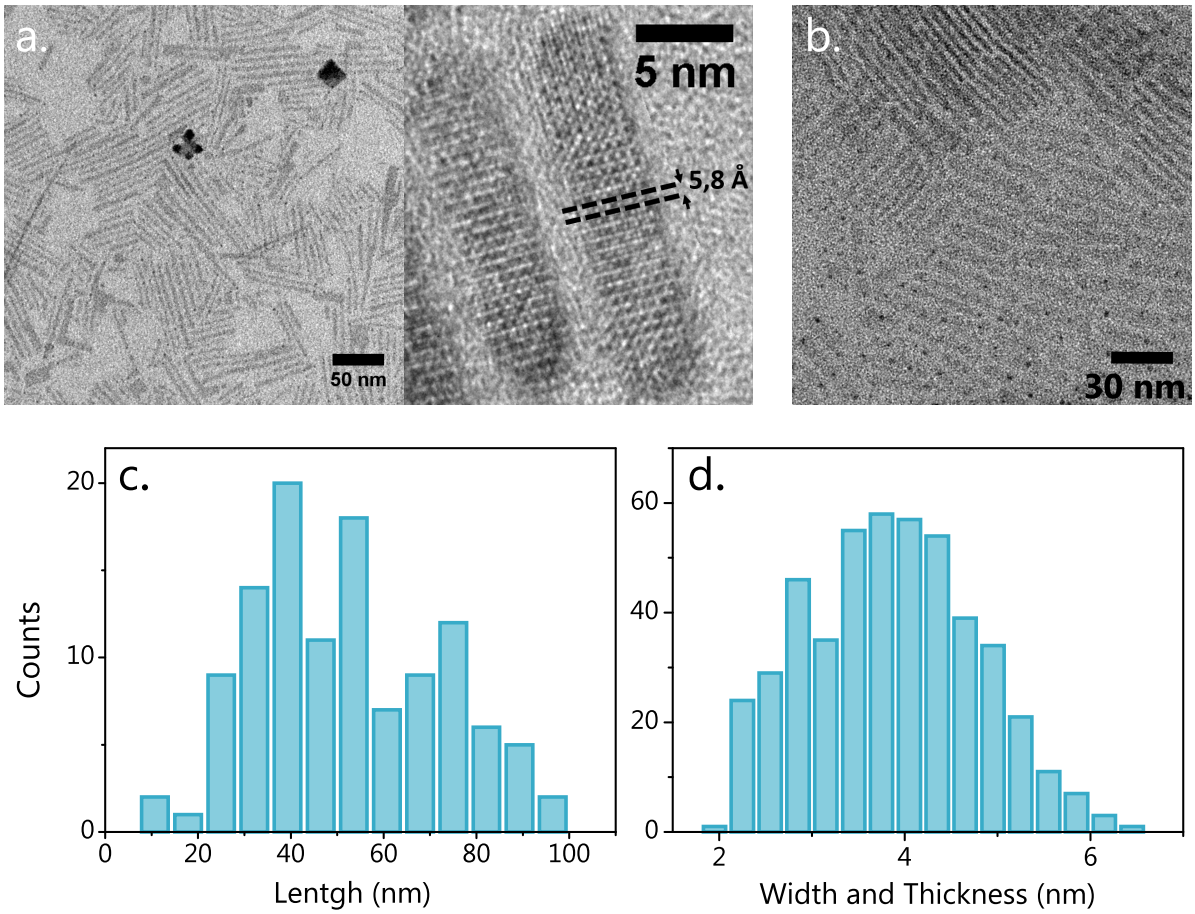

Fig. VI.3 *(a) TEM picture of elongated NSTs obtained from the synthesis described in the text (left) and a HRTEM picture of the same NSTs, highlighting the 0.58 nm thickness, a, of an octahedral layer (right). (b) TEM picture of NSTs obtained from another batch, where the two arrangements of the NSTs with respect to the substrate is clearly visible. Histograms of the distribution of lengths (c), widths and thicknesses (d) of the NSTs shown in (a).*

In the following, we will focus on the optical properties of the nanocrystals presented in figure VI.3.a. The histogram presented in figure VI.3.c shows the length distribution of these NSTs: it is fairly broad (ranging from 10 to 90 nm) and has a mean value at 40 nm. For these NSTs, it is impossible to differentiate width and thickness from the TEM images, as the difference between 'flat' lying and 'edge' lying NSTs can not be readily made. For this reason figure VI.3.d presents the distribution of the two as a whole. They are found between 2 nm and 6 nm. The Bohr radius of the exciton in bulk $CsPbBr_3$ is estimated to be equal to 3.2 nm, from the 40-band $\mathbf{k}\cdot\mathbf{p}$ model. We can thus expect confinement in both the width and thickness directions in these NSTs.

b) Optical characterization

Figure VI.4.a presents the absorption spectrum, at room temperature (RT) and at 12 K, of a film of 'freshly' NSTs (drop-casting of the NSTs solution on a glass slide and absorption measurements performed a few hours after the synthesis), while figure VI.4.c presents the

absorption of a similar 'aged' film, recorded four months after the initial deposition (the film was kept in the dark, at room temperature and in air). Let us note first, that both spectra evolve similarly as the temperature is lowered: (i) the peaks become much narrower, due to the reduced exciton-phonon coupling at low temperature (which reveals several transitions, invisible at room temperature) and, (ii) both spectra red-shift when the temperature is lowered. This red-shift, as opposed to what is observed in II-VI semiconductors, is characteristic of perovskite structures [32]. The upcoming analysis is based on the absorption spectra taken at low temperature, where the different excitonic transitions are well-resolved in energy.

Except for the similar evolution with the temperature, we see that the two absorption spectra are drastically different, showing that the 'fresh' film of NSTs evolved in time to form different objects in the 'aged' film . In the 'fresh' film, several peaks are grouped in energy around 2.8 eV and other less pronounced peaks are present at higher energy. In the 'aged' film, however, the peaks are more spread out and the characteristic transition energies range from 2.32 eV to 2.7 eV. Let us first focus on the analysis of the spectrum of the 'aged' film (figure VI.4.c), considering that it is somehow easier to explain and, as we will see, its study will help to analyze the spectrum of the 'fresh' film of NSTs.

'Aged' film of NSTs

The large number of absorption peaks in the absorption spectrum of figure VI.4.c shows that objects with a large variety of size are present in the 'aged' film. The first relevant point is that the lower transition, at 2.32 eV, fits nicely with the one of the bulk exciton. Indeed on the basis of the 40 bands $\mathbf{k} \cdot \mathbf{p}$ method, our collaborators estimated the energy of the band-gap, E_{gap}, of bulk $CsPbBr_3$ at 2.37 eV and the binding energy of the bulk exciton, $E_{binding}$, at 32 meV resulting into an exciton transition in the bulk at $E_{bulk} = 2.34$ eV. We thus attribute the lower peak in energy to the excitonic transition of large crystals of $CsPbBr_3$, in which there is no manifestation of the electronic confinement. This peak shows that, despite the aging of the objects present in the film, we are still in presence of $CsPbBr_3$ crystals. From the bulk transition at 2.32 eV, the peaks at higher energy have to be related to excitonic transitions in objects where confinement plays a role.

As described in Chapter I, the exciton energy in a bulk semiconductor is equal to the band-gap energy, E_{gap}, minus the binding energy of this exciton, $E_{binding}$, which is related to the Coulombic attraction between the two charge carriers. In a confined structure, an energy related to the confinement of the electron and the hole has to be added to the overall exciton energy. In the effective mass approximation and for an infinite quantum well with an infinite potential along the confined direction, the energy related to the confinement takes the form $E^{1s}_{e/h} = \frac{\hbar^2\pi^2}{2m^*_{e/h}L_z^2}$ for the first excited carriers (1s) and where $m^*_{e/h}$ are the effective masses of the electron and the hole and L_z is the dimension of the object in the confined direction.

On top of these terms, related to electronic confinement, terms related to the dielectric confinement (due to the large mismatch in dielectric constant between the colloidal semiconductor and its surrounding ligands and outside medium) have also to be taken into account when computing the exciton energy. As discussed in Chapter I, two contributions related to this dielectric confinement are competing: self-energy terms, which will increase the exciton energy and an increase in the binding-energy of the exciton, decreasing the overall exciton energy [44]. Along with these dielectric considerations, the binding energy of the exciton also increases when the thickness of the well is reduced and in a very narrow well it theoretically tends toward four times the binding energy of the bulk exciton [41]. In the last part of this

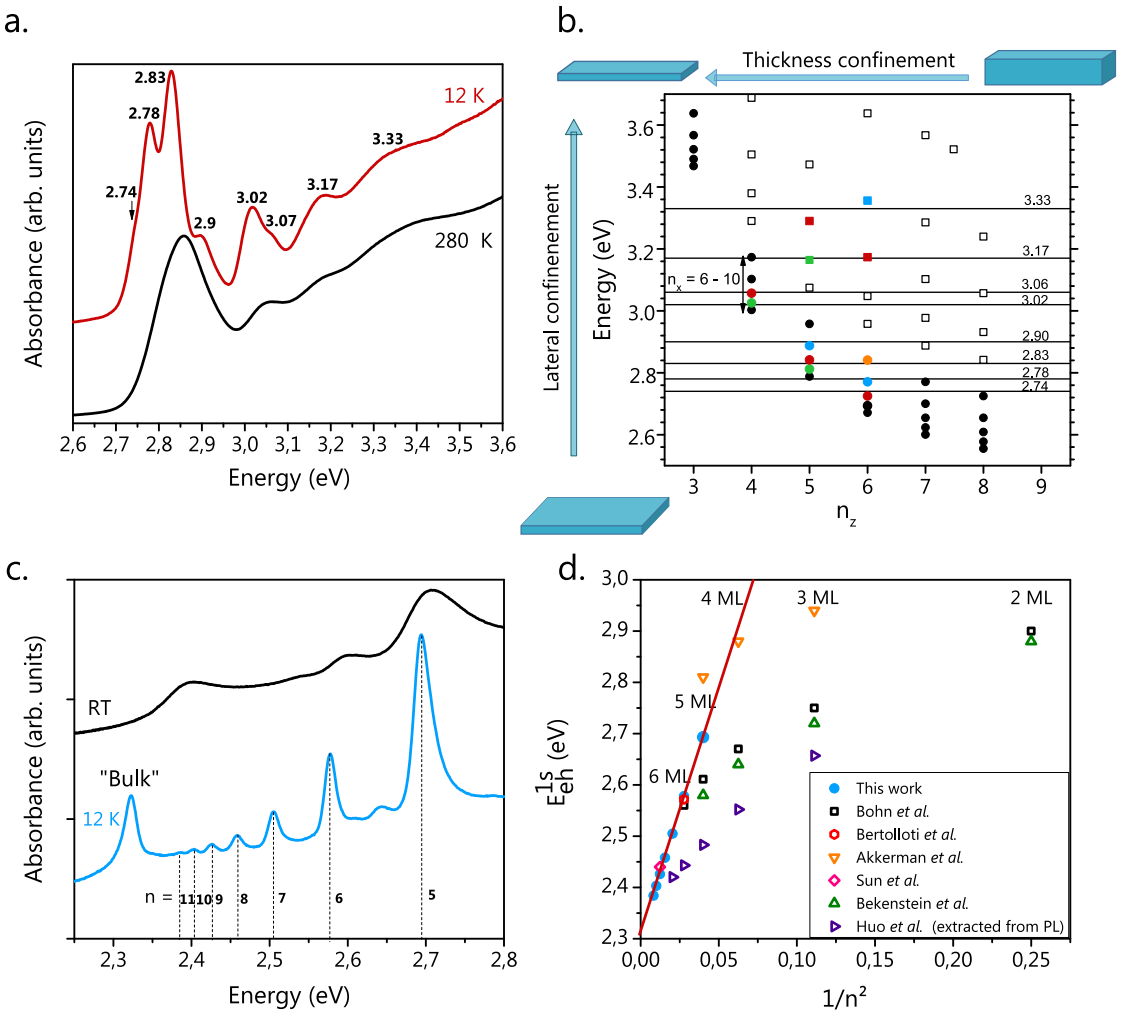

Fig. VI.4 *(a) Absorption spectrum of a 'fresh' film of NSTs at room temperature (RT) and 12 K. (b) First (full circle) and second (open square) theoretical excitonic transitions, calculated with equation VI.3, as a function of n_z. For each value of n_z, the transitions are calculated for n_x ranging between 6 and 10. The black horizontal lines correspond to the energy of the experimental transitions. The colorful symbols correspond to theoretical transitions close to the experimental ones. (c) Absorption spectrum of an 'aged' film of NSTs (film kept in the dark for four months in air, at room temperature), at room temperature and 12 K. (d) Evolution of the experimental transition energy of the 1s exciton as a function of $1/n^2$. The data presented in (c) are represented in filled blue circles. The other remaining data are extracted from different works in the literature. The following data are obtained from absorption spectra at room temperature: (black open square) Bohn et al. [150], (red open circle) Bertolotti et al. [36], (orange open triangle) Akkerman et al. [34], (pink open square) Sun et al. [139], (green open triangle) Bekenstein et al. [35]. Finally, the purple open triangle is obtained from PL measurements at 5 K from the work of Huo et al. [151].*

section, we will show with the help of numerical simulations that these different contributions (increase in $E_{binding}$ with reduced thicknesses and dielectric terms) do not absolutely compensate (even if partially cancelling each other) in NPLs and NSTs with a number of MLs larger than 4. However, their algebraic sum is nearly constant with the NPL thickness, consequently they will contribute to the transitions energies adjustment under the form of a systematic shift in the linear analysis.

As already mentioned, the presence of the excitonic bulk transition in the absorption spectra shows that the sample is still composed of $CsPbBr_3$. We can thus express L_z as $L_z = na$, where a is the thickness of a single octahedral ML and n the number of MLs. The ground state exciton energy, in an 'entity' where we assume that only one dimension is confined, is then:

$$E_{e,h}^{1s} = E_{gap} - E_{binding} + E_e^{1s} + E_h^{1s} = E_{gap} - E_{binding} + \frac{\hbar^2\pi^2}{2\mu(na)^2}, \tag{VI.1}$$

where $\mu = m_e^{*-1} + m_h^{*-1}$ is the reduced mass of the exciton.

We can attribute to the different peaks appearing in the absorption an integer n, corresponding to the number of MLs, while equation VI.1 is used to verify that the evolution of $E_{e,h}^{1s}$ as a function of $1/n^2$ is linear. The highest transition at 2.69 eV is attributed to $n = 5$ and from then n is incremented, up to $n = 11$ at 2.39 eV. The evolution of the transition energies is plotted as a function of $1/n^2$ in figure VI.4.d. Using equation VI.1, a very satisfying linear fit is obtained. From the fit, we find $E_{gap} - E_{binding} = 2.31$ eV, consistent with the bulk transition at 2.32 eV. The slope of the fit provides $E_0 = \frac{\hbar^2\pi^2}{2\mu a^2} = 9.56$ eV. The 40 bands $\mathbf{k}\cdot\mathbf{p}$ model gives for the exciton reduced mass $\mu = 0.117\ m_0$, where m_0 is the free electron mass [143]. With such a value for μ, the ML thickness $a = 0.58$ nm is also retrieved, consistent with both the HRTEM image of figure VI.3.a and the literature [34, 36]. Using the value experimentally determined in ref. [152] of $\mu = 0.126\ m_0$, we find $a = 0.56$ nm, also in good agreement with the experimental value ($a = 0.58$ nm).

This analysis shows that thicker objects than the initial NSTs presented in figure VI.3.a are present in the 'aged' film. The aggregation of NPLs in films has been observed previously [153, 154]. Dang *et al.* specifically studied this phenomenon in solution and in films. After 2 months, the authors showed that an initial solution of NPLs of 5 MLs evolved into nanoplates and nanotiles with thickness equal to the width of the initial NPLs and lateral dimensions of several hundreds of nm [154]. A similar evolution was monitored through the evolution of PL emission in spin-coated films. A continuous red-shift of the emission is observed, consistent with the formation of thicker objects. According to the authors, the desorption of ligands at the surface of the NPLs leads to the merging of neighbouring objects resulting at the end in the formation of larger nanotiles. A similar process seems to be at play in the film of NSTs studied here (explaining the apparition of excitonic transitions related to a reduced confinement).

Let us now compare the energies of the excitonic transitions with those reported in the literature, keeping in mind that most of the values reported in figure VI.4.d are extracted from absorption spectra of NPLs at room temperature (except for the data of Huo *et al.* which are taken from emission data at 5 K [151]). We note that for 9 MLs and 6 MLs cases, there is an excellent agreement between the transition reported here and the literature [36, 139, 150]. At 5 MLs, the value of the transition falls in the set of reported values [34, 35, 150]. However, there is a large disagreement with the data of Huo *et al.* [151]. The energy of the transitions extracted from the PL spectra at 5 K is greatly different from the one we report here, as well as those reported in the literature. Finally, it is clear that for smaller n, the experimental tran-

sitions reported in the literature clearly deviate from the linear evolution given by equation VI.1, which would be the indication that the dielectric effects and the increase in the exciton binding energy do not compensate anymore in thinner objects. Sapori *et al.* theoretically studied the evolution of the dielectric constant in $CsPbBr_3$ NPLs and showed that dielectric effects were starting to have an impact for NPLs with less than 4 MLs [155], consistent with the observations made here.

'Fresh' film of NSTs

If we now go back to the spectrum of the 'fresh' film of NSTs, it is clear that the simple model of 1D confinement used above cannot explain the large variety of peaks grouped in energy. Moreover, the TEM picture indicates that the width and thickness are similar and close to the Bohr radius of the exciton $a_0 = 3.2$ nm. Hence, the confinement of the exciton in both x (width) and z (thickness) directions should be considered. We complete the model described above by adding the confinement term in the x-direction of the NSTs and obtain:

$$E_{e,h}^{m_x,m_z} = E_{gap} - E_{binding} + m_x^2 \frac{\hbar^2\pi^2}{2\mu L_x^2} + m_z^2 \frac{\hbar^2\pi^2}{2\mu L_z^2}, \tag{VI.2}$$

where m_x and m_z are the quantum numbers in the respective confining dimensions and L_x and L_z, the width and thickness of these NSTs.

The work of Bertolotti *et al.* showed that the different facets of a NPL present an arrangement similar to the one presented in figure VI.1.b [36]. It is thus possible to express $L_x = n_x a$ and $L_z = n_z a$, where the pair (n_x, n_z) characterizes the number of MLs along the width and thickness of a NST. We can then write equation VI.2 as:

$$E_{n_x,n_z}^{m_x,m_z} = E_{gap} - E_{binding} + m_x^2 \frac{E_0}{n_x^2} + m_z^2 \frac{E_0}{n_z^2}, \tag{VI.3}$$

where $E_0 = \frac{\hbar^2\pi^2}{2\mu a^2}$.

Fixing $E_{gap} - E_{binding}$ and E_0 to the values found from the fit of figure VI.4.d, we compute the energy of the transitions for different (n_x, n_z) pairs, with n_x ranging between 6 and 10 and n_z between 3 and 9. Figure VI.4.b shows as a function of n_z, the energy of these transitions (for each n_z the highest energy point corresponds to $n_x = 6$ down to $n_x = 10$ for the lowest energy point) and the filled circles correspond to the first transition ($m_x = 1$ and $m_z = 1$), while the open squares represent the second transition ($m_x = 2$ and $m_z = 1$).

Comparing these theoretical transitions with the peaks observed in the absorption spectrum, we can attribute each experimental peak to a (n_x, n_z) pair. The experimental transitions at 2.74 eV, 2.78 eV, 2.83 eV and 2.90 eV match well the theoretical values $E_{6,8}^{1,1} = 2.73$ eV, $E_{6,7}^{1,1} = 2.77$ eV, $E_{5,9}^{1,1} = 2.81$ eV, $E_{5,8}^{1,1} = 2.84$ eV and $E_{5,7}^{1,1} = 2.89$ eV. Moreover the large peaks at 3.17 eV and 3.33 eV can be rationalized by the second excitonic transition ($n_x = 2$) of these transitions at $E_{5,9}^{1,2} = 3.16$ eV, $E_{6,8}^{1,2} = 3.17$ eV, $E_{6,7}^{1,2} = 3.36$ eV and $E_{5,8}^{1,2} = 3.29$ eV. The transition at 2.90 eV could also be attributed to the transition $E_{6,6}^{1,1} = 2.84$ eV, however the second excitonic transition for these NSTs at $E_{6,6}^{1,2} = 3.64$ eV is too high to explain the broad line at 3.33 eV. There also exist smaller NSTs in the film with 4 MLs, since the experimental transitions at 3.02 eV and 3.07 eV can be attributed to the predicted transitions $E_{4,9}^{1,1} = 3.03$ eV and $E_{4,8}^{1,1} = 3.06$ eV.

The absorption spectrum can thus be rationalized with a reasonable numbers of (n_x, n_z) pairs: (8-9, 4), (7-9, 5) and (7-8, 6). These attributions are also consistent with the histogram

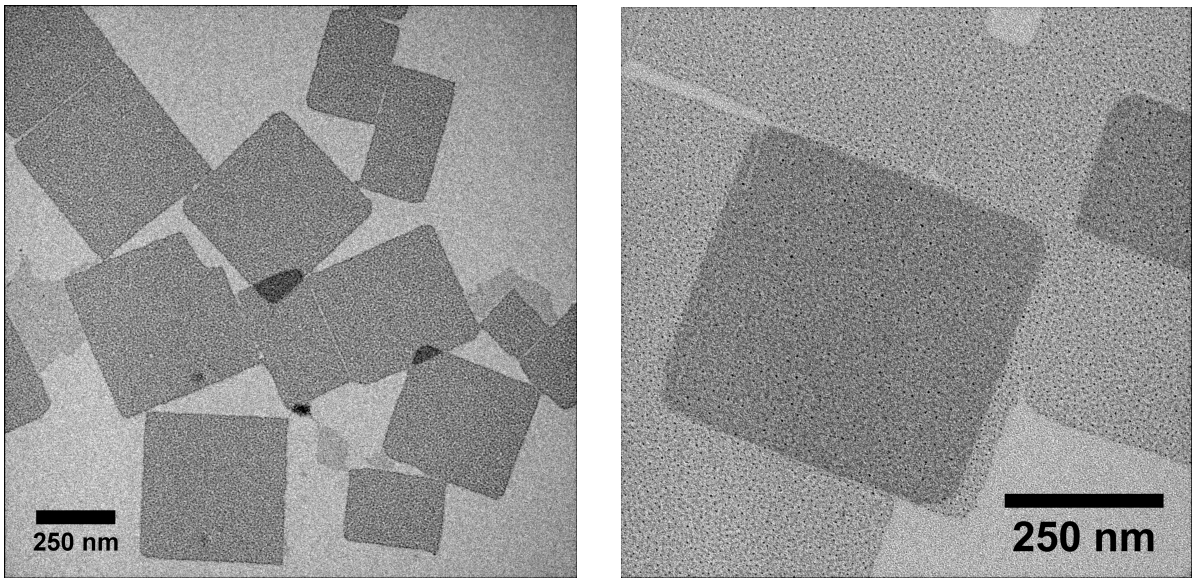

Fig. VI.5 *TEM pictures of large square NPLs, obtained from the synthesis described in the text completed with the addition of 240* µL *of HBr.*

of figure VI.3.d, since they lead to a width, $L_x = n_x a$, between 3.48 and 5.22 nm and a thickness, $L_z = n_z a$, between 2.32 and 3.48 nm. Despite the good agreement between the theoretical and experimental values, it is important to keep in mind that these attributions are not completely unambiguous as the different energy levels are really close and that for thin NSTs ($n = 4$), the theoretical values might be overestimated due to the different contributions neglected in equation VI.2. The great disparity in thickness and width renders the study of the fundamental excitonic properties rather difficult in NSTs. However, a slight modification of the synthesis allows one to obtain objects which are defined in a much better manner: large size NPLs.

VI.2.2 Perovskite NPLs

Another type of objects can be obtained by slightly modifying the synthesis presented above. Indeed, adding 240 µL of HBr to the precursors mixture, the synthesis leads to the formation of square shape NPLs (see figure VI.5), as large as $\sim$ 500 nm along each direction. The presence of HBr also leads to the formation of a population of thinner 4 MLs NPLs. According to ref. [34], by changing the acidity of the solution, the addition of HBr helps to protonate the oleylamine ligands which can then compete with the Cs^+ ions on the surface of the NPLs. This competition slows down the growing process leading to thinner NPLs. However, it remains unclear why the lateral shape of the NPLs (sticks versus squares) is so much affected by the addition of the hydrobromic acid.

Figure VI.6.a and b show the absorption and emission spectra for two different films of NPLs coming from two different batches. We can attribute the peaks at 2.84 eV (figure VI.6.a) and 2.90 eV (figure VI.6.b) to the transition of 4 MLs NPLs from the work of ref. [34]. In both spectra, this transition dominates, while transitions associated with 5 MLs and 6 MLs NPLs are also present in the absorption spectrum of figure VI.6.a.

If we now turn to the PL spectra, more peaks can be observed showing that a larger variety of thicknesses is also present in the film. The PL measurements being much more selective in

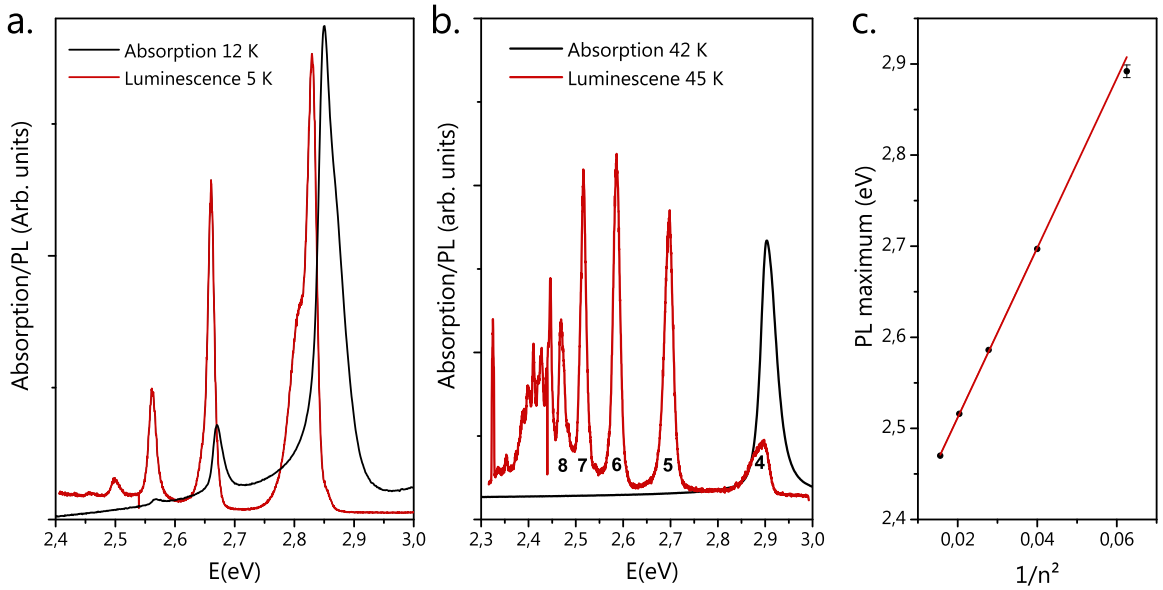

Fig. VI.6 *Absorption (black) and PL (red) spectra of two different NPLs films measured at ∼ 10 K (a) and ∼ 45 K (b). (c) Evolution of the PL emission maximum with $1/n^2$ and its linear fit. The error bars for $n > 4$ are smaller than the size of the symbols.*

real space, even if the 4 MLs NPLs are the majority, it is possible to find spots from which thicker NPLs'responses are recorded. In figure VI.6.b, we can attribute peaks to the emission of NPLs with $n = 4$ to 8. Figure VI.6.c shows the evolution of the energies of these transitions as a function of $1/n^2$. This evolution is clearly linear, showing that the model of a confinement along the z-direction only is appropriate, consistent with the large lateral dimensions of these NPLs. We thus use equation VI.1 to fit this evolution, leaving out the point found for 4 MLs NPLs since for such small thicknesses the different corrections (dielectric confinement and increase in the binding energies) cannot be neglected anymore (see following paragraph). The fit gives $E_{gap} - E_{binding} = 2.33$ eV and $a = 0.59$ nm, with $\mu = 0.117\ m_0$ ($\mu = 0.126\ m_0$ provides a close value $a = 0.57$ nm), in agreement with the results of the previous section.

NPLs are therefore better characterized than NSTs, which makes them easier to study on a fundamental level. Moreover, despite the existence of NPLs with different thicknesses in the same film, they can be addressed separately due to the large difference in energies between each transition.

VI.2.3 Corrections to the exciton transition energy

We would like to conclude this section by justifying the simple model used to determine the energy of the exciton transitions. Indeed, both the increase in the binding energy of the exciton with the reduction of the thickness of the NPLs and the dielectric effects have been neglected.

The energy of the exciton transition in these NPLs have been numerically estimated using a variational method presented in Appendix D, taking into account the effects of the dielectric confinement. The exciton energy can be decomposed in two terms: (i) the energy of an uncorrelated electron-hole pair in an infinite well of thickness L_z given by $E_0 = E_{gap} + \frac{\hbar^2\pi^2}{2\mu L_z^2}$

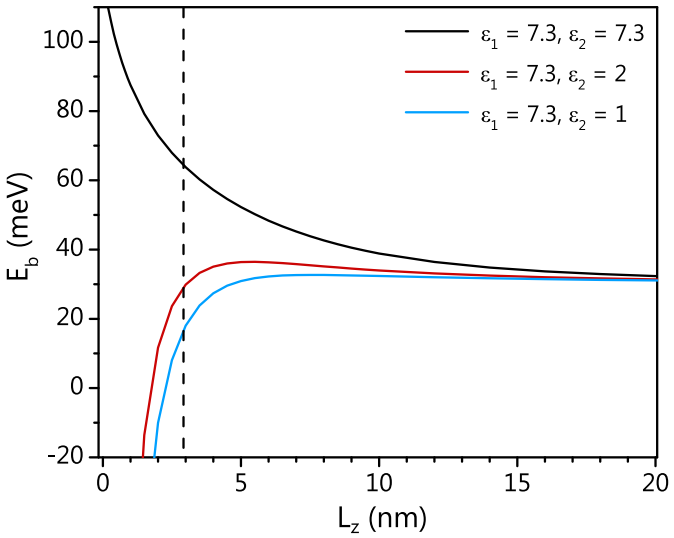

Fig. VI.7 *Evolution of E_b, comprising the binding energy of the exciton as well as the self energy terms, with the NPL thickness L_z for different dielectric environments characterized by ϵ_2. This evolution is obtained from numerical simulations using the variational method and explained in Appendix D.*

and (ii) the correction to this energy, written E_b, which we will define here as comprising the binding energy of the exciton (attractive Coulomb interaction) and the self-energy terms related to the dielectric mismatch between the dielectric constant of the NPL, ϵ_1, and the one of its surrounding environment, ϵ_2. The energy of the first excitonic state can then be written $E_{1s} = E_{gap} + \frac{\hbar^2\pi^2}{2\mu L_z^2} - E_b$.

Figure VI.7 shows the evolution of this correction term E_b as a function of the NPL thickness, L_z, and for different dielectric environments, ϵ_2. When there is no dielectric mismatch between the NPL and its environment ($\epsilon_1 = \epsilon_2$), E_b increases consistently with the enhancement of the binding energy of exciton in a quantum well when the thickness of the NPL decreases. In this case, E_b reaches the value 4 E_b^{bulk} as predicted theoretically for the pure 2D case ($L_z = 0$) [41]. However, when the dielectric mismatch is taken into account, E_b remains almost constant when L_z is decreased ($E_b = 33 \pm 3$ meV), before decreasing sharply when $L_z < 3$ nm. The vertical dashed line corresponds to a thickness of 5 MLs. For a dielectric environment of $\epsilon_2 = 2$, typical of ligands, neglecting the variation of E_b for NPLs with 5 MLs or more is thus justified.

VI.3 Excitonic fine structure: a preliminary study

The large electronic confinement added to the dielectric confinement is expected to lead to large exchange interaction terms in NPLs, compared to nanocrystals, meaning that the inter-state splitting in the electronic fine structure (EFS) could become important. The following work was thus undertaken with the aim of measuring the splitting between the different bright states and mainly between the dark and bright states using 'conventional' models. The study presented in this section is the beginning of these investigations. We first present our attempt

to use micro-photoluminescence to observe single NSTs emission, then we present a preliminary study of the relaxation dynamics of large NPLs.

VI.3.1 Attempt of single objects spectroscopy

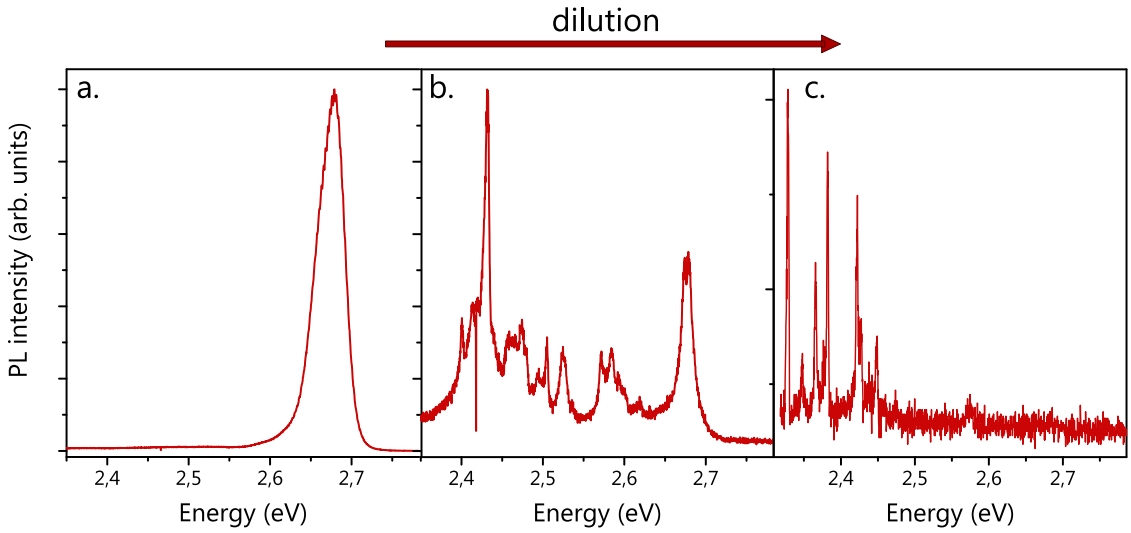

Fig. VI.8 *Evolution of the PL emission of a film of NSTs obtained by drop-casing the initial solution diluted: 10 (left), 800 (middle) and 2000 (right) times.*

As already highlighted in Chapter III, single object microscopy is a powerful tool to study fundamental excitonic properties. For perovskite structures, this technique was previously used to reveal the EFS of $CsPbBr_3$ [30,32,33] or to measure, with the help of a magnetic field, the dark state-bright states splitting in hybrid organic-inorganic $FAPbBr_3$ nanocrystals [82].

In order to obtain the response of single objects, we gradually dilute a solution of NSTs, characterized by an emission initially centered at 2.69 eV. Figure VI.8 shows the evolution of the emission of films as the dilution of the solution is increased from 10, to 800 and up to 2000 times. With a low factor of dilution of 10 (left of figure VI.8), the emission at 2.69 eV is still large and characteristic of a dense film. With a dilution factor of 800, the peak at 2.69 eV gets clearly narrower, showing that the NSTs' density is reduced. However, sharp peaks at lower energy (ranging from 2.6 eV to 2.4 eV) appear. Finally, when the dilution is increased up to 2000 times, the peak at 2.69 eV completely disappears and the emission is only characterized by sharp lines, between 2.3 and 2.5 eV. These lines are likely characteristic of much thicker single objects emission. Several attempts to obtain the response of single NSTs and NPLs were done, systematically leading to the same results: the initial peak characteristic of highly confined objects could not be narrowed down more than what is presented in figure VI.8, and increasing the dilution from there only led to its 'disappearance' and denaturing of the initially synthesized system.

This disappearance of the line at 2.69 eV shows that the initially synthesized NSTs are no more present on the highly diluted films. In our opinion, a process, similar to the one at play in the transformation from the 'fresh' film of NSTs to the 'aged' one, is responsible for our observations. As the dilution is increased, the chemical equilibrium between ligands bound to and stabilizing the colloidal crystal and those diluted in the solution is pushed to the latter. With the dilution, the ligands tend to untie from the surface of the NSTs. The desorption

of ligands, leave the facets of NPLs free leading to their aggregation (either directly in the solution or when they are drop-casted on glass). These thicker objects have their emission red-shifted compared to the initial ones, explaining the evolution of the emission spectra.

Different strategies were tried to avoid this aggregation: diluting the NSTs (and NPLs) in polystyrene, in crystalline matrices or adding ligands while diluting to keep the chemical equilibrium constant. However, none of these approaches allowed us to go beyond the problem. A recently published work seems to have overcome the problem of aggregation by replacing the ligands capping the NPLs [156]. It would be very interesting to reproduce the protocol using this new NPLs generation.

VI.3.2 Exciton relaxation dynamics

Another approach, giving access to the EFS, is the study of the relaxation dynamics of the emission as a function of the temperature [53,82,93,157]. As already mentioned in Chapters III and IV, the population of the different levels of the EFS depends greatly on the temperature. For example, at low temperature the lower level will be the main populated one, while, when the temperature increases, 'back-transfer' from this lower level to higher ones can take place. Hence, modeling the evolution of the relaxation dynamics allows one to retrieve some of the parameters of the EFS, especially the bright state-dark state splitting.

The following study has been carried out on NPLs films (5 MLs), since contrary to the case of NSTs, they have a well characterized thickness as well as large lateral dimensions, limiting any important inhomogeneities effects when addressing the time-resolved photoluminescence (TRPL).

a) Experimental results

Films of 5 MLs NPLs used to measure the TRPL are obtained by moderately diluting (typically 50 - 100 times) the initial solution. With these factors of dilution, the aggregation processes described above are not observed. Only the response at 2.69 eV, characteristic of the emission of 5 MLs NPLs is studied here. The TRPL is recorded using two different instruments described in Chapter II: a synchro-scan streak camera, giving access to decays as fast as 10 ps but to a time window limited to 2 ns, and a time-correlated single photon counter (TCSPC) module, with a large time window (µs) but which has an instrument response of ~ 250 ps. The synchro-scan camera is used with a Ti:Sapphire laser pulsed at 82 MHz and doubled in frequency at 410 nm, while a laser diode pulsed at 40 MHz and emitting at 405 nm is used to excite the NPLs, when recording the TRPL with the TCSPC module.

Figures VI.9.a and b show, respectively, the decays measured with the TSCPC module and the synchro-scan camera for different temperatures, as well as, in black, the instrument response function (IRF) of each set-up. Starting with decays recorded with the TCSPC module, below 50 K, bi-exponential decays are observed with a short effective time below the instrument resolution and a long effective time which becomes shorter as the temperature is increased. As well as shortening, the slow component of the decay gains in amplitude over the fast one. Above 50 K, the fast component can not be observed anymore in the TRPL trace acquired with the TSCPC module and the long component dominates the decay. Moreover, a longer tail also appears when $T \geq 65$ K, with an amplitude of only some percent of the overall decay. The following analysis is performed neglecting this long tail of the decay, which is weak in amplitude and only appears at high temperature.

If we now look at the data collected with the synchro-scan camera, the bi-exponential

behavior appears clearly for temperatures above 35 K. Below this temperature, the long decay is too long and weak in intensity to be detected by the synchro-scan camera. However, we see that for every temperature the short lifetime remains measurable and much longer than the IRF of the set-up.

The bi-exponential fit of the decay (obtained with the synchro-scan camera) allows us to measure the fast decay rate, Γ_S, presented in figure VI.9.c, as well as the slow decay rate, Γ_L, for $T \geq 50$ K, presented in figure VI.9.d. From the TRPL measured with the TSCPC module, Γ_L is obtained from a bi-exponential fit for $T \leq 55$ K and a mono-exponential fit for T > 55 K (discarding the remaining long-lived tail). As the temperature increases, Γ_L, as Γ_S, increases. We see that between 55 K and 85 K, there exists some discrepancies in the estimation of Γ_L between the two instruments. In this region, both instruments show their limitations. With the synchro-scan camera the characteristic time is close to the time window and the fit of the decays tends to underestimate the long lifetime. With the TCSPC module, the estimation of lifetime below 1 ns can be impaired by the IRF of the set-up and complex deconvolution of the signal would be needed to obtain a better estimation of Γ_L. All in all, we believe that the range, defined by the Γ_L values retrieved from both instruments, gives a good estimation of the actual Γ_L.

b) Models

The bi-exponential behavior of the TRPL signal is characteristic of a system composed of two emissive states and was already observed in numerous nanocrystals [53, 82, 93, 157]. As already described, the EFS of perovskite nano-objects is composed of a single dark state and a triplet of bright states. In the following, we will consider that the three bright states can be considered as one, since they should all have similar decay rates. The system is thus composed of three levels: the ground state $|G\rangle$, a bright state $|B\rangle$ and a dark state $|D\rangle$, separated from $|B\rangle$ by an energy ΔE. The bright (dark) state is characterized by a relaxation recombination rate Γ_B (Γ_D), with $\Gamma_B > \Gamma_D$. The decay rate of the dark state has a finite value, due to different relaxations in the selection rule (see Chapter IV and ref. [83]). It is important to note here, that the two types of emissive levels are not spectrally resolved and that the collected TRPL arises from the relaxation of both the bright and dark states.

The relaxation dynamics of such a three-levels system have been so far modeled with two mechanisms, which differ in their modeling of the thermalization inside the bright and dark states manifold. Here, we present and confront both models to our experimental observations.

One phonon thermalization

In the 'simplest' of the two models, the thermalization between the bright and dark states is ensured by the absorption and emission of a single phonon whose energy matches the bright state-dark state splitting, ΔE. The systems previously studied in the literature had splitting in the meV range or less, energies corresponding to the range of acoustic phonons. For larger splitting, it is possible to consider that optical phonons could also be used to ensure the thermalization. To the best of our knowledge, this model was first described in ref. [53] for nanocrystals of CdSe. A sketch describing it can be found in figure VI.10.a. With γ_0 the zero temperature rate of the $|B\rangle \rightarrow |D\rangle$ transition (spin relaxation rate) and $n = 1/[\exp\left(-\frac{\Delta_E}{k_B T}\right) - 1]$ the Bose-Einstein phonons number at the temperature T, the rate of the transition $|B\rangle \rightarrow |D\rangle$ at T reads $\gamma_0 + \gamma_{th} = \gamma_0(n+1)$, while the one of the transition $|D\rangle \rightarrow |B\rangle$ is equal to $\gamma_{th} = \gamma_0 n$.

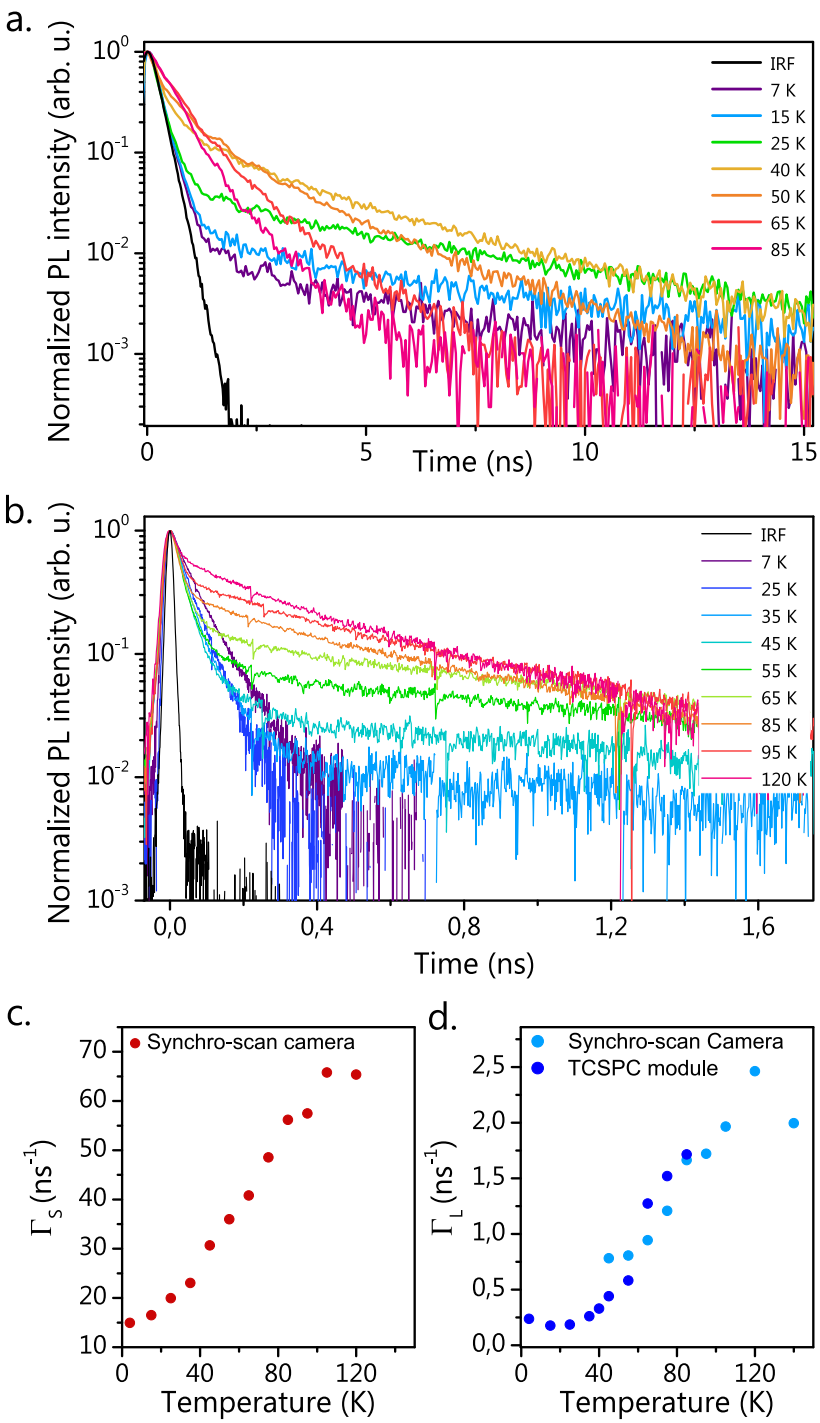

Fig. VI.9 *TRPL of a film of 5 MLs NPLs emitting at 2.69 eV: (a) between 0 and 15 ns, obtained with the TCSPC module and (b) between 0 and 1.6 ns, obtained with the synchro-scan camera. In black the instrument response function (IRF) of each set-up is also plotted. (c) Fast decay constant, Γ_S, obtained from the bi-exponential fits of the synchro-scan TRPL traces and (d) Slow decay constant, Γ_L, obtained from the fits of both synchro-scan and TCSPC module TRPL traces.*

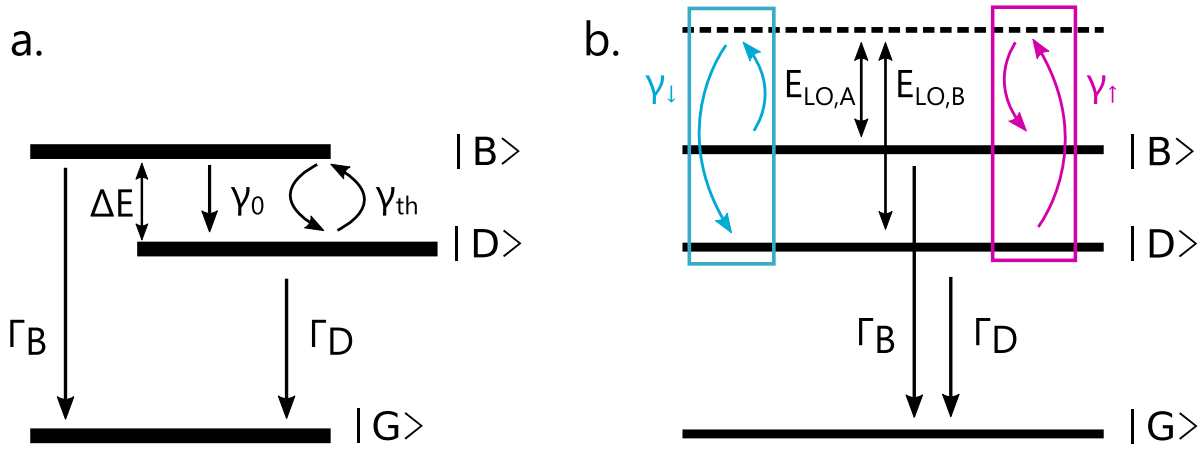

Fig. VI.10 *(a) Three-levels system where the transition between the bright and dark states is ensured by a single phonon, whose energy matches the bright state-dark state splitting, ΔE. (b) Three-levels system where the transition between the bright and dark states is ensured by the simultaneous absorption and emission of two optical phonons at energies $E_{LO,A}$ and $E_{LO,B}$, such that $\Delta E = E_{LO,B}$ -$E_{LO,A}$.*

The population N_B (N_D) of the bright (dark) state can thus be described by the following differential equations:

$$\begin{cases} \frac{dN_B}{dt} = -(\Gamma_B + \gamma_0(n+1))N_B + \gamma_0 n N_D \\ \frac{dN_D}{dt} = -(\Gamma_D + \gamma_0 n)N_D + \gamma_0(n+1)N_B \end{cases} \tag{VI.4}$$

The evolution in time of the bright and dark states populations, $N_B(t)$ and $N_D(t)$, are found by solving these two equations. They both follow a bi-exponential decay characterized by two decay rates that are the eigenvalues of the linear system associated to equation VI.4: the fast decay Γ_S (associated to a 'short' lifetime) and the slow decay Γ_L (associated to a 'long' lifetime), are given by:

$$\Gamma_{S/L} = \frac{1}{2}\left(\gamma_0 \coth\left(\frac{\Delta E}{2k_BT}\right) + \Gamma_B + \Gamma_D \pm \sqrt{(\Gamma_B - \Gamma_D + \gamma_0)^2 + \gamma_0 \sinh^{-2}(\frac{\Delta E}{2k_BT})}\right). \tag{VI.5}$$

The overall photoluminescence intensity being proportional to $N_B(t) + N_D(t)$, the TRPL also decays following a bi-exponential law with the same characteristic rates. We do not enter into the details of the expressions providing the amplitudes of the slow and fast components; even if they allow complementary elements in the analysis. Indeed, our experimental set-up does not allow us to retrieve enough reliable amplitude values throughout the whole temperature range and we limit our analysis to the evolution of the two rates with the temperature.

We thus try to fit the evolution of the experimental values of Γ_S and Γ_L as a function of temperature with equation VI.5. To help in the fitting procedure, we make use of the limit values at low temperature ($k_BT \ll \Delta E$): $\Gamma_L \to \Gamma_D$ and $\Gamma_S \to \Gamma_B + \gamma_0$ and fix the value of Γ_D to 0.15 ns^{-1}, while the sum of $\Gamma_B + \gamma_0$ is kept close to 15 ns^{-1}. Γ_D is actually found to be relatively large for the decay rate of a dark state (an order of magnitude larger than what was found in $FAPbI_3$ [157]). The results of the two most characteristic fits are shown in figure VI.11. The red curves are obtained with $\Delta E = 2$ meV, $\Gamma_B = 7$ ns^{-1} and $\gamma_0 = 7$ ns^{-1}. It

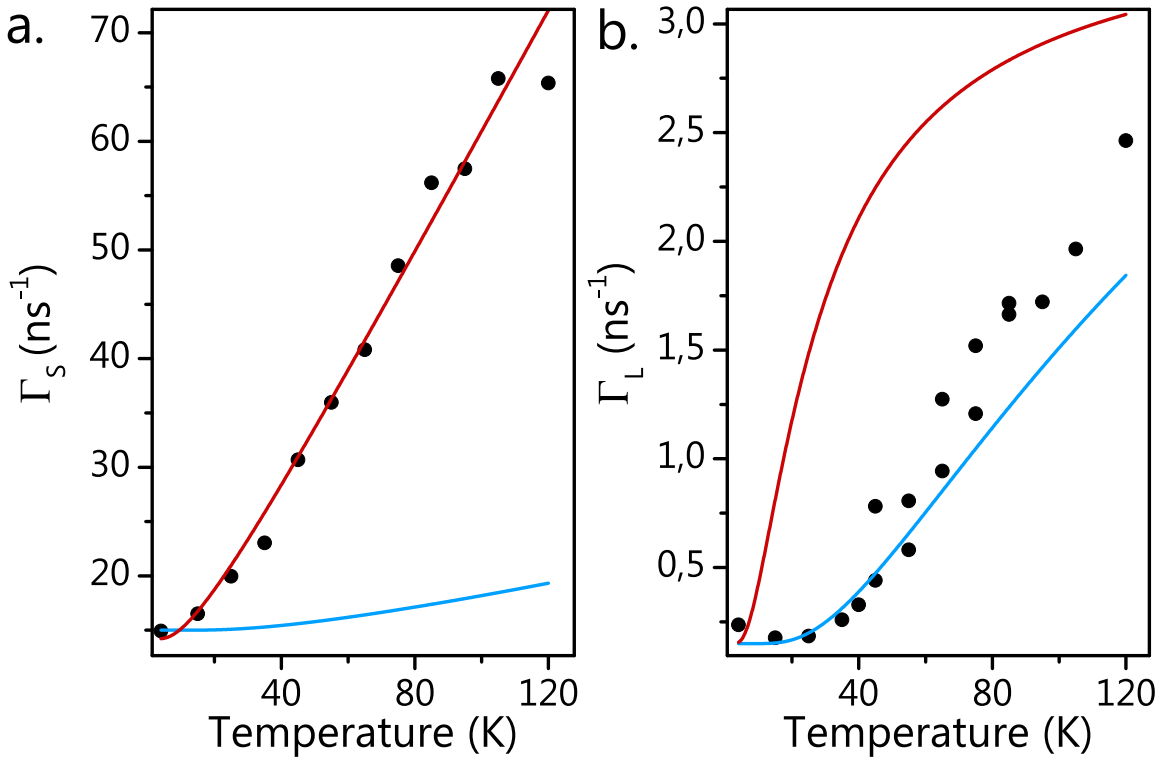

Fig. VI.11 *Adjustment of the experimental data using the one-phonon thermalization process. Evolution with the temperature of: (a) the fast decay rate Γ_S and (b) the slow decay rate Γ_L. The lines are obtained from the fit of Γ_S and Γ_L (equation VI.5) with (in red) ΔE = 2.2 meV, Γ_B = 7 ns^{-1}, Γ_D = 0.15 ns^{-1} and γ_0 = 7.2 ns^{-1} and (in blue) ΔE = 8.9 meV, Γ_B = 10.9 ns^{-1}, Γ_D = 0.15 ns^{-1} and γ_0 = 4.1 ns^{-1}*

fits well $\Gamma_S(T)$, however, it fails to reproduce the evolution of $\Gamma_L(T)$. The blue curves are obtained with ΔE = 9 meV, Γ_B = 11 ns^{-1} and γ_0 = 4 ns^{-1} and inversely $\Gamma_L(T)$ is better adjusted but the evolution of $\Gamma_S(T)$ is not reproduced at all. No set of parameters allowing the adjustment of both Γ_S and Γ_L is found. The same model where the order of bright and dark state is inverted (upper dark state and lower bright one) is also considered (not shown here) but does not improve the adjustment of the curves.

Hence, we are led to conclude that the thermalization between the bright and dark states can not be modeled with a one-phonon mixing mechanism in $CsPbBr_3$ NPLs (under the condition that the properties of the inhomogeneous PL are indeed representative of single NPLs). A second model using a two-phonon mixing mechanism is thus also tested.

Two-phonon thermalization

In hybride organic-inorganic $FAPbI_3$ and $FAPbBr_3$ nanocrystals, the model described above was also not able to rationalize the evolution of the relaxation dynamics with the temperature [82, 157]. The authors of these works have thus used an alternative model, based on two-phonon thermal mixing. The transition between the bright and dark states is ensured by

the emission and absorption of two longitudinal optical (LO) phonons, LO_A and LO_B, whose difference in energy, $E_{LO,B} - E_{LO,A} = \Delta E$ (see figure VI.10.b).

In this model the transition rate between the upper and lower levels are given by $\gamma_\uparrow$ and $\gamma_\downarrow$ which can be written as [157]:

$$\begin{cases} \gamma_\uparrow = \gamma_0 n_B(1+n_A) \\ \gamma_\downarrow = \gamma_0 n_A(1+n_B) \end{cases} \tag{VI.6}$$

where $n_{A/B} = 1/[\exp\left(-\frac{E_{LO,A/B}}{k_B T}\right) - 1]$ are the Bose-Einstein phonons numbers of both optical phonon modes and γ_0 is a two-phonon mixing rate.

The evolution of the bright and dark states populations, N_B and N_D are thus given by:

$$\begin{cases} \frac{dN_B}{dt} = -(\Gamma_B + \gamma_\downarrow)N_B + \gamma_\uparrow N_D \\ \frac{dN_D}{dt} = -(\Gamma_D + \gamma_\uparrow)N_D + \gamma_\downarrow N_B \end{cases} \tag{VI.7}$$

Solving these equations give once again two characteristic decay rates which are, this time, equal to:

$$\Gamma_{S/L} = \frac{1}{2}\left(\Gamma_B + \Gamma_D + \gamma_\uparrow + \gamma_\downarrow \pm \sqrt{(\Gamma_B - \Gamma_D + \gamma_\downarrow - \gamma_\uparrow)^2 + 4\gamma_\uparrow\gamma_\downarrow}\right), \tag{VI.8}$$

with:

$$\begin{cases} \gamma_\uparrow + \gamma_\downarrow = \frac{\gamma_0}{2}(\coth\left(\frac{E_{LO,A}}{2k_B T}\right)\coth\left(\frac{E_{LO,B}}{2k_B T}\right) - 1) \\ \gamma_\downarrow - \gamma_\uparrow = \frac{\gamma_0}{2}(\coth\left(\frac{E_{LO,A}}{2k_B T}\right) - \coth\left(\frac{E_{LO,B}}{2k_B T}\right)) \\ \gamma_\downarrow\gamma_\uparrow = \frac{\gamma_0^2}{16}\sinh^{-2}(\frac{E_{LO,A}}{2k_B T})\sinh^{-2}(\frac{E_{LO,B}}{2k_B T}) \end{cases} \tag{VI.9}$$

Due to the large number of parameters and the complexity of equation VI.8, it is difficult to perform a proper fit of the experimental data, when leaving all the parameters free. Instead, we decide to compare our experimental values to the evolution given by equation VI.8 for different fixed values of the ΔE parameter. To do so, we estimate the values of Γ_B and Γ_D from the low temperature limits. In this model, one has $\Gamma_S \to \Gamma_B$ and $\Gamma_L \to \Gamma_D$, when $k_B T \ll E_{LO,A/B}$. Hence, we fix $\Gamma_B = 15$ ns^{-1} and $\Gamma_D = 0.15$ ns^{-1}, the values of Γ_S and Γ_L at low temperature. Then, the splitting ΔE is spanned between 5 meV and 20 meV, while γ_0 and the energies of the two phonons, $E_{LO,A/B}$, are left free to adjust the data.

Figure VI.12 shows the results of such a procedure. It is noticeable that the experimental results are better adjusted with this model. ΔE = 12-15 meV leads to the best adjustment of the data; for ΔE = 15 meV (12 meV), with γ_0 = 16.2 ns^{-1} (19.5 ns^{-1}), $E_{LO,A}$ = 3 meV (4 meV) and $E_{LO,B}$ = 18 meV (16 meV). However, we find that a large numbers of sets (γ_0, $E_{LO,A}$, $E_{LO,B}$) leads to an acceptable fit and the discrimination is not achieved yet on the basis of the available data. More data, such as the amplitudes of the different components of the decays, are needed to obtain a more accurate estimation of γ_0, $E_{LO,A}$ and $E_{LO,B}$ as done in ref. [82, 157]. The bright state-dark state splitting found from these adjustments is large compared to what has been measured so far in perovskite nanocrystals, but could be explained by the enhancement of the exchange interactions due to the relatively high level of confinement characterizing these structures.

In the case of hybrid organic-inorganic perovskite several arguments exist to justify the use of a two-phonon thermal mixing model. In $FAPbI_3$, the dark state-brigh state splitting is small (0.3 meV) and due to the existence of an acoustic phonon bottleneck in these small

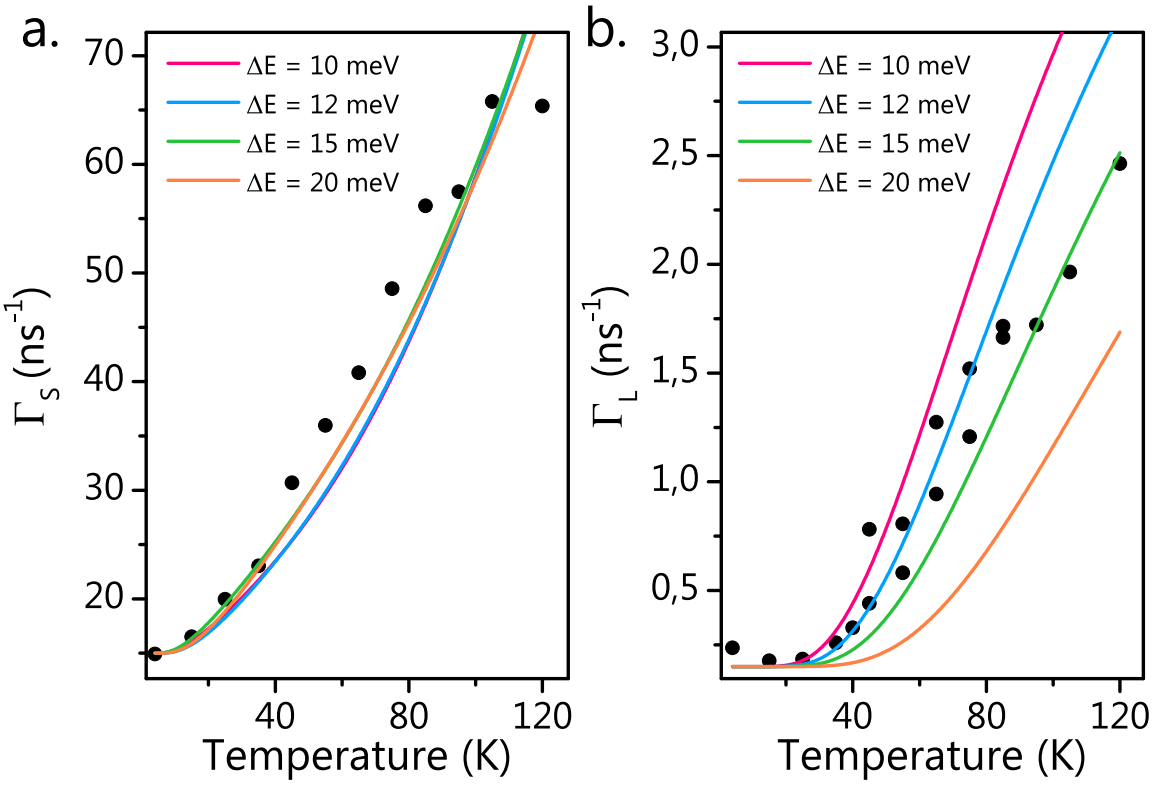

Fig. VI.12 *Simultaneous fits of Γ_S and Γ_L for different fixed values of ΔE and with for the four curves $\Gamma_B = 15$ ns^{-1}, $\Gamma_D = 0.15$ ns^{-1} and in: (pink) $\gamma_0 = 12.5$ ns^{-1}, $E_{LO,A} = 3$ meV and $E_{LO,B} = 13$ meV, (blue) $\gamma_0 = 19.5$ ns^{-1}, $E_{LO,A} = 4$ meV and $E_{LO,B} = 16$ meV, (green) $\gamma_0 = 16.2$ ns^{-1}, $E_{LO,A} = 3$ meV and $E_{LO,B} = 18$ meV and (orange) $\gamma_0 = 25$ ns^{-1}, $E_{LO,A} = 4$ meV and $E_{LO,B} = 24$ meV.*

nanocrystals ($\sim$ 10 nm), there are no acoustic phonons available around these small energies. Moreover the Fröhlich coupling with optical phonon was shown to be large in these structures, justifying the use of the two-phonon mixing model [157]. In $FAPbBr_3$, the bright state-dark state splitting is found to be much larger (3 meV), but at energies larger than the acoustic phonon modes and smaller than the LO phonon ones, justifying that a more complex relaxation process (combining two phonons) would be at play. However, in the case of $CsPbBr_3$ NPLs it is not so clear why a two-phonon mixing model would be necessary. Indeed, at $\Delta E = 12$-15 meV, there should exist optical phonon modes allowing the transitions from bright to dark states in a one-phonon process [158–160]. This value of 12-15 meV for the bright state-dark state splitting can only be seen as a first estimation, keeping in mind that important improvements would be expected from the extraction of the fast and slow components amplitudes.

The difficulties met to reconcile the experimental data with a thermalization model show, in our opinion, that the TRPL traces measured here are still hindered by some inhomogeneities and could not be treated as representative of the intrinsic dynamics of $CsPbBr_3$ NPLs. The measurements are performed on a continuously covered film instead of single objects like the work described in ref. [53, 82, 157]. Even if inhomogeneities in thicknesses or in the lateral sizes of the NPLs can be discarded, inhomogeneities in the surface passivation of the NPLs

or in the dielectric environment could still hinder the measurement of the actual dynamics. The long tail in the decays at high temperature, which was neglected in the analysis above, should also be included in a forthcoming analysis. It is also important to realize that the models described above consider relaxation rates for the bright and dark states independent of the temperature. However, it is possible that non-radiative channels open as the temperature is increased, modifying the value of Γ_B and Γ_D. The study of the dynamics at the single NPLs scale would, in addition, allow one to prevent any NPLs interactions interfering in the dynamics.

Conclusion

In the first section, the very general properties of the lead halide perovskite semiconductor are presented, insisting on the differences between this material and II-VI types semiconductors. Then, in the second section, we present a combined study (structural and optical) of nanosticks (NSTs) and nanoplatelets (NPLs). We show that a basic model considering only confinement in a single direction is enough to explain the evolution of the exciton transition energies with the thickness in a system where the lateral confinement effects can be neglected ('stitched' NSTs and large area NPLs). In NSTs, the transition energy is characterized by a confinement of the exciton along both the width and the thickness direction. Our investigations also show the moderate structural stability of the synthesized systems, which hinders the general study of the excitonic properties. The monitored evolution from the 'fresh' to the 'aged' film is, in our opinion, due to the aggregation of thin NSTs leading to the formation of thicker and larger objects. This is a typical illustration of the issue that has to be overcome. Another instance of the tenuous stability was experienced in the course of the dilution process that should classically provide an access to the single NPL study. Attempts to obtain single NPLs' and NSTs' PL response were not successful. Hence, in the last section, the EFS main structure was addressed under the angle of the PL dynamics. The comparison between the experimental data and models using one and two-phonon mixing does not allow us to retrieve the bright state-dark state splitting with a high confidence. Following this work, we will focus on NPLs stabilized by a new kind of ligands preventing the aggregation of these objects upon dilution [156]. Such modifications will open the path to single object spectroscopy. From there, the role of the confinement in the electronic fine structure could be studied through the study of NPLs with different thicknesses. To complete these experimental investigations, theoretical calculations of the exchange interactions in these perovskite NPLs and NSTs are under way, leading to an estimation of the splitting between the different excitonic levels.

Conclusion

In this work, we studied the excitonic properties through optical means of three different 2D colloidal nano-structures: core/crown CdSe/CdTe nanoplatelets (NPLs), core/alloyed crown CdSe/$CdSe_{1-x}Te_x$ NPLs and $CsPbBr_3$ inorganic perovskite NPLs.

In Chapters III and IV, a study of the indirect exciton in core/crown CdSe/CdTe NPLs is presented. First, the basic optical properties of this original hetero-structure (absorption and photoluminescence) have been studied as a function of the temperature, highlighting the large linewidth of the indirect exciton emission. The observation of single NPLs emission, coupled to numerical simulations, allowed us to show that the emission is dominated by the recombination of the neutral indirect exciton. This exciton is strongly coupled to an optical phonon at ~ 20 meV, as seen from the numerous vibronic replicas observable in the emission spectra of single NPLs. On top of this large exciton-phonon coupling, the emission spectrum is furthermore broadened by spectral diffusion. This phenomenon has its origin in the fluctuations of the electro-static environment, modifying the energy of the excitonic transitions. The numerical simulations showed that the apparition of charges on the surface of the NPL or at its hetero-interface could be held responsible for the shifts in energy observed experimentally.

While single object spectroscopy did not allow us to undertake the study of the electronic fine structure, this point was addressed with the help of high magnetic field experiments performed at the High Field Magnet Laboratory in Nijmegen. The degree of polarisation, as well as the time-resolved luminescence, were recorded as a function of the magnetic field. From these measurements, we characterized the spin relaxation lifetime of the indirect exciton to be above 500 ns at low temperature. Moreover, an excitonic fine structure composed of two linearly polarized bright states is highlighted through the measurements of the degree of circular polarization, consistent with the theoretical predictions. A modeling of these data allowed us to estimate the bright state-bright state splitting to be ~ 50 µeV. The measurements also pointed to a relatively weak coupling between the bright and dark states in these structures.

At present time, the position of the dark states in the electronic fine structure remains an open question. In our opinion, self-organized films of NPLs would greatly help in tackling this issue. Indeed, it was demonstrated that phases of perfectly 'flat-lying' and 'edge-lying' NPLs could be prepared resorting to an interfacial self-assembly method in solution [129]. With such systems, the effects of the magnetic field would be the same for all the objects in the film, instead of a mix of different effects (splitting and mixing of the excitonic levels), as observed here in a randomly oriented film of NPLs. It would thus be much easier to model the experimental data, to isolate the Faraday and Voigt configurations in the studies and to finally pinpoint the dark states signature. Parallel to such experimental works, theoretical study should be undertaken to estimate the magnitude of the exchange interactions in these hetero-structures, helping in the determination of the dark states position. Perspectives lie also in the synthesis and study of a similar hetero-structure: core/shell CdSe/CdTe NPLs,

where the CdTe domains would be grown vertically, instead of laterally, on the initial CdSe core. These structures would show a different symmetry, somewhat closer to the one of type-II epitaxial quantum wells and superlattices, allowing one to study the impacts of the symmetry on the excitonic properties. The effect of charge defects at the interface could also be modulated compared to the core/crown geometry where the interface extension weekly depends on the NPL size.

In Chapter V, an alternative hetero-structure was studied, with an alloyed $CdSe_{1-x}Te_x$ crown. For Te content, x, ranging between 0.6 and 0.8, the NPLs film show a striking bicolor emission, as the recombinations from both the indirect exciton and the direct exciton of the crown take place. Single NPLs responses study showed that this bicolor emission was indeed intrinsic to single objects. Following a simple thermodynamic approach, we showed that the bicolor emission arises from a competition between two driving forces which are: (i) the band offsets between the core and the crown, and (ii) the binding energy of the direct exciton of the crown. When the amplitudes of these two parameters are similar, the formation of the indirect exciton is not so energetically favorable, leading to the appearance of the crown direct exciton emission. The time-resolved photoluminescence was recorded in these NPLs for different Te content and showed that a non-radiative transfer was at play when the Te amount increases. Even if it was not demonstrated in this work, the opening of this relaxation channel is very likely associated with the formation of the indirect exciton, whose importance clearly increases in the photoluminescence spectrum as x increases. Future works should thus consider the mechanisms by which the indirect exciton is formed, regarding the dynamical aspects, as done in non-alloyed systems [25, 27].

Finally, in Chapter VI, a preliminary study of the exciton properties in cesium lead bromide 2D structures was presented. The structural characterization of nanosticks and nanoplatelets was done from their optical properties and transmission electron microscopy imaging. A simple model considering an infinite barrier potential along one (NPLs) or two directions (nanosticks) allows us to rationalize the evolution of the excitonic energy transitions as a function of the thickness. We evidenced the 'stitching' of nanosticks deposited in films with time, leading to the formation of thicker objects. Despite numerous efforts, it was impossible to reach the single NPL response and thereby address the electronic fine structure. It is clear that the aggregation, probably occurring in the course of the dilution process, systematically hindered the study of single NPL properties through classical micro-spectroscopy. Another approach was thus considered by recording the time-resolved photoluminescence of relatively dense films. The dynamics of the photo-luminescence can be described by bi-exponential decays, as expected from previous works and theoretical considerations. Nonetheless, the existing models developed in the literature did not allow us to finely adjust our experimental data, leading us to think that our measurements were still severely affected by inhomogeneities due to the large numbers of objects under study and their possible interaction.

After this first attempt, a lot of work remains to be done on these perovskite NPLs. First the study of NPLs with a new kind of ligands that prevent aggregation upon dilution is planned in order to observe single NPLs responses [156]. Important fundamental studies could then be considered: systematic study of the excitonic fine structure as a function of the thickness will provide data for theoretical and numerical investigations and the estimation of the exchange interaction in highly confined inorganic perovskite materials. On a longer time-scale, additional magneto-optical studies could also help characterize the exciton structure (Bohr radius) through the study of the diamagnetic shift as done in CdSe NPLs [161]. Finally the investigation of spin relaxation and spin coherence properties in perovskite materials are

still in their early stages and have so far only considered bulk-like materials [162, 163]. It is now time to start exploring the spin properties and the spin control possibility in perovskite systems exhibiting a strong confinement.

Appendix A

Dielectric contrast effect

In core-crown CdSe/CdTe NPLs the fine structure of indirect excitons was found to be composed of two linearly polarized states associated to dipoles contained in the NPL plane and having orthogonal orientations [80]. Due to the large difference in the dielectric constant of the CdSe and CdTe semiconductor materials and the surrounding medium (vacuum in the case of the single NPLs study and polystyrene in the case of the magneto-optical study) the electric field penetrating the NPL is reduced. This local field effect drastically depends on the nanocrystal geometry and changes the photon coupling to an exciton [44]. In order to reach a realistic estimation of the field modification in a simplified picture, NPLs are modelled as flattened homogeneous ellipsoids of revolution ($\epsilon_{CdSe} \approx \epsilon_{CdTe} = \epsilon_{in}$, ϵ being the relative permittivity) characterized by the semi-axis length a, b and c (in the X, Y and Z directions respectively).
The projection of the electric field inside, E_α^{in}, and outside, E_α^{out}, the nanocrystal ($\alpha = X$, Y, Z) are related as [44]:

$$E_\alpha^{in} = \frac{E_\alpha^{out}}{1 + n^\alpha(k-1)} \, , \tag{A.1}$$

where $k = \epsilon_{in}/\epsilon_{out}$ and n^α is the depolarisation factor along the direction α. Calculations by Landau and Lifshitz [164] provide:

$$n^\alpha = \frac{1}{2}abc \int_0^\infty \frac{ds}{(s+\beta^2)\sqrt{(s+a^2)(s+b^2)(s+c^2)}} \, , \tag{A.2}$$

with β= a (for $\alpha = X$), b ($\alpha = Y$) or c ($\alpha = Z$).

The probability to emit light for each level composing the fine structure is reduced by the screening factor, $D_\alpha = (E_\alpha^{in}/E_\alpha^{out})^2$ [83].

The following table summarizes the values found for each types of NPLs studied in Chapters III and IV, with $\epsilon_{in} = 10$, $\epsilon_{out} = \epsilon_{ligands} = 2$ when the NPLs are directly dropcasted on glass (Chap. III) and $\epsilon_{out} = \epsilon_{polystyrene} = 2.7$ when the NPLs are embedded in polystyrene (Chap. VI). The ratio D_X/D_Y is proportional to the ratio of the intensities emitted along the X and Y axes of the NPLs.

	a	b	c	n^X	n^Y	$\epsilon_{in}/\epsilon_{out}$	D_X/D_Y
LC NPLs (Chap. III)	65	18	1.3	0.0093	0.0638	5	1.5
SC NPLs (Chap. III)	33	19	1.3	0.0247	0.0557	5	1.2
NPLs of Chap. IV	50	20	1.3	0.0143	0.0559	3.7	1.2

Appendix B

Time-resolved DCP

Finally, we were interested in modelling the evolution of the *DCP* in time. To keep the calculation tractable, the development is based on the assumption that the medium is composed of 'flat' lying NPLs only. To compute *DCP* as a function of time, we consider the evolution of the population $N_+(t)$ and $N_-(t)$ under a pulsed excitation. In this case the evolution of the populations in time after a laser pulse can be described by the differential equations:

$$\begin{cases} \frac{dN_+}{dt} = -(\Gamma + \frac{\gamma}{2})N_+ + \frac{\bar{\gamma}}{2}N_- \\ \\ \frac{dN_-}{dt} = -(\Gamma + \frac{\bar{\gamma}}{2})N_- + \frac{\gamma}{2}N_+ \end{cases} \tag{B.1}$$

Solving Equations (B.1), with $N_+(0)$ and $N_-(0)$ as the initial population just after the absorption of the laser pulse, gives:

$$\begin{pmatrix} N_+(t) \\ N_-(t) \end{pmatrix} = Ae^{-\lambda_1 t}\begin{pmatrix} 1 \\ \frac{\gamma}{\bar{\gamma}} \end{pmatrix} + Be^{-\lambda_2 t}\begin{pmatrix} 1 \\ -1 \end{pmatrix} \tag{B.2}$$

with:

$$\begin{cases} \lambda_1 = \Gamma \\ \lambda_2 = \Gamma + \frac{\gamma+\bar{\gamma}}{2} \end{cases} \quad \text{and} \quad \begin{cases} A = \frac{\bar{\gamma}}{\gamma+\bar{\gamma}}(N_+(0) + N_-(0)) \\ \\ B = \frac{1}{\gamma+\bar{\gamma}}(\gamma N_+(0) + \bar{\gamma}N_-(0)) \end{cases} \tag{B.3}$$

The *DCP(t)* being defined as $DCP(t) = \frac{I_+(t)-I_-(t)}{I_+(t)+I_-(t)}$, it can be written, with the help of Equations (ref) and (B.2), as:

$$DCP(t) = sin(2\alpha)[\frac{2}{\gamma+\bar{\gamma}}\frac{\gamma N_+(0) - \bar{\gamma}N_-(0)}{N_+(0)+N_-(0)}e^{-\frac{\gamma+\bar{\gamma}}{2}t} - DCP_{eq}] \tag{B.4}$$

where

$$sin(2\alpha) = \frac{g_{ex}\mu_B B}{\sqrt{(g_{ex}\mu_B B)^2 + \delta_1^2}} \quad \text{and} \quad DCP_{eq} = tanh(\frac{\delta}{2k_B T}) \tag{B.5}$$

The *DCP* is damped with a time constant equal to $\tau_s = \frac{2}{\gamma+\bar{\gamma}}$ which is usually referred in the literature as the spin relaxation lifetime. In our work it was obtained from an exponential fit of the time-resolved *DCP* that is itself obtained from the σ^+/σ^- analysis of the time resolved PL.

Appendix C

Observation of quantum beats with photo-induced differential transmission

The platelets being arranged flatwise in the sample, their eigen-axes X and Y are in the plane orthogonal to the common direction of the pump and probe beams. The present calculation of the photo-induced differential transmission of the probe beam, in the case of collinear polarizations for both beams, is made following the lines of [119], and especially the ones of its appendix B.
After a pump pulse has passed through a platelet, at t=0, the quantum state of this platelet is described by the populations $\rho_X(t)$ and $\rho_Y(t)$ of the $|X\rangle$ and $|Y\rangle$ states:

$$\begin{cases} \rho_X(t) = cos^2\theta sin^2\Omega_0\tau e^{-t/\tau_R} \\ \rho_Y(t) = sin^2\theta sin^2\Omega_0\tau e^{-t/\tau_R} \end{cases} \tag{C.1}$$

where θ is the angle of the linear polarization with the X axis ($-\pi/2 \leq \theta < +\pi/2$), Ω_0 is the Rabi frequency associated to the pump pulse, τ is the time integral of the normalized pulse profile, τ_R is the recombination time of the $|X\rangle$ and $|Y\rangle$ excitons; and by the coherence $\rho_{XY}(t)$ between the $|X\rangle$ and $|Y\rangle$ states:

$$\rho_{YX}(t) = sin\theta cos\theta sin^2\Omega_0\tau e^{-i\omega_1 t}e^{-t/T_2} \tag{C.2}$$

where T_2 is the characteristic coherence time, and $\delta_1 = \hbar\omega_1$ the energy shift between $|X\rangle$ and $|Y\rangle$. The fine-structure splitting δ_1 is assumed not to be resolved by the pump spectral width.

The probe pulse crosses the sample, at time t=Δt, $\Delta t > 0$. The coherent dipole it induces in the platelet is proportional to $[A]\vec{e}_0$, with $\vec{e}_0$ the electric envelope of the probe beam, and $[A]$ a tensor with components:

$$A_{XX} = \rho_g(\Delta t) - \rho_X(\Delta t), \quad A_{YY} = \rho_g(\Delta t) - \rho_Y(\Delta t), \quad A_{YX} = A^*_{XY} = -\rho_{YX}(\Delta t) \tag{C.3}$$

in the X and Y axes; $\rho_g(t) = 1 - \rho_X(t) - \rho_Y(t)$ is the population of the ground state. The eigenvalues $A_\pm$ of $[A]$ are associated to the eigenvectors $\vec{e}_{0\pm}$:

$$\vec{e}_{0+} = \begin{pmatrix} cos\phi \\ -sin\phi e^{-i\omega_1\Delta t} \end{pmatrix}, \quad \vec{e}_{0-} = \begin{pmatrix} sin\phi e^{i\omega_1\Delta t} \\ cos\phi \end{pmatrix}, \tag{C.4}$$

with ϕ defined by:

$$tan(2\phi) = -\frac{|sin2\theta|}{cos2\theta} exp(-(\frac{1}{T_2} - \frac{1}{\tau_R})\Delta t) \tag{C.5}$$

and $0 < \phi < \pi/2$. The electric field $\vec{e}_0$ being expressed in the ($\vec{e}_{0+}$,$\vec{e}_{0-}$) basis: $\vec{e}_0$=$C_+\vec{e}_{0+}$ + $C_-\vec{e}_{0-}$, the electric field radiated by a collection of platelets possesses the expression:

$$\vec{E}_0^{rad} \ \alpha \ C_+A_+\vec{e}_{0+} + C_-A_-\vec{e}_{0-} \tag{C.6}$$

Finally, the mean power of the probe beam after the sample writes:

$$P_{probe} \ \alpha \ |\vec{e}_0 + K\vec{E}_0^{rad}|^2, \tag{C.7}$$

where K is a real and negative constant. After calculation, P_{probe} is found to be:

$$P_{probe} \ \alpha \ 1+K[2-sin^2\Omega_0\tau(3+cos^2 2\theta)e^{-\Delta t/\tau_R} - sin^2\Omega_0\tau|sin2\theta|sin2\theta e^{-\Delta t/T_2}cos\omega_1\Delta t] \tag{C.8}$$

And, noting P^0_{probe} the probe power in absence of the pump beam, the signal of photo-induced differential transmission reads:

$$\frac{P_{probe} - P^{(0)}_{probe}}{P^{(0)}_{probe}} \ \alpha \ [(3 + cos^2 2\theta)e^{-\Delta t/\tau_R} + |sin2\theta|sin2\theta e^{-\Delta t/T_2}cos\omega_1\Delta t]sin^2\Omega_0\tau \tag{C.9}$$

Appendix D

Numerical calculations of the exciton energy in large $CsPbBr_3$ nanoplatelets

A NPL of thickness L_z and of lateral dimensions L_x, $L_y \gg L_z$ is considered. The dielectric constants are defined as ϵ_1 in the NPL and ϵ_2 outside the NPL.

The Hamiltonian describing the exciton in such a NPL can be written:

$$H = H_0^e + H_0^h + V_{self}^e(\mathbf{r_e}) + V_{self}^h(\mathbf{r_h}) + U(\mathbf{r_e}, \mathbf{r_h}), \tag{D.1}$$

with:

- $H_0^{e/h}$ the Hamiltonian of the free electron/hole in the NPL, such that:

$$H_0^{e/h} = -\frac{\hbar^2}{2m_{e/h}^*}\Delta_{e/h} + V_{conf}(\mathbf{r_{e/h}}), \tag{D.2}$$

  with $V_{conf}(\mathbf{r_{e/h}})$ the confining potential of the electron/hole.

- $V_{self}^{e/h}(\mathbf{r_{e/h}})$ the self-energy of the electron/hole. According to the work of Kumagai et Takagahara [43], these terms can be expressed as:

$$V_{self}^i(\mathbf{r_i}) = \frac{e^2}{4\pi\epsilon_0\epsilon_1} \sum_{n=\pm1,\pm2...} \frac{\beta^{|n|}}{2|z_i - (-1)^2 z_i + nL_z|}. \tag{D.3}$$

- $U(\mathbf{r_e}, \mathbf{r_h})$ the Coulombic interaction between the two carriers, which can be written as [43]:

$$U(\mathbf{r_e}, \mathbf{r_h}) = -\frac{e^2}{4\pi\epsilon_0\epsilon_1} \sum_{n=-\infty}^{n=+\infty} \frac{\beta^{|n|}}{[(\rho_\mathbf{e} - \rho_\mathbf{h})^2 + (z_e - (-1)^n z_h + nL_z)^2]^{1/2}}, \tag{D.4}$$

  where $\rho_\mathbf{i} = (x_i, y_i)$ and $\beta = \frac{\epsilon_1 - \epsilon_2}{\epsilon_1 + \epsilon_2}$.

The independent resolution of the two Hamiltonians H_0^e and H_0^h gives the eigenenergies of a non-interacting electron-hole pair in a quantum well with infinite potential barriers:

$$E_{n_e,n_h} = E_{gap} + E_{n_e}^e + E_{n_h}^h = E_{gap} + n_e^2 \frac{\hbar^2\pi^2}{2m_e^* L_z^2} + n_h^2 \frac{\hbar^2\pi^2}{2m_h^* L_z^2}, \tag{D.5}$$

where n_e and n_h are the electron and hole quantification numbers.

Let us only consider the electron-hole pair ground state energy:

$$E_{1,1} = E_{gap} + E_1^e + E_1^h = E_{gap} + \frac{\hbar^2\pi^2}{2\mu L_z^2}, \tag{D.6}$$

where $\mu = m_e^{*-1} + m_h^{*-1}$ is the reduced mass of the exciton.

To compute the exciton ground state energy, we use the variational method. A 'trial wave-function' for the exciton with one or more parameters is chosen and an estimation of the ground state energy and wave-function is then obtained by minimizing the expectation value of the energy, with respect to these parameters.

As a 'trial' wave-function for the exciton in the NPL we use:

$$\Psi(\mathbf{r_e}, \mathbf{r_h}) = N(a)\frac{e^{i\mathbf{K}_\parallel\cdot\mathbf{R}_\parallel}}{\sqrt{L_x L_y}} \exp\left\{-\frac{1}{a}\sqrt{(x_e - x_h)^2 + (y_e - y_h)^2 + \alpha(z_e - z_h)^2}\right\}\chi(z_e)\chi(z_h), \tag{D.7}$$

where $\chi(z_i) = \sqrt{\frac{2}{L_z}}\cos\left(\frac{\pi z_i}{L_z}\right)$, $\mathbf{R}_\parallel$ and $\mathbf{K}_\parallel$ the position and momentum vectors of the center of mass of the exciton in the $(x,\ y)$ plane of the NPL, finally a and α are the differentiable parameters. Here, the lateral confinement is neglected and the motion of the center of mass of the exciton in the plane of the NPL is described by a plane wave.

The expectation value of the exciton energy given by $\langle\Psi| H |\Psi\rangle$ is thus minimized with respect to a and α and we define $E_b = E_{1,1} - \langle\Psi| H |\Psi\rangle$, which comprises both the binding energy of the exciton, related to the Coulombic interaction, and the self-energy terms, related to dielectric contrast between the NPL and its environment. Figure VI.7 shows the evolution of E_b with L_z for different values of ϵ_2, the dielectric constant of the environment.

Bibliography

[1] A. Ekimov, A. Efros & A. Onushchenko; «Quantum size effect in semiconductor microcrystals»; Solid State Communications **56**, p. 921–924 (1985). 1

[2] R. Rossetti, S. Nakahara & L. E. Brus; «Quantum size effects in the redox potentials, resonance Raman spectra, and electronic spectra of CdS crystallites in aqueous solution»; The Journal of Chemical Physics **79**, p. 1086–1088 (1983). 1

[3] C. B. Murray, D. J. Norris & M. G. Bawendi; «Synthesis and characterization of nearly monodisperse CdE (E = sulfur, selenium, tellurium) semiconductor nanocrystallites»; Journal of the American Chemical Society **115**, p. 8706–8715 (1993). 1

[4] M. A. Hines & P. Guyot-Sionnest; «Synthesis and Characterization of Strongly Luminescing ZnS-Capped CdSe Nanocrystals»; The Journal of Physical Chemistry **100**, p. 468–471 (1996). 1, 14

[5] A. P. Alivisatos; «Semiconductor Clusters, Nanocrystals, and Quantum Dots»; Science **271**, p. 933–937 (1996). 1

[6] J. M. Klostranec & W. C. W. Chan; «Quantum Dots in Biological and Biomedical Research: Recent Progress and Present Challenges»; Advanced Materials **18**, p. 1953–1964 (2006). 1

[7] P. Alivisatos; «The use of nanocrystals in biological detection»; Nature Biotechnology **22**, p. 47–52 (2004). 1

[8] T. Erdem & H. V. Demir; «Colloidal nanocrystals for quality lighting and displays: milestones and recent developments»; Nanophotonics **5**, p. 74–95 (2016). 1

[9] E. Lhuillier & P. Guyot-Sionnest; «Recent Progresses in Mid Infrared Nanocrystal Optoelectronics»; IEEE Journal of Selected Topics in Quantum Electronics **23**, p. 1–8 (2017). 1

[10] T. Yang, F. Li & R. Zheng; «Recent Progress on Cesium Lead Halide Perovskites for Photodetection Applications»; ACS Applied Electronic Materials **1**, p. 1348–1366 (2019). 1

[11] D. V. Talapin, J.-S. Lee, M. V. Kovalenko & E. V. Shevchenko; «Prospects of Colloidal Nanocrystals for Electronic and Optoelectronic Applications»; Chemical Reviews **110**, p. 389–458 (2010). 1

[12] P. Moraitis, R. Schropp & W. van Sark; «Nanoparticles for Luminescent Solar Concentrators - A review»; Optical Materials **84**, p. 636–645 (2018). 1

[13] Y. S. Park, S. Guo, N. S. Makarov & V. I. Klimov; «Room Temperature Single-Photon Emission from Individual Perovskite Quantum Dots»; ACS Nano **9**, p. 10 386–10 393 (2015). 1, 97

[14] S. Ithurria & B. Dubertret; «Quasi 2D colloidal CdSe platelets with thicknesses controlled at the atomic level»; Journal of the American Chemical Society **130**, p. 16 504–16 505 (2008). 1, 22

[15] A. Yeltik, S. Delikanli, M. Olutas, Y. Kelestemur, B. Guzelturk & H. V. Demir; «Experimental Determination of the Absorption Cross-Section and Molar Extinction Coefficient of Colloidal CdSe Nanoplatelets»; Journal of Physical Chemistry C **119**, p. 26 768–26 775 (2015). 1, 32, 88

[16] M. D. Tessier, C. Javaux, I. Maksimovic, V. Loriette & B. Dubertret; «Spectroscopy of Single CdSe Nanoplatelets»; ACS Nano **6**, p. 6751–6758 (2012). 1, 36, 39, 53, 91

[17] B. Guzelturk, Y. Kelestemur, M. Olutas, S. Delikanli & H. V. Demir; «Amplified Spontaneous Emission and Lasing in Colloidal Nanoplatelets»; ACS Nano **8**, p. 6599–6605 (2014). 2

[18] B. Mahler, B. Nadal, C. Bouet, G. Patriarche & B. Dubertret; «Core/Shell Colloidal Semiconductor Nanoplatelets»; Journal of the American Chemical Society **134**, p. 18 591–18 598 (2012). 2

[19] A. Prudnikau, A. Chuvilin & M. Artemyev; «CdSe-CdS nanoheteroplatelets with efficient photoexcitation of central CdSe region through epitaxially grown CdS wings»; Journal of the American Chemical Society **135**, p. 14 476–14 479 (2013). 2

[20] S. Pedetti, S. Ithurria, H. Heuclin, G. Patriarche & B. Dubertret; «Type-II CdSe/CdTe core/crown semiconductor nanoplatelets»; Journal of the American Chemical Society **136**, p. 16 430–16 438 (2014). 2, 16, 22, 29, 32, 35, 36

[21] M. D. Tessier, P. Spinicelli, D. Dupont, G. Patriarche, S. Ithurria & B. Dubertret; «Efficient Exciton Concentrators Built from Colloidal Core/Crown CdSe/CdS Semiconductor Nanoplatelets»; Nano Letters **14**, p. 207–213 (2014). 2

[22] E. L. Ivchenko & G. Pikus; *Superlattices and other heterostructures: symmetry and optical phenomena*; tome 110 (Springer Science & Business Media) (1997). 2, 9, 16, 18, 19

[23] T. S. Shamirzaev, J. Rautert, D. R. Yakovlev, J. Debus, A. Y. Gornov, M. M. Glazov, E. L. Ivchenko & M. Bayer; «Spin dynamics and magnetic field induced polarization of excitons in ultrathin GaAs/AlAs quantum wells with indirect band gap and type-II band alignment»; Physical Review B **96**, p. 035 302 (2017). 2, 15, 16, 19, 61

[24] C. Gourdon & P. Lavallard; «Fine structure of heavy excitons in GaAs/AlAs superlattices»; Physical Review B **46**, p. 4644–4650 (1992). 2, 15, 16, 74, 76

[25] R. Pandya, R. Y. Chen, A. Cheminal, M. Dufour, J. M. Richter, T. H. Thomas, S. Ahmed, A. Sadhanala, E. P. Booker, G. Divitini, F. Deschler, N. C. Greenham, S. Ithurria & A. Rao; «Exciton-Phonon Interactions Govern Charge-Transfer-State Dynamics in CdSe/CdTe Two-Dimensional Colloidal Heterostructures»; Journal of the American Chemical Society **140**, p. 14 097–14 111 (2018). 2, 29, 32, 34, 35, 36, 37, 38, 39, 57, 93, 120

[26] E. Cassette, S. Pedetti, B. Mahler, S. Ithurria, B. Dubertret & G. D. Scholes; «Ultrafast exciton dynamics in 2D in-plane hetero-nanostructures: delocalization and charge transfer»; Physical Chemistry Chemical Physics **19**, p. 8373–8379 (2017). 2, 35, 36, 37, 38

[27] K. Wu, Q. Li, Y. Jia, J. R. McBride, Z.-x. Xie & T. Lian; «Efficient and Ultrafast Formation of Long-Lived Charge-Transfer Exciton State in Atomically Thin Cadmium Selenide/Cadmium Telluride Type-II Heteronanosheets»; ACS Nano **9**, p. 961–968 (2015). 2, 29, 32, 35, 36, 37, 93, 120

[28] R. Scott, S. Kickhöfel, O. Schoeps, A. Antanovich, A. Prudnikau, A. Chuvilin, U. Woggon, M. Artemyev & A. W. Achtstein; «Temperature dependent radiative and non-radiative recombination dynamics in CdSe–CdTe and CdTe–CdSe type II hetero nanoplatelets»; Physical Chemistry Chemical Physics **18**, p. 3197–3203 (2016). 2, 34, 35, 36, 37

[29] L. Protesescu, S. Yakunin, M. I. Bodnarchuk, F. Krieg, R. Caputo, C. H. Hendon, R. X. Yang, A. Walsh & M. V. Kovalenko; «Nanocrystals of Cesium Lead Halide Perovskites ($CsPbX_3$, X = Cl, Br, and I): Novel Optoelectronic Materials Showing Bright Emission with Wide Color Gamut»; Nano Letters **15**, p. 3692–3696 (2015). 2, 97

[30] M. Fu, P. Tamarat, H. Huang, J. Even, A. L. Rogach & B. Lounis; «Neutral and Charged Exciton Fine Structure in Single Lead Halide Perovskite Nanocrystals Revealed by Magneto-optical Spectroscopy»; Nano Letters **17**, p. 2895–2901 (2017). 2, 97, 98, 100, 109

[31] D. Canneson, E. V. Shornikova, D. R. Yakovlev, T. Rogge, A. A. Mitioglu, M. V. Ballottin, P. C. M. Christianen, E. Lhuillier, M. Bayer & L. Biadala; «Negatively Charged and Dark Excitons in $CsPbBr_3$ Perovskite Nanocrystals Revealed by High Magnetic Fields»; Nano Letters **17**, p. 6177–6183 (2017). 2, 55, 76, 77, 97

[32] J. Ramade, L. M. Andriambariarijaona, V. Steinmetz, N. Goubet, L. Legrand, T. Barisien, F. Bernardot, C. Testelin, E. Lhuillier, A. Bramati & M. Chamarro; «Fine structure of excitons and electron–hole exchange energy in polymorphic $CsPbBr_3$ single nanocrystals»; Nanoscale **10**, p. 6393–6401 (2018). 2, 38, 40, 97, 98, 99, 100, 102, 109

[33] M. A. Becker, R. Vaxenburg, G. Nedelcu, P. C. Sercel, A. Shabaev, M. J. Mehl, J. G. Michopoulos, S. G. Lambrakos, N. Bernstein, J. L. Lyons, T. Stöferle, R. F. Mahrt, M. V. Kovalenko, D. J. Norris, G. Rainò & A. L. Efros; «Bright triplet excitons in caesium lead halide perovskites»; Nature **553**, p. 189–193 (2018). 1707.03071. 2, 97, 98, 99, 109

[34] Q. A. Akkerman, S. G. Motti, A. R. Srimath Kandada, E. Mosconi, V. D'Innocenzo, G. Bertoni, S. Marras, B. A. Kamino, L. Miranda, F. De Angelis, A. Petrozza, M. Prato & L. Manna; «Solution Synthesis Approach to Colloidal Cesium Lead Halide Perovskite Nanoplatelets with Monolayer-Level Thickness Control»; Journal of the American Chemical Society **138**, p. 1010–1016 (2016). 2, 97, 98, 100, 103, 104, 106

[35] Y. Bekenstein, B. A. Koscher, S. W. Eaton, P. Yang & A. P. Alivisatos; «Highly Luminescent Colloidal Nanoplates of Perovskite Cesium Lead Halide and Their Oriented Assemblies»; Journal of the American Chemical Society **137**, p. 16 008–16 011 (2015). 2, 97, 103, 104

[36] F. Bertolotti, G. Nedelcu, A. Vivani, A. Cervellino, N. Masciocchi, A. Guagliardi & M. V. Kovalenko; «Crystal Structure, Morphology, and Surface Termination of Cyan-Emissive, Six-Monolayers-Thick $CsPbBr_3$ Nanoplatelets from X-ray Total Scattering»; ACS Nano **13**, p. 14 294–14 307 (2019). 2, 98, 100, 103, 104, 105

[37] H. Haug & S. W. Koch; *Quantum theory of the optical and electronic properties of semiconductors: fivth edition* (World Scientific Publishing Company) (2009). 5, 6, 7

[38] R. Benchamekh, N. A. Gippius, J. Even, M. O. Nestoklon, J.-M. Jancu, S. Ithurria, B. Dubertret, A. L. Efros & P. Voisin; «Tight-binding calculations of image-charge effects in colloidal nanoscale platelets of CdSe»; Physical Review B **89**, p. 035 307 (2014). 6, 9, 10, 48, 50, 94

[39] V. I. Klimov; *Nanocrystal quantum dots* (CRC Press) (2010). 8, 9, 12, 16, 17, 18

[40] M. Richter; «Nanoplatelets as material system between strong confinement and weak confinement»; Physical Review Materials **1**, p. 016 001 (2017). 8, 9, 100

[41] G. Bastard, E. E. Mendez, L. L. Chang & L. Esaki; «Exciton binding energy in quantum wells»; Physical Review B **26**, p. 1974–1979 (1982). 8, 102, 108

[42] F. Rajadell, J. I. Climente & J. Planelles; «Excitons in core-only, core-shell and core-crown CdSe nanoplatelets: Interplay between in-plane electron-hole correlation, spatial confinement, and dielectric confinement»; Physical Review B **96**, p. 035 307 (2017). 9, 45, 48, 50

[43] M. Kumagai & T. Takagahara; «Excitonic and nonlinear-optical properties of dielectric quantum-well structures»; Physical Review B **40**, p. 12 359–12 381 (1989). 9, 129

[44] A. V. Rodina & A. L. Efros; «Effect of dielectric confinement on optical properties of colloidal nanostructures»; Journal of Experimental and Theoretical Physics **122**, p. 554–566 (2016). 10, 41, 102, 123

[45] L. V. Keldysh; «Excitons in Semiconductor–Dielectric Nanostructures»; physica status solidi (a) **164**, p. 3–12 (1997). 10

[46] M. Royo, J. I. Climente, J. L. Movilla & J. Planelles; «Dielectric confinement of excitons in type-I and type-II semiconductor nanorods»; Journal of Physics: Condensed Matter **23**, p. 015 301 (2011). 10

[47] P. Yu & M. Cardona; *Fundamentals of semiconductors: physics and materials properties* (Springer Science & Business Media) (2010). 10, 11

[48] R. C. Hilborn; «Einstein coefficients, cross sections, f values, dipole moments, and all that»; American Journal of Physics **50**, p. 982–986 (1982). 0202029. 11

[49] G. W. p't Hooft, W. A. J. A. van der Poel, L. W. Molenkamp & C. T. Foxon; «Giant oscillator strength of free excitons in GaAs»; Physical Review B **35**, p. 8281–8284 (1987). 11

[50] R. J. Elliott; «Intensity of Optical Absorption by Excitons»; Physical Review **108**, p. 1384–1389 (1957). 11

[51] R. Scott; *Colloidal CdSe nanoparticles : linear and nonlinear properties of the electronic system under high fields and high intensities*; Doctoral thesis; Technische Universität Berlin; Berlin (2017). http://dx.doi.org/10.14279/depositonce-6132. 12

[52] R. Scott, J. Heckmann, A. V. Prudnikau, A. Antanovich, A. Mikhailov, N. Owschimikow, M. Artemyev, J. I. Climente, U. Woggon, N. B. Grosse & A. W. Achtstein; «Directed emission of CdSe nanoplatelets originating from strongly anisotropic 2D electronic structure»; Nature Nanotechnology **12**, p. 1155–1160 (2017). 12

[53] O. Labeau, P. Tamarat & B. Lounis; «Temperature Dependence of the Luminescence Lifetime of Single CdSe/ZnS Quantum Dots»; Physical Review Letters **90**, p. 257 404 (2003). 12, 37, 38, 110, 111, 116

[54] X. Brokmann; *Fluorescence properties of single CdSe nanocrystals*; Theses; Université Pierre et Marie Curie - Paris VI (2004). https://tel.archives-ouvertes.fr/tel-00007873. 13

[55] S. Rudin, T. L. Reinecke & B. Segall; «Temperature-dependent exciton linewidths in semiconductors»; Physical Review B **42**, p. 11 218–11 231 (1990). 13

[56] L. Besombes, K. Kheng, L. Marsal & H. Mariette; «Acoustic phonon broadening mechanism in single quantum dot emission»; Physical Review B **63**, p. 155 307 (2001). 13

[57] S. A. Empedocles & M. G. Bawendi; «Quantum-Confined Stark Effect in Single CdSe Nanocrystallite Quantum Dots»; Science **278**, p. 2114–2117 (1997). 13, 51, 53

[58] S. A. Empedocles & M. G. Bawendi; «Influence of Spectral Diffusion on the Line Shapes of Single CdSe Nanocrystallite Quantum Dots»; The Journal of Physical Chemistry B **103**, p. 1826–1830 (1999). 13, 39, 53

[59] C. de Mello Donegá; «Formation of nanoscale spatially indirect excitons: Evolution of the type-II optical character of CdTe/CdSe heteronanocrystals»; Physical Review B **81**, p. 165 303 (2010). 14, 15, 16

[60] L. P. Fu, F. T. Bacalzo, G. D. Gilliland, R. Chen, K. K. Bajaj, J. Klem & D. J. Wolford; «Microscopic mechanisms governing exciton-decay kinetics in type-II GaAs/AlAs superlattices»; Physical Review B **52**, p. 2682–2687 (1995). 15

[61] L. Butov; «Excitonic devices»; Superlattices and Microstructures **108**, p. 2–26 (2017). 15

[62] K. Park, Z. Deutsch, J. J. Li, D. Oron & S. Weiss; «Single Molecule Quantum-Confined Stark Effect Measurements of Semiconductor Nanoparticles at Room Temperature»; ACS Nano **6**, p. 10 013–10 023 (2012). 15

[63] H. W. van Kesteren, E. C. Cosman, W. A. J. A. van der Poel & C. T. Foxon; «Fine structure of excitons in type-II GaAs/AlAs quantum wells»; Physical Review B **41**, p. 5283–5292 (1990). 15, 16, 17

[64] M. Alloing, M. Beian, M. Lewenstein, D. Fuster, Y. González, L. González, R. Combescot, M. Combescot & F. Dubin; «Evidence for a Bose-Einstein condensate of excitons»; EPL (Europhysics Letters) **107**, p. 10 012 (2014). 15

[65] A. A. High, J. R. Leonard, M. Remeika, L. V. Butov, M. Hanson & A. C. Gossard; «Condensation of Excitons in a Trap»; Nano Letters **12**, p. 2605–2609 (2012). 15

[66] P. Andreakou, S. V. Poltavtsev, J. R. Leonard, E. V. Calman, M. Remeika, Y. Y. Kuznetsova, L. V. Butov, J. Wilkes, M. Hanson & A. C. Gossard; «Optically controlled excitonic transistor»; Applied Physics Letters **104**, p. 091 101 (2014). 15

[67] S. Kim, B. Fisher, H.-J. Eisler & M. Bawendi; «Type-II Quantum Dots: CdTe/CdSe(Core/Shell) and CdSe/ZnTe(Core/Shell) Heterostructures»; Journal of the American Chemical Society **125**, p. 11 466–11 467 (2003). 15

[68] J. E. Halpert, V. J. Porter, J. P. Zimmer & M. G. Bawendi; «Synthesis of CdSe/CdTe Nanobarbells»; Journal of the American Chemical Society **128**, p. 12 590–12 591 (2006). 16

[69] P. T. K. Chin, C. de Mello Donegá, S. S. van Bavel, S. C. J. Meskers, N. A. J. M. Sommerdijk & R. A. J. Janssen; «Highly Luminescent CdTe/CdSe Colloidal Heteronanocrystals with Temperature-Dependent Emission Color»; Journal of the American Chemical Society **129**, p. 14 880–14 886 (2007). 16

[70] J. Nanda, S. A. Ivanov, M. Achermann, I. Bezel, A. Piryatinski & V. I. Klimov; «Light Amplification in the Single-Exciton Regime Using Exciton-Exciton Repulsion in Type-II Nanocrystal Quantum Dots»; The Journal of Physical Chemistry C **111**, p. 15 382–15 390 (2007). 16

[71] D. J. Milliron, S. M. Hughes, Y. Cui, L. Manna, J. Li, L.-W. Wang & A. Paul Alivisatos; «Colloidal nanocrystal heterostructures with linear and branched topology»; Nature **430**, p. 190–195 (2004). 16

[72] M. Jones, S. Kumar, S. S. Lo & G. D. Scholes; «Exciton Trapping and Recombination in Type II CdSe/CdTe Nanorod Heterostructures»; The Journal of Physical Chemistry C **112**, p. 5423–5431 (2008). 16

[73] E. Groeneveld & C. De Mello Donegá; «Enhanced exciton-phonon coupling in colloidal type-II CdTe-CdSe heteronanocrystals»; Journal of Physical Chemistry C **116**, p. 16 240–16 250 (2012). 16, 43, 45

[74] A. Granados del Águila, E. Groeneveld, J. C. Maan, C. de Mello Donegá & P. C. M. Christianen; «Effect of Electron–Hole Overlap and Exchange Interaction on Exciton Radiative Lifetimes of CdTe/CdSe Heteronanocrystals»; ACS Nano **10**, p. 4102–4110 (2016). 16, 77

[75] Q. Li, Z. Xu, J. R. McBride & T. Lian; «Low Threshold Multiexciton Optical Gain in Colloidal CdSe/CdTe Core/Crown Type-II Nanoplatelet Heterostructures»; ACS Nano **11**, p. 2545–2553 (2017). 16

[76] A. H. Khan, G. H. V. Bertrand, A. Teitelboim, C. Sekhar M., A. Polovitsyn, R. Brescia, J. Planelles, J. I. Climente, D. Oron & I. Moreels; «CdSe/CdS/CdTe Core/Barrier/Crown Nanoplatelets: Synthesis, Optoelectronic Properties, and Multiphoton Fluorescence Upconversion»; ACS Nano **14**, p. 4206–4215 (2020). 16

[77] M. Z. Maialle, E. A. de Andrada e Silva & L. J. Sham; «Exciton spin dynamics in quantum wells»; Physical Review B **47**, p. 15 776–15 788 (1993). 16, 18, 78, 79

[78] M. Bayer, G. Ortner, O. Stern, A. Kuther, A. A. Gorbunov, A. Forchel, P. Hawrylak, S. Fafard, K. Hinzer, T. L. Reinecke, S. N. Walck, J. P. Reithmaier, F. Klopf & F. Schäfer; «Fine structure of neutral and charged excitons in self-assembled In(Ga)As/(Al)GaAs quantum dots»; Physical Review B **65**, p. 195 315 (2002). 16, 17, 18, 19, 64, 65, 81

[79] M. I. Dyakonov & A. Khaetskii; *Spin physics in semiconductors*; tome 1 (Springer) (2017). 18

[80] R. Pandya, V. Steinmetz, Y. Puttisong, M. Dufour, W. M. Chen, R. Y. Chen, T. Barisien, A. Sharma, G. Lakhwani, A. Mitioglu, P. C. Christianen, L. Legrand, F. Bernardot, C. Testelin, A. W. Chin, S. Ithurria, M. Chamarro & A. Rao; «Fine Structure and Spin Dynamics of Linearly Polarized Indirect Excitons in Two-Dimensional CdSe/CdTe Colloidal Heterostructures»; ACS Nano **13**, p. 10 140–10 153 (2019). 19, 27, 55, 75, 123

[81] E. V. Shornikova, L. Biadala, D. R. Yakovlev, D. Feng, V. F. Sapega, N. Flipo, A. A. Golovatenko, M. A. Semina, A. V. Rodina, A. A. Mitioglu, M. V. Ballottin, P. C. M. Christianen, Y. G. Kusrayev, M. Nasilowski, B. Dubertret & M. Bayer; «Electron and Hole g -Factors and Spin Dynamics of Negatively Charged Excitons in CdSe/CdS Colloidal Nanoplatelets with Thick Shells»; Nano Letters **18**, p. 373–380 (2018). 1710.00593. 19, 34, 57, 61, 67, 76, 77

[82] P. Tamarat, M. I. Bodnarchuk, J.-B. Trebbia, R. Erni, M. V. Kovalenko, J. Even & B. Lounis; «The ground exciton state of formamidinium lead bromide perovskite nanocrystals is a singlet dark state»; Nature Materials **18**, p. 717–724 (2019). 19, 38, 40, 81, 100, 109, 110, 111, 114, 115, 116

[83] A. V. Rodina & A. L. Efros; «Radiative recombination from dark excitons in nanocrystals: Activation mechanisms and polarization properties»; Physical Review B **93**, p. 155 427 (2016). 19, 81, 111, 123

[84] A. V. Antanovich, A. V. Prudnikau, D. Melnikau, Y. P. Rakovich, A. Chuvilin, U. Woggon, A. W. Achtstein & M. V. Artemyev; «Colloidal synthesis and optical properties of type-II CdSe–CdTe and inverted CdTe–CdSe core–wing heteronanoplatelets»; Nanoscale **7**, p. 8084–8092 (2015). 22

[85] M. Dufour, V. Steinmetz, E. Izquierdo, T. Pons, N. Lequeux, E. Lhuillier, L. Legrand, M. Chamarro, T. Barisien & S. Ithurria; «Engineering Bicolor Emission in 2D Core/Crown CdSe/CdSe 1– x Te x Nanoplatelet Heterostructures Using Band-Offset Tuning»; The Journal of Physical Chemistry C **121**, p. 24 816–24 823 (2017). 22, 39, 53, 85, 88

[86] S. Ithurria, G. Bousquet & B. Dubertret; «Continuous Transition from 3D to 1D Confinement Observed during the Formation of CdSe Nanoplatelets»; Journal of the American Chemical Society **133**, p. 3070–3077 (2011). 22

[87] R. Scott, A. W. Achtstein, A. V. Prudnikau, A. Antanovich, L. D. Siebbeles, M. Artemyev & U. Woggon; «Time-Resolved Stark Spectroscopy in CdSe Nanoplatelets: Exciton Binding Energy, Polarizability, and Field-Dependent Radiative Rates»; Nano Letters **16**, p. 6576–6583 (2016). 29

[88] V. Steinmetz, J. I. Climente, R. Pandya, J. Planelles, F. Margaillan, Y. Puttisong, M. Dufour, S. Ithurria, A. Sharma, G. Lakhwani, L. Legrand, F. Bernardot, C. Testelin, M. Chamarro, A. W. Chin, A. Rao & T. Barisien; «Emission State Structure and Linewidth Broadening Mechanisms in Type-II CdSe/CdTe Core–Crown Nanoplatelets: A Combined Theoretical–Single Nanocrystal Optical Study»; The Journal of Physical Chemistry C **124**, p. 17 352–17 363 (2020). 29

[89] Y.-H. Li, A. Walsh, S. Chen, W.-J. Yin, J.-H. Yang, J. Li, J. L. F. Da Silva, X. G. Gong & S.-H. Wei; «Revised ab initio natural band offsets of all group IV, II-VI, and III-V semiconductors»; Applied Physics Letters **94**, p. 212 109 (2009). 31, 38, 48

[90] Y. Varshni; «Temperature dependence of the energy gap in semiconductors»; Physica **34**, p. 149–154 (1967). 33, 89

[91] M. Tamargo; *II-VI Semiconductor Materials and their Applications*; *Optoelectronic Properties of Semiconductors and Superlattices*, tome 12 (CRC Press) (2002). 33

[92] F. T. Rabouw, J. C. Van Der Bok, P. Spinicelli, B. Mahler, M. Nasilowski, S. Pedetti, B. Dubertret & D. Vanmaekelbergh; «Temporary Charge Carrier Separation Dominates the Photoluminescence Decay Dynamics of Colloidal CdSe Nanoplatelets»; Nano Letters **16**, p. 2047–2053 (2016). 35, 36, 93

[93] L. Biadala, F. Liu, M. D. Tessier, D. R. Yakovlev, B. Dubertret & M. Bayer; «Recombination Dynamics of Band Edge Excitons in Quasi-Two-Dimensional CdSe Nanoplatelets»; Nano Letters **14**, p. 1134–1139 (2014). 35, 36, 37, 60, 110, 111

[94] Q. Li, B. Zhou, J. R. McBride & T. Lian; «Efficient Diffusive Transport of Hot and Cold Excitons in Colloidal Type II CdSe/CdTe Core/Crown Nanoplatelet Heterostructures»; ACS Energy Letters **2**, p. 174–181 (2017). 37, 38, 93

[95] F. V. Antolinez, F. T. Rabouw, A. A. Rossinelli, J. Cui & D. J. Norris; «Observation of Electron Shakeup in CdSe/CdS Core/Shell Nanoplatelets»; Nano Letters **19**, p. 8495–8502 (2019). 41

[96] J. L. Movilla, J. Planelles & J. I. Climente; «Dielectric Confinement Enables Molecular Coupling in Stacked Colloidal Nanoplatelets»; The Journal of Physical Chemistry Letters **11**, p. 3294–3300 (2020). 1912.04182. 41

[97] B. Henderson & G. Imbusch; *Optical Spectroscopy of Inorganic Solids* (Oxford University Press) (2006). 43, 45

[98] S. A. Empedocles, D. J. Norris & M. G. Bawendi; «Photoluminescence Spectroscopy of Single CdSe Nanocrystallite Quantum Dots»; Physical Review Letters **77**, p. 3873–3876 (1996). 45, 50

[99] J. Llusar, J. Planelles & J. I. Climente; «Strain in Lattice-Mismatched CdSe-Based Core/Shell Nanoplatelets»; The Journal of Physical Chemistry C **123**, p. 21 299–21 306 (2019). 45, 48

[100] E. V. Shornikova, D. R. Yakovlev, L. Biadala, S. A. Crooker, V. V. Belykh, M. V. Kochiev, A. Kuntzmann, M. Nasilowski, B. Dubertret & M. Bayer; «Negatively Charged Excitons in CdSe Nanoplatelets»; Nano Letters **20**, p. 1370–1377 (2020). 49

[101] J. Planelles, A. W. Achtstein, R. Scott, N. Owschimikow, U. Woggon & J. I. Climente; «Tuning Intraband and Interband Transition Rates via Excitonic Correlation in Low-Dimensional Semiconductors»; ACS Photonics **5**, p. 3680–3688 (2018). 50

[102] S. Nomura & T. Kobayashi; «Exciton–LO-phonon couplings in spherical semiconductor microcrystallites»; Physical Review B **45**, p. 1305–1316 (1992). 50

[103] M. A. Stroscio & M. Dutta; *Phonons in Nanostructures* (Cambridge University Press) (2001). 51

[104] M. J. Fernée, T. Plakhotnik, Y. Louyer, B. N. Littleton, C. Potzner, P. Tamarat, P. Mulvaney & B. Lounis; «Spontaneous Spectral Diffusion in CdSe Quantum Dots»; The Journal of Physical Chemistry Letters **3**, p. 1716–1720 (2012). 53

[105] A. P. Beyler, L. F. Marshall, J. Cui, X. Brokmann & M. G. Bawendi; «Direct Observation of Rapid Discrete Spectral Dynamics in Single Colloidal CdSe-CdS Core-Shell Quantum Dots»; Physical Review Letters **111**, p. 177 401 (2013). 53

[106] M. J. Fernée, B. Littleton, T. Plakhotnik, H. Rubinsztein-Dunlop, D. E. Gómez & P. Mulvaney; «Charge hopping revealed by jitter correlations in the photoluminescence spectra of single CdSe nanocrystals»; Physical Review B **81**, p. 155 307 (2010). 53

[107] L. Coolen, X. Brokmann, P. Spinicelli & J.-P. Hermier; «Emission Characterization of a Single CdSe-ZnS Nanocrystal with High Temporal and Spectral Resolution by Photon-Correlation Fourier Spectroscopy»; Physical Review Letters **100**, p. 027 403 (2008). 53

[108] D. M. Sagar, R. R. Cooney, S. L. Sewall, E. A. Dias, M. M. Barsan, I. S. Butler & P. Kambhampati; «Size dependent, state-resolved studies of exciton-phonon couplings in strongly confined semiconductor quantum dots»; Physical Review B - Condensed Matter and Materials Physics **77**, p. 1–14 (2008). 53

[109] A. Brodu, M. V. Ballottin, J. Buhot, E. J. van Harten, D. Dupont, A. La Porta, P. T. Prins, M. D. Tessier, M. A. M. Versteegh, V. Zwiller, S. Bals, Z. Hens, F. T. Rabouw, P. C. M. Christianen, C. de Mello Donega & D. Vanmaekelbergh; «Exciton Fine Structure and Lattice Dynamics in InP/ZnSe Core/Shell Quantum Dots»; ACS Photonics **5**, p. 3353–3362 (2018). 55

[110] A. Granados del Águila, G. Pettinari, E. Groeneveld, C. de Mello Donegá, D. Vanmaekelbergh, J. C. Maan & P. C. M. Christianen; «Optical Spectroscopy of Dark and Bright Excitons in CdSe Nanocrystals in High Magnetic Fields»; The Journal of Physical Chemistry C **121**, p. 23 693–23 704 (2017). 55, 60, 81

[111] B. Siarry, B. Eble, F. Bernardot, P. Grinberg, C. Testelin, M. Chamarro & A. Lemaître; «Magnetic-field control of the exciton quantum beats phase in InGaAs/GaAs quantum dots»; Physical Review B **92**, p. 155 315 (2015). 57, 64, 76

[112] B. Siebers, L. Biadala, D. R. Yakovlev, A. V. Rodina, T. Aubert, Z. Hens & M. Bayer; «Exciton spin dynamics and photoluminescence polarization of CdSe/CdS dot-in-rod nanocrystals in high magnetic fields»; Physical Review B **91**, p. 155 304 (2015). 1501.01169. 57

[113] E. Johnston-Halperin, D. D. Awschalom, S. A. Crooker, A. L. Efros, M. Rosen, X. Peng & A. P. Alivisatos; «Spin spectroscopy of dark excitons in CdSe quantum dots to 60 T»; Physical Review B **63**, p. 205 309 (2001). 59

[114] E. V. Shornikova, A. A. Golovatenko, D. R. Yakovlev, A. V. Rodina, L. Biadala, G. Qiang, A. Kuntzmann, M. Nasilowski, B. Dubertret, A. Polovitsyn, I. Moreels & M. Bayer; «Surface spin magnetism controls the polarized exciton emission from CdSe nanoplatelets»; Nature Nanotechnology **15**, p. 277–282 (2020). 60, 81, 82

[115] E. Tsitsishvili, R. v. Baltz & H. Kalt; «Exciton spin relaxation in single semiconductor quantum dots»; Physical Review B **67**, p. 205 330 (2003). 61, 79

[116] M. Trif, P. Simon & D. Loss; «Relaxation of Hole Spins in Quantum Dots via Two-Phonon Processes»; Physical Review Letters **103**, p. 106 601 (2009). 0902.2457. 62

[117] M. Furis, H. Htoon, M. A. Petruska, V. I. Klimov, T. Barrick & S. A. Crooker; «Bright-exciton fine structure and anisotropic exchange in CdSe nanocrystal quantum dots»; Physical Review B **73**, p. 241 313 (2006). 68

[118] W. van der Poel, A. Severens & C. Foxon; «Quantum beats in the exciton emission of type II GaAs/AlAs quantum wells»; Optics Communications **76**, p. 116–120 (1990). 74

[119] F. Bernardot, E. Aubry, J. Tribollet, C. Testelin, M. Chamarro, L. Lombez, P.-F. Braun, X. Marie, T. Amand & J.-M. Gérard; «Linear and dynamical photoinduced dichroisms of InAs/GaAs self-assembled quantum dots: Population relaxation and decoherence measurements»; Physical Review B **73**, p. 085 301 (2006). 74, 127

[120] S. Bar-Ad & I. Bar-Joseph; «Absorption quantum beats of magnetoexcitons in GaAs heterostructures»; Physical Review Letters **66**, p. 2491–2494 (1991). 74

[121] A. I. Tartakovskii, J. Cahill, M. N. Makhonin, D. M. Whittaker, J.-P. R. Wells, A. M. Fox, D. J. Mowbray, M. S. Skolnick, K. M. Groom, M. J. Steer & M. Hopkinson; «Dynamics of Coherent and Incoherent Spin Polarizations in Ensembles of Quantum Dots»; Physical Review Letters **93**, p. 057 401 (2004). 76

[122] M. D'yakonov & V. Perel; «Spin orientation of electrons associated with the interband absorption of light in semiconductors»; JETP **33**, p. 1053 (1971). 79

[123] A. V. Khaetskii & Y. V. Nazarov; «Spin-flip transitions between Zeeman sublevels in semiconductor quantum dots»; Physical Review B **64**, p. 125 316 (2001). 0003513. 79

[124] M. J. Fernée, C. Sinito, Y. Louyer, C. Potzner, T.-L. Nguyen, P. Mulvaney, P. Tamarat & B. Lounis; «Magneto-optical properties of trions in non-blinking charged nanocrystals reveal an acoustic phonon bottleneck»; Nature Communications **3**, p. 1287 (2012). 79

[125] E. V. Shornikova, L. Biadala, D. R. Yakovlev, V. F. Sapega, Y. G. Kusrayev, A. A. Mitioglu, M. V. Ballottin, P. C. M. Christianen, V. V. Belykh, M. V. Kochiev, N. N. Sibeldin, A. A. Golovatenko, A. V. Rodina, N. A. Gippius, A. Kuntzmann, Y. Jiang, M. Nasilowski, B. Dubertret & M. Bayer; «Addressing the exciton fine structure in colloidal nanocrystals: the case of CdSe nanoplatelets»; Nanoscale **10**, p. 646–656 (2018). 80

[126] K. Kowalik-Seidl, X. P. Vögele, B. N. Rimpfl, S. Manus, J. P. Kotthaus, D. Schuh, W. Wegscheider & A. W. Holleitner; «Long exciton spin relaxation in coupled quantum wells»; Applied Physics Letters **97**, p. 011 104 (2010). 80

[127] M. Beian, M. Alloing, E. Cambril, C. G. Carbonell, J. Osmond, A. Lemaître & F. Dubin; «Long-lived spin coherence of indirect excitons in GaAs coupled quantum wells»; EPL (Europhysics Letters) **110**, p. 27 001 (2015). 80

[128] A. Rodina & A. L. Efros; «Magnetic Properties of Nonmagnetic Nanostructures: Dangling Bond Magnetic Polaron in CdSe Nanocrystals»; Nano Letters **15**, p. 4214–4222 (2015). 81

[129] Y. Gao, M. C. Weidman & W. A. Tisdale; «CdSe Nanoplatelet Films with Controlled Orientation of their Transition Dipole Moment»; Nano Letters **17**, p. 3837–3843 (2017). 83, 119

[130] M. Dufour; *Heterostructures, doping and surface chemistry: control of the structure and optical properties of cadmium chalcogenide nanoplatelets*; Theses; Sorbonne Université (2019). https://hal.archives-ouvertes.fr/tel-02305694. 85

[131] R. Tenne, S. Pedetti, M. Kazes, S. Ithurria, L. Houben, B. Nadal, D. Oron & B. Dubertret; «From dilute isovalent substitution to alloying in CdSeTe nanoplatelets»; Physical Chemistry Chemical Physics **18**, p. 15 295–15 303 (2016). 85, 86

[132] H. C. Poon, Z. C. Feng, Y. P. Feng & M. F. Li; «Relativistic band structure of ternary II-VI semiconductor alloys containing Cd, Zn, Se and Te»; Journal of Physics: Condensed Matter **7**, p. 2783–2799 (1995). 85, 86

[133] Y. Kelestemur, B. Guzelturk, O. Erdem, M. Olutas, T. Erdem, C. F. Usanmaz, K. Gungor & H. V. Demir; «CdSe/CdSe 1– x Te x Core/Crown Heteronanoplatelets: Tuning the Excitonic Properties without Changing the Thickness»; The Journal of Physical Chemistry C **121**, p. 4650–4658 (2017). 86, 88, 93

[134] A. W. Achtstein, A. Schliwa, A. Prudnikau, M. Hardzei, M. V. Artemyev, C. Thomsen & U. Woggon; «Electronic Structure and Exciton–Phonon Interaction in Two-Dimensional Colloidal CdSe Nanosheets»; Nano Letters **12**, p. 3151–3157 (2012). 94

[135] K. Heidrich, H. Künzel & J. Treusch; «Optical properties and electronic structure of $CsPbCl_3$ and $CsPbBr_3$»; Solid State Communications **25**, p. 887–889 (1978). 97

[136] «NREL efficiency chart»; `https://www.nrel.gov/pv/cell-efficiency.html`. 97

[137] H. Huang, M. I. Bodnarchuk, S. V. Kershaw, M. V. Kovalenko & A. L. Rogach; «Lead Halide Perovskite Nanocrystals in the Research Spotlight: Stability and Defect Tolerance»; ACS Energy Letters **2**, p. 2071–2083 (2017). 97

[138] F. Hu, C. Yin, H. Zhang, C. Sun, W. W. Yu, C. Zhang, X. Wang, Y. Zhang & M. Xiao; «Slow Auger Recombination of Charged Excitons in Nonblinking Perovskite Nanocrystals without Spectral Diffusion»; Nano Letters **16**, p. 6425–6430 (2016). 97

[139] S. Sun, D. Yuan, Y. Xu, A. Wang & Z. Deng; «Ligand-Mediated Synthesis of Shape-Controlled Cesium Lead Halide Perovskite Nanocrystals via Reprecipitation Process at Room Temperature»; ACS Nano **10**, p. 3648–3657 (2016). 97, 103, 104

[140] J. Cho, H. Jin, D. G. Sellers, D. F. Watson, D. H. Son & S. Banerjee; «Influence of ligand shell ordering on dimensional confinement of cesium lead bromide ($CsPbBr_3$) perovskite nanoplatelets»; Journal of Materials Chemistry C **5**, p. 8810–8818 (2017). 97, 98, 100

[141] S. Hirotsu, T. Suzuki & S. Sawada; «Ultrasonic Velocity around the Successive Phase Transition Points of $CsPbBr_3$»; Journal of the Physical Society of Japan **43**, p. 575–582 (1977). 98

[142] F. Bertolotti, L. Protesescu, M. V. Kovalenko, S. Yakunin, A. Cervellino, S. J. L. Billinge, M. W. Terban, J. S. Pedersen, N. Masciocchi & A. Guagliardi; «Coherent Nanotwins and Dynamic Disorder in Cesium Lead Halide Perovskite Nanocrystals»; ACS Nano **11**, p. 3819–3831 (2017). 98

[143] V. Steinmetz, J. Ramade, L. Legrand, T. Barisien, F. Bernardot, E. Lhuillier, M. Bernard, M. Vabre, I. Saïdi, A. Ghribi, K. Boujdaria, C. Testelin & M. Chamarro; «Anisotropic shape of $CsPbBr_3$ colloidal nanocrystals: from 1D to 2D confinement effects»; submitted to Nanoscale, under minor revisions (2020). 98, 99, 104

[144] J. Even, L. Pedesseau, J.-M. Jancu & C. Katan; «Importance of Spin–Orbit Coupling in Hybrid Organic/Inorganic Perovskites for Photovoltaic Applications»; The Journal of Physical Chemistry Letters **4**, p. 2999–3005 (2013). `arXiv:1309.4215v1`. 99

[145] J. Even; «Pedestrian Guide to Symmetry Properties of the Reference Cubic Structure of 3D All-Inorganic and Hybrid Perovskites»; The Journal of Physical Chemistry Letters **6**, p. 2238–2242 (2015). 99

[146] R. Ben Aich, I. Saïdi, S. Ben Radhia, K. Boujdaria, T. Barisien, L. Legrand, F. Bernardot, M. Chamarro & C. Testelin; «Bright-Exciton Splittings in Inorganic Cesium Lead Halide Perovskite Nanocrystals»; Physical Review Applied **11**, p. 034 042 (2019). 99, 100

[147] P. C. Sercel, J. L. Lyons, N. Bernstein & A. L. Efros; «Quasicubic model for metal halide perovskite nanocrystals»; The Journal of Chemical Physics **151**, p. 234 106 (2019). 99, 100

[148] M. Kepenekian, R. Robles, C. Katan, D. Sapori, L. Pedesseau & J. Even; «Rashba and Dresselhaus Effects in Hybrid Organic–Inorganic Perovskites: From Basics to Devices»; ACS Nano **9**, p. 11 557–11 567 (2015). 99

[149] K. Tanaka, T. Takahashi, T. Kondo, K. Umeda, K. Ema, T. Umebayashi, K. Asai, K. Uchida & N. Miura; «Electronic and Excitonic Structures of Inorganic–Organic Perovskite-Type Quantum-Well Crystal $(C_4H_9NH_3)_2PbBr_4$»; Japanese Journal of Applied Physics **44**, p. 5923–5932 (2005). 100

[150] B. J. Bohn, Y. Tong, M. Gramlich, M. L. Lai, M. Döblinger, K. Wang, R. L. Z. Hoye, P. Müller-Buschbaum, S. D. Stranks, A. S. Urban, L. Polavarapu & J. Feldmann; «Boosting Tunable Blue Luminescence of Halide Perovskite Nanoplatelets through Postsynthetic Surface Trap Repair»; Nano Letters **18**, p. 5231–5238 (2018). 103, 104

[151] C. Huo, C. F. Fong, M.-R. Amara, Y. Huang, B. Chen, H. Zhang, L. Guo, H. Li, W. Huang, C. Diederichs & Q. Xiong; «Optical Spectroscopy of Single Colloidal $CsPbBr_3$ Perovskite Nanoplatelets»; Nano Letters **20**, p. 3673–3680 (2020). 103, 104

[152] Z. Yang, A. Surrente, K. Galkowski, A. Miyata, O. Portugall, R. J. Sutton, A. A. Haghighirad, H. J. Snaith, D. K. Maude, P. Plochocka & R. J. Nicholas; «Impact of the Halide Cage on the Electronic Properties of Fully Inorganic Cesium Lead Halide Perovskites»; ACS Energy Letters **2**, p. 1621–1627 (2017). 104

[153] M. Ozcan, S. Ozen, G. Topcu, M. M. Demir & H. Sahin; «Color-Tunable All-Inorganic $CsPbBr_3$ Perovskites Nanoplatelet Films for Photovoltaic Devices»; ACS Applied Nano Materials **2**, p. 5149–5155 (2019). 104

[154] Z. Dang, B. Dhanabalan, A. Castelli, R. Dhall, K. C. Bustillo, D. Marchelli, D. Spirito, U. Petralanda, J. Shamsi, L. Manna, R. Krahne & M. P. Arciniegas; «Temperature-Driven Transformation of $CsPbBr_3$ Nanoplatelets into Mosaic Nanotiles in Solution through Self-Assembly»; Nano Letters **20**, p. 1808–1818 (2020). 104

[155] D. Sapori, M. Kepenekian, L. Pedesseau, C. Katan & J. Even; «Quantum confinement and dielectric profiles of colloidal nanoplatelets of halide inorganic and hybrid organic-inorganic perovskites»; Nanoscale **8**, p. 6369–6378 (2016). 105

[156] J. Shamsi, D. Kubicki, M. Anaya, Y. Liu, K. Ji, K. Frohna, C. P. Grey, R. H. Friend & S. D. Stranks; «Stable Hexylphosphonate-Capped Blue-Emitting Quantum-Confined $CsPbBr_3$ Nanoplatelets»; ACS Energy Letters **5**, p. 1900–1907 (2020). 110, 117, 120

[157] M. Fu, P. Tamarat, J.-B. Trebbia, M. I. Bodnarchuk, M. V. Kovalenko, J. Even & B. Lounis; «Unraveling exciton–phonon coupling in individual FAPbI3 nanocrystals emitting near-infrared single photons»; Nature Communications **9**, p. 3318 (2018). 110, 111, 113, 114, 115, 116

[158] M. Liao, B. Shan & M. Li; «In Situ Raman Spectroscopic Studies of Thermal Stability of All-Inorganic Cesium Lead Halide ($CsPbX_3$, X = Cl, Br, I) Perovskite Nanocrystals»; The Journal of Physical Chemistry Letters **10**, p. 1217–1225 (2019). 116

[159] Z. Nie, X. Gao, Y. Ren, S. Xia, Y. Wang, Y. Shi, J. Zhao & Y. Wang; «Harnessing Hot Phonon Bottleneck in Metal Halide Perovskite Nanocrystals via Interfacial Electron–Phonon Coupling»; Nano Letters **20**, p. 4610–4617 (2020). 116

[160] J. Ramade, L. M. Andriambariarijaona, V. Steinmetz, N. Goubet, L. Legrand, T. Barisien, F. Bernardot, C. Testelin, E. Lhuillier, A. Bramati & M. Chamarro; «Exciton-phonon coupling in a CsPbBr 3 single nanocrystal»; Applied Physics Letters **112**, p. 072 104 (2018). 116

[161] A. Brumberg, S. M. Harvey, J. P. Philbin, B. T. Diroll, B. Lee, S. A. Crooker, M. R. Wasielewski, E. Rabani & R. D. Schaller; «Determination of the In-Plane Exciton Radius in 2D CdSe Nanoplatelets via Magneto-optical Spectroscopy»; ACS Nano **13**, p. 8589–8596 (2019). 120

[162] V. V. Belykh, D. R. Yakovlev, M. M. Glazov, P. S. Grigoryev, M. Hussain, J. Rautert, D. N. Dirin, M. V. Kovalenko & M. Bayer; «Coherent spin dynamics of electrons and holes in $CsPbBr_3$ perovskite crystals»; Nature Communications **10**, p. 673 (2019). 1810.04081. 121

[163] D. Giovanni, H. Ma, J. Chua, M. Grätzel, R. Ramesh, S. Mhaisalkar, N. Mathews & T. C. Sum; «Highly Spin-Polarized Carrier Dynamics and Ultralarge Photoinduced Magnetization in $CH_3NH_3PbI_3$ Perovskite Thin Films»; Nano Letters **15**, p. 1553–1558 (2015). 121

[164] L. Landau & E. M. Lifshitz; *Course of theoretical Physics, Vol. 8: Electrodynamics of Continuous Media* (Pergamon: Oxford) (1960). 123

Violette STEINMETZ **5 Octobre 2020**

Sujet : Propriétés optiques et excitoniques de nanocristaux colloïdaux 2D: hétéro-structures CdSe/CdTe et nanoplaquettes pérovskite $CsPbBr_3$

Résumé : Les nanoplaquettes (NPLs) colloïdales sont des objets cristallins 2D, obtenus par voie chimique et stabilisés en solution par les ligands qui les entourent. Le fort confinement qui existe dans la direction de leur épaisseur est à l'origine de propriétés intéressantes pour un certain nombre d'applications. Une compréhension des mécanismes fondamentaux en jeu dans ces structures est cependant nécessaire pour les envisager. Cette thèse de doctorat est dédiée à l'étude des propriétés excitoniques de deux types de NPLs. Premièrement, nous étudions des hétéro-NPLs cœur/couronne de CdSe/CdTe, où l'alignement de bande de type-II conduit à la formation d'un exciton indirect (l'électron étant confiné dans le cœur de CdSe et le trou dans la couronne de CdTe). La spectroscopie d'objet unique nous permet de montrer comment le fort couplage exciton/phonon-LO et la diffusion spectrale contribuent à l'élargissement du spectre d'émission. Ensuite, des mesures du degré de polarisation et de luminescence résolue en temps en fonction du champ magnétique permettent de montrer que la structure fine électronique est composée de deux états brillants linéairement polarisés et séparés par une énergie $\delta_1 \sim 50$ µeV. Un temps de relaxation de spin relativement long (> 500 ns) est aussi mis en évidence à 1,6 K. Dans les NPLs cœur/couronne alliagée $CdSe/CdSe_{1-x}Te_x$, une émission bicolore est observée et expliquée par la recombinaison à la fois de l'exciton indirect et de l'exciton direct de la couronne. Finalement, une étude préliminaire est effectuée sur des NPLs pérovskite $CsPbBr_3$. Nous réalisons une caractérisation structurale des objets grâce à des mesures d'optique couplées à de l'imagerie TEM et nous nous identifions les réponses de NPLs, où le confinement est 1D, et celles où un confinement 2D est présent (nanobâtonnets). La dynamique de recombinaison de l'exciton dans ces structures est aussi étudiée et comparée aux modèles théoriques existants basés sur les transferts entre états de la structure fine.

Mots clés : Nanoplaquette, exciton, structure fine électronique, dynamique d'émission, spectroscopie d'objet unique, magnéto-optique

Subject : Optical and excitonic properties of 2D colloidal nanocrystals: type-II CdSe/CdTe core/crown hetero-structures and $CsPbBr_3$ perovskite nanoplatelets

Abstract: Colloidal nanoplatelets (NPLs) are 2D crystalline objects, chemically synthesized, and stabilized by a shell of ligands. Strong and homogeneous quantum confinement in the thickness direction leads to interesting properties for a large field of applications ranging from light display to lasing material. An understanding of the fundamental mechanisms at play in these structures is necessary to consider any of these applications. In this context, this PhD is dedicated to the study of the excitonic properties of two different types of NPLs. First, we study CdSe/CdTe core/crown hetero-NPLs, which support indirect excitons (electron being confined in the CdSe core and the hole being confined in the CdTe crown). Single object spectroscopy allows us to highlight how the strong LO phonon/exciton coupling and the spectral diffusion shape the emission spectrum. Then, measurements of the degree of polarization and time-resolved photoluminescence carried out as a function of the magnetic field allow us to unravel the electronic fine structure of these hetero-NPLs (two linear bright states split by an energy $\delta_1 \sim 50$ µeV dominate the emission). A long spin relaxation lifetime (> 500 ns) is also evidenced at 1.6 K. In core/alloyed crown $CdSe/CdSe_{1-x}Te_x$, a bicolor emission is observed and explained by the recombination of both the spatially indirect exciton and the direct exciton of the CdTe crown. Finally, a preliminary study on $CsPbBr_3$ perovskite NPLs is conducted. We perform a structural characterization of these objects through optical measurements coupled to TEM imaging and highlight the difference between NPLs, characterized by 1D confinement, and nanosticks, where 2D confinement is at play. The exciton recombination dynamics are also studied and compared to the existing models describing the energy relaxation within the fine structure manifold.

Keywords : Nanoplatelet, exciton, electronic fine structure, emission dynamics, single object spectroscopy, magneto-optics